

Mathematical Model of Ventricular Activation in an Anatomically Accurate Deforming Heart

by Gregory Sands

**Supervised by Professor Peter Hunter
and Associate Professor Bruce Smaill**

**A thesis submitted in partial fulfilment of the requirements for the degree of
Doctor of Philosophy at the University of Auckland**



**Department of Engineering Science
School of Engineering
The University of Auckland
New Zealand**

November 1996

Abstract

The last forty years have seen an enormous growth in the physiological understanding of the structure and function of cardiac muscle, and in the creation of mathematical models which attempt to quantify the observed mechanical, electrical and biochemical behaviour of the heart. These models have, in general, been developed independently of one another, and there has been little attempt to integrate the various mechanisms, even though the processes are clearly interdependent.

The work presented in this thesis illustrates the first stages of development of a unified model of cardiac structure and function, with particular reference to modelling cardiac activation. We are building on a base which has already been constructed describing the geometry and microstructure of ventricular muscle. Models of mechanical deformation are also under construction, and this work proposes a solution technique which allows the electrical processes to be integrated with these, and other, models of cardiac structure and function.

A new collocation method is developed which constructs a grid of collocation points defined at specific material locations throughout the ventricular finite element mesh. A finite difference based solution technique uses local metric information to solve the activation equations on this grid. In general, the collocation grid is non-uniformly spaced, and will deform with the movement of the finite element mesh.

This collocation method is used to simulate activation using a multiple-purpose solution program on a range of one, two and three-dimensional geometries, with a number of variations. Initial test simulations in two dimensions examine the performance of the method on a square, isotropic domain using a simple ionic current model to demonstrate convergence with both spatial and temporal

resolution. The various parameters are then changed incrementally to incorporate such variations as an irregular domain, anisotropic conductivities using a range of fibre fields, and various ionic current models. Simulations using multiple stimuli show the effect of anisotropy on reentrant behaviour. The dimensionality of the solution domain is also altered, with a one-dimensional solution showing the interaction of the Purkinje network with a myocardial sheet, and a range of examples are defined on several three-dimensional geometries including a cube and an anatomically accurate ventricular mesh.

We also investigate coupling of the myocardial activation model to two other models of cardiac function. Firstly, the bidomain model is used to couple the myocardial potential solution with a calculation of torso potential. The activation model is also coupled to a model of mechanical deformation. This electromechanical coupling is demonstrated in two dimensions using two ionic current models on both a square domain, and a mesh generated from a ventricular cross-section. A final three-dimensional solution presents preliminary results showing the activation model coupled to a model of deformation in an anatomically accurate ventricular mesh.

Acknowledgements

There are many people to thank for their assistance in the work contributing to this thesis. In particular, I thank my main supervisor, Associate Professor Peter Hunter, who has not only guided and encouraged the work here, but has always chosen to seek for the very best for me, and for all those in his research group. His example is one that every student wishes for in a supervisor. Associate Professor Bruce Smaill has had less to do with the day-to-day workings, but has often cast a keen, and welcome eye on the proceedings.

The lab in which I have worked has always been a competitive and dynamic melting-pot of sensible and irrational ideas. Thanks first and foremost to Martyn Nash, who has worked on complementary research for the same length of time, and who has gracefully consented to finish even later than I do. We began the two halves together, barely hoping to believe that they would be integrated during our postgraduate studies, and have been astonished to see it happen anyway. Many others have come and gone (though some won't leave), and rare wisdom has occasionally come from Chris Bradley, Glen Harris, Ivan Brunton, Curt Hjorring, Mark Sagar, Mark Trew, Karl Tomlinson, and the numerous others who have drifted through. Several faculty and staff members have contributed in different ways — thanks to Andrew Pullan, David Bullivant and Poul Neilsen for useful ideas at necessary times, to Andrew Mason for constant encouragement, and to Jim Greenslade for his time spent helping to create the CDs.

My gratitude to Ian Le Grice and Alistair Hookings for giving me a platform to work from, and my commiserations to Martin Buist who has “volunteered” to try to continue from where I leave off — thanks also, Martin, for allowing me to include your example showing Purkinje fibre activation. Ian, a special thank you for holding

the job for me — I'm sure you'll let me know of plenty of ways I can make it up to you!

To all those (Hi Ellie!) who have kept asking me “How much longer now?” — that question finally has an answer I'm not embarrassed to give. Thanks to Mike and Robyn, the youth group, and lots of other friends for keeping my life outside my thesis interesting.

Thanks to my flatmates (DJ, Ratman and Q), especially for still allowing me to sleep at the flat at nights even if I'm never there any other time (and owe several months rent!). Perhaps my credit card can now shout you guys dinner.

Thank you to my parents for their unfailing support — Mum who completed her second M.A. in no time and Dad who is racing to complete his doctorate before I do (and I only had a few years head start — Good luck!). I've often needed your encouragement, and it has always been there, even from several thousand miles away. Thanks to the rest of my family as well (Megan and Jono, Aunty Val), even if none of you ever quite knew exactly what I was doing.

Big thanks to God — there's a lot more to life than just a thesis.

Finally, and most importantly, I want to give a special thank you to my fiancée Kathryn for her patience, support, encouragement, and love over the past few years, and especially the last, difficult, six months. Your belief in me has helped me when I've been banging my head against a brick wall. Thank you.

To Kathryn, with my love

I dedicate this *Affair with the Heart*
to my *Affair of the Heart*
and having completed the former
I continue forever the latter

Contents

<i>List of Figures</i>	xii
<i>List of Tables</i>	xvi
<i>List of Symbols</i>	xvii
1 Introduction	1
1.1 Modelling cardiac function	3
1.2 Scope of this thesis	5
2 Structure and Function of the Heart	7
2.1 Cardiac Anatomy and Function	8
2.1.1 Macroscopic description	8
2.1.2 Microscopic description	9
2.1.3 Connective tissue structure	14
2.2 Activation	15
2.2.1 Normal activation sequence	15
2.2.2 Activation at a cellular level	17
2.2.3 Cellular resting potential	18
2.2.4 Ion channel behaviour	19
2.2.5 Types of ionic current	20
2.2.6 Action potential shape	21
2.2.7 Excitation-contraction coupling	23
2.2.8 Cellular conduction	25
2.3 Applications For This Research	27
2.3.1 Arrhythmic activation patterns	27
2.3.2 Ischemia	29
2.3.3 Reentrant waves	30

2.3.4	Mechanically-induced changes in electrophysiology	30
2.4	A Cardiac Mapping System	30
3	Cardiac Activation Modelling	32
3.1	Non-Propagating (Dipole) Models	33
3.2	Empirical Models	35
3.2.1	Cellular automata models	36
3.2.2	Huygen's wavefront method	42
3.3	The Bidomain Model	45
3.3.1	Definition of the bidomain framework	47
3.3.2	Mathematical derivation of the bidomain model	49
3.3.3	Applications of the bidomain model	53
4	Ionic Current Models	56
4.1	Biophysically Based Ionic Current Models	57
4.1.1	Hodgkin-Huxley Model	58
4.1.2	Noble (1962) Model	66
4.1.3	McAllister-Noble-Tsien Model	71
4.1.4	Beeler-Reuter Model	82
4.1.5	Ebihara-Johnson Model	87
4.1.6	Drouhard-Roberge Model	91
4.1.7	Di Francesco-Noble Model	93
4.1.8	Luo-Rudy I Model	103
4.1.9	Luo-Rudy II Model	106
4.2	Simplified Ionic Current Models	111
4.2.1	Polynomial Models	112
4.2.2	FitzHugh-Nagumo Model	114
4.2.3	Van Capelle-Durrer Model	117
4.2.4	Karma Model	121
5	The Collocation Model	123
5.1	Existing Solution Techniques	124
5.1.1	The finite difference method	124
5.1.2	The finite element method	128
5.1.3	The need for a new technique	130

5.2	The Finite Element Method	132
5.2.1	Notation	133
5.2.2	Basis functions	134
5.2.3	Base vectors	143
5.2.4	Metric tensors	144
5.2.5	Measures of curvature	146
5.2.6	Reference coordinate systems	147
5.2.7	Material coordinates	150
5.3	Definition of the Collocation-Derived Finite Difference Method	154
5.3.1	Collocation point definition	154
5.3.2	Solution method	157
5.3.3	Tracking a deforming geometry	164
5.3.4	Dynamic tracking of the active region	164
6	Two-Dimensional Activation using the Collocation Method	166
6.1	Accompanying Movie Files	167
6.2	The CMISS Solution Environment	169
6.3	Single Stimulus Activation	170
6.3.1	The initial problem	171
6.3.2	Use of DTAR	173
6.3.3	Convergence	173
6.3.4	Size of time step	174
6.3.5	Resolution of collocation points	176
6.3.6	Convergence implications	177
6.3.7	Non-orthogonal geometry	179
6.3.8	Anisotropy with a constant fibre angle	180
6.3.9	Point stimulus with varying fibre angle	180
6.3.10	Line stimulus with varying fibre angle	183
6.3.11	Using the FitzHugh-Nagumo model	183
6.3.12	Using the van Capelle-Durrer model	186
6.3.13	Biophysically-based models	187
6.4	Reentrant Waves from Multiple Stimuli	189
6.4.1	Point re-stimulus	191

6.4.2	Line re-stimulus	191
6.4.3	Reentry and anisotropy	193
6.5	Using The Bidomain Model	200
6.5.1	The coupled bidomain model	201
6.5.2	Coupling to a torso model	208
6.6	Purkinje Fibre Network	209
6.7	Optimisation of Material Parameters	212
7	Three Dimensional Collocation Solutions	222
7.1	Activation in a Cube	223
7.1.1	Isotropic activation	223
7.1.2	Transversely isotropic conductivities	225
7.1.3	Orthotropic conductivities	227
7.1.4	Variation in fibre angle	227
7.1.5	A reentrant scroll wave	227
7.2	A Finite Element Model of Ventricular Anatomy	230
7.2.1	Ventricular geometry	231
7.2.2	Myocardial fibre orientations	232
7.3	Ventricular Activation	236
7.3.1	Isotropic conductivities	239
7.3.2	Transversely isotropic conductivities	239
7.3.3	Orthotropic conductivities	240
8	Coupled Electromechanics	245
8.1	Weakly-Coupled Electromechanics	246
8.2	Strongly-Coupled Electromechanics	250
8.2.1	Steady-state $[Ca]_i$ -tension relationship	251
8.2.2	Plane wave propagation	252
8.2.3	Spiral wave propagation using the VCD model	255
8.2.4	Using a physiological model of $[Ca]_i$	262
8.2.5	Coupled electromechanics on a 2D cross-section	272
8.3	Coupled Electromechanics on a Ventricular Domain	278
9	Conclusions and Future Work	280

A Hammer Projection	285
B CMISS Command Files	286
B.1 Two-dimensional coupled electromechanics	286
B.2 Three-dimensional coupled electromechanics	289
 <i>References</i>	 295
 <i>Index</i>	 308

List of Figures

2.1	Cross-section of the heart	9
2.2	Cardiac muscle cell structure	10
2.3	Schematic of cardiac microstructure	14
2.4	Schematic of the activation sequence	15
2.5	Action potential configurations in different regions of the mammalian heart	21
2.6	The ventricular action potential	22
2.7	Excitation-contraction coupling	24
2.8	A propagating impulse in a strand of cardiac muscle	25
3.1	Nearest neighbours of an active cell	37
3.2	Action potential from cellular automata model	39
3.3	Change in cell variables	41
3.4	Two-dimensional example of Huygen's wavefront method	43
3.5	The bidomain model	48
4.1	Hodgkin and Huxley electrical circuit representation of the cell membrane	59
4.2	Hodgkin-Huxley sodium gate variables m and h	63
4.3	Hodgkin-Huxley potassium gate variable n	63
4.4	Hodgkin-Huxley action potential and currents	65
4.5	Equivalent electrical circuit for Purkinje fibre membrane.	67
4.6	Noble action potential and gate variables	69
4.7	Ionic currents defined by the Noble model	70
4.8	MNT action potential	72
4.9	MNT sodium current and gate variables m and h	73
4.10	MNT secondary current and gate variables d and f	75
4.11	MNT potassium currents and gate variables s , x_1 and x_2	78
4.12	MNT chloride current and gate variables q and r	79
4.13	MNT background currents	81
4.14	Beeler-Reuter action potential	82
4.15	Beeler-Reuter sodium current and m , h and j gate variables	83
4.16	Beeler-Reuter slow inward current and gate variables d , f and x_1	85
4.17	Beeler-Reuter model of intracellular calcium concentration	86
4.18	Beeler-Reuter time dependent outward current	87
4.19	Beeler-Reuter time-independent potassium current	88

4.20	Beeler-Reuter Ebihara-Johnson action potential	89
4.21	Beeler-Reuter Ebihara-Johnson sodium current	90
4.22	Beeler-Reuter Drouhard-Roberge action potential	91
4.23	Beeler-Reuter Drouhard-Roberge sodium current	92
4.24	Di Francesco-Noble action potential	93
4.25	DFN model: i_f current	95
4.26	DFN model: time-dependent potassium current	96
4.27	DFN model: time-independent potassium current	97
4.28	DFN model: Na^+ - Ca^{2+} exchange current	98
4.29	DFN model: sodium current and gate variables	99
4.30	DFN model: Intracellular calcium concentration	101
4.31	Schematic diagram of the LR-II model	106
4.32	Action potential produced by the LR-II model	108
4.33	Form of the polynomial models	113
4.34	Action potential generated by FitzHugh-Nagumo model	115
4.35	Action potential generated by FitzHugh-Nagumo-Rogers model	116
4.36	Functional form of the VCD model	117
4.37	VCD generated action potential and recovery	119
4.38	" S_1 - S_2 " stimulus protocol	120
4.39	Action potential generated by the Karma model	121
5.1	Finite difference grid	125
5.2	One-dimensional linear element	135
5.3	Bilinear element	136
5.4	Linear basis functions applied to three one-dimensional elements	137
5.5	Quadratic element	138
5.6	Quadratic Lagrange basis functions	139
5.7	Cubic Hermite one-dimensional element	140
5.8	Cubic Hermite Basis Functions	141
5.9	Curvilinear ξ_i -coordinate system defined using finite elements	143
5.10	Description of a vector u in terms of vector components and base vectors	145
5.11	Cylindrical polar coordinate system	148
5.12	Prolate spheroidal coordinate system	149
5.13	Definition of the wall coordinate system	152
5.14	Creation of a collocation grid from a finite element mesh	155
5.15	Definition of material coordinates from fibre direction	156
5.16	Definition of local solution element	159
5.17	No-flux boundary conditions for collocation scheme	161
6.1	Solution points for example square mesh	171
6.2	Isochronal contours of activation time	172
6.3	Correlation between wavefront velocity and conductivity	174
6.4	Influence of time step change	175

6.5	Influence of collocation point density	178
6.6	Activation time isochrones for trapezoidal mesh	179
6.7	Activation times for constant anisotropy	181
6.8	Activation times for varying conductivity ratios	181
6.9	Activation times with a varying fibre angle	182
6.10	Effect of fibre curvature on wavefront propagation	182
6.11	Activation using the FHN model	184
6.12	Activation using the modified Rogers-FHN model	184
6.13	Activation using the modified VCD model	186
6.14	Activation using the Beeler-Reuter ionic current model	188
6.15	Activation using the Beeler-Reuter/Drouhard-Roberge ionic current model	188
6.16	Spiral waves produced from a point stimulus	190
6.17	Spiral wave produced from a line stimulus	192
6.18	Spiral wave in a constant anisotropic domain	194
6.19	Spiral wave with a curved fibre angle	195
6.20	Spiral wave with an S-shaped fibre angle	197
6.21	Spiral wave with an S-shaped fibre angle and the BR model	198
6.22	Previous figure continued	199
6.23	Cubic bidomain equation with zero boundary conditions	203
6.24	FHN bidomain equation with zero boundary conditions	204
6.25	Cubic bidomain equation with no-flux boundary conditions	206
6.26	FHN bidomain equation with no-flux boundary conditions	207
6.27	Partially coupled bidomain model	208
6.28	Grid points on Purkinje fibre network	210
6.29	Activation of tissue through Purkinje network	211
6.30	Electrode configuration for optimisation problem	213
6.31	Sample electrode recordings	214
6.32	Map of activation time	215
6.33	Contour plots of activation time	216
6.34	Activation times using optimised parameters	218
6.35	Activation times of a smaller problem using optimised parameters	220
7.1	Isotropic conductivity in a cube	224
7.2	Transversely isotropic conductivity in a cube	224
7.3	Orthotropic conductivity in a cube	226
7.4	Rotated material coordinate system	226
7.5	Surface transmembrane potential for scroll wave	228
7.6	Approximate wavefront position of scroll wave	229
7.7	Ventricular finite element material coordinates	231
7.8	Finite element model of the ventricular wall geometry	233
7.9	The fibre angle, α	234
7.10	Fibre orientations at the ventricular surfaces.	235

7.11	Collocation grid on ventricular domain	236
7.12	Epicardial activation time for isotropic conductivity	237
7.13	Ventricular solution using isotropic conductivities	238
7.14	Epicardial activation time for transversely isotropic conductivity	240
7.15	Ventricular solution using transversely isotropic conductivities	241
7.16	Epicardial activation time for orthotropic conductivity	242
7.17	Ventricular solution using orthotropic conductivities	243
8.1	The undeformed square membrane	247
8.2	Deformation imposed on membrane	248
8.3	Spiral wave produced on a deforming mesh	249
8.4	Plane waves in an electromechanically coupled domain	253
8.5	Plane waves in an electromechanically coupled domain	254
8.6	Coupled electromechanics with a reentrant wave	256
8.7	Coupled electromechanics with a reentrant wave	257
8.8	Two spiral waves with $\tau_{Ca} = 20$	259
8.9	Two spiral waves with $\tau_{Ca} = 30$	260
8.10	Two spiral waves with $\tau_{Ca} = 50$	261
8.11	Isotropic conductivity using the Beeler-Reuter model on a non-deforming mesh	265
8.12	2:1 conductivity on a non-deforming mesh with a constant fibre field	266
8.13	2:1 conductivity on a non-deforming mesh with a varying fibre field	267
8.14	Isotropic conductivity on a deforming mesh with fixed edges	269
8.15	2:1 conductivity on a deforming mesh with a constant fibre field	270
8.16	2:1 conductivity on a deforming mesh with a varying fibre field	271
8.17	Isotropic conductivity on a deforming mesh with sliding edges	273
8.18	2:1 conductivity on a deforming mesh with a constant fibre field	274
8.19	2:1 conductivity on a deforming mesh with a varying fibre field	275
8.20	Undeformed finite element mesh for heart cross-section	276
8.21	Activation on a 2D heart cross-section	277

List of Tables

2.1	Normal activation sequence	17
2.2	Intracellular and extracellular ion concentrations and equilibrium potentials .	19
3.1	State table for three-state cellular automata model	38
3.2	State table for a two variable cellular automata model	40
4.1	Values of the constants in the Hodgkin-Huxley equations.	64
4.2	Values of the constants in the Noble model.	71
4.3	MNT constants	72
4.4	Constants used in the Beeler-Reuter model.	88
4.5	Currents in the LR-II model	107
4.6	Modified VCD parameter constants	120
5.1	Comparison of finite difference formulations	127
5.2	Nodal values of the solution variable u	137
6.1	Location of movie files	169
6.2	Constants for test problem	172
6.3	Constants for FHN model	185
6.4	Constants for VCD model	186

List of Symbols

V_m	Transmembrane potential
ϕ_i	Intracellular potential
ϕ_e	Extracellular potential
ϕ_o	Extramyocardial potential
σ_i	Effective intracellular conductivity tensor
σ_e	Effective extracellular conductivity tensor
σ_o	Extramyocardial conductivity tensor
σ	Effective conductivity tensor in monodomain
σ_f	Component of σ in fibre direction
σ_s	Component of σ in sheet direction
σ_c	Component of σ in sheet-normal (cross-sheet) direction
C_m	Membrane capacitance per unit area
A_m	Surface-to-volume ratio of the cell membrane
J_i	Intracellular current density
J_e	Extracellular current density
I_m	Transmembrane current density per unit area
I_s	Externally imposed source current per unit volume
I_{ion}	Ionic current function
g_{ion}	Conductance of ionic current
$\overline{g_{ion}}$	Maximal conductance of ionic current
α_i, β_i	Ionic rate constant
E_{ion}	Reversal potential of ionic current
i_q	Ionic current associated with a gate or channel
ξ_i	Local elemental coordinate system
ν_α	Local material coordinate system
Ψ_i	Lagrange basis function

ψ_n^i	Hermite basis function
\mathbf{g}_i	Covariant base vector
\mathbf{g}^i	Contravariant base vector
g_{ij}	Covariant metric tensor
g^{ij}	Contravariant metric tensor
Γ_{ij}^k	Christoffel symbol
$\mathbf{u}_{,k}$	Partial derivative of a vector \mathbf{u} with respect to k
$\mathbf{u} _k$	Covariant derivative of a vector \mathbf{u} with respect to k
(x, y, z)	Global rectangular cartesian coordinate system
(r, θ, z)	Cylindrical polar coordinate system
(λ, μ, θ)	Prolate spheroidal coordinate system
$(\mathbf{f}, \mathbf{g}, \mathbf{h})$	Cardiac wall coordinate system
$(\mathbf{a}, \mathbf{b}, \mathbf{c})$	Microstructural material coordinate system
α	Fibre angle
β	Imbrication angle
γ	Sheet angle
Δx	Grid point spacing
Δt	Time step
$[\text{Ca}]_i$	Intracellular calcium concentration
τ_{Ca}	Calcium time constant
$T_0(\lambda)$	Isometric tension

Chapter 1

Introduction

In 1985, the World Health Organisation published a report on “Sudden Cardiac Death” in which they state that sudden cardiac death is the number one health problem in the developed countries of the world. In the United States of America, it is responsible for some 400,000 deaths every year which is approximately 1 in 5 deaths, or about 0.16% of the total population. According to the 1995 New Zealand Official Year Book, ischemic heart disease contributed towards 26% of all deaths in 1992 in New Zealand, which totals around 7000 deaths. As the expected lifespan increases, the proportion of deaths due to cardiac failure is likely to increase even further. These deaths are most often caused by an electrical malfunction within the heart, due either to infarcted or damaged tissue, or to abnormal passage of electrical conduction. In either case, the normal pattern of cardiac activation is disturbed, and the heart enters into ventricular tachycardia (VT) and fibrillation.

Physiologists have a reasonably good understanding of the normal cardiac activation sequence, in which natural pacemaker tissue and specialised conducting pathways activate the atrial and ventricular myocardium in the correct sequence so that the heart contracts efficiently and blood is pumped throughout the body. What is not so well understood is the breakdown of this normal activation into fibrillation which leads to a non-contracting heart. As Lab (1991, p. 29) states,

“Despite the fact that heart disease together with arrhythmia is a potent cause of sudden death in the western world, their precise mechanisms remain unclear, and the treatment on the whole is disappointing. The

initiating cause of the first ectopic that precipitates lethal arrhythmia in the first hours of myocardial ischemia is not understood, neither are the mechanisms that sustain the arrhythmia.”

This quote illustrates several of the important areas of research which are required, starting from a better understanding of the normal activation process. A “normal” heart does not remain in a constant state throughout its lifetime. External factors on the body result in stress to the heart, a varied diet introduces chemical substances which change cellular composition and behaviour, and exercise (or lack thereof) changes the cellular structure of the heart according to the level of fitness. The fact that a normal heart continues to function for many years in spite of these substantial changes indicates that there are regulating factors that constrain the activation process to follow a somewhat normal course, even though the precise sequence may be altered. At some stage, however, the changes to cardiac structure and composition become too great for the heart itself to correct, and an arrhythmic pattern is started. In order to understand the transition to arrhythmia, the process of non-arrhythmic activation in an abnormal heart must also be understood from the cellular and subcellular level through to the complete myocardium.

There are many forms of arrhythmia which lead to abnormal cardiac function. Simply by observing and cataloguing these phenomena in many patients over several decades, doctors have formulated an empirical working knowledge of the characteristics of arrhythmia and methods for treating them. This approach is clinically useful, as it allows diagnosis and treatment based on previously observed conditions, and much of modern medicine is based on this technique. In general it does not provide any understanding of the causes of the arrhythmia, and may only diagnose and treat it. An understanding of the underlying causes would allow the prediction and, hopefully, prevention of many of these cases.

In order to understand the underlying causes it is not sufficient to simply observe behaviour once it has occurred. Determining cause-and-effect relationships through experimental research is a valuable method for noting some causes of arrhythmia, though limited to the specific situations investigated. Another, preferable, approach is to construct a model of the activation process, the parameters of which are determined through experimental means. Such a model allows the extension of the observed behaviour to predict what may occur in cases not able to be experimentally studied. A mathematical model attempts to construct a framework which explains

what is already known, and quantifies the parameters of the structure.

1.1 Modelling cardiac function

There are several fields of research within the scope of modelling cardiac function and dysfunction. In a model of mechanical behaviour the heart is treated as a very complicated pump and the deformation and associated stresses and strains are important. Alternatively, the energetic function or metabolism of cardiac cells is studied, and the function of the heart is related to the change in concentration and movement of various ions and chemicals. An electrical model describes cardiac function according to the activation process and changes in membrane potential. Usually, there is very little overlap between the research in different areas, yet the different processes are certainly influencing and influenced by the other aspects of function. This thesis begins to integrate some of the aspects of electrical and mechanical function so that the relationships between the two can be studied in the future.

The advantage of a model is that a large problem can be broken down into small sections, and each part described separately. The work in this thesis concentrates on developing a general model of cardiac activation which is designed to be integrated with models of other aspects of cardiac function. As a model of each particular sub-function (such as mechanical contraction, cell energetics, protein kinase movements and so on) is updated and improved, the individual models can be incorporated into their place in a global model.

There are a number of details that were considered significant when determining the formulation of this model of activation. The first of these is that the region over which the model is to be solved is not predetermined, and therefore the model should be general enough to solve in any solution domain in either two or three dimensions, and this domain should be able to be specified in the most convenient coordinate system. At this stage, the model is restricted to that of ventricular activation (due to the complexity of this region alone), though the model should not be restricted to this region, and should be extensible to atrial activation and Purkinje fibre modelling. A model of full ventricular activation requires an accurate

description of the physical structure of the heart. This includes both a precisely measured geometry and a detailed description of the microstructural composition of cardiac muscle. The solution domain is considered to be, in general, inhomogeneous and orthotropic. Additionally, the region may be undergoing deformation during the activation process (either imposed externally or in response to the activation wave) and the model needs to be able to maintain registration with material points as they move.

The cardiac activation process possesses a number of qualities which also help to determine the requirements for the model. Firstly, the activation process has a very small space constant in that activation is propagated on a cell-to-cell basis. However, the cellular coupling has been shown by others to have a negligible effect on activation, and gives justification for using a continuum model of cellular structure by which the cellular properties can be averaged over a length scale somewhat greater than that of a single cell. This scale is still small, on the order of 1 mm, and requires a high resolution of solution points. The activation process also has a wide range of time constants, where cellular depolarisation occurs in about 1 ms, while the full activation cycle is on the order of 1 s. This requires the solution process to be able to solve at small time increments where necessary.

The understanding of cellular activation continues to grow, and a variety of models of cellular membrane behaviour have been, and are continuing to be developed. The model needs to be able to use the most appropriate cellular model for the results that are being sought. The activation process is also influenced by outside factors, particularly physical deformation.

The final result is a large and complex model capable of solving in solution domains defined in two or three dimensions, constrained in its complexity by the computational speed and memory of modern computers. When coupled with other models, such as those of mechanical deformation or torso electric field mapping, the size of the full model is much larger again. An efficient solution technique needs to be developed which makes use of the available computing resources.

A finite element based collocation method is developed to solve a class of partial differential equations that model electrical activation. This scheme combines the accuracy of a high order finite element based description of geometry with the speed

of a finite difference method. The bidomain representation of cardiac tissue is used together with any of a number of ionic current descriptions as the activation model, and is solved using the collocation method. This solution scheme is applied to an anatomically accurate model of the geometry combined with a detailed description of the microstructural arrangement of cardiac muscle.

1.2 Scope of this thesis

The cardiac modelling research group here at the University of Auckland has already developed a sophisticated model of ventricular geometry and microstructure which has been extensively used for modelling cardiac mechanical function. A Huygen's wavelet model has provided a simple computation of the movement of the activation wavefront, but this is an empirical technique. The work presented in this thesis demonstrates the integration of a ionic current based continuum model of electrical activation into the existing framework. This has been done so that several advantages result. Firstly, the comprehensive model of ventricular anatomy and microstructure, which is based on extensive physiological measurements, is available to the activation model and provides a realistic environment in which the model can be solved. Secondly, the activation model can accommodate any of the existing models of cellular activation, as well as being able to incorporate future models as they are developed. Such models are usually formulated for a particular type of tissue, and different models may be used in different regions of the heart as required.

The third advantage is the most significant, and enables a new feature of activation to be investigated for the first time. The solution technique used in the activation model defines the solution points to be attached to material locations within the myocardium, and this complete integration with the mechanical model allows the investigation of the effect of deformation on the activation process. The coupling between the models is bidirectional, although at this stage less is known of the stretch-dependence of the cellular activation process. It is clearly shown that the deformation of the tissue has a significant effect on the nature of the activation, and in particular when the wavefront is reentrant.

Due to the complexity of the electro-mechanical interaction it is difficult to construct experimental techniques which can be used to validate the model. In this sense, much of the work presented is proof of concept, and has not been experimentally verified. The development of an apparatus to do this (combining biaxial mechanical testing with confocal imaging of activation wavefronts) is underway but not available to be used at this stage.

In Chapter 2 a basic outline is given of cardiac structure and function, and the physiological background is given for a mathematical model of activation. Chapter 3 discusses the various types of activation models which have been used by others in earlier work, and determines their deficiencies for the objectives stated above. It also covers the formulation of the bidomain model, which we use. In Chapter 4 a history of the development of models of cellular ionic current behaviour is presented, showing the progress in understanding of membrane processes, and the complexity that is present. Several simplified models, which are non-physiological but practically useful in some situations are also outlined together with their advantages and disadvantages. Chapter 5 looks at solution methods which have been commonly used for solving mathematical activation models, and derives the collocation method which has been constructed specifically to enable the solution to meet the above requirements. A number of two-dimensional solutions are given in Chapter 6 which show how the model works, and shows integration of the method with a model of torso electric potential and body surface mapping. A specific application of the method is illustrated in an example of parameter estimation using a nonlinear optimising technique to determine material parameters based on an experimentally measured activation sequence. Three-dimensional solutions are given in Chapter 7, including solutions on an anatomically accurate model of ventricular geometry. Finally, the process of electromechanical coupling is explored in Chapter 8, where both two-dimensional and three-dimensional examples are given of the activation problem being coupled to a simple model of the mechanical deformation.

Chapter 2

Structure and Function of the Heart

A realistic model of the electrical activation needs to be based on an accurate description of the structure and function of the heart. Qualitative anatomical information has been available since the first substantial dissection experiments in the 16th century (although physicians in ancient Greece and other early civilisations probably also examined the internal structure of the human body, but may not have linked form to function), and this information has continued to become more accurate as surgeons and scientists gain a greater understanding of the way in which the heart works. Descriptions of the cell structure and function have come much more recently as microscopic techniques have improved, and detailed measurements of the processes occurring inside the cell and through the cell membrane are only now becoming available as new techniques in molecular biology are developed. A mathematical model also requires quantitative measurements and these are more difficult to obtain, and the necessary detailed microstructural studies have only recently begun to be performed. This chapter outlines a qualitative background to cardiac structure and function, while a description of the mathematical model used to simulate cardiac activation is outlined in Chapter 3.

2.1 Cardiac Anatomy and Function

The description of cardiac physiology given here is only a basic outline, with greater detail on a few points which are relevant to the problem of activation modelling. For a more in-depth coverage of this subject, a textbook such as *PHYSIOLOGY Section V: The Cardiovascular System* (Berne and Levy 1988) should be consulted, or for a more specific look at only the heart, an excellent reference is *PHYSIOLOGY OF THE HEART* (Katz 1992).

2.1.1 Macroscopic description

The heart is situated near the centre of the chest cavity between the right and left lungs, and is supported inside a membranous structure, the pericardial sac. There are four major chambers in the heart and various accessory tissues as shown in Figure 2.1. The heart is divided into left and right halves by the interventricular septal wall, such that there are no internal connections between the opposing chambers. The larger lower chambers are the *ventricles* (the left and right ventricles are abbreviated as “LV” and “RV” respectively) and the smaller upper chambers are the left and right *atria* (given abbreviations “LA” and “RA”). The bottom of the ventricles is called the *apex* and the top of the ventricles is termed the *base*.

Blood returns to the heart from the rest of the body via the superior and inferior vena cava and enters the right atrium. It flows from this chamber into the right ventricle which pumps the blood to the lungs via the pulmonary artery where the blood is oxygenated through the diffusion of oxygen across the alveolar membrane. The blood then returns to the heart through the pulmonary vein and enters the left atrium, passes into the left ventricle, and is subsequently pumped via the aorta to the rest of the body. For this reason the left ventricle is considerably larger than the right, and exhibits a greater change in pressure during the cardiac cycle. The period during which the heart is being filled with blood is called *diastole*, and the period of contraction during which blood is pumped from the heart into the lungs and circulatory system is called *systole*. The flow of blood from the RA to the RV is controlled by the tricuspid valve, and the mitral valve controls blood flow between the LA and LV. The pulmonary valve is at the outflow tract of the RV into the

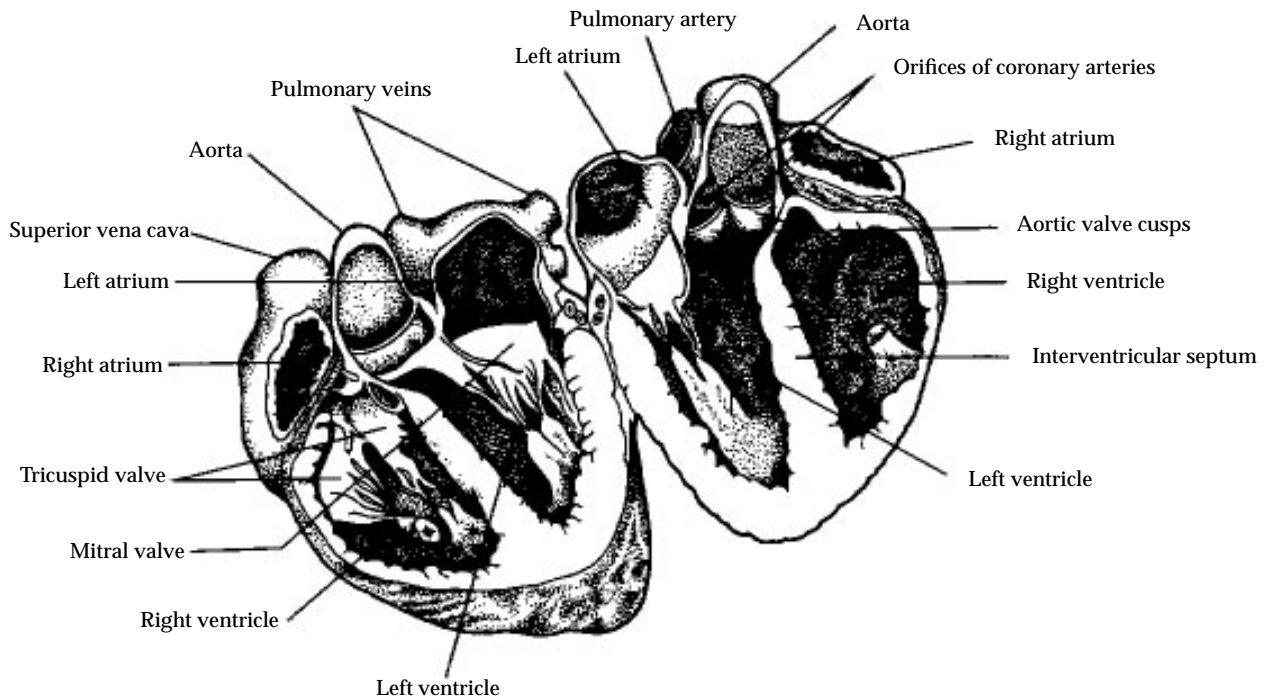


FIGURE 2.1: Longitudinal cross-section of the heart. From Katz (1992, Fig 1.1, p. 3).

pulmonary artery, and the aortic valve at the connection of the aorta to the LV.

Papillary muscles in both the LV and RV tether the mitral and tricuspid valves to the ventricular wall during systole. The LV papillary muscles are large protrusions from the endocardial wall, and occupy a significant portion of the cavity, whereas the RV muscles are relatively small, and attached only by their bases to the ventricular wall. These muscles prevent the valves from inverting and entering the atria during systole, but the opening of the valves is solely due to the pressure difference between the chambers, and not to muscular contraction. The pulmonary and aortic valves are not tethered because they are only preventing blood flow during the slower passive filling phase.

2.1.2 Microscopic description

Cardiac muscle cells or *myocytes* are roughly cylindrical with a length in human ventricular tissue of 80 to 100 μm and a diameter of 10 to 20 μm , and are bounded by

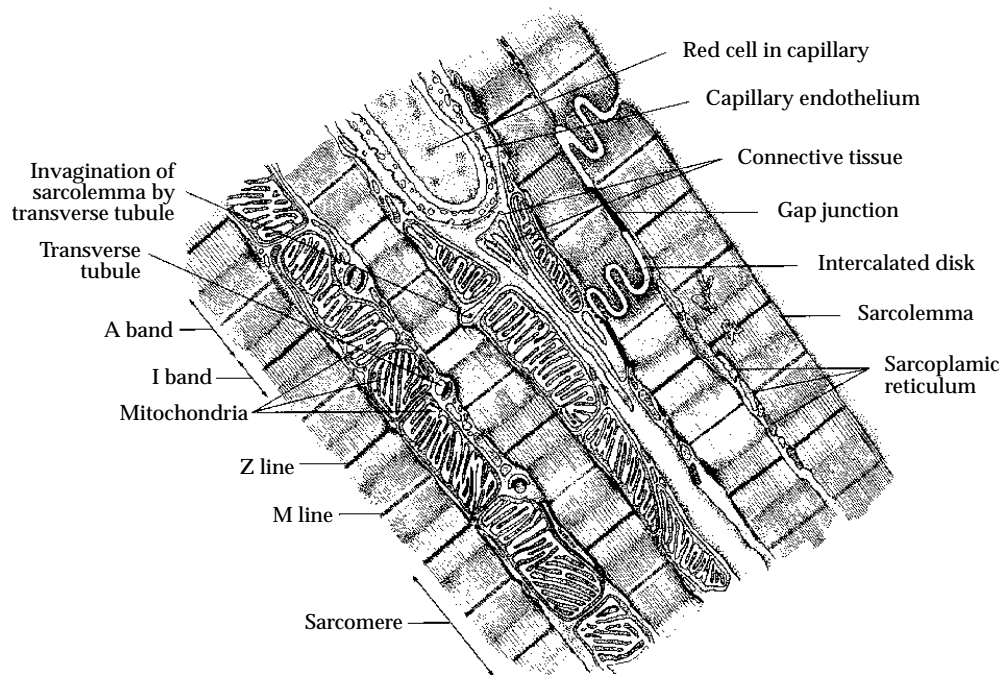


FIGURE 2.2: Diagram showing the structure of a cardiac muscle cell. A capillary runs between two adjacent cells. From Berne and Levy (1988, Fig 28–2, p. 432).

the cell membrane or *sarcolemma*. A diagrammatic representation of the cell is given in Figure 2.2 and has been reconstructed from an electron micrograph. There are two sets of filaments present in muscle cells: *thin filaments* composed of a globular protein called *actin*, and *thick filaments* formed as an aggregate of a much larger protein called *myosin*. The thick and thin filaments interdigitate to form a *sarcomere* between the thin filament tethering points at Z lines, and this sarcomere is the basic contractile unit. The myosin molecule is composed of a pair of heavy chains which hinge outwards near the end of the chain and attached to the end of this “tail” are two globular “heads” and two pairs of light chains. The tail and heads are hinged with respect to the rest of the molecule which is buried within the filament. According to the most common theory of contraction, these appendages, or *crossbridges*, cause the thick and thin filaments to move relative to each other according to the proposed four-stage *crossbridge cycle*. An important compound involved in this process is ATP (adenosine triphosphate) which is usually bound to myosin in its resting state due to the very high affinity between them. ATP inhibits the interaction of myosin with actin. The first stage of contraction is the hydrolysis of ATP to form ADP (adenosine diphosphate) and P_i (inorganic phosphate), both of which remain associated with

myosin. In this state, the myosin head interacts with the actin to form the active complex *actomyosin*. The chemical energy expended by dissociation of ADP and P_i from the complex performs mechanical work: the motion of the crossbridge. This allows ATP to bind again to the myosin and dissociates the crossbridge and the thin filament, returning to the resting state. Each cycle causes the thick and thin filaments to move by about 10 nm relative to each other.

A large number of sarcomeres are present in a single cell. Cells are joined to other cells through intercalated disks both end-to-end and also by branching to connect with neighbouring, nearly parallel cellular strands. Electrical connection between adjacent cells is through gap junctions which are located in the intercalated disks. Additionally, there are several important internal structures. Due to the almost constant energy requirements of repeated cellular contraction in the cardiac cell there are a large number of mitochondria which provide oxygen to the cell. A network of sarcoplasmic reticulum (SR) provides a large region of uptake pumps which remove Ca^{2+} from the cellular matrix and stores it in the junctional SR (JSR) awaiting release for enabling contraction. Deep invaginations of the sarcolemma into the fibre are known as the transverse tubular system or T-tubules. This system is used primarily to conduct the action potential down into the cell, and additionally to transport components from the interstitial fluid surrounding the cell deep into the cell, and is of particular importance in the excitation-contraction coupling (see Section 2.2.7).

An averaged myocyte direction can be defined at any point, which is known as the *local fibre orientation*. Early papers by MacCallum (1900) and Mall (1911) investigating the muscular architecture of the heart suggest that ventricular myocardium is an assembly of discrete muscle layers arranged in nested shells, or discrete fibre bundles (Le Grice 1992). This view of the microstructure was generally accepted until Hort (1957) and Streeter and Bassett (1966) performed the first quantitative measurements of fibre orientation and found a smooth transmural variation in fibre angle, which led to the predominant view being that myocardium is a *uniformly continuous, transversely isotropic* medium. A uniformly continuous medium is one in which there are no discontinuous changes in the local fibre orientation, and a transversely isotropic medium is one in which the material structure is isotropic in all directions orthogonal to the fibre. In other words, the fibre orientation is the only local measure of microstructural composition, and can be regarded as a local axis of symmetry.

Later studies by Streeter, Spotnitz, Patel, Ross and Sonnenblick (1969) and others were more thorough and tended to confirm this view. Streeter (1979) did acknowledge, however, that the muscular architecture is discontinuous at both a macroscopic and microscopic level. There were some problems associated with the methods used to produce these results, as measurements were made only at a limited number of sites, and the measurement points could not be accurately located within a standard ventricular geometry.

Measurements of fibre orientation at a large number of sites spread throughout the ventricular myocardium were made by Nielsen (1987) and McLean and Prothero (1987). Their approaches involved cutting the ventricles into thick serial slices transverse to the base-apex axis. These techniques have problems, including difficulty in spatial registration between slices due to distortion, and loss of detail through averaging. McLean, Ross and Prothero (1989) measured fibre angles from both transverse and longitudinal slices, though the fibre orientation could not be measured from two orthogonal slices taken from the same heart.

Many of the problems associated with earlier studies have been overcome in the work of Le Grice (1992), which, building on the techniques developed by Nielsen (1987), is the most comprehensive and thorough quantitative study of cardiac microstructure to date. In the research described, a measurement rig was developed on which a fixed heart could be mounted. A pointer determined the physical position of a point on the surface of the heart, and the projection of a shadow was aligned with the local fibre direction. After obtaining data from a number of points on the epicardium a small thickness of tissue (approximately 0.5 mm) was removed from the entire ventricular surface using a dermatome, and the process was repeated. The mounting ensured that the successive data sets preserved spatial registration. This technique allowed measurement of fibre orientation throughout the ventricular wall, and the absolute coordinates of each measurement point could be recorded for alignment with the measured geometry. This technique was a time-consuming process as it needed to be performed manually, however the results obtained provide an accurate definition of both cardiac geometry and microstructure. Details of the method and results are more fully described in a paper by Nielsen, Le Grice, Smaill and Hunter (1991).

Measurements obtained by Le Grice and coworkers are broadly consistent with

those reported by Streeter and others, but also reveal a new understanding of the global nature of cardiac microstructure. Their studies suggest that the ventricular myocardium is not a uniform continuum, but rather a composite of discrete layers of fibres, which are called *sheets* (Le Grice 1992; Smaill and Hunter 1991; Le Grice, Hunter and Smaill 1994). Recorded fibre angles are the edges of these branching sheets, and because fibres traverse the sheets at a small angle, these measured angles are only projections of the true angle. However, Streeter (1979) reports that these small angles, known as *imbrication angles*¹ have a magnitude of at most 3° to 5° at the epicardium where the angles are greatest, and therefore this variation is often ignored.

The sheets are on average four cells thick, with neighbouring layers of sheets branching into one another, and the sheets are surrounded by a matrix of collagenous connective tissue. The nature and arrangement of the branching and of the connective structure varies according to position within the ventricular wall. Sheet orientation is generally radial to the ventricular surfaces, though they appear to become almost tangential to the epicardial surface. A simple structural model describing these features of the myocardium has been developed by the Cardiac Research Group at the University of Auckland², and details of the model are presented in several papers (Hunter, Nielsen, Smaill, Le Grice and Hunter 1993; Hunter, Smaill, Nielsen and Grice 1996). Hunter, Smaill, Nielsen and Grice (1996, p. 3) outline the model of ventricular myocardium, which

... is represented as an interconnected hierarchy of muscle layers whose three-dimensional orientation varies through the ventricular wall. The extent of coupling between adjacent layers or sheets also varies transmurally to accommodate the changes in sheet orientation. For a section cut tangential to the epicardial ventricular surface, the cut edges of the sheets define the fibre orientation. Alternately, the cleavage planes revealed in transmural base-apex sections indicate the radial orientation of the sheets.

Figure 2.3 shows a schematic view of the cardiac microstructure as predicted by this model. No similar studies have yet been performed on atrial tissue, though this will be required for a complete cardiac model at a later date.

¹The *imbrication angle* (not, as occasionally written, embrication angle) at the epicardium is the angle at which the fibre intersects the epicardial surface (from the Latin *imbricare* which describes the overlapping of roof tiles). A value of 0° indicates a fibre orientation parallel to the surface.

²Department of Engineering Science, University of Auckland, New Zealand

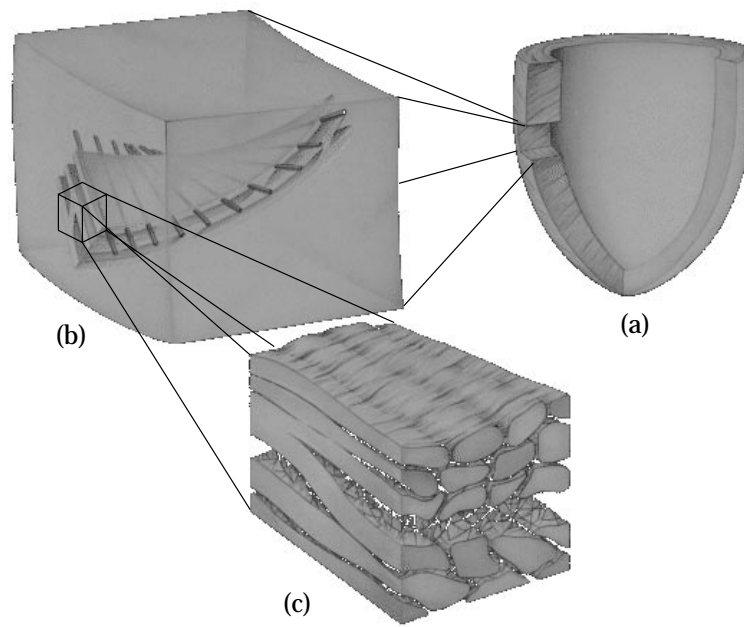


FIGURE 2.3: Schematic of cardiac microstructure. (a) Ventricular wall. (b) A transmurular block showing fibre orientation and branching sheet structures. Note the transmural variation of fibre angle. (c) The muscle fibres are bound by collagen fibres into sheets 3 to 4 cells thick.

2.1.3 Connective tissue structure

There also exists a comprehensive organisation of extracellular connective tissue, including a substantial hierarchy of collagen structures which constrain the movement of the muscle fibres and sheets. This constraining network is more important when modelling mechanical behaviour than it is when modelling electrical activation. However, the constraints it places on the microstructure will become significant as the electromechanical coupling is investigated. Various studies have begun to quantify the nature of the connective tissues (Caulfield and Borg 1979; MacKenna 1994).

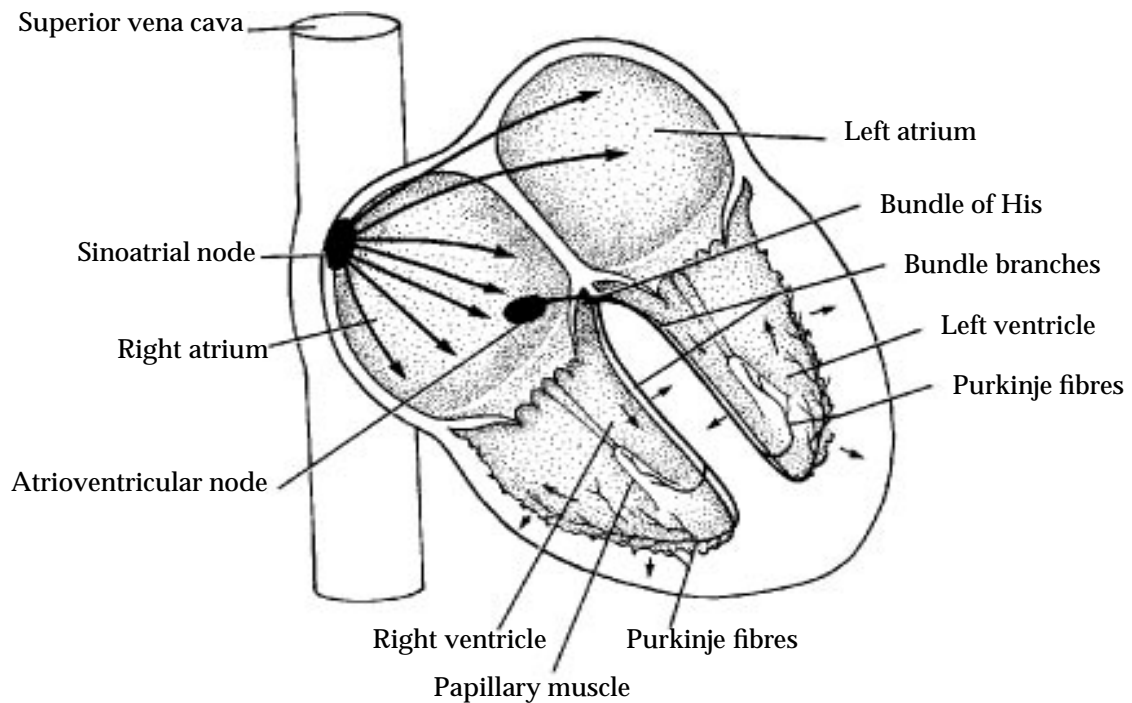


FIGURE 2.4: Schematic of the activation sequence. From Berne and Levy (1988, Fig 27–23, p. 414)

2.2 Activation

Mechanical contraction of the heart is caused by the electrical activation of the myocardial cells. The heart is electrically self-contained, having the ability to initiate its own beat with a regular period, and will continue to beat after being removed from the body. Cells capable of initiating electrical activity are called *pacemaker* cells, and exist in several places throughout the heart.

2.2.1 Normal activation sequence

The normal sequence of activation is shown diagrammatically in Figure 2.4. Only those pacemaker cells with the fastest rate of pacemaker discharge control the electrical activity of the entire heart. The region of tissue with the shortest period of spontaneous electrical activity is the *sinoatrial* (SA) node, which is located on the

atrial wall near the junction of the superior vena cava and the right atrium, and consists of a cluster of pacemaker cells. Action potentials are normally generated in the SA node at the rate of 60 to 100 per minute. From the SA node, the action potential is propagated from cell to cell through firstly the right atrium, followed closely by the left atrium at a conduction velocity of approximately $1 \text{ m} \cdot \text{s}^{-1}$ until it reaches the *atrioventricular* (AV) node. The AV node consists of pacemaker-type cells similar to those found in the SA node, but because they beat spontaneously at a slower rate (approximately 40 to 55 beats per minute) they are governed by the propagation from the SA node. In the event that the SA node is removed or destroyed, or that conduction is slowed through the atria, the cells in the AV node will take over as pacemaker for the heart.

Conduction through the AV node is at a much slower rate (around $0.05 \text{ m} \cdot \text{s}^{-1}$) giving time for the atria to contract and pump blood into the ventricles before the action potential conducts through the ventricles and causes them to contract. The AV node is normally the only electrical connection between the atria and the ventricles. From the AV node, the electrical propagation enters the *bundle of His* which is the upper portion of the ventricular conduction system and runs down the right side of the septum, and this common bundle divides after a short distance into right and left *bundle branches*. The right branch continues down the right septal wall, and the left perforates the septum and splits into two further main branches on the left septal wall. All of these branches continue to subdivide into a complex network of fibres called the *Purkinje fibre network*, spreading across the endocardial surface of both ventricles and into the subendocardial region of the ventricular myocardium. Due to this arrangement of connecting fibres the septum is activated first and normally pushes in towards the left ventricular wall (Durrer, van Dam, Freud, Janse, Meijler and Arzbaecher 1970). The papillary muscles are also activated early so that they can prevent the AV valves from inverting during systole. Due to the faster conduction of approximately $2 \text{ m} \cdot \text{s}^{-1}$ through the bundle and Purkinje fibres, the entire endocardium is excited almost simultaneously. The apical regions contract first and the basal regions are usually the last regions to be excited. Excitation spreads outwards through the ventricular wall at a rate of about 0.3 to $0.4 \text{ m} \cdot \text{s}^{-1}$, and the first epicardial region to be excited is the thinnest portion of the right ventricular wall. This activation process is summarised in Table 2.1.

NORMAL SEQUENCE OF ACTIVATION	CONDUCTION VELOCITY (m · sec ⁻¹)	TIME FOR IMPULSE TO TRAVERSE STRUCTURE (sec)	RATE OF PACEMAKER CELL DISCHARGE (min ⁻¹)
SA node	< 0.01	⊥	60–100
↓		~ 0.15	
Atrial myocardium	1.0–1.2	⊥	None
↓			
AV node	0.02–0.05	⊥	Most rapid in
↓		:	lower fibres:
Bundle of His	1.2–2.0	:	40–55
↓		~ 0.08	
Bundle branches	⊥	:	⊥
↓		:	25–40
Purkinje network	⊥	⊥	⊥
↓			
Ventricular myocardium	0.3–1.0	~ 0.08	None

TABLE 2.1: Normal activation sequence. (From Katz (1992, Table 20.1, p. 475))

2.2.2 Activation at a cellular level

From an electrical perspective, the cell membrane is a *dielectric phospholipid bilayer* separating intracellular and extracellular conducting electrolytic solutions, thus forming a capacitor (Guevera 1991). There is a potential difference across the membrane, known as the *transmembrane potential* V_m and changes in this quantity are given by

$$\frac{dV_m}{dt} = -\frac{\sum I_{ion}}{C_m} \quad (2.1)$$

where C_m is the cell membrane capacitance, and the I_{ion} are the various ionic currents flowing across the cell membrane.

Ionic currents are caused by the flow of different species of ions (especially sodium (Na^+), potassium (K^+) and calcium (Ca^{2+})) through individual channels in the

membrane. Channels differ in their selectivity of ion species, and in the way they respond to changes in the transmembrane potential (Hille 1984). Molecular biologists have developed techniques by which individual channels may be isolated and studied, and from the results of these experiments mathematical models of the ion channels are formulated. Such models exist for many types of cardiac cells including the SA node (Noble and Noble 1984; Clark, Shumaker, Murphey and Giles 1991), atrial tissue (Hilgemann and Noble 1987), Purkinje fibre (Noble 1962; McAllister, Noble and Tsien 1975; Di Francesco and Noble 1985) and ventricular muscle (Beeler and Reuter 1977; Luo and Rudy 1991; Luo and Rudy 1994a), all of which are based on the form of the original Hodgkin and Huxley (1952) model for nerve. Chapter 4 discusses these and other ionic current models in more detail.

2.2.3 Cellular resting potential

The concentrations of the various ions sets up an electrochemical gradient across the cell membrane according to the Nernst equation in Equation (2.2). According to this equation, the equilibrium potential E_X of an ion X is given by the ratio of the intracellular and extracellular concentrations ($[X]_i$ and $[X]_o$ respectively) of that ion:

$$E_X = -\frac{RT}{zF} \cdot \log \left(\frac{[X]_i}{[X]_o} \right) \quad (2.2)$$

where R is the gas constant, F is Faraday's constant, T is the temperature and z is the valence of the ion. At the body temperature of 37°C the value of $\frac{RT}{F} = 61.5$ mV. Approximate concentrations and the corresponding equilibrium potential generated from each of the major ions is given in Table 2.2. In a resting state, the cell membrane is highly permeable to potassium ions, but much less permeable to sodium, calcium or chloride ions, and therefore the resting potential of the cell is determined largely by the potassium gradient across the cell membrane. Typical cell resting potentials are slightly lower, at between -80 mV and -90 mV, due largely to the electrogenicity of the Na^+/K^+ pump allowing a small permeability to sodium.

<i>Ion</i>	<i>z</i>	<i>Extracellular</i>	<i>Intracellular</i>	<i>Equilibrium</i>
		<i>Concentrations</i>	<i>Concentrations</i>	<i>Potential</i>
		(mM)	(mM)	(mV)
Na ⁺	1	145	10	70
K ⁺	1	4	135	− 94
Ca ²⁺	2	2	10 ^{−7} – 10 ^{−4}	132
Cl [−]	−1	100	15	− 51

TABLE 2.2: Intracellular and extracellular ion concentrations in cardiac muscle cells, and their corresponding equilibrium potentials generated from the Nernst equation. (From Berne and Levy (1988, p. 400) and Katz (1992, p. 440))

2.2.4 Ion channel behaviour

The movement of ions through the cell membrane is a passive process requiring no energy to be expended, because the ions move down their natural electrochemical gradients. There are portions of the membrane which allow ions to travel across the membrane more easily than at other places, and these are called *ion channels*. Ion channels are *ion-selective*, which means that only one or two particular ions can travel through a given channel.

Until recently, it has been thought that ion channels have three functional states, though recent research (Bean 1990; Mazzanti and DeFelice 1990) has indicated an additional variation. There are two closed states of the membrane channel. In a *resting* state, the channel will open in response to an appropriate stimulus, while in a *refractory* or *inactive* state the channel will not open under any circumstances. It had been thought that there was only a single *open* state, though single channel studies have shown that two distinct modes exist: brief openings (called *mode 1*) and long-lasting openings (*mode 2*). The channel may spontaneously change between either of these two states. In general, a channel moves in a cycle from the resting state to the open states to the refractory state and back to the resting state. Transitions between states are controlled largely by changes in membrane potential, though chemical factors and drugs cause additional modifications.

The first description of the nature of ion channels was developed by Hodgkin and Huxley (1952) for the squid axon. They proposed a *gating mechanism* which

controlled the opening and closing of *gates* within sodium and potassium channels. The state of these gates determined whether or not a particular channel is open to allow an ion to pass through.

According to the Hodgkin-Huxley (HH) model, the sodium channel can be described by the existence of two gates. The first gate is activated (opened) by a depolarisation of the cell membrane, and is therefore called an *activation gate*, which Hodgkin and Huxley denoted with the symbol “*m*”. There seemed to be three *m* gates located near the outside of the membrane which worked cooperatively. The second gate, located at the intracellular surface of the membrane closes in response to a depolarisation, and is called an *inactivation gate*, also termed an “*h*” gate. When the sodium channel is in a closed resting state, the *h* gate is open but the *m* gate is closed. In order for sodium ions to pass through the channel, both sets of gates must be open, which means that the *m* gate must open much faster than the *h* gate closes when the membrane is depolarised. The HH model is discussed in more detail in Section 4.1.1 where the mathematical model is outlined and the various time-dependent properties of the gates are described more fully.

2.2.5 Types of ionic current

There are three types of behaviour of an ion channel, determined by the way in which the current responds to a change in voltage. When a voltage-clamped channel with a steady-state current is clamped to a new voltage, the current will either:

- immediately attain a new steady-state value, termed a *time-independent current* or a *background current*
- gradually approach a new steady-state value, termed a *time-dependent activation current*
- begin to activate, but then inactivate, which is called a *time-dependent activation-inactivation current*

The mathematical forms for models of these three types of membrane channel are outlined in Section 4.1.1.

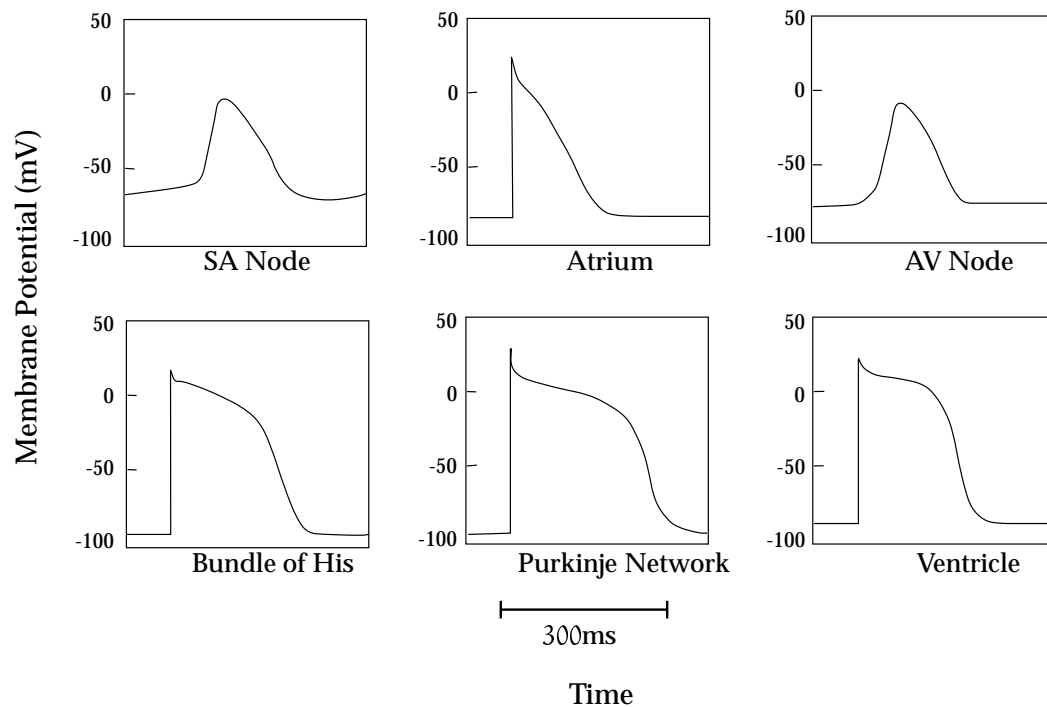


FIGURE 2.5: Action potential configurations in different regions of the mammalian heart. (Adapted from Katz (1992, Fig 19.13, p. 463))

Also present are several pump and exchange mechanisms which transfer ions across the membrane, but are not voltage-dependent. The sodium-potassium pump extrudes sodium from the cell and replaces potassium inside the cell, which helps to maintain the concentration gradients for these ions, and generates a net outward current. The sodium-calcium pump removes calcium from the cell in exchange for sodium generating a net inward current, and the calcium pump removes calcium from the cell, which generates an outward current. These pumps work against the natural electrochemical gradients, and therefore require the usage of energy.

2.2.6 Action potential shape

In each of the regions, the shape of the propagating action potential is slightly different, as shown in Figure 2.5. In ventricular tissue and other non-pacemaker cells the transmembrane potential is held by an ionic current balance at a steady *resting potential*. In both the SA node and the AV node there is a steady depolarisation due to a leakage of calcium ions over the membrane. As soon as the potential reaches a

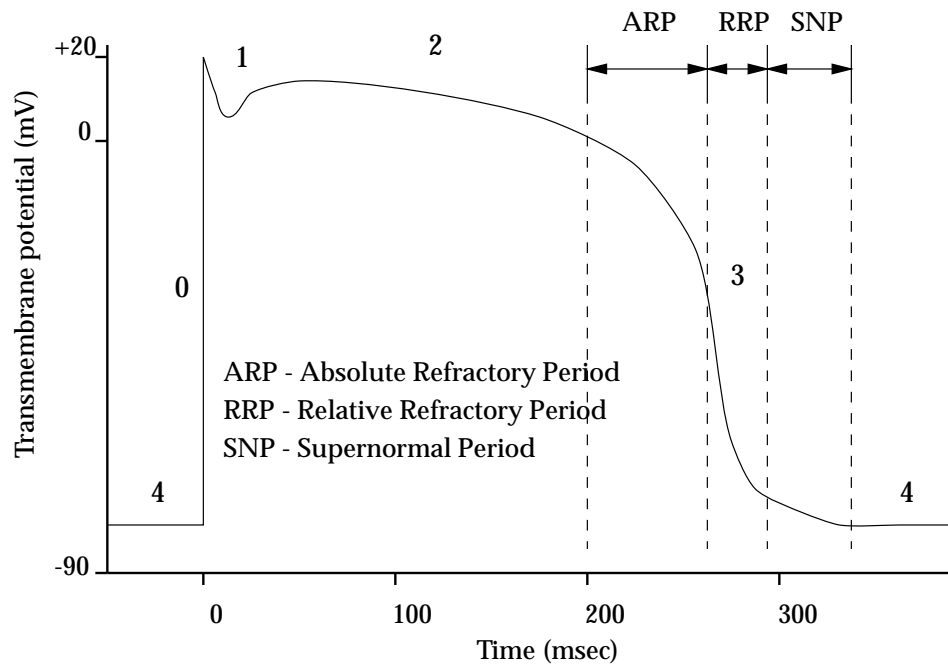


FIGURE 2.6: The five stages in a ventricular action potential (described in the text).

Adapted from Katz (1992, Fig 19.2, p. 439).

critical value called the *threshold*, then an action potential is triggered. Differences in shape and duration of action potentials in the other tissues are due to the varying influence of the ions.

The ventricular action potential (Figure 2.6) lasts over 300 ms and consists of five phases. The resting potential (phase 4) has already been discussed, and in ventricular cells the potential is fairly constant. This is the phase during which the heart is passively filling with blood (diastole). The initial rapid upstroke (phase 0) is due largely to the opening of the sodium channel, increasing the permeability of the membrane to sodium and therefore altering the transmembrane potential. The depolarisation of the membrane due to this inward sodium current is very fast.

A short period of early repolarisation (phase 1) occurs largely because of the closure of sodium channels, though in addition several outward currents contribute. This is followed by the plateau (phase 2) which is maintained by the secondary inward current, a current carried by calcium ions entering the membrane through calcium conductance channels. The plateau can last for well over 100 ms but is only present in the Purkinje and ventricular cells. The duration of the action potential is partially

determined by the length of the preceding diastolic interval, so that a more rapid heart beat results in a shorter Action Potential Duration (APD) .

Repolarisation (or recovery) of the membrane potential (phase 3) can be further subdivided into three parts. The *absolute refractory period* (ARP) is the early repolarisation in which no stimulus can initiate a propagated response. The *relative refractory period* (RRP) follows the ARP, and is an interval during which a stimulus exceeding the normal threshold will produce a propagating wave. This is followed by the *supernormal period* (SNP) during which stimuli slightly less than normal threshold will initiate another action potential. These latter two activation waves propagate more slowly than a standard action potential due to the recovering tissue that the wavefront is propagating into, and therefore the full recovery time is the interval until a stimulation would produce a normally propagating action potential.

2.2.7 Excitation-contraction coupling

As the wavefront passes over cardiac tissue, the action potential causes the cell membrane to depolarise. Figure 2.7 shows the cellular processes involved in excitation-contraction coupling. The action potential is constructed by the superposition of the many ionic currents which change the relative electric potential of the intracellular to the extracellular space. The first ionic current is called the *fast inward sodium current* (I_{Na}) which is responsible for the very fast initial depolarisation of the membrane. This current has a short duration, but initiates a second, slower inward current I_{Si} which transports calcium ions across the membrane. The calcium acts both to further depolarise the cell, and more importantly to trigger the release of a large amount of calcium from internal stores in the sarcoplasmic reticulum in a process called *calcium-induced calcium release*. The incoming calcium travels into the JSR through the dihydropyridine (DHP) receptor, which then triggers release of calcium from the JSR through the calcium release channel at the ryanodine receptor. The calcium that is released into the cytoplasm binds to troponin C molecules within the contractile proteins. The number of bound calcium sites affects the number of actin-myosin interactions, which determines the degree of contraction of the tissue. In a model of cardiac activation it is often possible to represent, as a first approximation, the level of activation by the concentration of intracellular calcium.

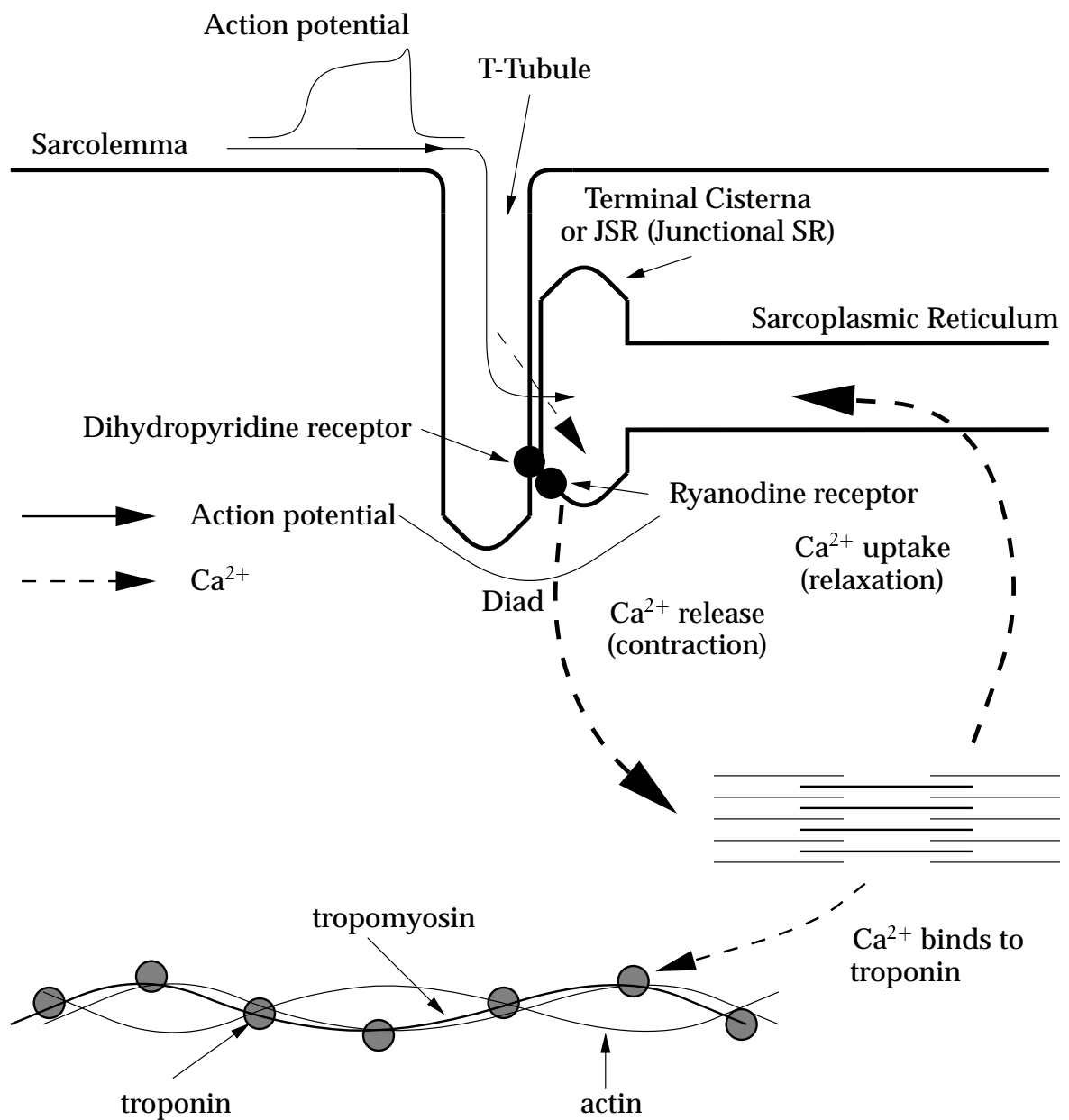


FIGURE 2.7: Excitation-contraction coupling in a cardiac cell. The method of calcium-induced calcium release and calcium movement within the cell is shown.

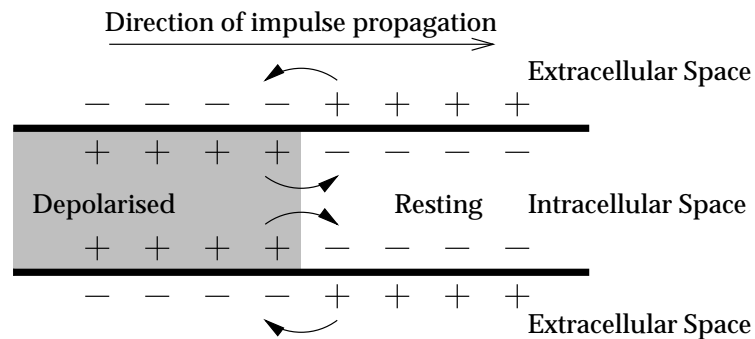


FIGURE 2.8: A propagating impulse from left to right in a strand of cardiac muscle. Arrows indicate directions of positive current flow from the electron flux, which are currents between the depolarised tissue (*shaded*) and resting tissue. (From Katz (1992, Fig 21.1, p. 518).)

There are also several ways in which the deformation of the muscle cell affects the activation process. The most obvious is the change in path length as the lengths of cells change. Additionally there appear to be stretch dependent ion channels which alter the number or ratio of ions that they pass through the membrane depending on the degree of stretching of the muscle.

2.2.8 Cellular conduction

Four physiological variables primarily determine conduction velocity:

- action potential amplitude
- the rate of rise of the action potential
- threshold
- internal and external electrical resistances

The currents which propagate an impulse along a cardiac fibre are caused by electron flow (*electrotonic*), and are generated by the ionic currents of the action potentials. The flow of electrons causing this current requires that current flows in two directions as shown in Figure 2.8. Electrons flow towards the resting tissue

on the outside of the cells, and the electrotonic current returns through the inside of the cell membrane. These electrotonic currents cause resting excitable cells to depolarise, and initiate an action potential. The spread of excitation is caused by this propagation of a wave of depolarisation.

Action potential amplitude and rate of depolarisation

The spread of electrotonic currents is much faster than the propagation of a wave of depolarisation. This explains the dependence of conduction velocity on the action potential amplitude and the rate of depolarisation. Amplitude determines the size of the depolarising current, determining how far the electrotonic currents are propagated ahead of the wavefront. An increased rate of depolarisation causes a more rapid spread of current into the resting tissue. Therefore large, rapidly depolarising action potentials propagate more quickly than small slower action potentials because they induce large electrotonic currents which depolarise cells a greater distance ahead of the wavefront. This explains part of the reason for slow conduction in the SA node and the AV node, as their action potentials are of small amplitude, and have a slow depolarisation (see Section 2.2.6).

In addition the rate of activation is governed by the electrical state of the tissue so that if an action potential is generated while the cell is still in a relative refractory state, the rate of propagation of the activation wave will be slowed. This is because cells further ahead of the wavefront are still in the absolute refractory state and cannot begin to be reactivated. This is part of the process which can initiate reentrant waves.

Threshold

The *threshold* is the amount of current required in order to initiate a propagated action potential, and therefore reducing the threshold will increase the rate of conduction by generating action potentials further ahead of the wavefront. The threshold is related to the number of ion channels that need to be opened for a depolarisation wave to be self-sustaining, independent of the initial stimulus.

Resistance

Connections between the intracellular spaces of neighbouring cells is through the *intercalated discs* which separate the cells. The connecting tissue is called the *nexus* or *gap junction*, and these have lower resistances than the plasma membrane, allowing rapid longitudinal propagation of current between cells. The number of gap junctions which exist changes the conduction velocity, and when these channels are closed, adjacent heart cells can become uncoupled.

2.3 Applications For This Research

A model of cardiac activation is useful simply in determining the natural process of ventricular activation. There are also abnormal conditions, called *arrhythmia*, in which the activation process is changed in some way, and it is useful to have a model which will enable the study of these situations also in order that cardiologists can gain a better understanding of the various factors involved. A model is also useful in explaining results gathered either in experimental work or as part of surgical procedures.

2.3.1 Arrhythmic activation patterns

There are a number of conditions in which the sequence of activation is altered, in most cases due to a physical defect. The first has been mentioned already. When there is a failure in the SA node, or in the conduction from the SA node to the AV node, then the AV node will assume the pacemaker responsibility for providing an activation wave to the ventricles. In this case the pattern of activation is markedly changed in the atria, but only slightly changed in the ventricles, and some form of contraction at a lower rate and lower pressure may still occur. Many other abnormalities have a more serious result, though the heart has in place a number of “backup” facilities which can deal with some of the problems.

Bundle block

Conduction may be impaired in any of the bundle branches (two in the left ventricle and one in the right) to cause *bundle branch block*. This results in a variety of activation sequences and characteristic electrocardiographic patterns. If either of the main branches are blocked then that ventricle receives the activation from the propagation of the wave through from the other ventricle, and contraction in that ventricle is slowed. A block in either of the left sub-branches results in slowed left ventricular conduction. Because of the dense network of Purkinje fibres intertwining over the endocardial surface a block in any of these usually has only a very local effect.

Accessory Pathways - WPW

The activation sequence may bypass its normal route through the spurious placement of additional tissue. One example is the *Wolff-Parkinson-White* (WPW) syndrome in which a small bridge of tissue connects the atria and the ventricles over the top of the insulating atrioventricular ring. This causes a premature excitation of the ventricles from the basal epicardial surface, and a corresponding change in the contraction process leading to depressed ventricular pressure. This condition is easily diagnosed, though the exact position of the accessory tissue may be difficult to detect. Various cardiac mapping techniques may help to pinpoint its location.

Wenckebach phenomenon

This is a rate-dependent block in which some activation waves may not be completely propagated through their full sequence. Often the AV node causes the block which is usually expressed as a conduction rate $N : M$, where N is the number of atrial stimuli and M is the number of ventricular responses. Commonly N and M are small integers, and common ratios are 2:1, 3:2 and 4:3. The block is due to decreased conductivity in a refractory zone of a previous wave, or alternatively slow recovery of excitability.

Altered heart rate

There are two general types of arrhythmia describing an altering of the heart rate: *tachycardias* which represent an increase in the rate and *bradycardias* in which the heart rate is too slow, and each may occur in any of the tissues in the heart. Bradycardias are caused by areas of decremental conduction and regions of unidirectional block, where conduction may proceed in one direction but not another. These features are easily incorporated into a model of cellular conduction. Tachycardia is a regular sequence of premature systoles, more rapid depolarisation is called *flutter*, and the extreme case where the electrical wave is completely disorganised and there is no effective pumping is called *fibrillation*. There are many mechanisms which cause tachycardia including abnormal pacemaker activity, abnormal conduction, inhomogeneous action potential characteristics and several others. The same mechanisms can cause either a slowed or an increased cardiac rate and therefore determining the result of a known defect can be difficult without a model. The transition from tachycardia to fibrillation is not yet well understood, and a model could be used to great advantage in determining the processes involved.

2.3.2 Ischemia

Due to the large consistent consumption of energy the heart requires an uninterrupted supply of oxygen. An ischemic heart lacks sufficient oxygen to contract normally and there are two results: loss of contractile function causing arrhythmia, and subsequently death of the cells which is known as myocardial infarction. An infarct can have substantial effect on the contractile process because it inhibits both the mechanical and electrical function in that region. By changing the parameters on a model of the ionic currents, some of these effects can be modelled, but a complete mathematical description would require coupling of the electrical model to both the mechanical processes and a model of the coronary vasculature.

2.3.3 Reentrant waves

A byproduct of some of the above physical defects is the possible creation of a reentrant wave. A unidirectional block, especially in conjunction with an infarcted region could allow an activation wave to reenter a previously excited region of myocardium and this reentry may continue giving rise to a tachycardic state. Alternatively the existence of an *ectopic focus* (which is a region which spontaneously activates) could cause a spiral wave if the event occurred in the relative refractory period of the action potential.

2.3.4 Mechanically-induced changes in electrophysiology

Recent experiments have shown that not only does the process of electrical activation cause cellular contraction, but also that changes in both stress and strain within the muscle leads directly to changes in electrical function and cause arrhythmia (Lab 1982; Lab and Holden 1991; Taggart, Sutton and Lab 1992). There is evidence that changes may occur in action potential duration, cellular excitability and in the form of the electrocardiogram. A coupled model of electrical and mechanical function is required to investigate the interaction between these processes.

2.4 A Cardiac Mapping System

Determining the large scale process of activation is most easily accomplished with a cardiac mapping system. There are several components in a mapping system. Electrodes are used to measure electrical signals from small regions of the cardiac tissue. The electrodes may be constructed in different ways depending on the measurements required. In order to record epicardial signals over the ventricular surface, a “sock” is constructed, made of some slightly elastic material, and the electrodes are attached (usually by sewing into the sock) at a number of points. This sock then slips over the heart, covering the ventricular epicardium. A denser array of electrodes can also be constructed which provides more detail on a small epicardial region, and a number of electrodes may also be spaced along the length

of a “pin”, which allows for three-dimensional recording of the signals. Endocardial recordings may be made using a balloon which has been inserted through a catheter and inflated inside the ventricle. The electrodes may be either unipolar or bipolar, depending on the recording requirements.

Due to the large number of electrodes potentially required (which will in general be many more than for a standard 12-lead ECG) specialised computer hardware and software needs to be developed to acquire the electrical information. We have provided the software for a mapping system called EMAP which is developed in conjunction with the Biorobotics Group at M.I.T.³ A further description of the software can be found in Bullivant (1994) and a description of the next generation of hardware is available in Bullivant (1996).

This system is currently in use at several hospitals and research centres around the world, including our own research group. The two centres with whom our research group has the closest contact are Green Lane Hospital⁴ where the primary focus is as a diagnostic tool in a surgical environment, and Cedars Sinai Medical Research Institute⁵ where the system is mainly used in experimental research. In each situation the apparatus is used to provide quantitative measurements in an easily understood fashion. One aim of the activation modelling is to supplement the experimental data with an analysis which may lead to a greater understanding of the situation.

³<http://biorobotics.mit.edu/>

⁴Auckland, New Zealand

⁵Los Angeles, California, U.S.A.

Chapter 3

Cardiac Activation Modelling

There are a number of different approaches to the problem of simulating cardiac electrical activity. These models vary according to the knowledge of the processes involved and the sophistication of measurement and analysis techniques available at the time of construction. The oldest models, which are still in use in a clinical setting as the basis of standard electrocardiogram (ECG) analysis, represent the entire cardiac electrical state as a single time-varying vector or dipole in an infinite homogeneous medium. A description of the cardiac state is constructed by interpreting voltage-time diagrams which show the difference in potential between various extremities as a function of time. Though the model is simple and the results are crude, ECG analysis still produces many results which are useful to the practising physician. While a dipole model can give a basic global picture of cardiac condition, it is difficult to accurately model localised phenomena.

Later models discretise the heart into a large number of cells of some small finite volume, each of which has locally defined properties and a number of variables which describe the state of the tissue within that volume. The first of these approaches were again rather simple, due to a lack of adequate knowledge of the workings of the cardiac cell, and to computers being small and slow. As experimental techniques have improved, further research has given researchers a greater understanding of cellular electrical activity. Additionally, the level of computing power available has increased which makes more detailed models computationally tractable. This enables a more accurate and detailed model of the

electrical processes, but one which is continuing to increase in complexity as the combination of knowledge and computing power continues to increase.

Even though the understanding of the workings of the cell is small, though continually growing, there is always more that is known than can be fully modelled. Even with a level of computational power likely to be available in the next five years, there will still be insufficient computing resources to construct a model of the most advanced current knowledge of cardiac cellular processes for every cell in the heart for a single heartbeat, let alone include the additional mechanical and biochemical models, or modelling the processes at a molecular level. There must always be a stage at which a particular level of detail is deemed sufficiently accurate to give the solutions required, so that the assumptions made in constructing the model are acceptably small. This chapter discusses the development of various methods of modelling cardiac activation, culminating in a model which flexibly includes any given model of the ionic processes. The subsequent chapter outlines the important models of ionic movement and membrane currents, from those which are based on biophysical measurements and attempt to accurately describe every detail contributing to the action potential, to those which simplify all of these processes into approximate equations which produce results of a similar form to the biophysical models, but which have no underlying biophysical basis.

Some of the information contained in this chapter is adapted from review papers by Plonsey and Barr (1987) and Gulrajani (1988) which provide a more detailed and complete review of the various methods of modelling activation.

3.1 Non-Propagating (Dipole) Models

The simplest activation models belong to a class known as *dipole* models which describe the integrated effect of cardiac electrical activity rather than explicitly modelling the propagation of an action potential. Gulrajani (1988, p. 1) gives a brief background describing this class of models. The concept of a dipole model was formulated by Wilson, MacLeod and Barker (1933) who suggested that the electrical state of the heart could be described by defining a positive pole immediately in front of the excitation wavefront and a negative pole immediately behind the

wavefront, these two poles together forming a dipole. Savard, Roberge, Perry and Nadeau (1980) outline a method using a single moving dipole model which attempts to determine the location, orientation and magnitude of a single dipole so as to reconstruct measured body surface potentials with a least-squares estimator.

The dipole approach was later extended to include more than one dipole. An early model involving multiple dipoles was described by Selvester, Collier and Pearson (1965), who constructed an analogue computer simulation. This was later updated into a digital form and described in two subsequent papers (Selvester, Kalaba, Collier, Bellman and Kagiwada 1967; Selvester, Solomon and Gillespie 1968). In their model, the heart was divided into 20 regions with a dipole at the centre of each region. Dipole orientations were defined to be perpendicular to the average wavefront direction within the region, where the wavefronts were constructed from activation isochrones calculated from measurements made in dog heart by Scher and Young (1956). From the definition of the dipoles, vectorcardiograms (VCGs) on the torso surface could be calculated and compared with experimental measurements.

A pair of studies for normal (Miller and Geselowitz 1978a) and abnormal (Miller and Geselowitz 1978b) myocardium used the bidomain model (see Section 3.3) to compute dipoles. They constructed an anatomical model of the ventricles from approximately 4000 points, and divided it into 23 regions, each containing a single dipole. Data obtained by Durrer et al. (1970) of activation isochrones within the isolated human heart were used for computing the dipole orientations. Body-surface potential maps and ECGs were calculated and compared with experimental observations.

In each case the body-surface potential maps, ECGs or VCGs obtained by the dipole method are in good agreement with those obtained by experimental measurement. However, the dipole method cannot be used to determine information about the processes of activation and propagation themselves, as that would require at least the measurement of activation wavefronts on the epicardium. It is therefore necessary to develop models which also model action potential propagation, and determine the position of wavefronts from this. In many cases dipoles are subsequently calculated from the computed wavefronts and the same analysis and comparisons as given here are performed. Two main classes of propagation-based models exist. The simplest are empirical models which use a *black-box* or *rule-based*

representation of the action potential and its propagation. More sophisticated and realistic models attempt to model the membrane currents (see Section 2.2.4) and compute the cellular activation process from this.

3.2 Empirical Models

The next major class of activation models are *ad hoc* or *empirical* models (Gulrajani 1988). These (and all following) models describe localised electrical activity rather than only an integrated sum over the entire heart. This is achieved by discretising the cardiac geometry into a number of small *cells*. These cells are not related in any way to the physical cells which make up cardiac muscle, but are simply small three-dimensional “building blocks” occupying a finite volume which are connected together so that their combined volume fills the space of the original geometry. Each cell has a number of properties associated with it which describe the state of the cell, for example the conductivity at that point, the fibre direction, the transmembrane potential, and other static or dynamic properties. There is some scheme specified for each model describing how a cell is electrically connected to its *neighbours* and additionally some set of rules which defines the propagation of the wavefront. The combination of all this information provides a means for modelling the activation process at each point, and the global sum of the state of each cell defines the state of the heart at a given time.

Empirical models do not attempt to model the membrane currents which define the action potential, but instead construct a stylised action potential and enable propagation according to a predefined pattern. There are two such methods in common usage. Models based on the cellular automata method use a set of rules to specify how cells are activated from neighbouring active cells. The second empirical method is based upon a Huygen’s wavelet approach which determines propagation according to spherical or ellipsoidal wavelets. Each of these models can incorporate an anisotropic conduction velocity, but the membrane kinetics are not taken into account.

3.2.1 Cellular automata models

The cellular automata approach assumes that we can divide the geometry of the cardiac tissue into a regular matrix of cells, each representing some small volume of tissue. Activation is described by a stylised action potential, and a rule-based method is used to define the activation process. A system is defined for the set of cells which comprises

1. a set of two or more different *states*, where a given state describes the electrical state of a given cell at any point in time, and
2. a set of *rules*, which define when the cell will move from one state to another.

In addition to these definitions, the cellular automata model requires a geometrical description of the domain in which the model needs to be solved, and also a definition of the *cell neighbourhood*. The cell neighbourhood defines the set of neighbouring cells over which the state of a central cell will have an influence. In a square 2D grid, each cell may influence either four or eight neighbours (in general), while in a hexagonal 2D grid, six neighbours is most likely. A 3D model will often have cuboid cells, and therefore each cell has 26 nearest neighbours, although a more closely packed hexagonal arrangement is also possible. Some possible 2D neighbours are shown in Figure 3.1.

The earliest cellular automata model (and in fact the earliest computer model of activation) was a two-dimensional model of a sheet of atrial tissue constructed by Moe, Reinbolt and Abildskov (1964). An active cell would excite its six neighbours after some time delay, and then follow a stylised action potential whereby it would be in an absolute refractory state for one time step and in a relative refractory state for some number of further time steps. Using this model with a spatially varying refractory period generated waves resembling atrial fibrillation. Reinboldt, Ledly, Abildskov and Oestreich (1963) construct a similar model for the ventricles, but in three dimensions with cubic blocks.

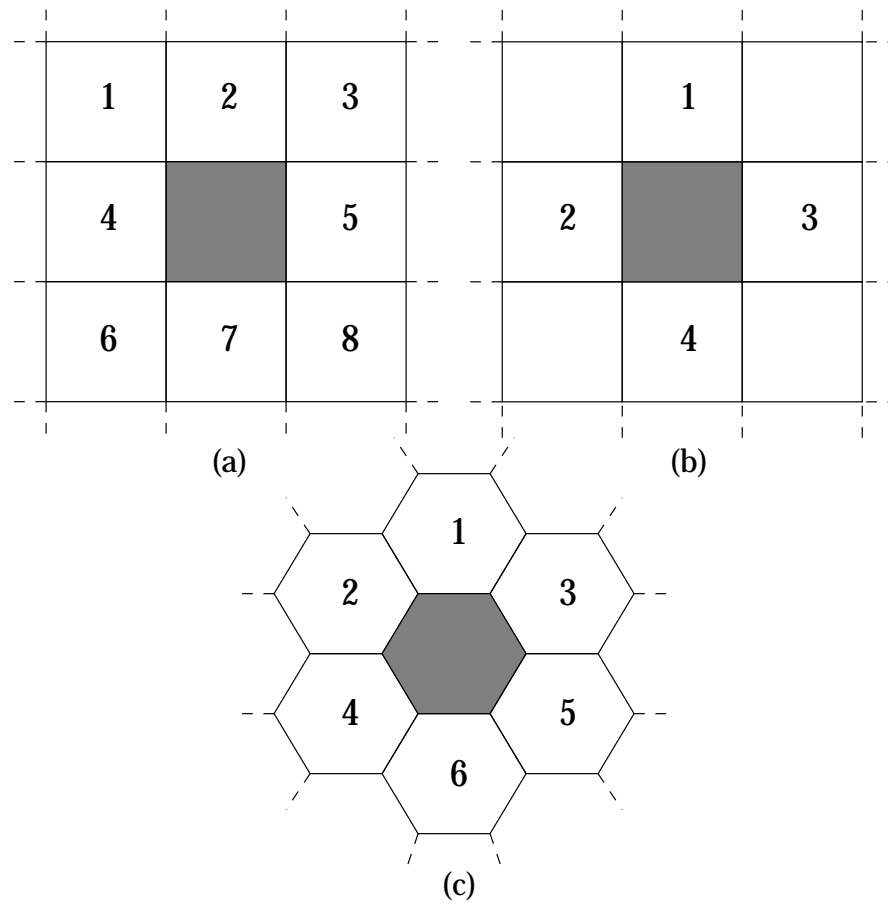


FIGURE 3.1: The nearest neighbours of an active (shaded) cell according to three possible rules in two dimensions. (a) 8 neighbours. (b) 4 neighbours. (c) 6 neighbours on a hexagonal grid.

A three-state model incorporating re-entry

Bailie, Mitchell and Anderson (1990) describe a three-state cellular automata model, with a quiescent (\mathbb{Q}) state, an excited (\mathbb{E}) state and a refractory (\mathbb{R}) state. These three states correspond to the basic three states of a membrane channel described in Section 2.2.4: resting, open and refractory states respectively. From that point of view, this three state model is the simplest physiologically reasonable cellular automata model. A two-state model does not provide sufficient information to allow a wavefront to propagate and then die away. For this problem the cell neighbourhood is defined in two dimensions as the eight nearest cells (as shown in Figure 3.1a).

$\text{State}_{(t)}$	$\text{Count}_{(t)}$	$\text{Neighbour}_{(t)}$	$\text{State}_{(t+1)}$	$\text{Count}_{(t+1)}$
Q	(any)	0	Q	0
Q	(any)	≥ 1	E	1
E	$< \mathbb{E}_0$	(any)	E	$\text{Count}_{(t)}+1$
E	\mathbb{E}_0	(any)	R	1
R	$< \mathbb{R}_0$	(any)	R	$\text{Count}_{(t)}+1$
R	\mathbb{R}_0	(any)	Q	1

TABLE 3.1: Three-state cellular automata model. Inputs are the cell state, count value and number of excited neighbouring cells at time (t). Output is new state and count value for subsequent time-step. From Bailie et al. (1990).

The rules which determine the change of state (called a *state transition* function) for this system are outlined in Table 3.1. Cells at rest in the Q state are activated by neighbouring cells (in this case, at the time-step immediately after a neighbouring cell enters the E state) entering the E state, and at the next time-step the cell activates any neighbouring cells which are in the Q state. After some length of time \mathbb{E}_0 the cell enters the R state for a time \mathbb{R}_0 , in which it will no longer activate neighbouring Q cells, nor can it be reactivated by neighbouring E cells. This state transition function results in a stylised action potential as shown in Figure 3.2.

This is the simplest system which will permit the generation of re-entrant phenomena, however the results printed in Bailie et al.'s (1990) paper show some of the limitations of the cellular automata approach. The model they use does not incorporate any microstructural information such as fibre orientation which would require anisotropic conductivity, as the propagation time from one cell to a neighbouring one is a single time-step (which they set to some realistic value). Cells are square and arranged on a rectangular grid, which influences the shape of the wavefront.

A four-state model including curvature and dispersion

Some cellular automata models attempt to include more sophisticated features of wave propagation in excitable media. A model constructed by Gerhardt, Schuster and Tyson (1990) includes two features not present in the earlier models: curvature

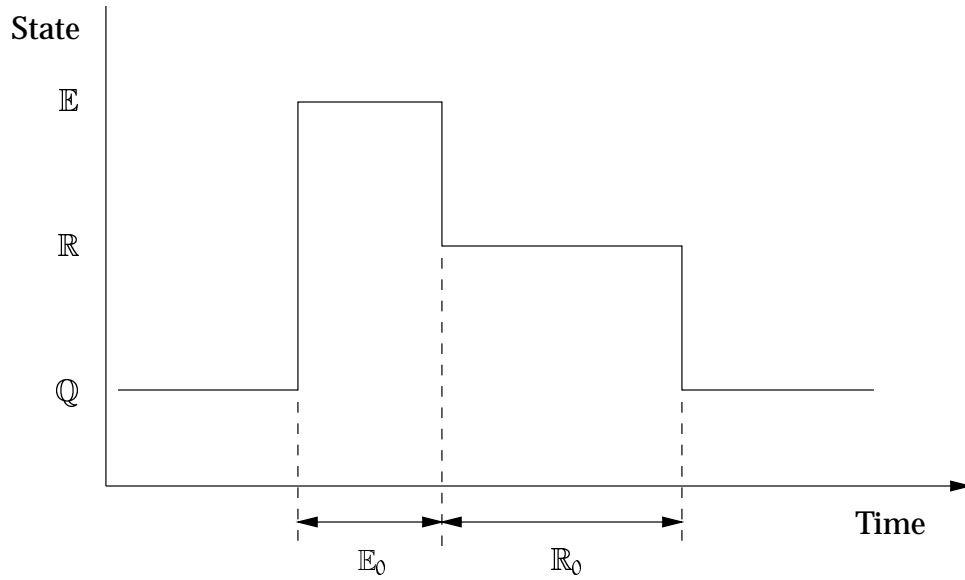


FIGURE 3.2: Stylised action potential produced by the state transition function given in Table 3.1. The diagram shows the passage of the cell through the three states and the time spent in the excited and recovering states.

of the wavefront influencing propagation, and dispersion of refractoriness. This is performed by incorporating delayed excitation and a relative refractory period into the model and giving an effective four states. A summary state table is shown in Table 3.2, and the paper contains a full description. Rather than using the state names Q , E and R as in the previous example, this model describes the cell state in terms of two state variables, u and v . u can take values of either 0 or 1 corresponding to resting and excited states respectively. The variable v is almost equivalent to the “Count” variable used above. It is bounded by the values 0 to v_{\max} and provides a measure of the refractoriness of the system.

The cell begins in a resting state ($u = 0, v = 0$) and remains there (Rule 1). Once the number of excited neighbours $exc_{i(t)}$ exceeds a threshold k_{exc} the cell becomes active by Rule 2 and enters an excited state ($u = 1, v > 0$). g_{up} is a positive integer which is a measure of the length of the “plateau”. The cell remains in an excited state by Rule 4 until either $v = v_{\max}$ (Rule 6) or the number of neighbouring cells in a resting or recovering state $reco_{(t)}$ exceeds the recovery threshold k_{reco} (Rule 5). The cell now enters a recovery state ($u = 0, v > 0$) and v begins to fall by Rules 3 and 1 at a rate g_{down} which is a positive integer representing the speed of the recovery process. While the cell is in an absolute refractory state ($u = 0, v \geq v_{exc}$) the cell

Rule	$u_{(t)}$	$v_{(t)}$	$exci_{(t)}$	$reco_{(t)}$	$u_{(t+1)}$	$v_{(t+1)}$
1	0	$< v_{exci}$	$< k_{exci}$	(any)	0	$v_{(t)} - g_{down}$
2	0	$< v_{exci}$	$\geq k_{exci}$	(any)	1	$v_{(t)} + g_{up}$
3	0	$\geq v_{exci}$	(any)	(any)	0	$v_{(t)} - g_{down}$
4	1	$< v_{max}$	(any)	$< k_{reco}$	1	$v_{(t)} + g_{up}$
5	1	$> v_{reco}$	(any)	$\geq k_{reco}$	0	$v_{(t)} - g_{down}$
6	1	v_{max}	(any)	(any)	0	$v_{(t)} - g_{down}$

TABLE 3.2: Two variable cellular automata model. Inputs are state variables u and v , $exci_{(t)}$ which is the number of excited neighbouring cells at time (t) and $reco_{(t)}$, the number of neighbouring resting or recovering cells ($reco_{(t)} = n - exci_{(t)}$ where n is the number of neighbours). Output is the value of the state variables for the subsequent time step. Note that v is bounded by 0 and v_{max} at each time step. From Gerhardt et al. (1990).

will not excite neighbouring cells, nor will it be reexcited. Once it enters the relative refractory state ($u = 0, v < v_{exci}$) it may become reexcited. The threshold variable k_{exci} adjusts so that if v is large then more excited neighbours are required to excite the cell. A diagram illustrating the change in the two variables is shown in Figure 3.3.

With judicious definition of the parameters $k_{exci, reco}$ and $g_{up, down}$ a good model of activation can be constructed. The model exhibits some of the physiological properties of a normal activation wave, such as curvature and dispersion of refractoriness inducing by a relative refractory period. The problem is that the complexity of the rules has greatly increased and there is still no information about what may actually be occurring within the tissue. This is the shortfall of using an empirical approach, rather than an approach which attempts to model the cellular processes.

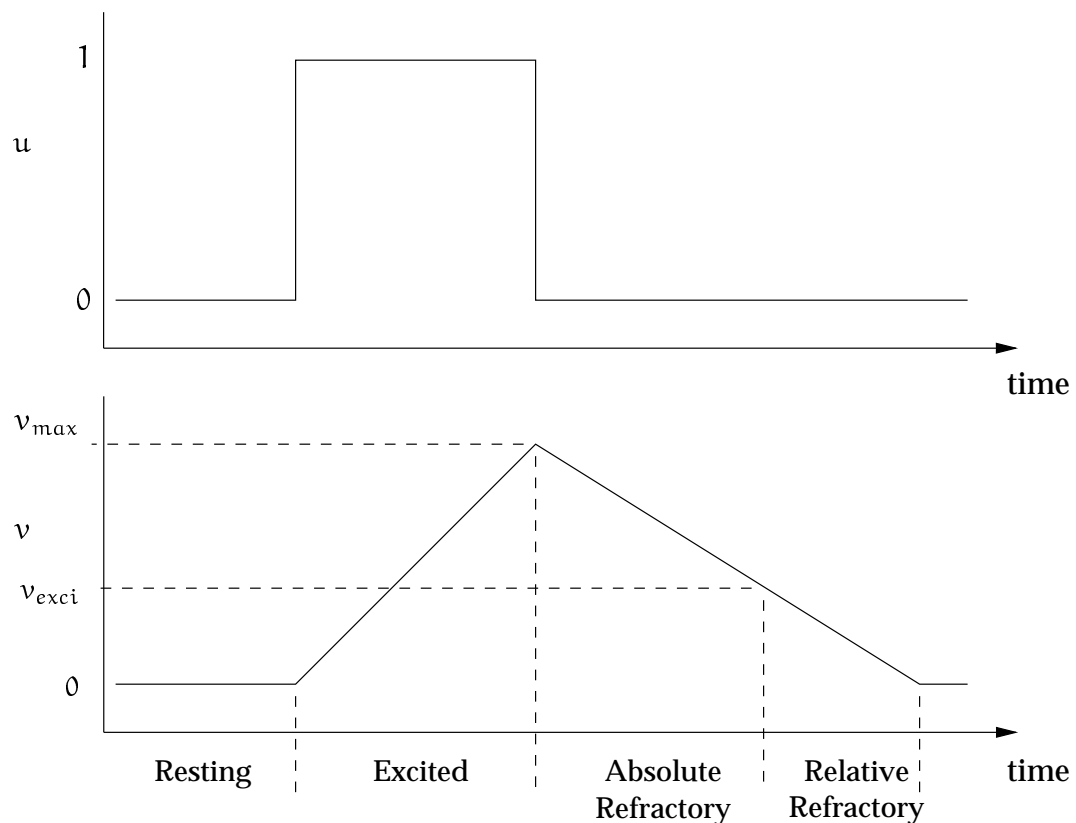


FIGURE 3.3: Two variable cellular automata model. The change in value of the variables gives rise to four effective cell states. From Gerhardt et al. (1990).

Other cellular automata models

Restivo, Craelius, Gough and El-Sharif (1990) describe a five-state model which has two explicit refractory states, and a slightly more sophisticated algorithm again for determining movement through the states, but there is still no membrane kinetics involved, nor any inclusion of microstructural information.

Leon and Horacek (1991) have constructed a much more sophisticated cellular automata model which uses the bidomain model and an anisotropic conductivity to more accurately specify the propagation. Each cell has four *macro-states*: the resting state, the excitatory state, the absolute refractory and relative refractory states. Each of these four macro-states has its own set of *micro-states* and its own state transition function. This model still suffers from having a limited number of discrete states to approximate the local action potential rather than a continuous approach. In

addition the model is still based on rules, and this makes it difficult to easily model abnormal activation patterns.

3.2.2 Huygen's wavefront method

The other main empirical technique is an approach derived from Huygen's principle of the propagation of light. This model only describes the activation process, and is often used where only this quantity is of interest. In some cases it has been coupled with a rule-based scheme describing the recovery process. Huygen's wavefront models are very similar in form to cellular automata models, and share many of the same advantages and disadvantages.

This model is solved either on an array of blocks or on a grid of solution points where each block or point represents a finite area or volume of excitable tissue. From all active points a spherical (or ellipsoidal) wavefront is constructed which represents the distance that an action potential would propagate in a time step Δt . If a solution point falls inside this augmented wavefront then it too is activated. The process repeats as shown for a two-dimensional example in Figure 3.4 until the activation wave spreads over the whole tissue. The construction of the ellipsoids can account for anisotropic or orthotropic conduction speeds by aligning the main axis of the ellipse with the fibre direction, and the conduction ratios can be spatially varying, together with a varying fibre orientation through the tissue.

A simple model employing Huygen's method is that of Okajima, Fujino, Kobayashi and Yamada (1968) who construct a ventricular model comprising 27,000 3 mm side-length cubic blocks. Isotropic conduction only was considered, and a wavefront approach specified the activation time of a block depending on its distance from all neighbouring active blocks. This model only generated isochrones based upon times of activation, and did not incorporate the recovery process. Solomon and Selvester (1973) extended their earlier work with a dipole model to include a Huygen's model of propagation and constructed a 750,000 node ventricular model with 1 mm spacing between nodes.

One of the most sophisticated isotropic Huygen's wavefront models was developed

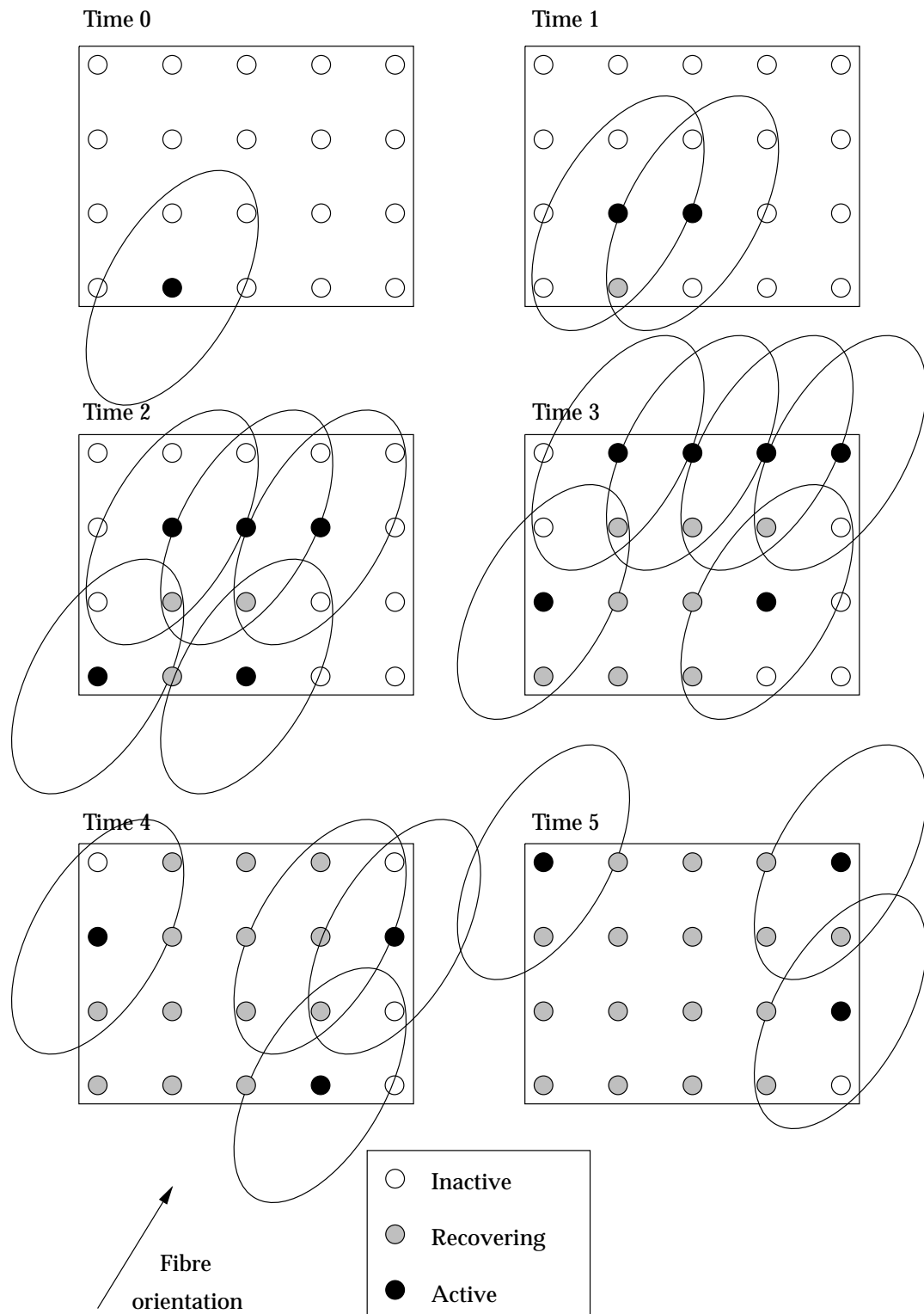


FIGURE 3.4: A simple two-dimensional simulation using Huygen's wavefront method. The entire domain is activated after 6 time steps. The ellipses representing the wavefront are aligned with the fibre direction and the axes are scaled to represent the ratio of conduction velocities.

at Dalhousie University¹ in the early 1970s, and uses a realistic model of the atrial and ventricular geometry (Gulrajani 1988). Rhombic dodecahedra were used as the volume-filling blocks because all twelve nearest neighbours are equidistant when packed in a honeycomb-like structure, and therefore an isotropic activation model is easy to implement. The model was constructed from 24,413 atrial blocks, 156,349 ventricular blocks and 19,283 blocks describing the Purkinje fibre network. The Purkinje blocks conduct at three times the rate of the other blocks. Once activated, each block follows a stylised action potential with variable length absolute and relative refractory periods. From the activation analysis, dipoles are constructed and are used to compare against ECGs generated using an inhomogeneous torso model.

An anisotropic Huygen's wavefront model was developed by the same group and used to investigate the WPW syndrome (Lorange and Gulrajani 1986). This model was based on the original Miller and Geselowitz (1978a) model with twice as many solution points in each direction. Ellipsoidal activation wavefronts were constructed so that activation spread quickly parallel to the epicardium and more slowly through the wall, with a velocity ratio of 1.94 computed from canine myocardial experiments by Roberts and Scher (1982). Because the ellipsoids were not oriented with the local fibre orientations the results differed somewhat from experimental measurements. Later models by Adam (1985), Saxberg, Grumbach and Cohen (1985) and Wach, Killmann, Dienstl and Eichtinger (1989) incorporate ellipsoids calculated along experimentally determined fibre orientations, with up to 1 mm resolution between solution points. Various action potential waveforms were used to describe activation at each site, and reconstruction of ECG and body torso signals tended to agree well with experimental data. However, this tends to occur because model parameters are adjusted so that the correlation is good, and often the parameters do not closely approximate experimental values. This restricts their usefulness in simulating abnormal conditions.

Another anisotropic Huygen's wavefront model was constructed by Hookings (1988) and uses the accurate model of cardiac microstructure developed by Nielsen et al. (1991). Only the activation process was simulated with this model, and transversely isotropic wavespeeds were assigned in directions which are aligned with the local fibre orientation. In order to obtain results which are well correlated

¹Halifax, Nova Scotia, Canada

with experimental measurements the wavespeed parameters were required to be somewhat higher than those recorded experimentally (Roberts and Scher 1982) showing need for further refinement of the model. This model was extended to incorporate the orthotropic structure evident in later histological studies by Le Grice (1992). There is no experimental wavespeed data available which is based on the laminar structure, and therefore the relative wavespeeds needed to be estimated from a combination of known values and observations of the myocardial structure. This results in the propagation rate in the third direction being determined by branching ratios of the sheet structures, and it varies transmurally. The wavespeeds used were 0.67 ms^{-1} in the fibre direction, 0.5 ms^{-1} in the sheet direction and between 0.34 ms^{-1} and 0.25 ms^{-1} through the wall. A scale factor of 3.0 was used to enhance the velocities in the Purkinje fibre network, which has been defined so as to penetrate the endocardial wall by up to several mm in order to be consistent with canine myocardial observations.

As with the cellular automata models, Huygen's wavefront models have the restriction that they are based on a set of rules which do not accurately represent the underlying electrophysiological behaviour of the cell membrane. Empirical models are useful for modelling relatively simple predefined situations, especially involving only activation. However, new rules must be developed and verified for every new problem, restricting their usefulness.

3.3 The Bidomain Model

The complete model of cardiac activation would be one in which an accurate model is formulated for each type of muscle cell. The model would completely describe the structure of the cell and detail every aspect of its electrophysiological function down to a molecular level, as well as the mechanical and energetic processes involved if this information was required. This cellular model would then be inserted into an anatomically accurate description of the global cardiac geometry, and solved on a cell-by-cell basis over the cardiac volume. There are many reasons why such a model has not yet been constructed. Firstly, it is difficult to obtain an accurate model of cell function. Many of the membrane processes are still being quantified, if they are known at all. Some recent improvements in this area are outlined in

Chapter 4. Secondly, an anatomically accurate definition of the cardiac geometry is still incomplete. Difficulties exist in measuring the position of the ventricular endocardium, and many models only describe the ventricular myocardium but not the atrial tissue or accessory structures. Coupled with this is a lack of a complete description of the cellular structure. The Auckland model (see Section 2.1.2) is the most detailed and accurate ventricular microstructural model to date, yet it has little information yet on the Purkinje network, and none at all on the atrial tissues. The process of propagation is again only partially understood, and a model describing even the conductivities in the orthogonal microstructural directions is yet to be formulated. Similar models of the energetic function and the passive and active mechanics are still under construction, and the concept of being able to couple the various components together in a total model is only beginning to be looked at. Even given the availability of this vast amount of information, there would still be one requirement lacking. Existing computational resources are barely adequate to solve a small region of tissue. Spach and Heidlage (1993) have developed a model solving activation equations for individual cells for a two-dimensional sheet model containing between 25,000 and 85,000 cells. Even though there is only a small number of cells in a 2D preparation, and the ionic model used is not the most complex presently available, the model requires the use of a high-performance supercomputer in order to solve the problem. While computational speeds are doubling approximately every eighteen months, a complete model involving all cardiac processes is still a long way from being computationally tractable.

Given that the current state of knowledge and the current computational capabilities preclude the use of a model completely representing the current state of knowledge of cardiac activation, we need to determine what level of detail is feasible yet sufficiently realistic so as to allow the investigation of various abnormal phenomena. The empirical models are no longer appropriate as they ignore the cellular processes. One commonly used method is to use a macroscopic model which uses a volume-averaged approach, known as the *bidomain model*. This model averages the electrical properties over some length scale which is greater than that of a single cell. In doing this with an appropriate choice of length scale, the effect of cell junctions on propagation can be ignored, and the discrete cellular structure may be replaced with a uniformly continuous structure. There are problems with this approach. If discrete cellular effects play a significant role in the propagation of activation, then either this will need to be incorporated or a new model will need to be constructed.

Alternatively, if a macroscopic model can provide results which are a reasonable approximation to the explicit microscopic model then the averaged model may be justified.

3.3.1 Definition of the bidomain framework

The physical arrangement of cardiac cells has led to the belief that the heart has electrical properties that are the same as a syncytium. Experimental work by Weidmann (1970) and Clerc (1976) on mammalian cardiac tissue confirmed that propagation either along the fibre axis or transverse to it produced results like a one-dimensional cable. Cable theory defines propagation along a membrane between two distinct spaces, or *domains*, and describes the one-dimensional version of the bidomain model. This theory can easily be extended to two and three dimensions for domains of higher order geometry.

The concepts behind the bidomain model were first proposed by Schmitt (1969) who suggested that two interpenetrating domains could be used to describe cardiac tissue, one representing volume-averaged quantities in the intracellular space and one for those of the extracellular space. A mathematical formulation of this proposal was constructed in several theses and papers by Tung (1978), Plonsey and Barr (1984), Miller and Geselowitz (1978a) and others. The bidomain model has been adopted by many other researchers in one form or another due to its convenience and simplicity. The model is discussed more fully in review papers by Henriquez (1993) and Plonsey and Barr (1987).

Different papers give different names to the various regions that are part of the bidomain model. The names that we have chosen reflect the generally accepted definitions (as given by Krassowska and Neu (1994)) which tie in with those that physiologists would use to describe cellular structure. When developing an activation model which is designed to be coupled with other models, it is necessary to maintain consistent definitions and distinctly identify each region.

The bidomain framework defines two domains which make up the cellular matrix. The *intracellular domain*, given the subscript “i”, is the region inside the cells, and the *extracellular domain* with subscript “e” is the region between cells. These

Extramyocardial (outside) Region

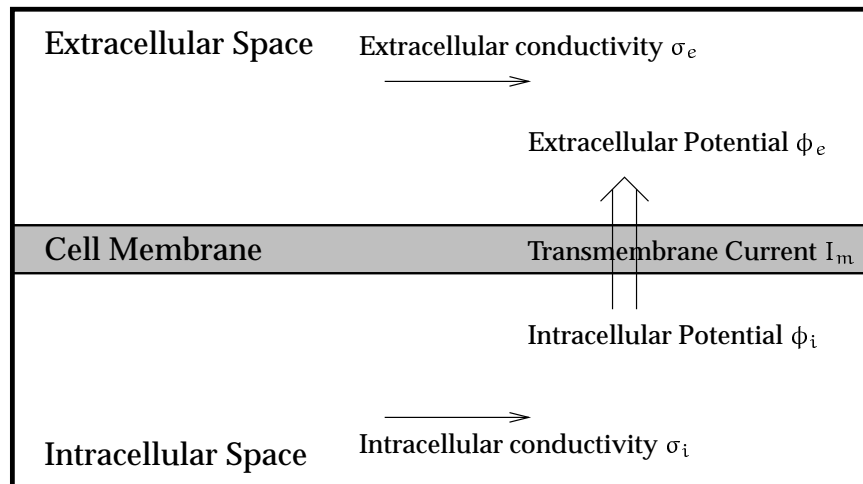


FIGURE 3.5: The bidomain model.

two domains are interpenetrating which means that they coexist at all points in space. Therefore the properties and state of the tissue at each point have separate components related to each domain with appropriate subscripts. For example, a single point in space will have a tensor quantity associated with it defining the conductivity in each of the intracellular and extracellular spaces. The intracellular and extracellular domains are separated by the cell membrane at all points, and all current flow between the two domains occurs solely through the cell membrane. Because of the continuum approach to the physiology of the tissue, this transmembrane current is volume-averaged. This averaging approach is required so that a length scale can be chosen such that the averaging produces little loss of information. Additionally, a third domain may be defined consisting of all regions outside of the cardiac muscle, such as the bath that the tissue is in, or the tissues within the torso cavity. This domain is referred to as the *extramyocardial (outside) region* and given the subscript “o”. Krassowska and Neu’s (1994) paper simply refers to this region as “outside”, but in a coupled problem it is unsure whether this should refer to a region outside the heart or outside the body. This naming convention is illustrated in Figure 3.5.

Some authors (including Pollard, Hooke and Henriquez (1993), Henriquez (1993), Plonsey and Barr (1987) and others), define the regions differently. In particular, what we term the extramyocardial region is defined as the extracellular space, and

what we call the extracellular domain is called the *interstitial domain*, often with “extracellular” also written in parentheses afterwards. This causes some confusion in the definitions of what constitutes extracellular space, and is inconsistent with the standard physiological definition of the extracellular matrix being the connective support structure and myoplasm surrounding cells. Therefore it seems best not to use the term “interstitial” at all, but to reserve the word “extracellular” for use in describing structure that is part of the extracellular matrix, and use another term for the medium surrounding the tissue, which in this case we have chosen to call “extramyocardial”. This agrees also with the tissue definitions of Clerc (1976) in his study of tissue conductivities which is cited as a definition for these terms by Pollard et al. (1993). It is true that the extramyocardial space is also technically extracellular, but it is not (by definition) part of the cardiac tissue structure, and because it is often not used in many bidomain simulations, it is sensible to use another name for this region. Some authors (Plonsey and Barr 1987) also use the subscript “o” for the extracellular space, but this seems much less standard, and is similarly confusing.

The bidomain model describes current flow through the cell membrane in a space-averaged sense. Instead of modelling a discrete cellular structure, the bidomain constructs a continuum model with effective conductivity tensors which is governed by continuous partial differential equations.

3.3.2 Mathematical derivation of the bidomain model

The most substantial mathematical description of the bidomain model is found in the review paper by Henriquez (1993), which presents a formal definition of the model from its origins in the core conductor model, and outlines many of the approximations that can be made under certain assumptions. The derivation presented here follows the pattern of this review, but only illustrates the details appropriate to the work carried out here. Small changes have been made in the notation and these are noted where they occur.

At a point, we define volume-averaged macroscopic potentials ϕ_i and ϕ_e in the intracellular and extracellular spaces respectively, where the values of the potentials are measured in mV. The transmembrane potential V_m is defined as the potential

difference across the cell membrane

$$V_m = \phi_i - \phi_e \quad (3.1)$$

and is also measured in mV.

From the definition of the cardiac microstructure, there is a local material coordinate system defined at every point with axes aligned with each of the local fibre, cross-fibre (sheet) and cross-sheet directions. In an undeformed geometry, these material axes are defined to be orthogonal. These three axes are used to define the principal directions of propagation. That is, we replace the discrete structure by effective conductivities which average out the discrete behaviour. In a coordinate system defined by the material axes, the effective conductivity tensors are diagonal. Allowing for different conductivities in each domain, we can construct two effective conductivity tensors σ_i and σ_e for the intracellular and extracellular domains respectively, with units $(\Omega\text{m})^{-1}$, or equivalently, Sm^{-1} . Henriquez uses the symbols g_i and g_e to describe the effective conductivities, with $\sigma_{i,e}$ being reserved for true conductivities. However, we choose to use the variable σ for the effective conductivities to emphasise that these are defined in the material coordinates rather than the global coordinates. Values for these tensors are still difficult to obtain as much of the experimental work has yet to be done, but using transversely isotropic measurements such as those by Clerc (1976) and using microstructural observations regarding path lengths can lead to a first approximation to the effective conductivities. The experimental work required will involve measuring three-dimensional plane wave propagation rates and relating them to observed microstructural details. In constructing effective conductivities, a continuum approach is taken whereby the discrete cell-to-cell coupling and the fibrous and sheet branching ratios are not explicitly modelled, but rather the averaged rate of propagation implicitly takes into account these microstructural features.

Restricting the relationship between the two domains can simplify the following equations greatly, especially for equal anisotropy or reciprocal anisotropy where the ratios between fibre and non-fibre directions are either the same or inverted in each domain, respectively, but these are only defined for a transversely isotropic medium. In this thesis, no such restriction is made, and independent orthotropic effective conductivity tensors are described for each domain.

Using Ohm's law, the intracellular and extracellular current densities J_i and J_e (with

units Am^{-1}) are derived as

$$J_i = -\sigma_i \nabla \phi_i \quad (3.2)$$

and

$$J_e = -\sigma_e \nabla \phi_e \quad (3.3)$$

where ∇ is the gradient operator, and the current densities are defined in the local material coordinate system.

All current leaving one domain crosses the cell membrane and enters the other domain, so that the change in current density between the two domains is equal and opposite, with allowance made for any source or sink current within either domain. The change in current density in each domain is equal to the current density across the membrane

$$-\nabla \cdot J_i = A_m I_m - I_s = \nabla \cdot J_e \quad (3.4)$$

where A_m (units m^{-1}) is the surface-to-volume ratio of the cell membrane, I_m (units Am^{-2}) is the transmembrane current density per unit area, and I_s (units Am^{-3}) is an externally imposed source current per unit volume. Ignoring the applied current, this gives the following conservation of current density equations:

$$\nabla \cdot (\sigma_i \nabla \phi_i) = A_m I_m \quad (3.5)$$

$$\nabla \cdot (\sigma_e \nabla \phi_e) = -A_m I_m \quad (3.6)$$

From Equations (3.5) and (3.6) and by using Equation (3.1) we can write

$$\nabla \cdot (\sigma_i \nabla \phi_i) = -\nabla \cdot (\sigma_e \nabla \phi_e) \quad (3.7)$$

$$\nabla \cdot (\sigma_i \nabla \phi_i) - \nabla \cdot (\sigma_i \nabla \phi_e) = -\nabla \cdot (\sigma_e \nabla \phi_e) - \nabla \cdot (\sigma_i \nabla \phi_e) \quad (3.8)$$

which gives

$$\nabla \cdot (\sigma_i \nabla V_m) = -\nabla \cdot ((\sigma_i + \sigma_e) \nabla \phi_e) \quad (3.9)$$

This is the conservation of current equation and describes the coupling of the two domains.

The transmembrane current can be described as the sum of a capacitive current given by the change in transmembrane potential and a ionic current governed by

a Hodgkin-Huxley type model for cardiac tissue (Hodgkin and Huxley 1952)

$$I_m = C_m \frac{\partial V_m}{\partial t} + I_{ion} \quad (3.10)$$

where C_m is the membrane capacitance per unit area ($\mu\text{F} \cdot \text{mm}^{-2}$) and I_{ion} is a nonlinear function representing the sum of all of the transmembrane ionic currents and other cellular currents, with units Am^{-2} . There are many possible functions which display behaviour resembling the ionic currents, and some of the history and usefulness of these functions is covered in Chapter 4.

From Equations (3.5) and (3.10), and substituting Equation (3.1), we obtain

$$\nabla \cdot (\sigma_i \nabla V_m) + \nabla \cdot (\sigma_i \nabla \phi_e) = A_m \left(C_m \frac{\partial V_m}{\partial t} + I_{ion} \right) - I_s \quad (3.11)$$

Equations (3.9) and (3.11) are together known as the bidomain equations. We have not made any assumptions at this stage about the geometry of the problem or the nature of the conductivity tensors, except that from geometry we assume that the principal axes of anisotropy are aligned for each domain, and therefore these partial differential equations are a completely general description of the bidomain model.

There is one assumption commonly made which reduces the bidomain equations to a single *monodomain equation* and considerably simplifies the computational effort required. This assumption can be made if the extracellular space is assumed to be highly conducting (i.e. σ_e is effectively infinite) or if the domains are equally anisotropic i.e. $\sigma_i = c \sigma_e$ where c is a constant. Making this assumption reduces Equations (3.9) and (3.11) to a single equation known as the monodomain equation

$$\nabla \cdot (\sigma \nabla V_m) = A_m \left(C_m \frac{\partial V_m}{\partial t} + I_{ion} \right) - I_s \quad (3.12)$$

where $\sigma = \sigma_i$ is the effective conductivity tensor of the single domain, and the transmembrane potential equals the intracellular potential because the extracellular potential is effectively constant and zero. In some places further on in the thesis, it becomes convenient to talk of either Equation (3.12) or Equation (3.11) being the transmembrane equation, and Equation (3.9) being the extracellular equation.

The potential in the extramyocardial domain satisfies Maxwell's equations, but because of the low frequency of cardiac events (less than 250 Hz) and the particular electrical material properties of the surrounding tissue, the capacitive, inductive and

propagative effects are small enough that they may safely be ignored. This results in the extramyocardial potential satisfying Laplace's equation

$$\nabla \cdot (\sigma_o \nabla \phi_o) = 0 \quad (3.13)$$

for a general inhomogeneous anisotropic medium. Advanced models of the torso incorporate the varying conductivities and anisotropies present in structures outside the heart, though the tissue immediately surrounding the heart is isotropic.

Boundary conditions

The intracellular domain is essentially self-contained, and therefore we can assume a no-flux boundary condition at all points where it is required, i.e.

$$\frac{\partial \phi_i}{\partial \mathbf{n}} = 0 \quad (3.14)$$

where \mathbf{n} is a unit outward normal vector to the domain boundary. The extracellular and extramyocardial domains are effectively linked, and therefore the potential and the normal current must be continuous at the tissue-bath interface

$$\phi_e|_{\Gamma} = \phi_o|_{\Gamma} \quad (3.15)$$

$$(\sigma_e \nabla \phi_e) \cdot \mathbf{n}|_{\Gamma} = \sigma_o \left. \frac{\partial \phi_o}{\partial \mathbf{n}} \right|_{\Gamma} \quad (3.16)$$

where Γ represents the interface between the domains and the extramyocardial domain is considered to be isotropic on Γ . Only Equation (3.14) is required for a monodomain simulation.

3.3.3 Applications of the bidomain model

The bidomain model of cardiac activation has gained some acceptance since its derivation in the late 1970s and early 1980s (Tung 1978). As mentioned earlier, papers by Plonsey and Barr (1987) and Henriquez (1993) present reviews of many of the simulations which use a bidomain approach. In many cases, a monodomain formulation is used, and as shown by Pollard et al. (1993), the results are often very similar whether one uses a bidomain or monodomain formulation. There

are two main reasons why a bidomain formulation would be used: firstly if the stimulus current is applied specifically to the extracellular domain, or secondly if the activation model was being coupled to an electrical model of the torso cavity to obtain body surface potentials.

Several papers have been important in describing the behaviour of the bidomain model. Plonsey and Barr (1984) examined patterns of current flow resulting from a given state of activation in an anisotropic two-dimensional sheet of fibres. The ratio of conductivities between the intracellular and extracellular domains was investigated, and behaviour modelled for three ratios: isotropy, reciprocal anisotropy and nominal anisotropy. Their results showed that, given a reciprocal anisotropy, the current flows in loops of about 2 mm in the resting portion of the tissue, which is markedly different from the results obtained in an isotropic model. Their results were confirmed in a later study by Sepulveda and Wikswo (1987) which used a finite element technique, and subsequent experiments (Staton, Friedman and Wikswo 1991) have shown current patterns consistent with those generated using the bidomain formulation, indicating that myocardium has unequal anisotropy ratios.

A number of other papers have defined the method of action potential propagation within a bidomain, the earliest of which seem to be a series of three theoretical papers by Muler and Markin (1977a; 1977b; 1978). Their studies focused on a two-dimensional bidomain with arbitrary anisotropy but homogeneous fibre orientation, and derived several equations describing the conduction velocity in the tissue. Their results indicate that a single-fibre core conductor model can only be extended to two or three dimensions under the monodomain assumption in which either there is the special case of equal anisotropy or the extracellular resistance is zero. Later numerical models by Barr and Plonsey (1984) confirmed the theoretical predictions of Muler and Markin (1977a) except for the case of reciprocal anisotropy where a diamond shape was formed rather than the predicted rounded square. However, that turned out to be due to the ionic current model used by (Henriquez 1993) and further simulations by Pollard et al. (1993), using an implicit technique and the Ebihara-Johnson model of the membrane kinetics (see Section 4.1.5), resulted in diagrams which qualitatively resembled the rounded square which had been predicted.

Many further models have used the monodomain assumption and additionally used a simplified model of the membrane kinetics (Section 4.2), particularly in the study of rotors or spiral waves in two and three dimensions. Much of the theoretical and modelling work in this area has come from Winfree who uses the FitzHugh-Nagumo equations in a generic monodomain model using a regular finite difference grid in both two and three dimensions (Henze, Lugosi and Winfree 1990, Winfree 1990a; 1990b; 1990c; 1991. Other papers by Rogers and McCulloch (1994a), Agladze, Keener, Müller and Panfilov (1994), Courtemanche and Winfree (1991), Karma (1993), Kogan, Karplus, Billett and Stevenson (1992), Panfilov and Holden (1993) and others use various monodomain models and various membrane kinetic models in their investigation of spiral waves and two-dimensional propagation. Some three-dimensional studies have also been performed by Panfilov and others, including a large scale finite difference model of a static heart. A complete heart simulation in which the cardiac tissue is free to move has not yet been accomplished.

Some progress has been made in the development of *eikonal* equations. These are non-linear elliptic equations describing solely the position of the wavefront, or alternatively the isochrones describing the activation time. Colli Franzone, Guerri and Rovida (1990) have developed zero-order eikonal equations by generalising the relationship between velocity and conductivity, and also equations of higher order in which the effect of the wavefront curvature is included in the model. Additional papers (Colli Franzone, Guerri and Tentoni 1990; Colli Franzone, Guerri and Taccardi 1993a; Colli Franzone, Guerri and Taccardi 1993b) develop the technique further to include three-dimensional tissues with fibre rotation and an anisotropic bidomain model. The eikonal technique involves only spatial parameters and is therefore easier to solve than the partial differential equations based on the membrane kinetics, but the information gained is more limited and the eikonal equations cannot describe any form of reentrant behaviour.

Chapter 4

Ionic Current Models

One assumption that has been made in developing the bidomain framework is that a mathematical model can be constructed which describes the membrane kinetics that cause an ionic current to flow across the cell membrane. Ideally, this ionic current model would describe each of the individual ion currents which flow through the ion channels and pumps, and in doing so maintain knowledge of the intracellular and extracellular concentrations of all ions involved in the activation process. The ionic current I_{ion} is defined as the sum of the individual currents.

There are two main ways in which an ionic current model can be constructed. One approach is to attempt to exactly describe all of the behaviour and construct a *biophysical* model, also called in some papers an *exact* or *complete* model. In some cases the theory contained within the model has been confirmed by later experiments, and in others the models have been developed in order to explain observed behaviour. There are two main problems with this approach. Firstly, the ionic processes are still not well understood, and the models are constantly being updated and revised in order to incorporate new information. There are experimental problems in accurately measuring cause-and-effect relationships to a significant level of detail at this small scale. Secondly, the models produced using this approach tend to be large and complex, and the computational time required to solve the system of equations becomes prohibitive for large problems.

The alternative approach is to construct much more simple models which produce

behaviour similar to that of the exact models, but which are not derived directly from physiological observation. The aim of these *simplified* models is to replicate certain key features of activation, such as propagation and recovery. The advantage is that they are typically very small and fast to solve, and therefore usable in large problems. The main disadvantage is that although the model will successfully predict the nature of a normal activation, it will not be able to determine the effect of some abnormality in the tissue with any degree of certainty as the physiological influences on the electrical processes are not being adequately modelled.

The ideal solution is to use the most appropriate model for a particular problem, and retain the flexibility to include any of a number of models. The first section of this chapter discusses the physiologically based models and the second section examines a few of the simpler models. The equations describing most of these models have been coded and solved using the NAG routine D02EBF (NAG 1993) for solving a system of first-order ordinary differential equations using a variable-order, variable-step method implementing the back differentiation formulae.

4.1 Biophysically Based Ionic Current Models

An exact model is constructed by deriving mathematical equations which describe specific actions within the cell membrane, such as the transfer of ions through a pump or the flow of ions through a gate which is caused by a concentration gradient. These models have developed either from fitting the parameters of an equation to experimentally measured data, or in some cases from defining an equation to match observed conditions which were later confirmed experimentally. The first models were derived for Purkinje fibres, based on the Hodgkin-Huxley model of nerve. Later models have quantified specific behaviours of atrial and ventricular tissue, and the models have grown in size as other currents are found to exist and become significant in the role of the action potential. The latest, most sophisticated models require a large amount of computing resources in order to be solved, and have to date only been used to model single cell behaviour and small two-dimensional domains. As computational speed increases and more memory is available, these models will begin to be used for three-dimensional studies, though this is prohibitive at the present time.

Each model described here builds on previous models, and all those described in this section are based on the cell membrane formulation developed by Hodgkin and Huxley for nerve fibres.

4.1.1 Hodgkin-Huxley Model

In a series of papers published in 1952, A.L. Hodgkin and A.F. Huxley present the results of a series of experiments in which they investigate the flow of electric current through the surface membrane of the giant nerve fibre of a squid. In the summary paper of the HH model (Hodgkin and Huxley 1952), the authors developed a mathematical description of the perceived behaviour of the membrane based upon these experiments which would account for the conduction and excitation of the fibre. The form of this description has been used as the basis for almost all other complete ionic current models of different excitable tissues, including Purkinje fibres and cardiac atrial and ventricular muscle.

The cell membrane

Hodgkin and Huxley derived an electrical circuit which they considered to be representative of the electrical behaviour of the cell membrane. This circuit is shown in Figure 4.1 with one small modification from the diagram illustrated in the original paper. Figure 4.1 has reversed the direction of positive current flow to conform with the convention proposed by Noble (see Section 4.1.2 for the reasons for this change) which has been commonly adopted for cardiac tissue. Hodgkin and Huxley proposed two parallel pathways for current to be carried through the membrane. These are the capacitive current through the membrane derived using Ohm's law (where the membrane capacitance is denoted by C_m), and the ionic current I_{ion} .

$$I = C_m \frac{\partial V_m}{\partial t} + I_{ion} \quad (4.1)$$

The ionic current is further divided into components carried by the sodium and potassium ions (i_{Na} and i_K respectively), and a leakage or background current i_L carried by chloride and other ions.

$$I_{ion} = i_{Na} + i_K + i_L \quad (4.2)$$

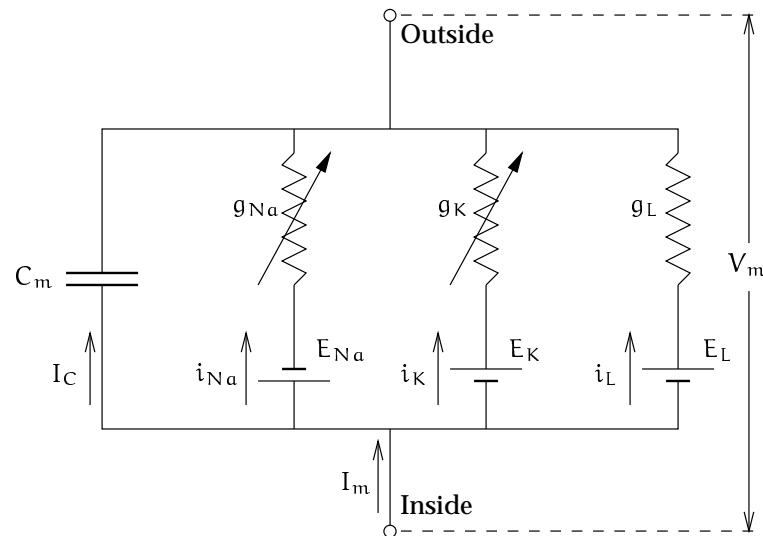


FIGURE 4.1: Electrical circuit representing the cell membrane. g_{Na} and g_K are functions of time and membrane potential; all other values are constant. Derived from Figure 1 in Hodgkin and Huxley (1952).

Each of these ionic currents can be expressed in terms of the ionic conductances g_{Na} , g_K and g_L respectively, which are the inverses of the respective resistances, and the electrical potential difference of the ion channel, using the relations

$$\begin{aligned} i_{Na} &= g_{Na}(V_m - E_{Na}) \\ i_K &= g_K(V_m - E_K) \\ i_L &= g_L(V_m - E_L) \end{aligned} \tag{4.3}$$

where E_{Na} , E_K and E_L are the equilibrium potentials or reversal potentials associated with each current and V_m is the transmembrane potential as defined in Equation (3.1).

Membrane channel current formulation

Each of the three types of ionic current described in Section 2.2.5 has a mathematical description of that membrane channel.

- **Time-independent or background currents**

Time-independent currents are only voltage-dependent, and can be described by

$$I = f(V_m) \quad \text{or} \quad (4.4)$$

$$I = g(V_m)(V_m - E_r) \quad (4.5)$$

where E_r is the reversal potential of the channel. The reversal potential is equal to the Nernst potential (see Equation (2.2)) for an ion if the channel is permeable only to that ion. The leakage current i_l is a time-independent current, and later ionic models add further background currents.

- **Time-dependent activation currents**

In order to describe an activation channel, Hodgkin and Huxley proposed the definition of a *gate variable* (or *activation coefficient*) which indicates the probability of that gate being open, and thus the channel being open. Using an activation coefficient x ($0 \leq x \leq 1$), the current produced by a time-dependent channel is

$$I = g(V_m)x(V_m - E_r) \quad (4.6)$$

where x satisfies a first-order differential equation

$$\frac{dx}{dt} = \alpha_x(V_m)(1 - x) - \beta_x(V_m)x \quad (4.7)$$

where α_x and β_x are the *rate coefficients* of the equation, and are generally non-linear functions of voltage but not time, and have units time^{-1} . The gate is fully open when $x = 1$ and current is maximal, but fully closed when $x = 0$. In some cases, the rate constant is raised to some power k if that is necessary to describe the observed behaviour of the channel, indicating that there are k identical gates combining together in one channel in series, and the state of the channel is dependent on the combination of the states of each of the gates.

Equation (4.7) can be rewritten as

$$\frac{dx}{dt} = -\frac{x - x_\infty}{\tau_x} \quad (4.8)$$

where

$$\tau_x = \frac{1}{\alpha_x + \beta_x} \quad (4.9)$$

$$x_\infty = \frac{\alpha_x}{\alpha_x + \beta_x} \quad (4.10)$$

If V_m is held constant, then the solution of Equation (4.8) is

$$x(t) = x_\infty - (x_\infty - x_0) \exp\left(-\frac{t}{\tau_x}\right) \quad (4.11)$$

where there is an exponential approach to x_∞ from x_0 as $t \rightarrow \infty$. An example of this type of current whose time dependence is described by an activation variable is the plateau potassium current i_K which is involved in repolarising the action potential.

- **Time-dependent activation-inactivation currents**

Channels displaying an activation-inactivation behaviour whereby the channel initially opens and then closes contain two or more gate variables. Currents of this type are described by equations of the form

$$I = g(V_m)xy(V_m - E_r) \quad (4.12)$$

where x is the activation variable as before, and y is an inactivation variable of an identical form, but with coefficients $\alpha_y(V_m)$ and $\beta_y(V_m)$. In general, the rate coefficients of the inactivation variable will be much slower than the activation rate constants to allow the channel to open before closing. One example of this type of channel is the sodium channel, i_{Na} as described in Section 2.2.4 and Section 4.1.1 which possesses the two gate variables m and h , and is responsible for the initial upstroke of the action potential.

The sodium conductance

Hodgkin and Huxley proposed two hypotheses which would describe the nature of the transient changes in sodium conductance. Both describe the movement of charged particles within the cell membrane which move to allow or prevent sodium ions from passing through the sodium-selective channel. The first hypothesis supposes that there is a single particle which moves to allow sodium ions to pass, and then undergoes a chemical change as the transmembrane potential increases which causes it to move back into a position which inhibits the transfer of sodium ions. In mathematical terms, this can be thought of as a single variable which is governed by a second-order differential equation. The alternative hypothesis would suggest two such particles. One, the activation particle, moves quickly from an inhibitory position to one where sodium ions are free to pass. A second inactivation

particle is initially in a non-inhibitory state, and moves much more slowly to block the flow of sodium ions. Mathematically, this corresponds to two variables, each of which is governed by a first-order differential equation. They chose the second alternative because it was simpler to formulate and use. This is the process described in Section 2.2.4.

According to this description of the sodium channel, the description of the sodium conductance becomes

$$g_{Na} = m^3 h \overline{g_{Na}} \quad (4.13)$$

where m is the activation coefficient, and h is the inactivation coefficient, and $\overline{g_{Na}}$ is a maximal sodium conductance with units $S \cdot \text{mm}^{-2}$. Raising m to the third power indicates that there are three m gates present in a single channel, all of which have to be fully open for the channel to be fully open. Both variables are governed by a differential equation of the form of Equation (4.7), which gives

$$\begin{aligned} \frac{dm}{dt} &= \alpha_m(1 - m) - \beta_m m \\ \frac{dh}{dt} &= \alpha_h(1 - h) - \beta_h h \end{aligned} \quad (4.14)$$

where the rate constants α and β are functions of voltage, but not of time, and have units of s^{-1} . Hodgkin and Huxley describe the kinetics of this system by defining the rate constants as

$$\begin{aligned} \alpha_m &= \frac{0.1(V_m + 25)}{\exp(0.1(V_m + 25)) - 1} \\ \beta_m &= 4 \exp(V_m/18) \\ \alpha_h &= 0.07 \exp(V_m/20) \\ \beta_h &= [\exp(0.1(V_m + 30)) + 1]^{-1} \end{aligned} \quad (4.15)$$

where these values were obtained by fitting curves to experimental data. These functions have the form shown in Figure 4.2. Note that this data is for nerve fibre only, but equations of similar forms are used in other descriptions of the cardiac ionic currents in other models described later.

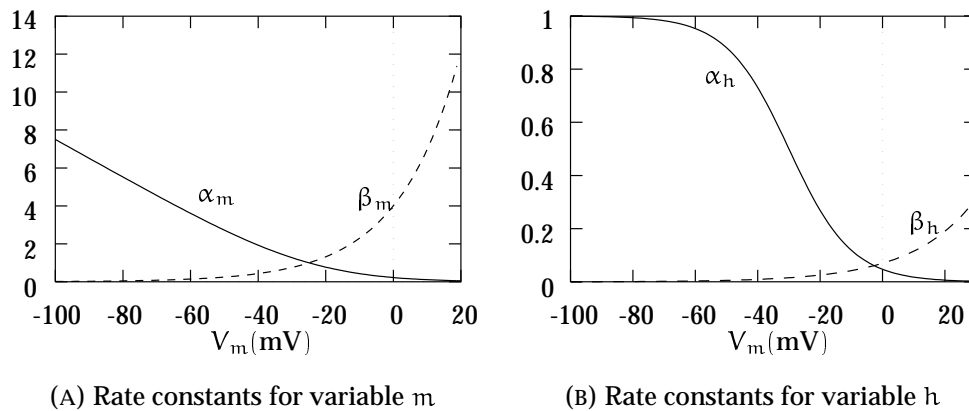


FIGURE 4.2: Form of the rate constants for the m and h gating variables of the Hodgkin-Huxley sodium current.

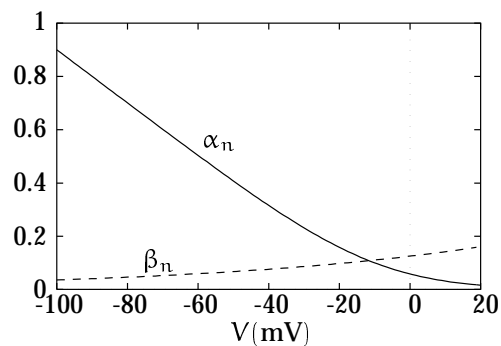


FIGURE 4.3: Form of the gating variable n for the Hodgkin-Huxley potassium current.

The potassium conductance

The potassium channel is an activation-only type channel, with four activation gates present in the channel. The total potassium conductance of this channel is

$$\begin{aligned}
 g_K &= n^4 \bar{g}_K \\
 \frac{dn}{dt} &= \alpha_n(1 - n) - \beta_n n
 \end{aligned}
 \tag{4.16}$$

where the variable used to represent the passage of potassium ions is n and \bar{g}_K is the maximal potassium conductance. The following functions give the form of the rate constants, which are graphed in Figure 4.3.

Constant	Units	Value
C_m	$\mu\text{F} \cdot \text{cm}^{-2}$	1.0
E_R	mV	-75
E_{Na}	mV	$E_R + 115$
E_K	mV	$E_R - 12$
E_L	mV	$E_R + 10.613$
$\overline{g_{\text{Na}}}$	$\text{mS} \cdot \text{cm}^{-2}$	120
$\overline{g_K}$	$\text{mS} \cdot \text{cm}^{-2}$	36
g_L	$\text{mS} \cdot \text{cm}^{-2}$	0.3

TABLE 4.1: Values of the constants in the Hodgkin-Huxley equations.

$$\alpha_n = \frac{0.01(V_m + 10)}{\exp(0.1(V_m + 10)) - 1} \quad (4.17)$$

$$\beta_n = 0.125 \exp(V_m/80)$$

Hodgkin and Huxley acknowledged that their equations may describe the basic mechanism of conduction in tissues other than the nerve axon they were defined for, but the values of the parameters would be substantially different. Models outlined in the following sections show the applicability of the HH model for cardiac tissue, and the modifications that need to be made to the model.

The complete Hodgkin-Huxley model

In addition to the two ion channels, Hodgkin and Huxley proposed a background leakage current i_L which maintains the membrane at a constant resting potential in the absence of any depolarisation.

Thus the full HH model has the following relations:

$$i_{\text{Na}} = \overline{g_{\text{Na}}} m^3 h (V_m - E_{\text{Na}}) \quad (4.18)$$

$$i_K = \overline{g_K} n^4 (V_m - E_K) \quad (4.19)$$

$$i_L = g_L (V_m - E_L) \quad (4.20)$$

where the reversal potentials are related to the resting potential E_R of the membrane. The values given by Hodgkin and Huxley for the constants in the above equations

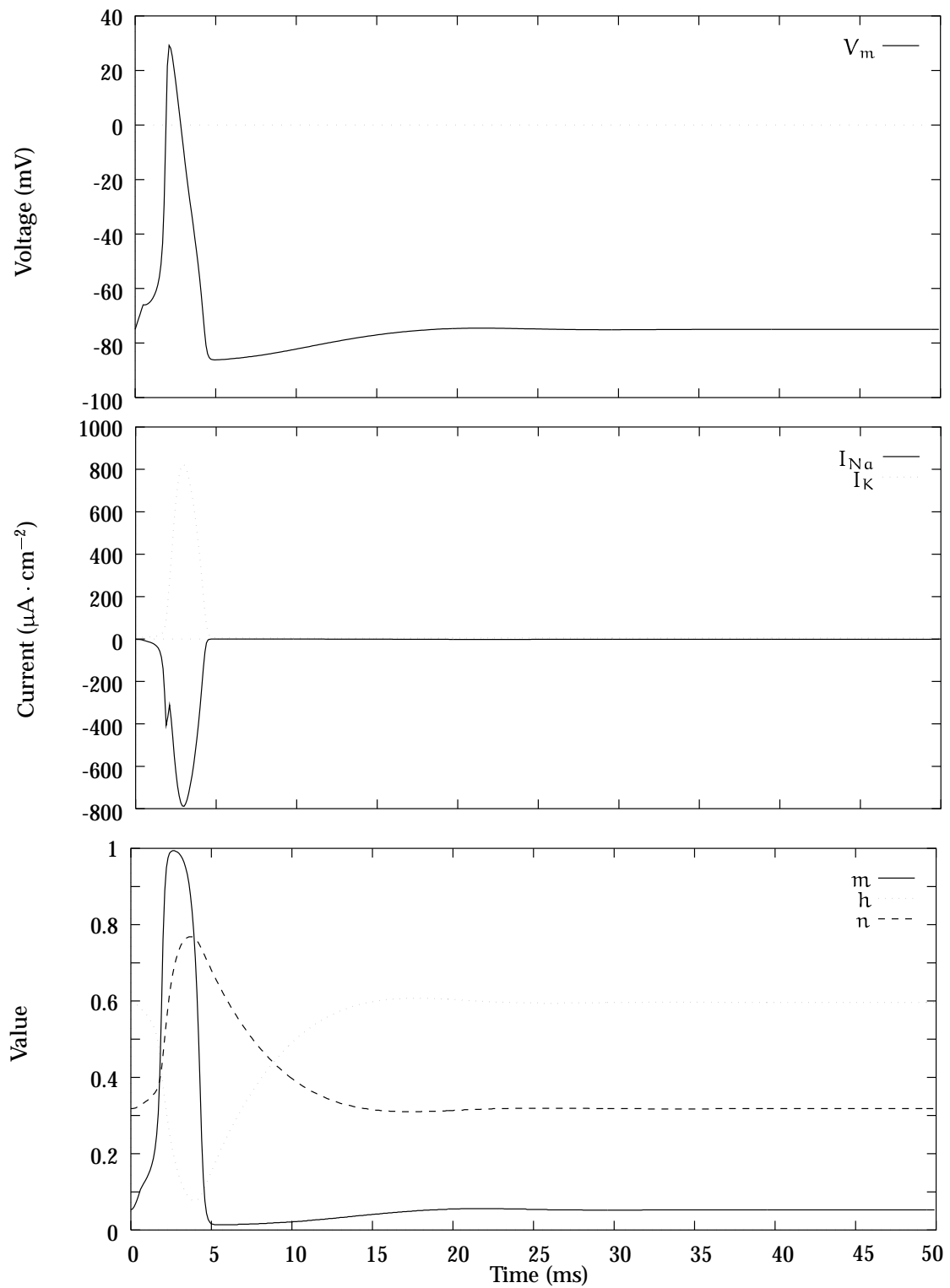


FIGURE 4.4: The Hodgkin-Huxley model results in the above action potential, which is maintained by the I_{Na} and I_K ionic currents shown, together with a leakage current, and these currents are defined by a combination of the gating variables m , h and n .

are presented in Table 4.1. Other researchers give slightly different values, especially for the reversal potentials due to difficulties in measuring intracellular and extracellular concentrations of the various ions accurately. Using the values given in Table 4.1, the Hodgkin-Huxley nerve model gives an action potential of the form shown in Figure 4.4. Note that the units used to measure current ($\mu\text{A} \cdot \text{cm}^{-2}$) are not SI units, but are the most commonly used units. Similarly, the values given for the constants in Table 4.1 and other tables are taken from the original papers where non-SI units are used. It seems preferable to use SI units, although the wealth of literature suggests otherwise. The discontinuity in the current in Figure 4.4 is due to the removal of the activating stimulus at that point as can be seen from the voltage diagram.

4.1.2 Noble (1962) Model

Cardiac cells have some ionic properties which are quite different from those of nerve cells, and this also varies between the different types of cardiac cell (see Section 2.2.2). The first models of cardiac action potentials were descriptions of Purkinje fibres for two reasons. Firstly the cells are most like nerve cells which means that the existing theories could easily be adapted, and secondly the large size of Purkinje cells made for easier experimental measurement of ionic properties.

Noble (1962) developed the first mathematical model of a cardiac cell, which was based directly on the 1952 model of Hodgkin and Huxley. The changes made fell into two categories. Firstly, the form of the model itself was changed slightly to describe the observed behaviour of the Purkinje potassium channel. Secondly, values of the constants were empirically fitted to new data acquired from Purkinje fibres. The HH electrical model of the cell membrane shown in Figure 4.1 was updated to the equivalent electrical circuit shown in Figure 4.5, and defines the total membrane current I_m in the same way as the HH model to be the sum of the ionic currents and the capacitive current.

$$I_m = C_m \frac{\partial V_m}{\partial t} + i_{\text{Na}} + i_{\text{K}} + i_{\text{L}} \quad (4.21)$$

The convention developed for describing current flow conforms to that used in experimental work with intracellular electrodes. The transmembrane potential is the potential of the inside with respect to the outside, and therefore the action potential is

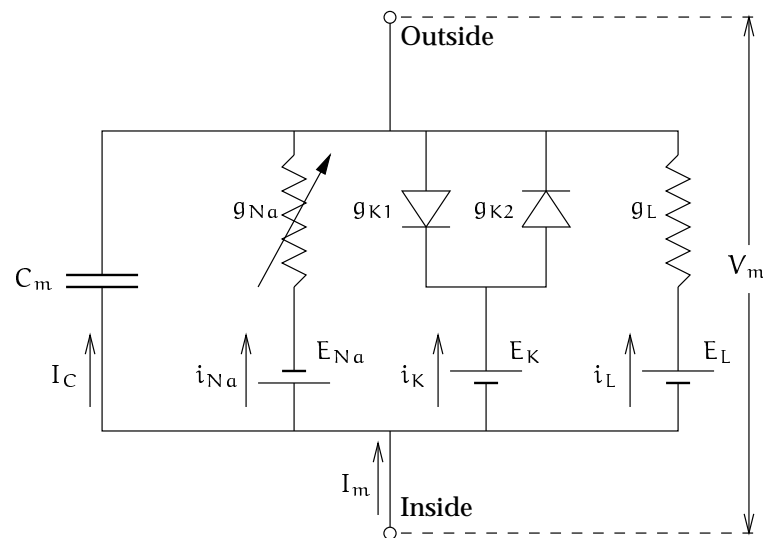


FIGURE 4.5: Equivalent electrical circuit for Purkinje fibre membrane. Derived from Noble (1962, Fig. 1).

a positive variation with respect to a negative resting potential, and positive currents are outward. This is opposite to that originally proposed by Hodgkin and Huxley, but is the convention most often used for describing cardiac cell membranes.

The sodium current

The form of the sodium current equation as proposed by Noble is almost identical to Equation (4.13) developed by Hodgkin and Huxley. The values of the rate constants have been altered to agree with the experimental measurements of Purkinje fibre depolarisation conducted by Weidmann (1952) and (1955). The revised equations describing the rate constants are

$$\begin{aligned}
 \alpha_m &= \frac{0.1(-V_m - 48)}{\exp\left(\frac{(-V_m - 48)}{15}\right) - 1} \\
 \beta_m &= \frac{0.12(V_m + 8)}{\exp\left(\frac{V_m + 8}{5}\right) - 1} \\
 \alpha_h &= 0.17 \exp\left(-\frac{V_m - 90}{20}\right) \\
 \beta_h &= \frac{1}{\exp\left(-\frac{V_m - 42}{10}\right) + 1}
 \end{aligned} \tag{4.22}$$

In addition, a small component of g_{Na} is assumed to be independent of V_m or t , in order to maintain an increase in sodium current during a long-lasting depolarisation. This results in the sodium current being described by the equation

$$i_{Na} = (\overline{g_{Na}} m^3 h + g_C)(V_m - E_{Na}) \quad (4.23)$$

where g_C is a constant conductance.

The potassium current

Noble observed that depolarisation decreases the membrane conductance and, because the chloride conductance of normal resting cardiac tissue is very small, the leakage current cannot be totally responsible for it. In order to explain this, Noble proposed two types of potassium channels in the cell membrane. The first channel has a time-independent current, and the conductance (g_{K1}) falls as the membrane depolarises. The other is an activation-only type channel of the same form as the potassium channel described in the HH model, and the conductance (g_{K2}) of this channel slowly increases as the membrane depolarises. This is represented in Figure 4.5 by two rectifiers in parallel, the first “inward rectifier” K^+ channel passing inward current, and the second “delayed rectifier” K^+ channel allowing outward current to pass after a delay.

The conductance of the first channel is described by the empirical equation

$$g_{K1} = 1.2 \exp\left(\frac{-V_m - 90}{50}\right) + 0.015 \exp\left(\frac{V_m + 90}{60}\right) \quad (4.24)$$

which describes an instantaneous function of V_m . The conductance of the second channel is described exactly by the HH potassium current equations in Equation (4.16) with 100-fold smaller rate constants in order to take into account the slower onset in Purkinje fibres as opposed to nerve. The rate equations become

$$\begin{aligned} \alpha_n &= \frac{0.0001(-V_m - 50)}{\exp\left(-\frac{V_m - 50}{10}\right) - 1} \\ \beta_n &= 0.002 \exp\left(-\frac{V_m - 90}{80}\right) \end{aligned} \quad (4.25)$$

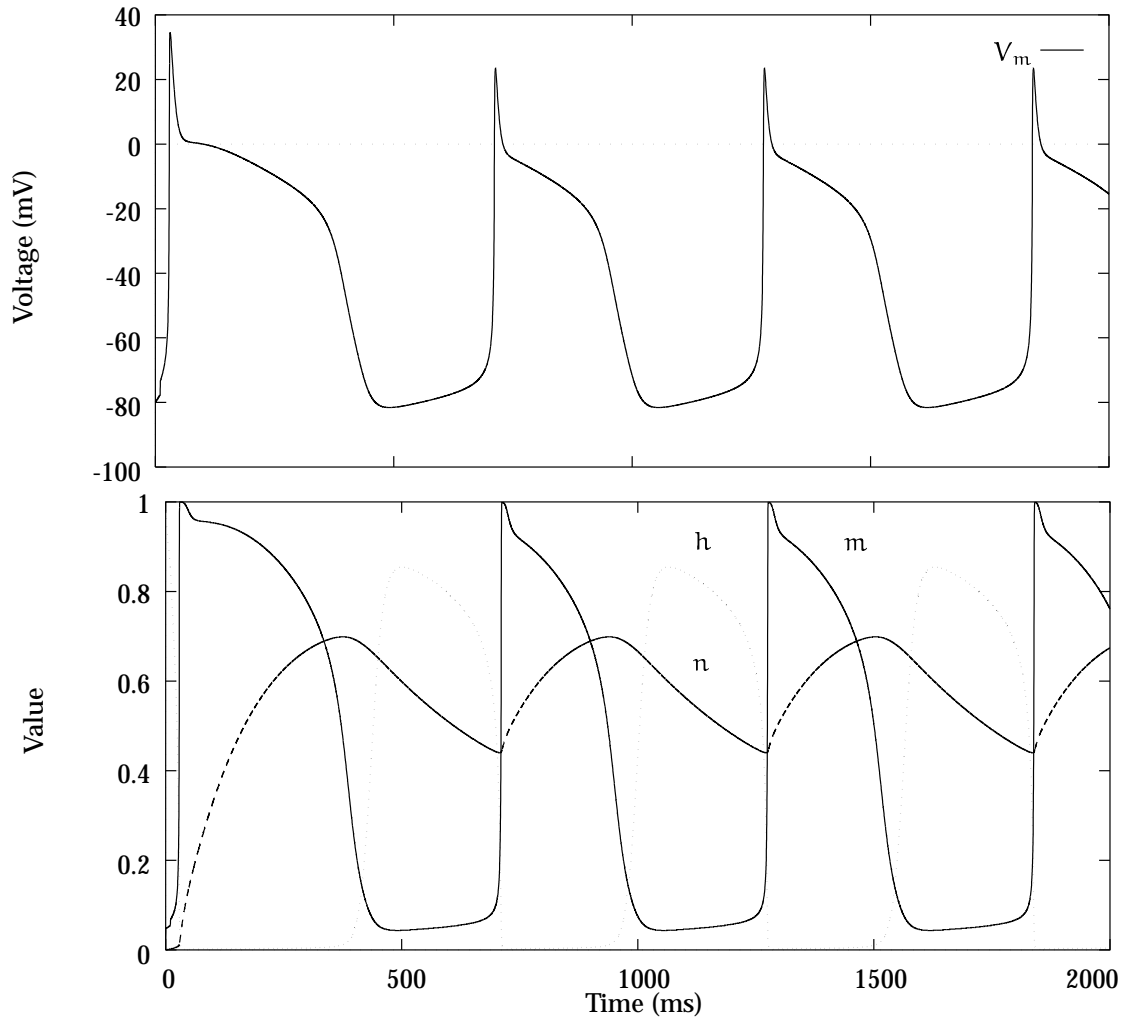


FIGURE 4.6: The Noble (1962) model results in the above action potential, and the gating variables produce the graphs shown above.

The complete Noble (1962) model

The Noble model also has a background leakage current I_L with the same form as in the HH model. Therefore, the complete model is

$$i_{Na} = (\overline{g_{Na}} m^3 h + g_C)(V_m - E_{Na}) \quad (4.26)$$

$$i_K = (g_{K1} + \overline{g_{K2}} n^4)(V_m - E_K) \quad (4.27)$$

$$i_L = g_L(V_m - E_L) \quad (4.28)$$

with values assigned for the constants shown in Table 4.2. Various values of g_L were used in the paper to produce different effects on the form and duration of the action potential. Using the above values of the constants, the Noble model

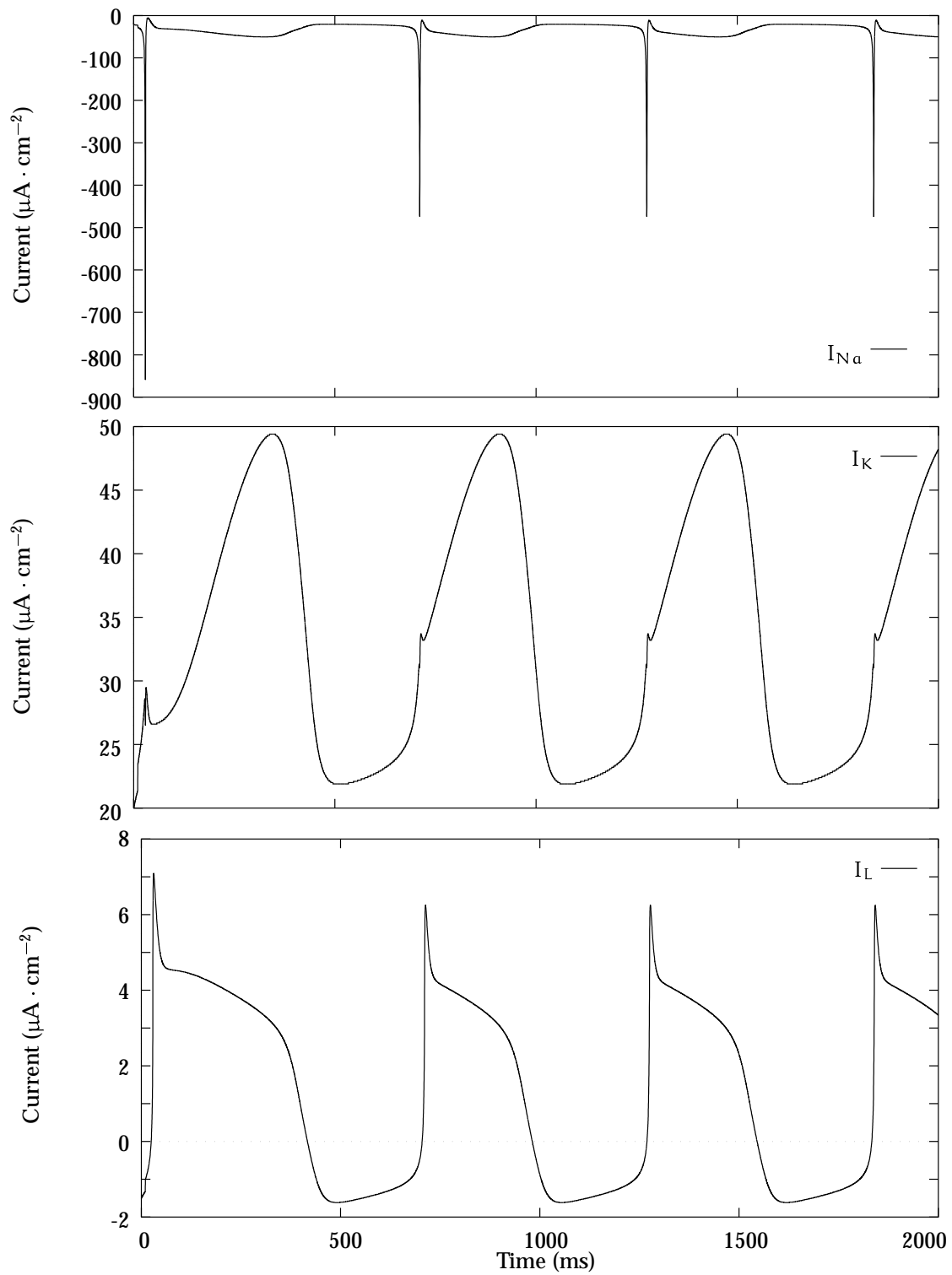


FIGURE 4.7: Ionic currents defined by the Noble model for Purkinje fibres.

Constant	Units	Value
C_m	$\mu\text{F} \cdot \text{cm}^{-2}$	12
E_{Na}	mV	40
E_{K}	mV	-100
E_{L}	mV	-60
$\overline{g_{\text{Na}}}$	$\text{mS} \cdot \text{cm}^{-2}$	400
g_{C}	$\text{mS} \cdot \text{cm}^{-2}$	0.14
$\overline{g_{\text{K2}}}$	$\text{mS} \cdot \text{cm}^{-2}$	1.2
g_{L}	$\text{mS} \cdot \text{cm}^{-2}$	0.075

TABLE 4.2: Values of the constants in the Noble model.

produces an action potential and time course of the gating variables as shown in Figure 4.6. Notice that the action potential changes shape and duration slightly due to the rate constants being unable to fully recover before the pacemaker nature of the Purkinje structure cause a spontaneous depolarisation. This pacemaker is not totally counteracted by the leakage current as the constant is much smaller than in the HH model. The time courses of the three ionic currents are shown in Figure 4.7.

4.1.3 McAllister-Noble-Tsien Model

The next significant development in cardiac membrane modelling occurred when McAllister, Noble and Tsien (1975) published a paper which formulated new ionic current equations that would describe the experimental information available at that time for Purkinje cells. The description of the kinetics of the currents is still based upon the Hodgkin-Huxley formalism, but the currents themselves incorporate some significant new changes. A second inward current, carried at least partly by calcium ions, is added to the fast sodium current of the Noble (1962) model. The single time-dependent potassium outward current is replaced by three time-dependent potassium currents, and there is now a transient outward chloride current. The single leakage current of the original models have been further decomposed into three separate background currents.

The resulting McAllister-Noble-Tsien (MNT) model is written as the sum of these

Reversal potentials (mV)		Maximum conductances (mS · cm ⁻²)	
E _{Na}	40	$\overline{g_{Na}}$	150
E _{si}	70	$\overline{g_{si}}$	0.8
E _s	- 52	$\overline{g_{si}'}$	0.04
E _K	-110	$\overline{g_{qr}}$	2.5
E _{Cl}	- 70	$\overline{g_{Na,b}}$	0.105
E _{K₁}	- 30	$\overline{g_{Cl,b}}$	0.01
C _m	10	μFcm^{-2}	

TABLE 4.3: Constants used in the MNT model.

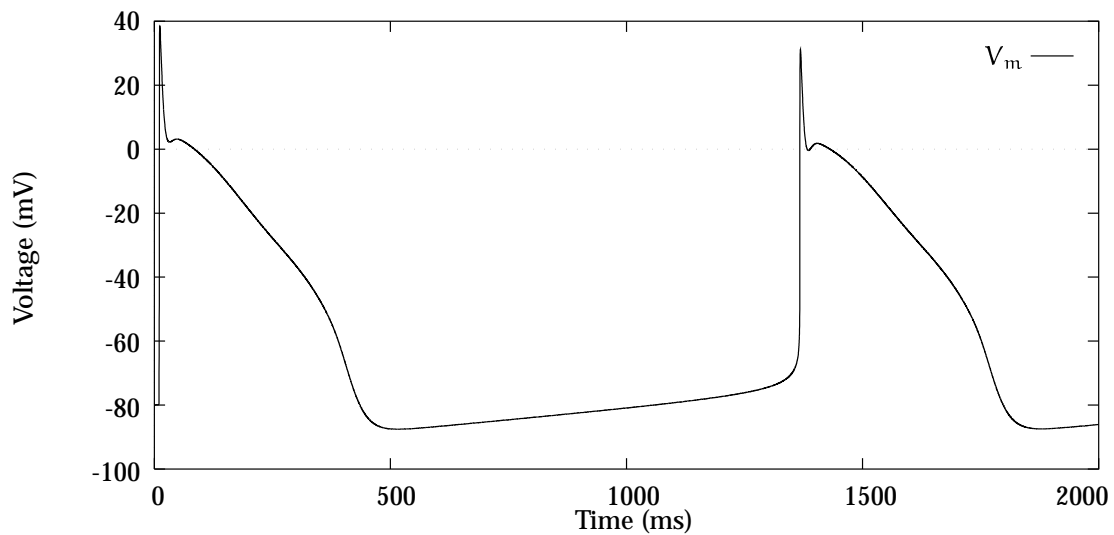


FIGURE 4.8: McAllister-Noble-Tsien action potential for a Purkinje fibre.

various ionic currents

$$I_{\text{ion(MNT)}} = i_{Na} + i_{si} + i_{K2} + i_{x1} + i_{x2} + i_{qr} + i_{K1} + i_{Na,b} + i_{Cl,b} \quad (4.29)$$

and becomes the most complex model to date.

Constants

The MNT model has assigned values for various constants which appear in the ionic equations as detailed in Table 4.3. The resulting action potential, shown in Figure 4.8

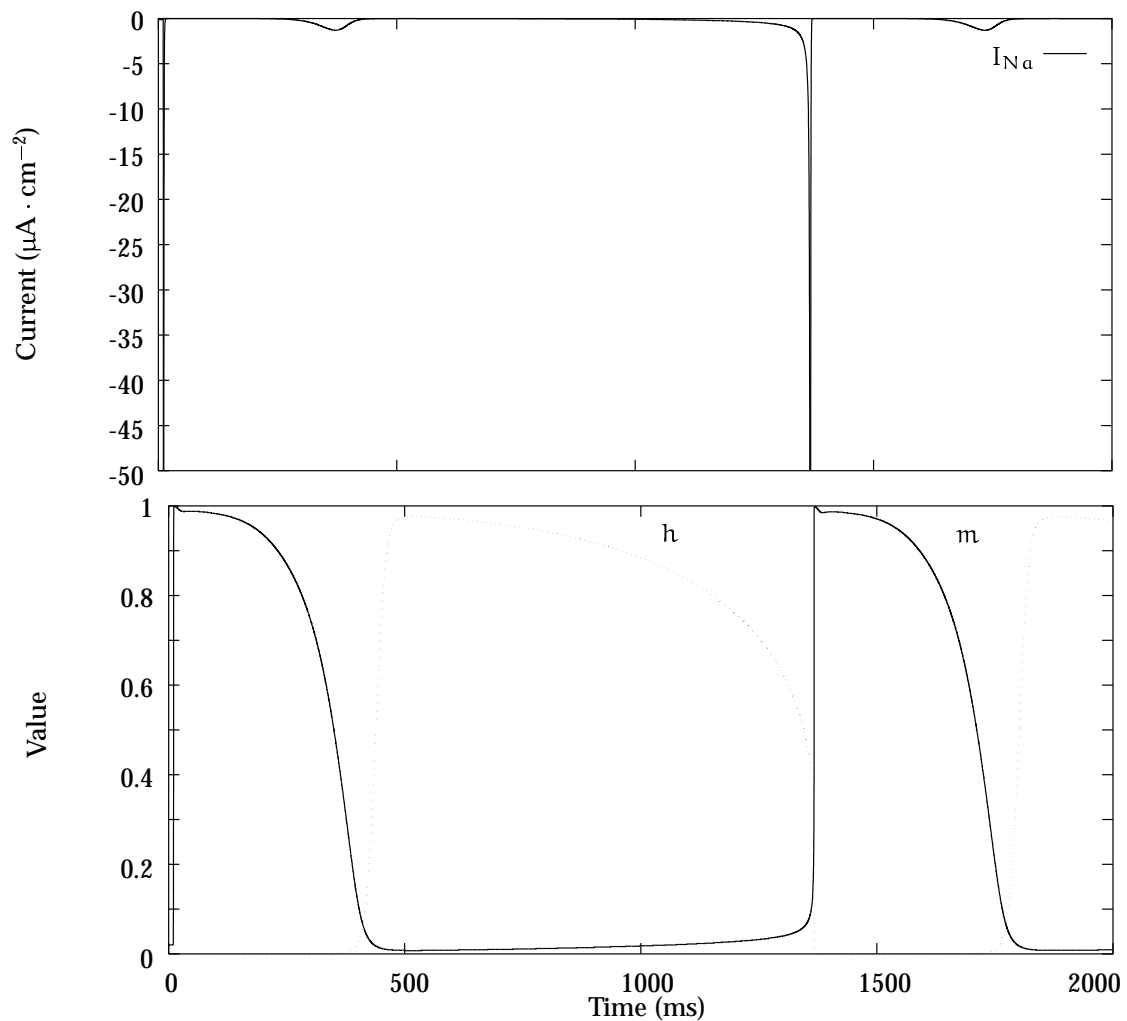


FIGURE 4.9: McAllister-Noble-Tsien sodium current, and associated gating variables m and h . The current is scaled in order to see the small fluctuation at the end of the action potential, and the largest current is around $-1000 \mu A \cdot cm^{-2}$.

matches the experimental measurements closely, as is detailed further in their paper. The model again models the pacemaker nature of the Purkinje fibre. The diagrams depicting the time-course of the various gate variables and the ionic currents are drawn at the place the appropriate current is described.

Inward currents

1. The fast sodium current (i_{Na})

The sodium current is basically the same as that given by Noble, except that further experimental work by Dudel and Rüdell (1970) had enabled a more detailed study of the time course of the current. These experiments contributed to an updated definition of the m kinetics, with the h rate constant still based on the experiments of Weidmann (1970), with a few modifications from the Noble model. There are however still many uncertainties at this stage regarding the exact form of the sodium current, and the value of the maximal Na^+ conductance. The equations for the rate coefficients as defined in the MNT model are

$$\begin{aligned}\alpha_m &= \frac{V_m + 47}{1 - \exp\left(-\frac{V_m + 47}{10}\right)} \\ \beta_m &= 40 \exp\left(-\frac{V_m + 72}{17.86}\right) \\ \alpha_h &= 0.0085 \exp\left(-\frac{V_m + 71}{5.435}\right) \\ \beta_h &= \frac{2.5}{\exp\left(-\frac{V_m + 10}{12.2}\right) + 1}\end{aligned}\tag{4.30}$$

and the sodium current equation is the same as in the HH model

$$i_{\text{Na}} = \overline{g_{\text{Na}}} m^3 h (V_m - E_{\text{Na}})\tag{4.31}$$

Using the constants defined in Table 4.3 gives a maximum rate of depolarisation of approximately 500 Vs^{-1} , which is better than Noble's (1962) model, but still not sufficient to describe observed rates of closer to 800 Vs^{-1} . The resulting sodium current is shown in Figure 4.9 along with the time-courses of the sodium gating variables m and h . The sodium current is only drawn to $-50 \mu\text{A} \cdot \text{cm}^{-2}$ so that the small fluctuation at the end of the action potential can be seen, but the full current reaches approximately $-1000 \mu\text{A} \cdot \text{cm}^{-2}$.

2. The secondary inward current (i_{si})

In the MNT model, the *secondary* (or sometimes *slow*) inward current activates much more slowly than the sodium current, and is responsible for holding up the plateau after the initial activation and controlling the duration of the action potential. This current is not as well-defined in Purkinje fibres (for which this model is constructed) as it is in some other types of cardiac muscle. At this time, it was assumed that the passage of both Na^+ and Ca^{2+} ions through the cell membrane was responsible for this current. In the absence of the fast sodium current, the magnitude of i_{si} may be sufficient to sustain an action potential.

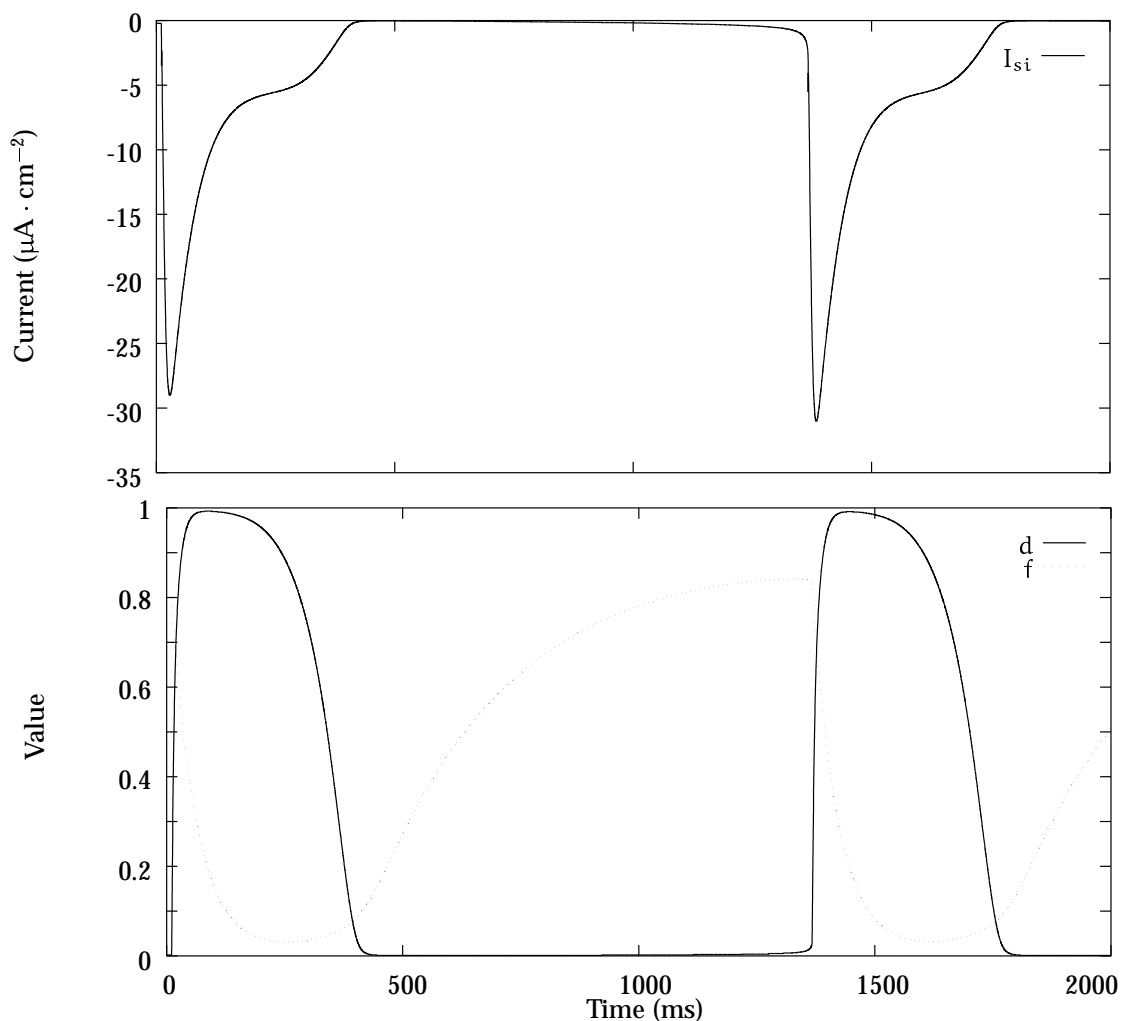


FIGURE 4.10: McAllister-Noble-Tsien secondary current, and associated gating variables d and f .

The channel responsible for this secondary inward current has an activation gate d which is similar in form to the m gate of the sodium current but somewhat slower, and also an inactivation gate f . It was observed in earlier experiments that some portion of this current would not completely inactivate, and this is represented by the second term which has an activation variable d' , but no deactivation variable.

$$I_{si} = \bar{g}_{si} df (V_m - E_{si}) + \bar{g}_{si}' d' (V_m - E_{si}) \quad (4.32)$$

The equations for the rate constants are

$$\begin{aligned}
 \alpha_d &= \frac{V_m + 40}{500 \left(1 - \exp\left(-\frac{V_m + 40}{10}\right)\right)} \\
 \beta_d &= 0.02 \exp\left(-\frac{V_m + 40}{11.26}\right) \\
 \alpha_f &= 0.000987 \exp\left(-\frac{V_m + 60}{25}\right) \\
 \beta_f &= \frac{0.02}{\exp\left(-\frac{V_m + 26}{11.5}\right) + 1}
 \end{aligned} \tag{4.33}$$

There are several possibilities for d' . One option is to set $d' = d$, or alternatively, the time-independent equation

$$d' = \left[1 + \exp\left(-\frac{V_m + 40}{6.667}\right)\right]^{-1} \tag{4.34}$$

gives an appropriate behaviour. The authors note that the final choice of expression will be determined by further experiments. Using Equation (4.34) and the above equations for the rate constants, the diagram of the secondary current shown in Figure 4.10 is obtained.

Outward currents

In contrast to the inward currents, there is a relatively complete understanding of the kinetics of the outward currents, though the description of the currents has changed slightly from the Noble (1962) model. Firstly, the time-independent current has been isolated into a separate background current i_{K_1} . Secondly, it was found in experiments performed by Noble and Tsien (1968) that there are components of the original i_{K_2} which are dependent on ions other than just potassium, and these are identified by the symbol i_x .

1. *The pacemaker potassium current (i_{K_2})*

This component of the outward current is activated in the pacemaker range of potentials, and therefore controls pacemaker activity. In contrast to the Noble (1962) i_{K_2} current, this current has a much more negative threshold making it a pacemaker rather than a repolarising current. The current is described in terms of a single gate

variable s

$$i_{K_2} = \overline{i_{K_2}} s \quad (4.35)$$

where s has rate coefficients

$$\alpha_s = \frac{0.001(V_m - E_s)}{1 - \exp\left(-\frac{V_m - E_s}{5}\right)} \quad (4.36)$$

$$\beta_s = 0.00005 \exp\left(-\frac{V_m - E_s}{15}\right)$$

The fully activated current flow $\overline{i_{K_2}}$ is a highly non-linear function of the transmembrane potential

$$\overline{i_{K_2}} = 2.8 \frac{\exp\left(\frac{V_m - E_K}{25}\right) - 1}{\exp\left(\frac{V_m + 60}{12.5}\right) + \exp\left(\frac{V_m + 60}{25}\right)} \quad (4.37)$$

with a reversal potential at E_K .

2. The plateau potassium currents (i_{x_1} and i_{x_2})

Each of these two currents are governed by simple first-order processes with gating variables x_1 and x_2 , respectively,

$$i_{x_1} = \overline{i_{x_1}} x_1 \quad (4.38)$$

$$i_{x_2} = \overline{i_{x_2}} x_2 \quad (4.39)$$

similar to that of i_{K_2} . The fully activated currents are

$$\overline{i_{x_1}} = 1.2 \frac{\exp\left(\frac{V_m + 95}{25}\right) - 1}{\exp\left(\frac{V_m + 45}{25}\right)} \quad (4.40)$$

$$\overline{i_{x_2}} = 25 + 0.385V_m \quad (4.41)$$

which are based on experiments performed by Noble and Tsien (1969) which show additional potassium currents which are activated in the plateau range of potentials.

The rate constants for the two gate variables are governed by the equations

$$\alpha_{x_1} = 5 \times 10^{-4} \frac{\exp\left(\frac{V_m + 50}{12.1}\right)}{1 + \exp\left(\frac{V_m + 50}{17.5}\right)} \quad (4.42)$$

$$\beta_{x_1} = 0.0013 \frac{\exp\left(-\frac{V_m + 20}{16.67}\right)}{1 + \exp\left(-\frac{V_m + 20}{25}\right)}$$

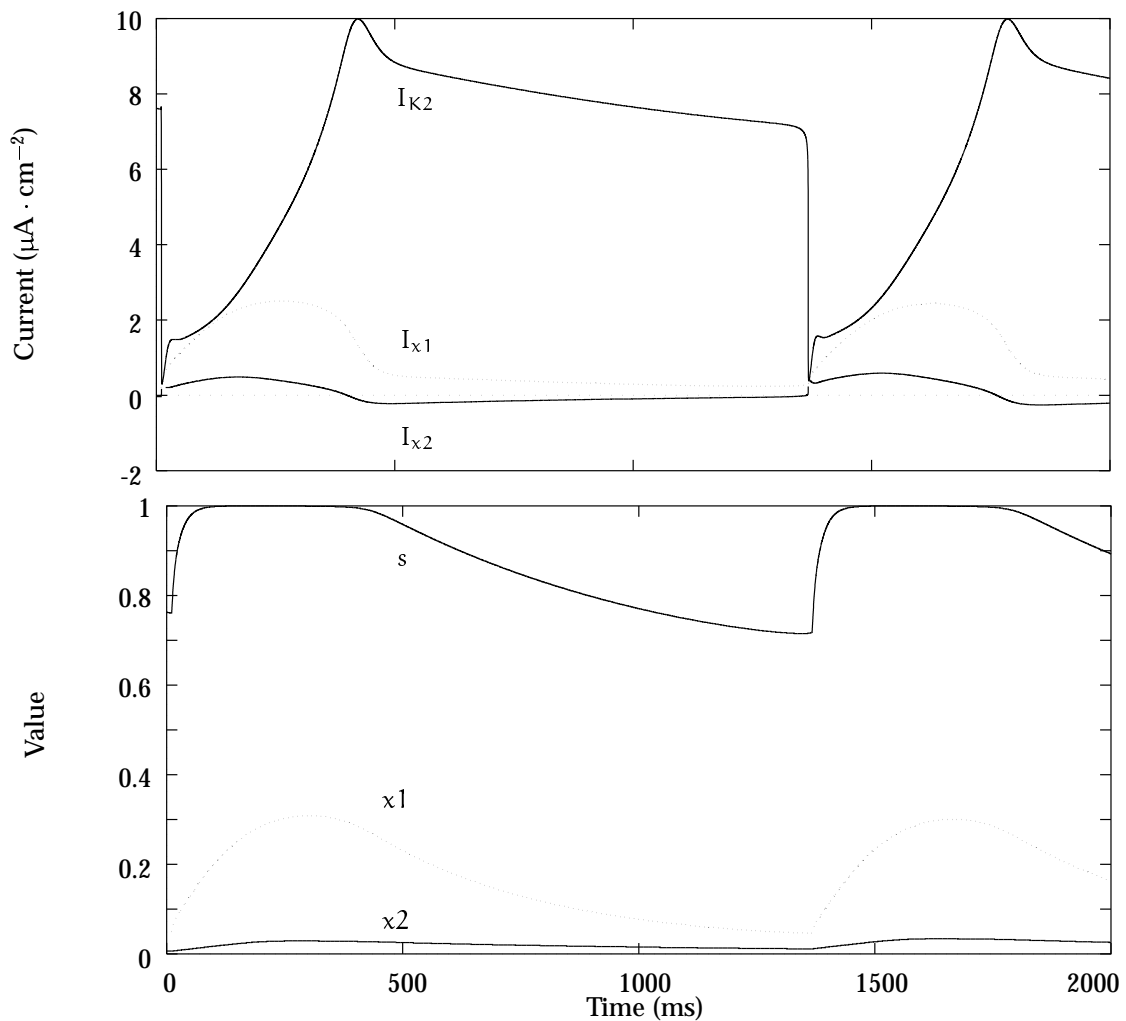


FIGURE 4.11: McAllister-Noble-Tsien potassium currents, and associated gating variables s , x_1 and x_2 .

and

$$\begin{aligned} \alpha_{x_2} &= 1.27 \times 10^{-4} \left[1 + \exp \left(-\frac{V_m + 19}{5} \right) \right]^{-1} \\ \beta_{x_2} &= 3 \times 10^{-4} \frac{\exp \left(-\frac{V_m + 20}{16.67} \right)}{1 + \exp \left(-\frac{V_m + 20}{25} \right)} \end{aligned} \quad (4.43)$$

If these two currents are removed from the model, the upstroke and notch are unchanged, but repolarisation fails to occur. The i_{x_1} current seems also to be responsible for a decreased APD and the disappearance of the notch if a second action potential is initiated during the period of restitution.

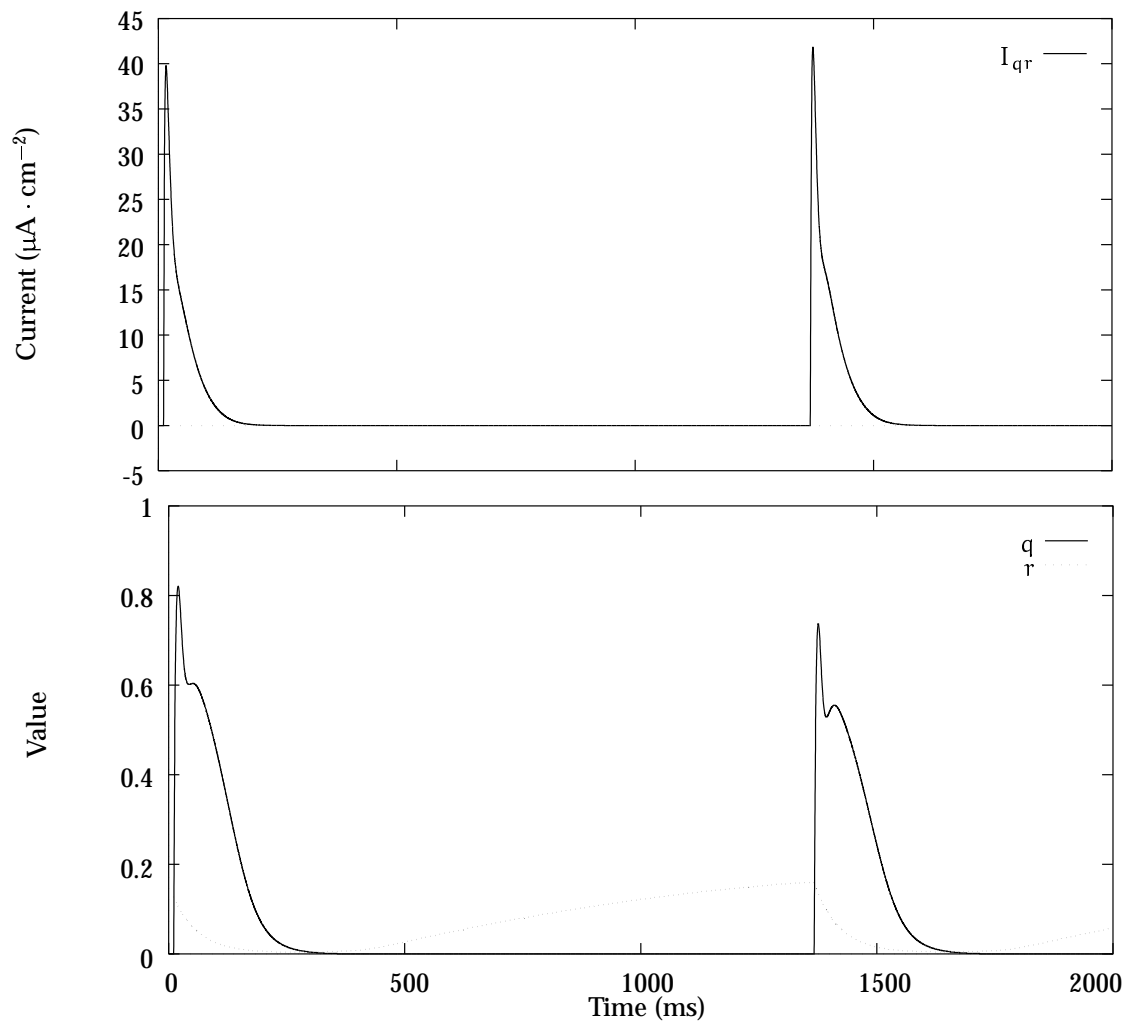


FIGURE 4.12: McAllister-Noble-Tsien chloride current, and associated gating variables q and r .

The form of the above three currents is shown in Figure 4.11 together with the gating variables s , x_1 and x_2 .

3. The transient chloride current (i_{qr})

In addition to the previously observed time-independent background chloride-based current, experimental evidence pointed towards the existence of a large transient chloride current was responsible for the rapid repolarisation from the peak of the spike to the start of the plateau. i_{qr} is an activation-inactivation type equation

$$i_{qr} = \overline{g_{qr}} qr (V_m - E_{Cl}) \quad (4.44)$$

with two gating variables q and r , which are governed by the equations

$$\begin{aligned}\alpha_q &= 0.008 \frac{V_m}{1 - \exp\left(-\frac{V_m}{10}\right)} \\ \beta_q &= 0.08 \exp\left(-\frac{V_m}{11.26}\right) \\ \alpha_r &= 0.00018 \exp\left(-\frac{V_m + 80}{25}\right) \\ \beta_r &= \frac{0.02}{\exp\left(-\frac{V_m + 26}{11.5}\right) + 1}\end{aligned}\tag{4.45}$$

A more extensive later study by Fozzard & Hiraoka (1973) redefined the behaviour of the inactivation kinetics according to the equations

$$\begin{aligned}\alpha_r &= 0.000033 \exp\left(-\frac{V_m}{17}\right) \\ \beta_r &= \frac{0.033}{\exp\left(-\frac{V_m + 30}{8}\right) + 1}\end{aligned}\tag{4.46}$$

In conjunction with the onset of i_{si} , a notch is developed in the action potential, where the chloride current causes a sudden repolarisation to about 15 mV, and the secondary inward current repolarises the membrane to about 5 mV. If $\overline{g_{qr}}$ is decreased, then the notch disappears, and there is a smooth transition from the upstroke to the plateau.

This current is shown together with the gate variables q and r in Figure 4.12, using the original definition for r as detailed in Equation (4.45).

Background currents

The leakage current defined in both the Noble (1962) and the Hodgkin & Huxley models is more appropriately titled a background current in the MNT model, and has been split into components carried by Na^+ or Cl^- . This splitting is somewhat tentative due to the lack of reliable experimental observations.

1. The outward time-independent potassium current (i_{k_1})

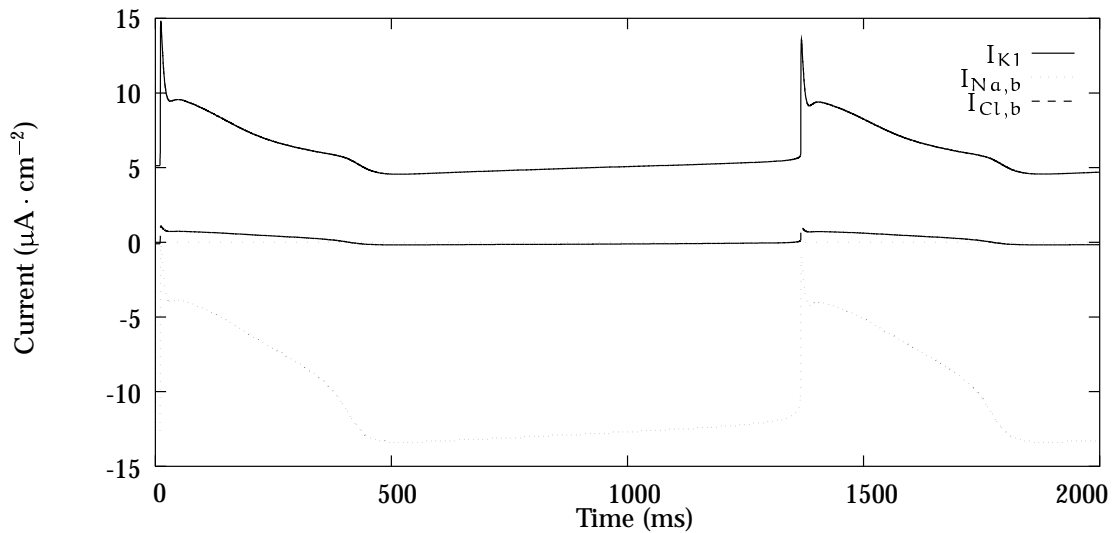


FIGURE 4.13: McAllister-Noble-Tsien background currents.

Most of the outward component is carried by K^+ ions, and is represented by i_{K_1} .

$$i_{K_1} = \frac{\overline{i_{K_2}}}{2.8} + 0.2 \frac{(V_m - E_{K_1})}{1 - \exp\left(-\frac{V_m - E_{K_1}}{25}\right)} \quad (4.47)$$

2. The inward background current ($i_{Na,b}$)

This current is responsible for maintaining the resting potential of the membrane at a point some 10 to 30 mV above the potassium reversal potential, and has at this stage been attributed to Na^+ ions.

$$i_{Na,b} = \overline{g_{Na,b}} (V_m - E_{Na}) \quad (4.48)$$

3. The background chloride current ($i_{Cl,b}$)

This current contributes to maintaining the plateau and helps to determine the action potential duration.

$$i_{Cl,b} = \overline{g_{Cl,b}} (V_m - E_{Cl}) \quad (4.49)$$

These three background currents are shown in Figure 4.13.

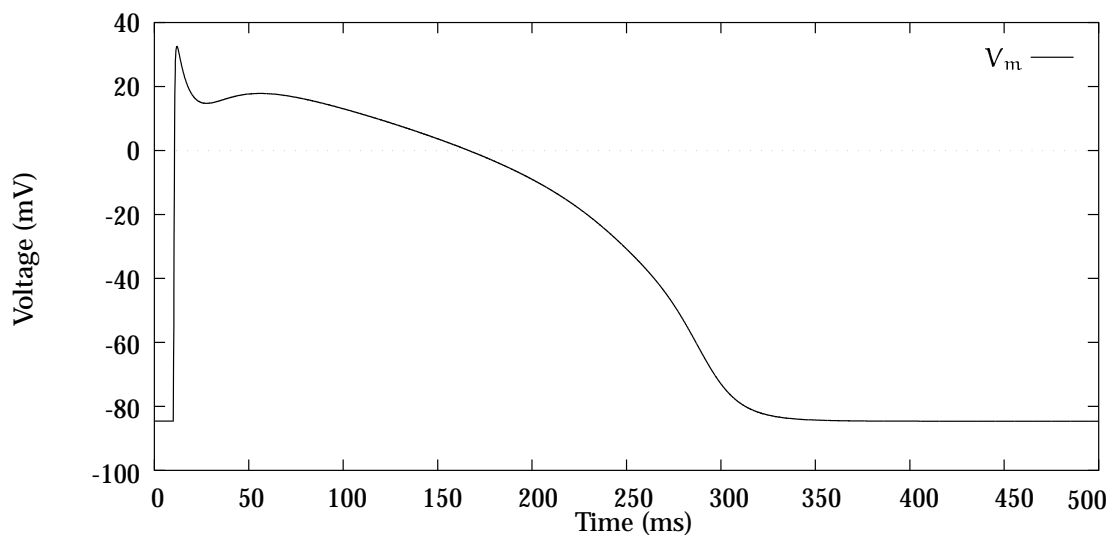


FIGURE 4.14: Beeler-Reuter model of the ventricular action potential.

4.1.4 Beeler-Reuter Model

In contrast to the earlier Purkinje fibre ionic current models of Noble (1962) and McAllister *et al.*, the Beeler and Reuter (1977) model was developed to describe the mammalian ventricular action potential. It was found that not all of the ionic currents relevant to a Purkinje fibre model are present in ventricular tissue, therefore this model is somewhat simpler than the MNT model, in that it describes only four ionic currents. A sodium inward current is included, together with an additional Ca^{2+} -based inward current, along with the background potassium current i_{K_1} and the plateau potassium current i_{x_1} . Left out of the Beeler-Reuter (BR) model are a slow component of the sodium current which is shown to be indistinguishable from other currents, the dynamic chloride current i_{Cl} in Equation (4.44) which does not appear to be present in ventricular studies, and the two additional outward currents i_{K_2} and i_{x_2} from Equations (4.35) and (4.39) seem not to be active in ventricular muscle either. i_{K_2} is the pacemaker current and ventricular cells do not exhibit spontaneous depolarisation. Also i_{x_2} is very slow and seems to be masked by other currents, if it exists at all. A model including i_{x_2} found that this current only has a noticeable influence during very rapid stimulation.

The result is an ionic current composed of four parts

$$I_{\text{ion(BR)}} = i_{\text{Na}} + i_s + i_{x_1} + i_{K_1} \quad (4.50)$$

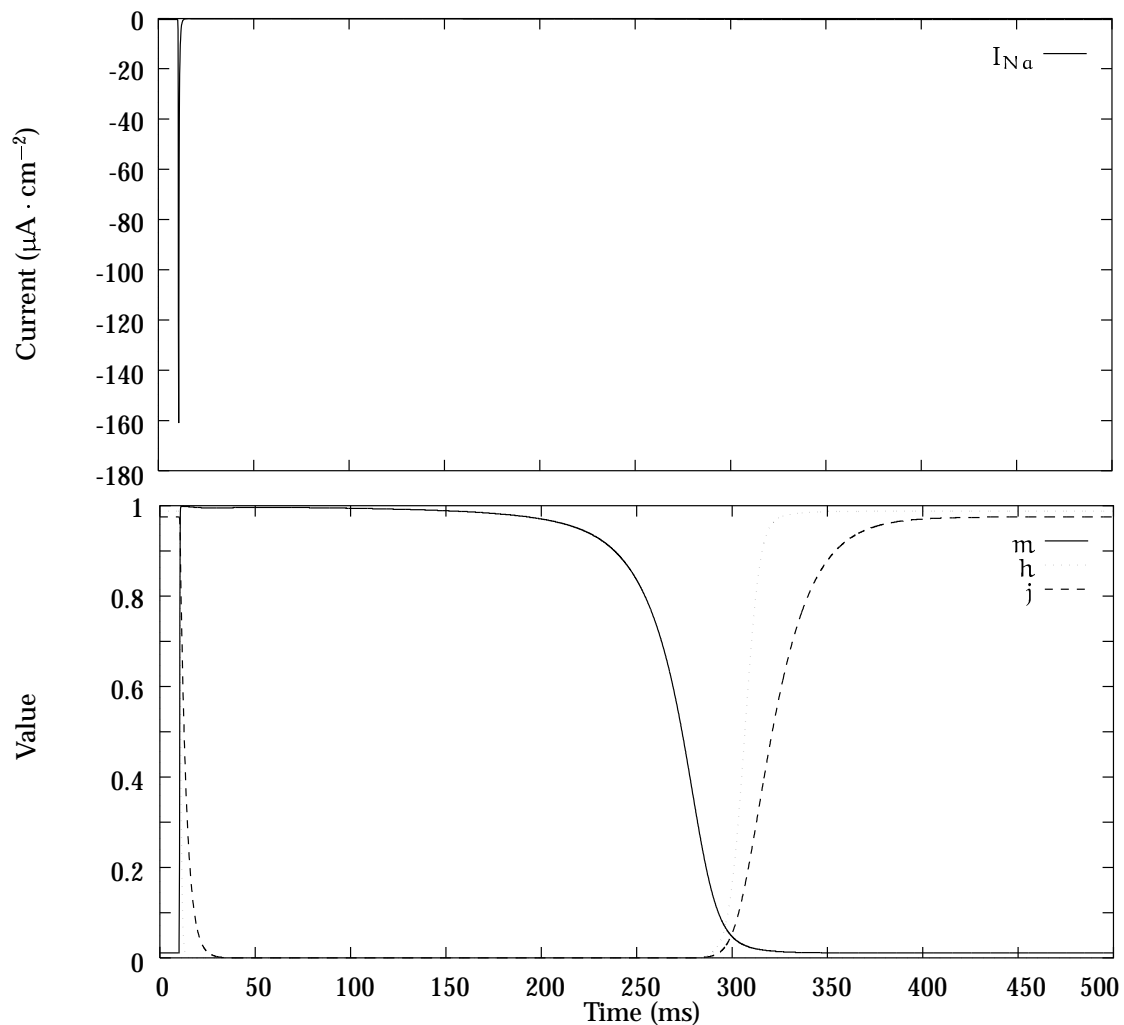


FIGURE 4.15: Beeler-Reuter sodium current and associated gating variables m , h and j .

which produces an action potential such as is shown in Figure 4.14. The main additional feature of the BR ionic current model is a representation of the intracellular Ca^{2+} concentration $[\text{Ca}]_i$.

1. The fast inward sodium current (i_{Na})

At the time at which this model was formulated, techniques had still not been developed to study the activation kinetics of the sodium channel using voltage clamp techniques, and the equations used for the m gate are identical to those given in the MNT model. Further experiments had, however, shown that the re-activation process of the Na^+ channel is much slower than the inactivation process, therefore

requiring two inactivation variables. In the BR model, this is done by including a second variable j , such that the description of the maximal sodium current is

$$\overline{i_{Na}} = \overline{g_{Na}} m^3 h j \quad (4.51)$$

where j has a slower time-course than h , and both are much slower than m . The equations for the rate constants of these three variables are HH-type rate equations.

$$\begin{aligned} \alpha_m &= \frac{-(V_m + 47)}{\exp(-0.1(V_m + 47)) - 1} \\ \beta_m &= 40 \exp(-0.056(V_m + 72)) \\ \alpha_h &= 0.126 \exp(-0.25(V_m + 77)) \\ \beta_h &= \frac{1.7}{\exp(-0.082(V_m + 22.5)) + 1} \\ \alpha_j &= \frac{0.055 \exp(-0.25(V_m + 78))}{\exp(-0.2(V_m + 78)) + 1} \\ \beta_j &= \frac{0.3}{\exp(-0.1(V_m + 32)) + 1} \end{aligned} \quad (4.52)$$

In addition to the time-dependent current, a steady-state background sodium current is included into the Na^+ current model which corresponds to the MNT current in Equation (4.48). The complete sodium model is therefore

$$i_{Na} = (\overline{g_{Na}} m^3 h j + g_{NaC})(V_M - E_{Na}) \quad (4.53)$$

where $\overline{g_{Na}}$ is the fully activated sodium conductance, g_{NaC} is the steady-state sodium conductance and E_{Na} is the sodium reversal potential. The resulting current is shown in Figure 4.15 together with the time-courses of the rate constants m , h and j .

2. The slow inward current (i_s)

This transient inward current is largely responsible for maintaining the plateau of the action potential, and as in the MNT model, has an activation gate d and an inactivation gate f . Experimental work shows that this current is carried predominantly by calcium ions.

$$i_s = \overline{g_s} d f (V_m - E_s) \quad (4.54)$$

where $\overline{g_s}$ is the fully activated conductance and E_s is the channel reversal potential, which is defined by the Nernst equation for internal Ca^{2+} concentration

$$E_s = -82.3 - 13.0287 \ln[Ca]_i \quad (4.55)$$

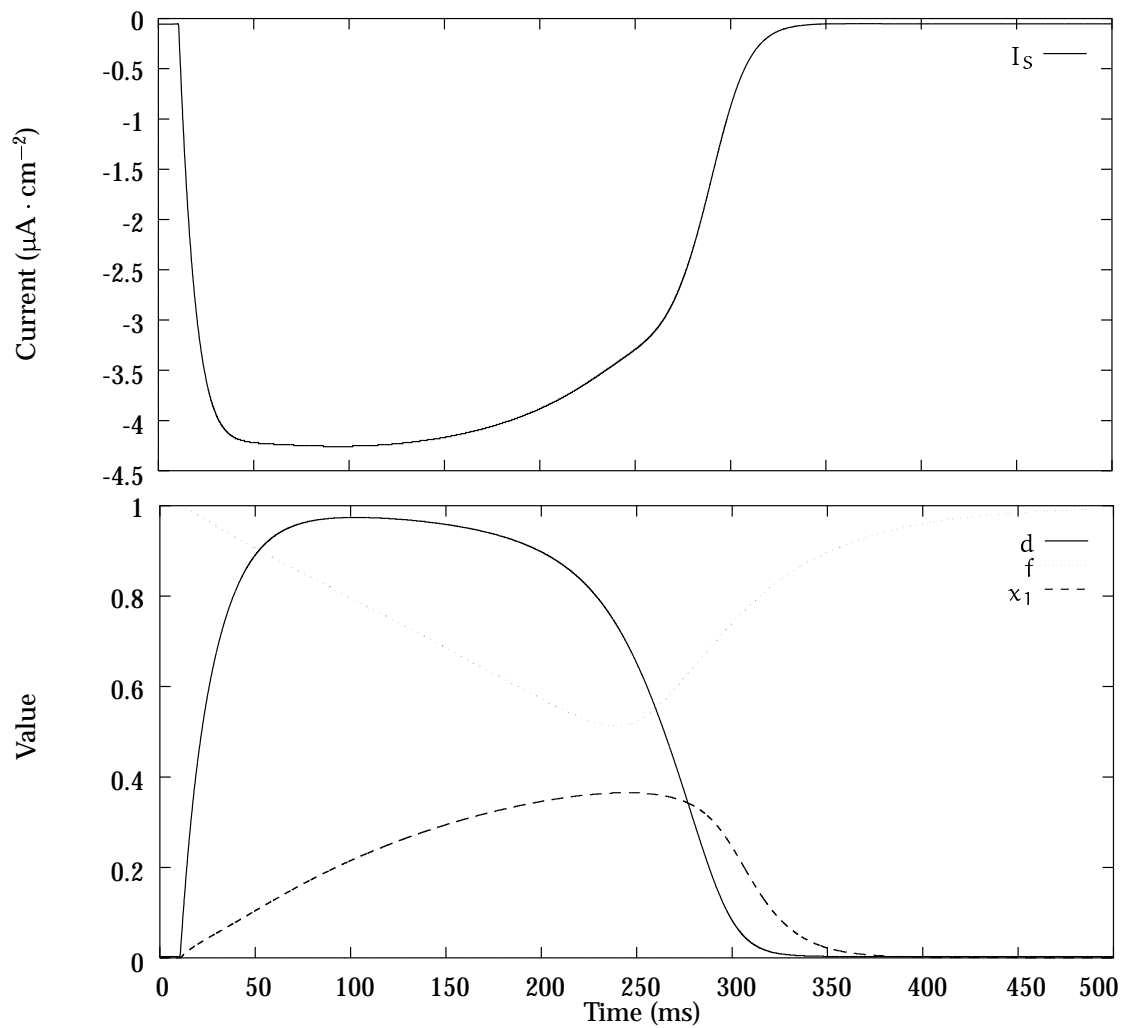


FIGURE 4.16: Beeler-Reuter action slow inward current and associated gating variables d and f , together with the outward current gate variable x_1 .

The change in $[Ca]_i$ (units mMol) is given in terms of the slow inward current as

$$\frac{d[Ca]_i}{dt} = -10^{-4}i_s + 0.07(10^{-4} - [Ca]_i) \quad (4.56)$$

and is shown in Figure 4.17. In the original paper, the units for $[Ca]_i$ were given as Mol, but this has been changed to correspond with later models. The gates d and f

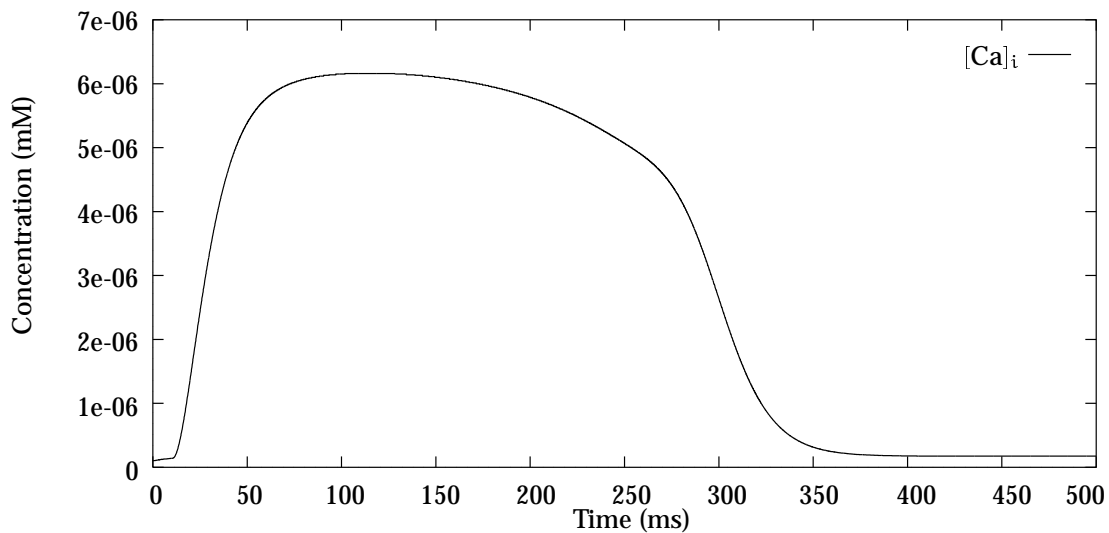


FIGURE 4.17: Beeler-Reuter representation of the intracellular calcium concentration.

obey the first-order HH-type equations, with parameters

$$\begin{aligned}
 \alpha_d &= \frac{0.095 \exp\left(-\frac{V_m - 5}{100}\right)}{1 + \exp\left(-\frac{V_m - 5}{13.89}\right)} \\
 \beta_d &= \frac{0.07 \exp\left(-\frac{V_m + 44}{59}\right)}{1 + \exp\left(\frac{V_m + 44}{20}\right)} \\
 \alpha_f &= \frac{0.012 \exp\left(-\frac{V_m + 28}{125}\right)}{1 + \exp\left(\frac{V_m + 28}{6.67}\right)} \\
 \beta_f &= \frac{0.0065 \exp\left(-\frac{V_m + 30}{50}\right)}{1 + \exp\left(-\frac{V_m + 30}{5}\right)}
 \end{aligned} \tag{4.57}$$

This results in the ionic current shown in Figure 4.16. The form of the rate constants is also shown, together with the form of the x_1 rate constant for the outward current.

3. The time-dependent outward current (i_{x_1})

The description of this current has the same form as for the MNT model, with a rescaling to account for an extracellular potassium concentration of 5.4 mM rather than the 2.7 mM used in the MNT model. Thus the equation for i_{x_1} becomes

$$i_{x_1} = x_1 0.8 \frac{(\exp[0.04(V_m + 77)] - 1)}{\exp[0.04(V_m + 35)]} \tag{4.58}$$

where the rate constants for x_1 are identical to those in Equation (4.42) for the MNT i_{x_1} current shown in Figure 4.16, and the resulting current is shown in Figure 4.18.

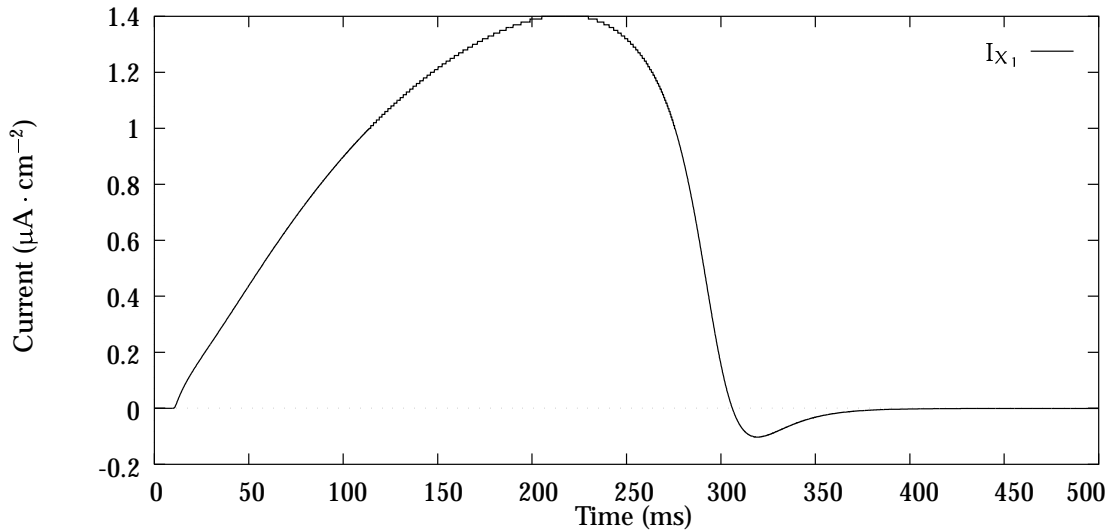


FIGURE 4.18: Beeler-Reuter time-dependent outward current i_{x_1} .

4. The time-independent outward potassium current (i_{k_1})

This current is again similar to the MNT model, with rescaling also applied to account for the change in extracellular potassium concentration

$$i_{k_1} = 0.35 \left[4 \frac{\exp[0.04(V_m + 85)] - 1}{\exp[0.08(V_m + 53)] + \exp[0.04(V_m + 53)]} + 0.2 \frac{V_m + 23}{1 - \exp[-0.04(V_m + 23)]} \right] \quad (4.59)$$

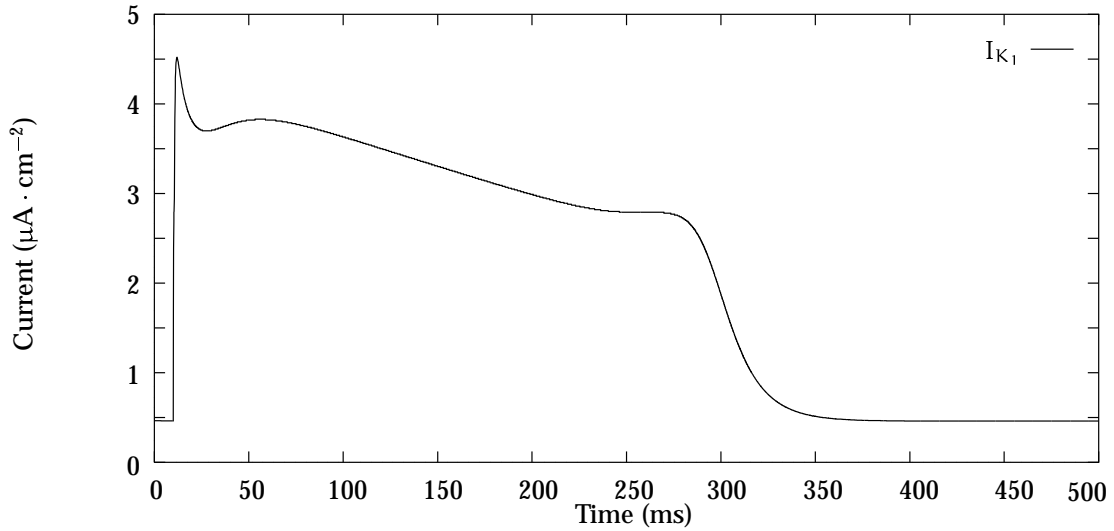
resulting in the graph drawn in Figure 4.19.

Constants

The constants used in the BR model are presented in Table 4.4, and these values have been used to produce the accompanying diagrams.

4.1.5 Ebihara-Johnson Model

The Ebihara-Johnson (EJ) model was the first to specifically target a single channel and attempt to quantify its parameters. A series of experiments performed by

FIGURE 4.19: Beeler-Reuter time-independent potassium current i_{K_1} .

Constant	Value
$C_m (\mu\text{Fcm}^{-2})$	1
$E_{\text{Na}} (\text{mV})$	50
$\overline{g_{\text{Na}}} (\text{mS} \cdot \text{cm}^{-2})$	4
$g_{\text{NaC}} (\text{mS} \cdot \text{cm}^{-2})$	0.003
$\overline{g_s} (\text{mS} \cdot \text{cm}^{-2})$	0.09

TABLE 4.4: Constants used in the Beeler-Reuter model.

Ebihara, Shigeto, Lieberman and Johnson (1980) obtained voltage-clamp data of the fast sodium current in cardiac muscle. The model was fitted to the experimental data, and showed a faster rise in potential during depolarisation, and this model exhibits a faster sodium current than the BR model. The EJ model follows the HH formulation (Hodgkin and Huxley 1952) and is represented by the equation

$$i_{\text{Na}} = \overline{g_{\text{Na}}} m^3 h (V_m - E_{\text{Na}}) \quad (4.60)$$

where $\overline{g_{\text{Na}}}$ is the maximal sodium conductance, m is the activation gate parameter, h is the inactivation gate parameter and E_{Na} is the sodium equilibrium potential. Spach and Heidlage (1993) gives values of $\overline{g_{\text{Na}}} = 28 \text{ mS} \cdot \text{cm}^{-2}$ and $E_{\text{Na}} = 33.45 \text{ mV}$ for normal conditions.

The m and h gates obey the standard first order equations with rate coefficients

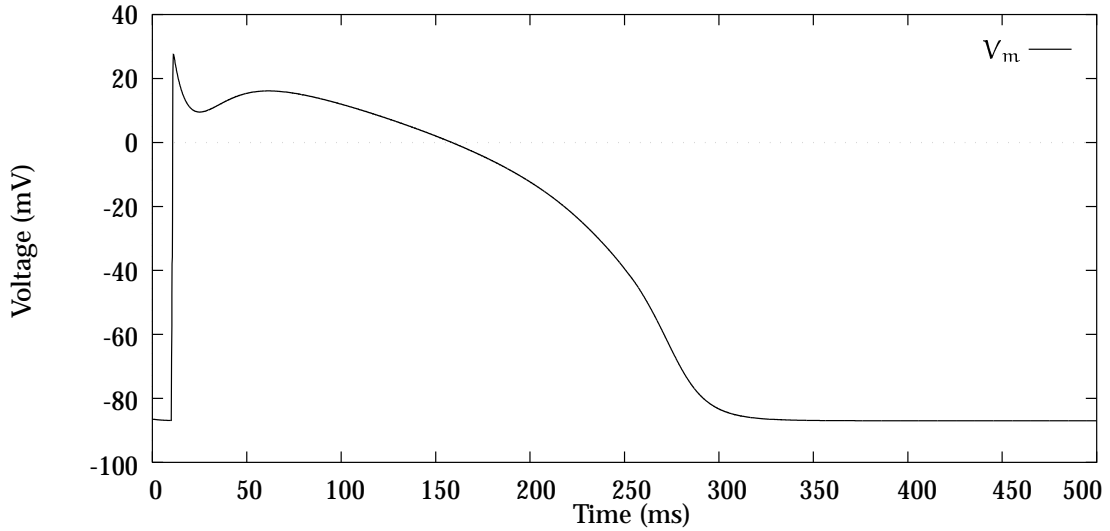


FIGURE 4.20: Beeler-Reuter Ebihara-Johnson action potential.

given by

$$\begin{aligned}
 \alpha_m &= \frac{0.32(V_m + 47.13)}{1 - \exp(-V_m - 47.13)} \\
 \beta_m &= 0.08 \exp(-V_m/11) \\
 \alpha_h &= \begin{cases} 0 & \text{if } V_m \geq -40 \text{ mV} \\ 0.135 \exp[(-80.0 - V_m)/6.8] & \text{if } V_m < -40 \text{ mV} \end{cases} \quad (4.61) \\
 \beta_h &= \begin{cases} \frac{1}{0.13(\exp[-(V_m+10.66)/11.1]+1)} & \text{if } V_m \geq -40 \text{ mV} \\ 3.56 \exp(0.079V_m) + 3.1 \times 10^5 \exp(0.35V_m) & \text{if } V_m < -40 \text{ mV} \end{cases}
 \end{aligned}$$

The equation for α_m was incorrectly stated in the original EJ paper (Ebihara and Johnson 1980), but appears as shown above in Spach and Heidlage (1993), who cite a later paper by Johnson as their source (Johnson 1983). This corrected value of α_m corresponds with the graph of the function for α_m given in the original paper. There is no variable corresponding to the j variable used in the BR model because the experimental results showed no need to include a second deactivation variable.

Spach *et al.* pair this model of the depolarising sodium current with a repolarisation, or leakage, current which is linearly dependent on the membrane voltage, and is identical to the HH leakage current given in Equation (4.20)

$$i_L = \bar{g}_L(V_m - E_L) \quad (4.62)$$

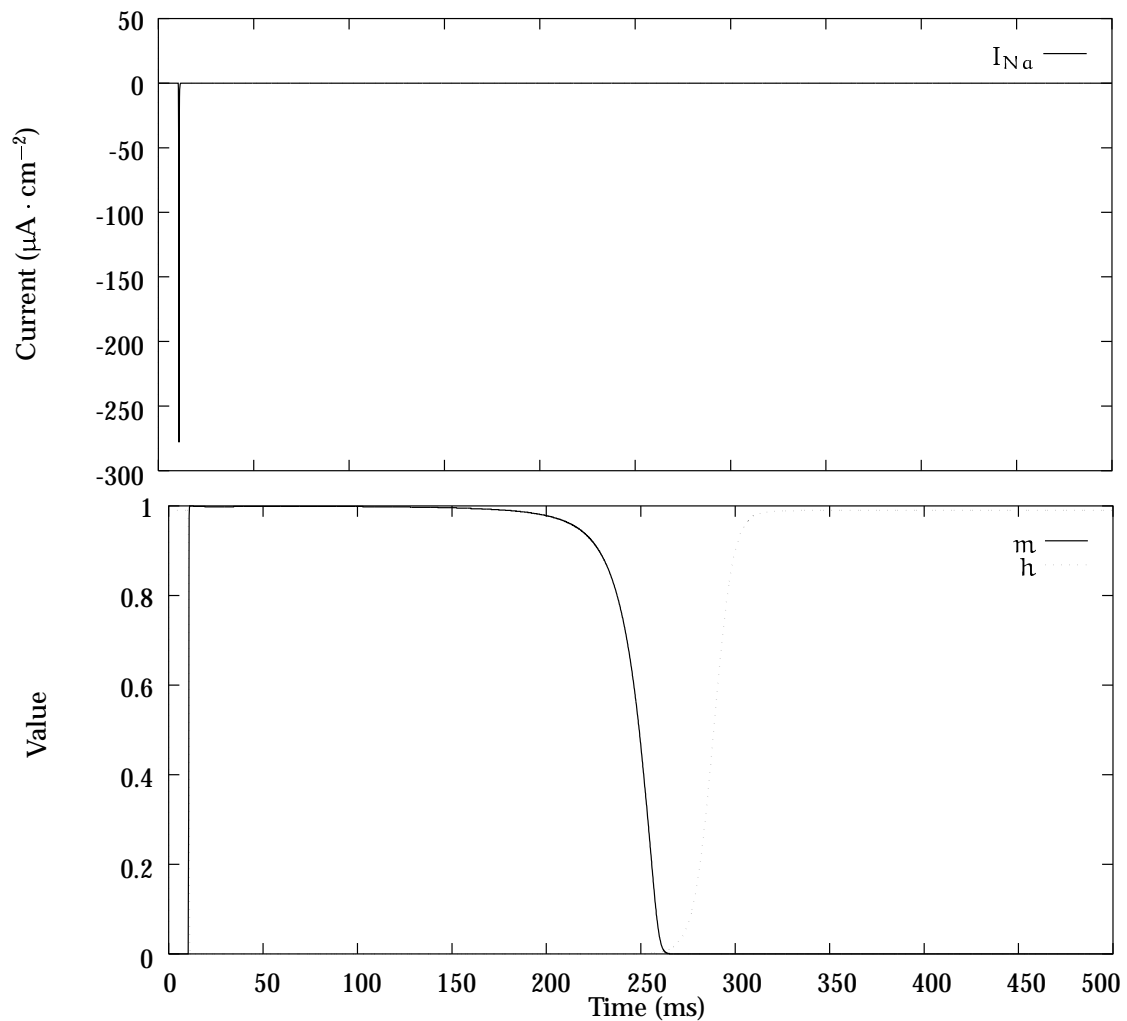


FIGURE 4.21: Beeler-Reuter Ebihara-Johnson sodium current and associated gating variables m and h .

where \bar{g}_L is the leakage conductance, which is the reciprocal of the membrane resistance. They set E_L to the value of the resting potential.

In other simulations, such as that of Pollard, Hooke and Henriquez (1993) the EJ model is coupled to the BR model as a direct replacement for the sodium current. When this is done, the resulting action potential looks as shown in Figure 4.20, and the sodium current and gate variables are graphed in Figure 4.21. The other currents are very similar to those found using just the BR model.

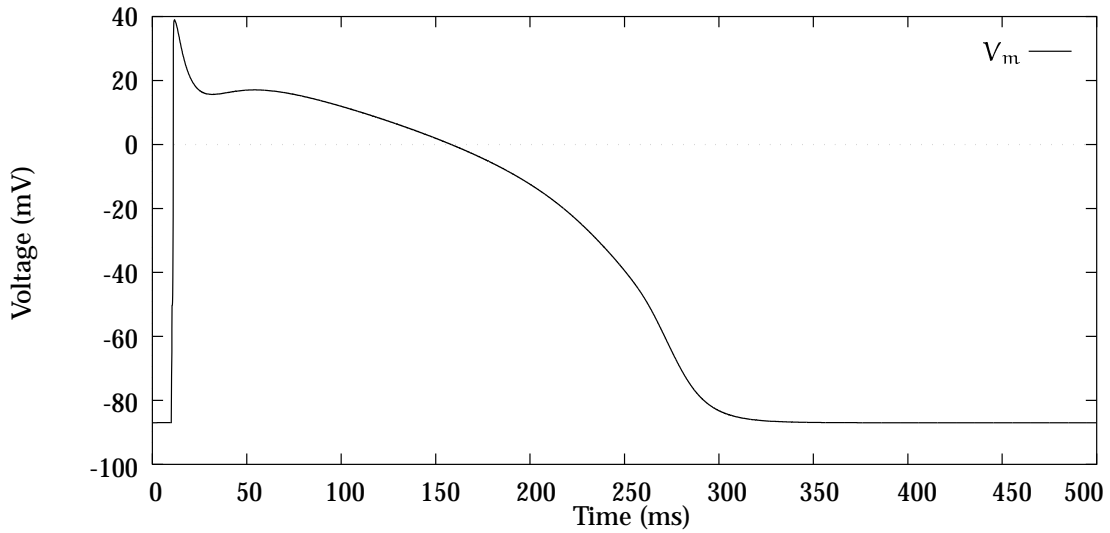


FIGURE 4.22: Beeler-Reuter Drouhard-Roberge action potential.

4.1.6 Drouhard-Roberge Model

The Drouhard-Roberge (DR) model was especially constructed by Drouhard and Roberge (1987) to improve the HH-type formulations to date of the Na^+ current in ventricular myocardial cells. Their improvements have ensured that the action potential upstroke is much faster, and the peak depolarisation is close to the Na^+ potential to be more in line with experimental observations. This is similar to the EJ model in that it can be used as a direct replacement for the sodium kinetics of the BR model.

The DR model used the HH formulation for the sodium membrane current (Equation 4.18) with only one inactivation variable h rather than the two of the BR model, because there was still much uncertainty regarding the existence and function of the j gate. The rate constants for the gates were fitted as in the other models described above to obtain the following expressions:

$$\begin{aligned}
 \alpha_m &= \frac{0.9(V_m + 42.65)}{1 - \exp[-0.22(V_m + 42.65)]} \\
 \beta_m &= 1.437 \exp[-0.085(V_m + 39.75)] \\
 \alpha_h &= 0.1 \exp[-0.193(V_m + 79.65)] \\
 \beta_h &= \frac{1.7}{1 + \exp[-0.095(V_m + 20.5)]}
 \end{aligned} \tag{4.63}$$

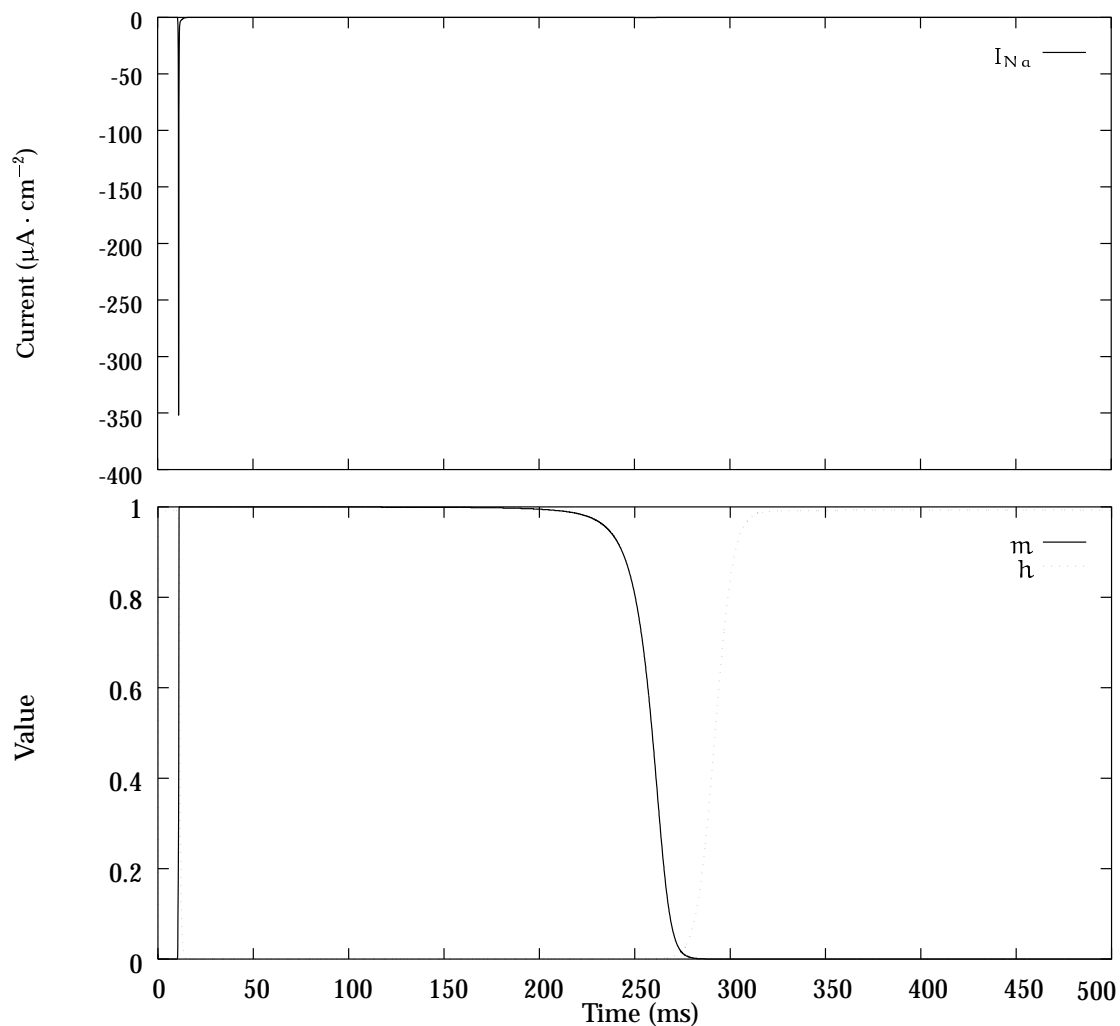


FIGURE 4.23: Beeler-Reuter Drouhard-Roberge sodium current and associated gate variables m and h .

They have chosen to use $\bar{g}_{Na} = 15 \text{ mS} \cdot \text{cm}^{-2}$ and $E_{Na} = 40 \text{ mV}$ as the values for the parameters in the sodium equation as being representative of the range of values found experimentally. Similar plots to those shown for the EJ model are shown in Figure 4.22 and Figure 4.23 where the DR action potential and sodium kinetics are graphed respectively.

A comparison between the BR model, the BR-EJ model and the BR-DR model shows that the BR-DR model exhibits a much faster rise in potential during depolarisation (\dot{V}_{max} is almost twice as large as for the BR-EJ model and more than three times as much as the original BR model) which is much closer to some values reported for the ventricular cell membrane at room temperature, though a little larger than some

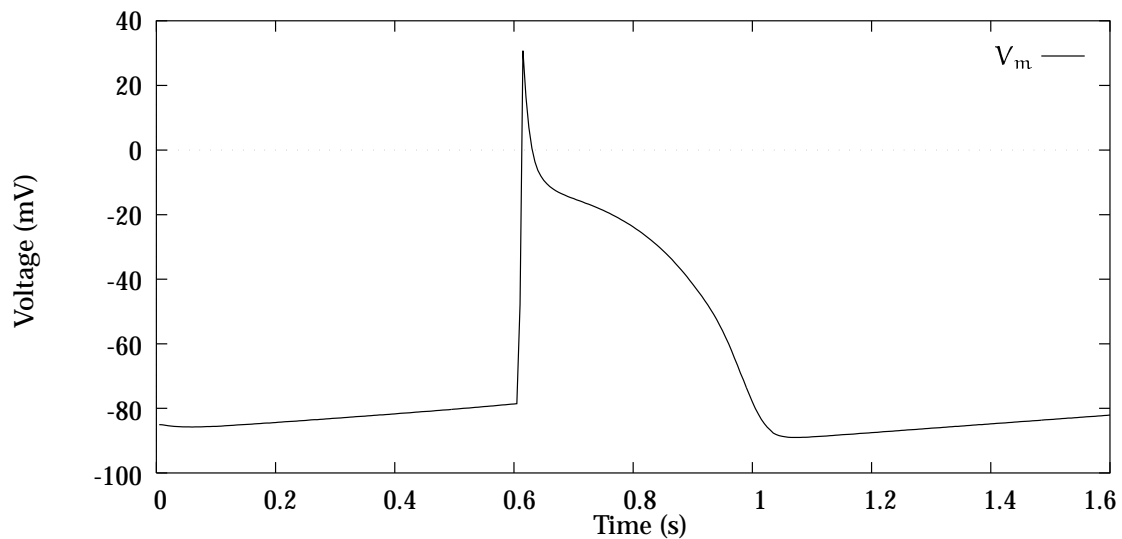


FIGURE 4.24: Di Francesco-Noble model of the action potential in Purkinje cells.

other measurements. In addition, the peak I_{Na} , the peak g_{Na} and V_{max} are somewhat increased over the other models.

4.1.7 Di Francesco-Noble Model

During the years following the formulation of the MNT model in 1975 and the BR model in 1977 a large number of experiments were performed which provided a greater insight into the working of the ion channels in cardiac tissue. Di Francesco and Noble (1985) constructed a new model of cardiac electrical activity which sought to incorporate much of this new data and, as the paper states, aims to

“fully integrate the electrophysiological description of gated channels in the heart with a description of the ionic pump and sequestering processes” (Di Francesco and Noble 1985, p. 392).

They do acknowledge that their representation of some of the currents are unlikely to remain the best available for very long, but this model has remained the most complete of all Purkinje fibre ionic current models to date.

The Di Francesco-Noble (DFN) model is a direct replacement for the MNT model in its description of Purkinje fibre electrical activity. In particular, it takes into account changes in interpretation of the i_{K2} system, incorporates more accurate experimental

data concerning the fast sodium current for Purkinje fibres (Colatsky 1980), and takes account of some intracellular and extracellular ion concentration changes by including various ion concentrations as variables and tracking some of the ionic pumps and exchange mechanisms. In addition, a start is made on accounting for calcium movement within the cell between the sarcoplasmic reticulum and the myoplasm.

Ionic currents

The total ionic current is now the sum of up to 12 individual components depending on the tissue being modelled.

$$I_{DN} = i_f + i_K + i_{K1} + i_{t0} + i_{b,Na} + i_{b,Ca} + i_p + i_{NaCa} + i_{Na} + i_{Ca,f} + i_{Ca,s} + i_{pulse} \quad (4.64)$$

These currents are described in more detail in the original paper, and only a brief description of the important features of each current is given here. i_{pulse} describes the applied current.

The model has been implemented as a translation from the OxSoft HEART¹ package and used with appropriate constants as specified in the original DFN paper and other sources for Purkinje cells. The resulting action potential as calculated using this form of the DFN model is graphed in Figure 4.24.

1. Hyperpolarizing-activated current (i_f)

This is a $Na^+ - K^+$ current which is the nearest equivalent to i_{K_2} in the original MNT formulation. Contributions by each ion are approximately equal, so that the normal net reversal potential is around 20 mV. The current is given by

$$i_f = y \bar{i}_f \quad (4.65)$$

where y is a gating variable representing the degree of activation of i_f and \bar{i}_f is the fully activated current, and is given by

$$\bar{i}_f = \left(\frac{[K]_c}{[K]_c + K_{m,f}} \right) (g_{f,K}(V_m - E_K) + g_{f,Na}(V_m - E_{Na})) \quad (4.66)$$

¹Originally developed at Oxford University

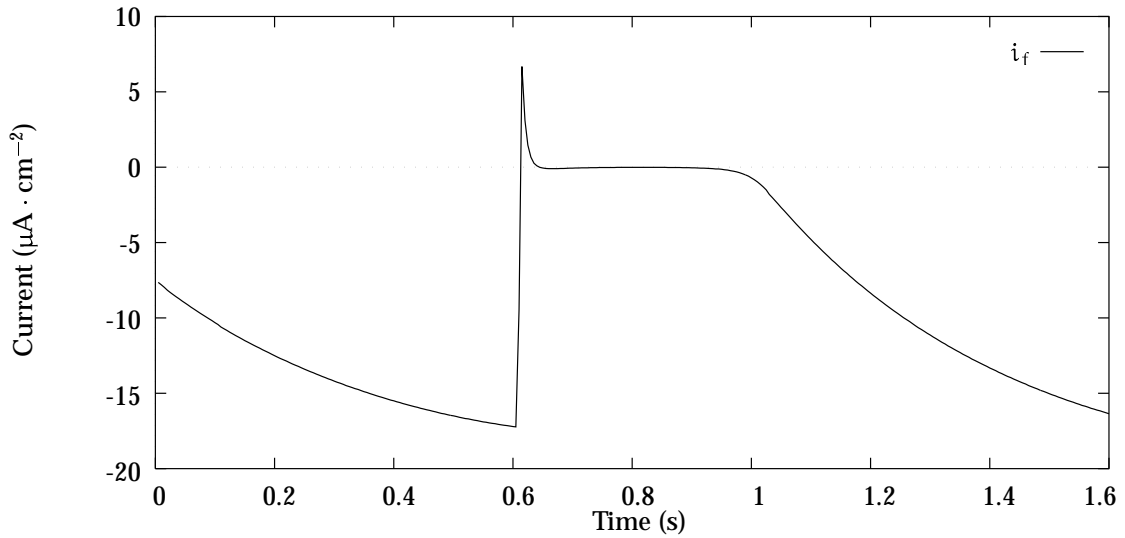


FIGURE 4.25: The i_f current described by the DFN model.

where $[K]_c$ is the cleft potassium concentration, $K_{m,f}$ is the concentration of the bulk potassium required for half activation of the current, and $g_{f,K}$ and $g_{f,Na}$ are the sodium and potassium conductances for the i_f channel respectively. E_K and E_{Na} are the reversal potentials of sodium and potassium, respectively, as in previous models.

The gating variable y is related to the s parameter in the MNT model as $y = 1 - s$, and behaves according to the HH-type gating differential equation (Equation 4.7) with coefficients

$$\begin{aligned} \alpha_y &= 0.025 \exp(-0.067(V_m + 52)) \\ \beta_y &= \frac{0.5(V_m + 52)}{1 - \exp(0.2(V_m + 52))} \end{aligned} \quad (4.67)$$

The resulting form of the i_f current is shown in Figure 4.25.

2. Time-dependent (delayed) K^+ current (i_K)

This is an outward current which is equivalent to the i_{x1} current from the MNT model and is controlled by a single gate given the symbol x , and a simple model of the kinetics

$$i_K = x \bar{i}_K \quad (4.68)$$

where \bar{i}_K is the fully-activated value of i_K and is derived from rate theory (Jack,

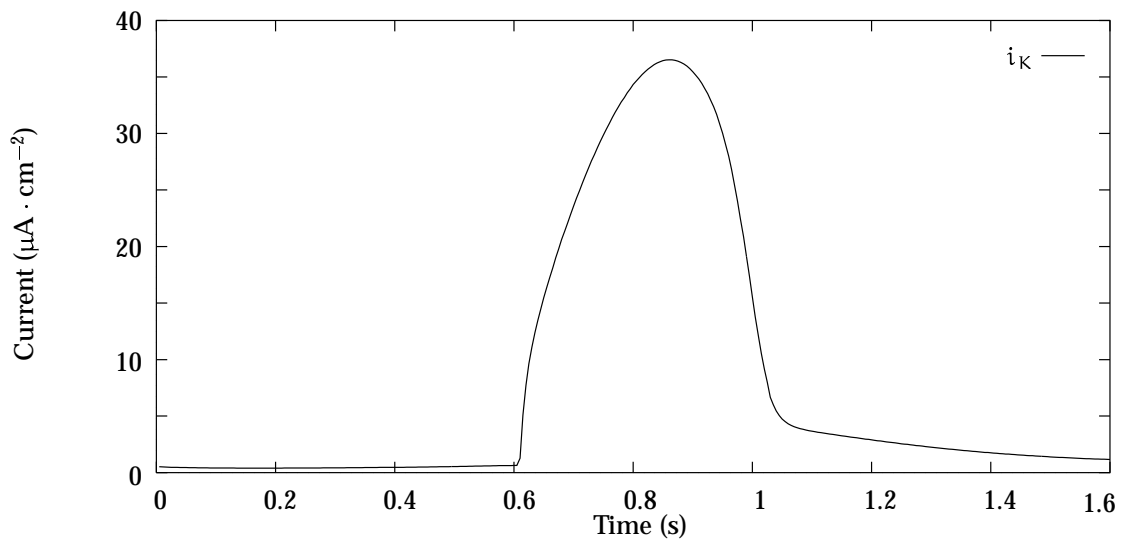


FIGURE 4.26: The time-dependent potassium current i_K described by the DFN model.

Noble and Tsien 1983) to give

$$\bar{i}_K = i_{K, \max} \left(\frac{[K]_i - [K]_c \exp(-V_m/25)}{140} \right) \quad (4.69)$$

This time dependent activation gate \bar{x} has rate constants described by the same equations as the x_1 gating variable has in the MNT model. The resulting form of the time-dependent potassium current is shown in Figure 4.26.

3. Time-independent (background) K^+ current (i_{K1})

A new equation for this current was developed and is an empirical formulation that is formulated from a variety of experimental work during the late 1970's and early 1980's:

$$i_{K1} = \bar{g}_{K1} \cdot \frac{[K]_c}{[K]_c + K_{m,K1}} \cdot \frac{V_m - E_K}{1 + \exp((V_m - E_K + 10)2F/RT)} \quad (4.70)$$

The resulting form of the time-independent potassium current is shown in Figure 4.27.

4. Transient outward current (i_{to})

This current replaced the I_{qr} chloride-based current of the MNT model, which was shown to be flawed. This current is an outward rectifier which is $[Ca]_i$ -activated,

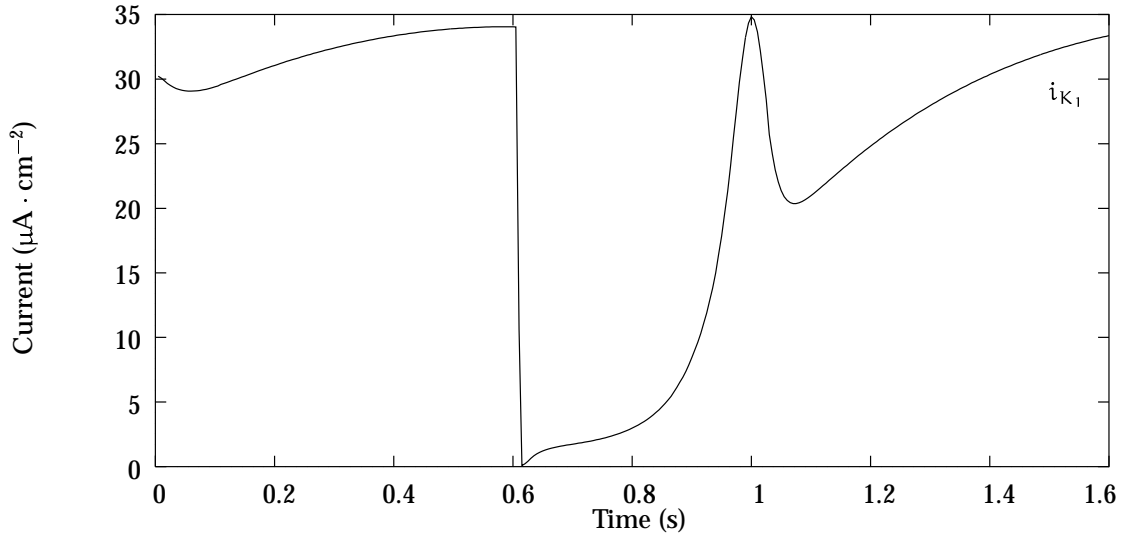


FIGURE 4.27: The time-independent potassium current i_{K1} described by the DFN model.

and which depends on $[K]_o$. The inactivation process of this channel was still not well understood at this stage, and was modelled with a first order equation for a rate variable r , so that

$$i_{to} = r \overline{i_{to}} \quad (4.71)$$

where $\overline{i_{to}}$ is the maximal current given by

$$\overline{i_{to}} = 0.28 \frac{0.2 + [K]_c}{K_{m,to} + [K]_c} \cdot \frac{[Ca]_i}{K_{act,to} + [Ca]_i} \cdot \frac{V_m + 10}{1 - \exp(-0.2(V_m + 10))} \cdot \frac{1}{([K]_i \exp(0.02V_m) - [K]_o \exp(-0.02V_m))} \quad (4.72)$$

5. Background sodium current ($i_{b,Na}$)

This is a simple background current very similar to $i_{Na,b}$ of the MNT model described by

$$i_{b,Na} = \frac{[Na]_o}{[Na]_{o,c}} \overline{g_{b,Na}} (V_m - E_{Na}) + i_{b,Ch} \quad (4.73)$$

where $[Na]_{o,c}$ is a control level of external sodium (usually 140 mM) and $i_{b,Ch}$ is a background current due to choline, or some other sodium substitute, and the conductance $\overline{g_{b,Na}}$ is set to 0.18 μS .

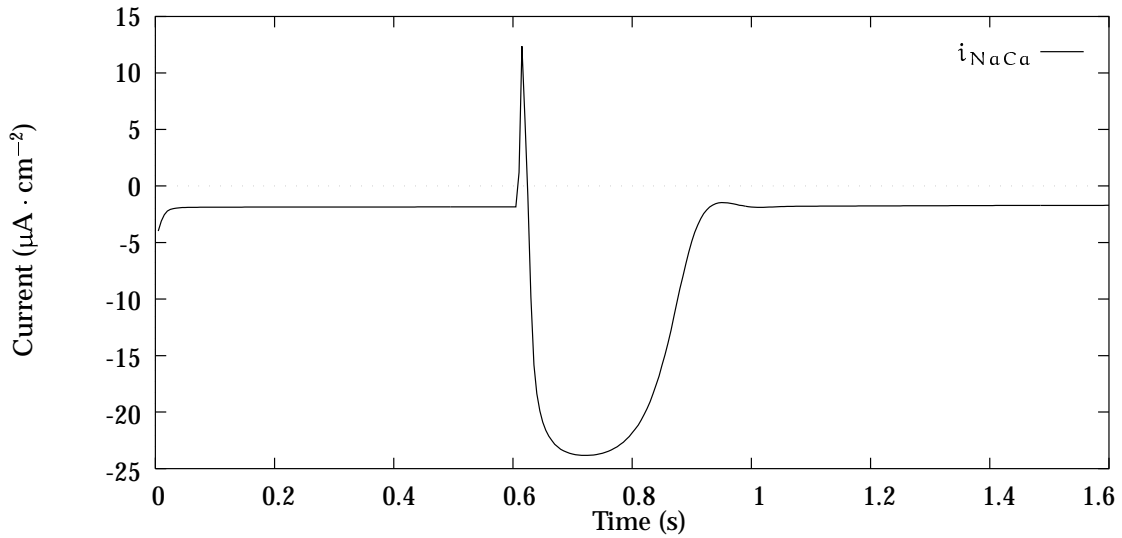


FIGURE 4.28: The Na^+ - Ca^{2+} exchange current i_{NaCa} described by the DFN model.

6. Background calcium current ($i_{b,\text{Ca}}$)

Another simple background current of the same form as $i_{b,\text{Na}}$:

$$i_{b,\text{Ca}} = \overline{g_{b,\text{Ca}}}(V_m - E_{\text{Ca}}) \quad (4.74)$$

7. Na^+ - K^+ exchange pump current (i_p)

This pump exchanges 3 Na^+ ions out for 2 K^+ ions into the cell producing a net outward current. The assumption is made that the pump is activated by external K^+ and internal Na^+ by first-order processes, such that

$$i_p = \overline{i_p} \frac{[\text{K}]_c}{K_{m,\text{K}} + [\text{K}]_c} \cdot \frac{[\text{Na}]_i}{K_{m,\text{Na}} + [\text{Na}]_i} \quad (4.75)$$

where $K_{m,\text{K}}$ and $K_{m,\text{Na}}$ are the respective concentrations required for half-activation.

8. Na^+ - Ca^{2+} exchange current (i_{NaCa})

The formulation of this current assumes that i_{NaCa} depends solely on the Na^+ and Ca^{2+} gradients and the transmembrane potential. The stoichiometry of the exchange is $3\text{Na}^+ : 1\text{Ca}^{2+}$ producing a net outward current.

$$i_{\text{NaCa}} = k_{\text{NaCa}} \sinh((V_m - E_{\text{NaCa}})F/RT) \quad (4.76)$$

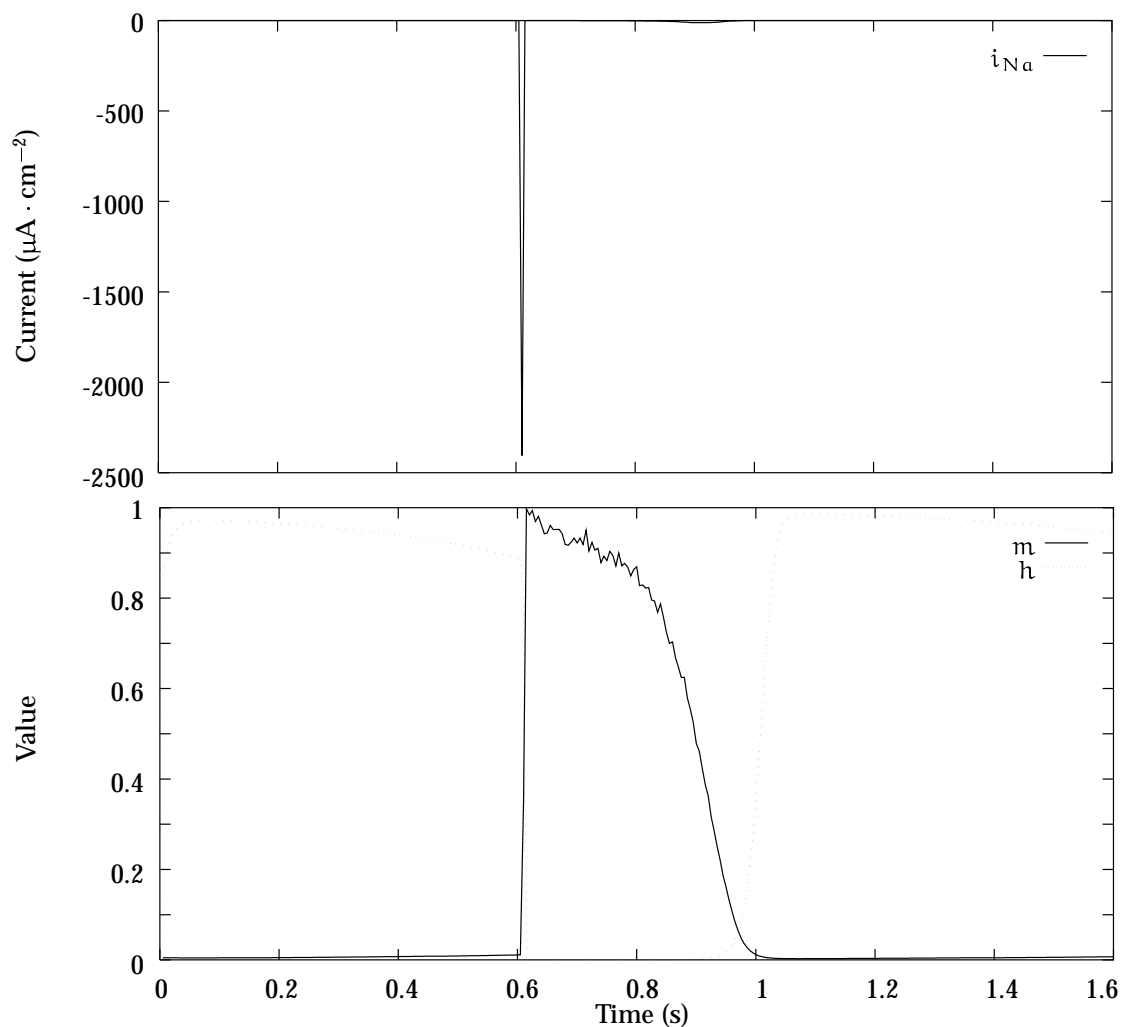


FIGURE 4.29: DFN sodium current and associated gate variable m and h .

where the reversal potential of the exchange is given by

$$E_{\text{NaCa}} = \frac{n_{\text{NaCa}} E_{\text{Na}} - 2E_{\text{Ca}}}{n_{\text{NaCa}} - 2} \quad (4.77)$$

where n_{NaCa} is the stoichiometry of the exchange. Using these parameters, the current develops a form shown in Figure 4.28.

9. Fast sodium current (i_{Na})

The DFN model reverts once again to a two-variable model of the sodium kinetics with new equations for m and h . It is acknowledged, however, that the model does not represent the slower components of Na^+ inactivation and recovery. It is also

assumed that the sodium channel shows a 12% permeability to potassium ions:

$$i_{Na} = m^3 h \bar{g}_{Na} (V_m - E_{mh}) \quad (4.78)$$

where the channel reversal potential is given by

$$E_{mh} = \frac{RT}{F} \ln \frac{[Na]_o + 0.12[K]_c}{[Na]_i + 0.12[K]_i} \quad (4.79)$$

and the gating variables m and h are governed by the rate constants

$$\begin{aligned} \alpha_m &= \frac{200(V_m + 41)}{1 - \exp[-0.1(V_m + 41)]} \\ \beta_m &= 8000 \exp[-0.056(V_m + 66)] \\ \alpha_h &= 20 \exp[-0.125(V_m + 75)] \\ \beta_h &= \frac{2000}{320 \exp[-0.1(V_m + 75)]} \end{aligned} \quad (4.80)$$

The resulting current is shown in Figure 4.29 together with the time-course of the gate variables.

10. *Second inward current* (i_{si})

The kinetics of the secondary inward current are still described in terms of two gate variables d and f , but the time constants for both the activation and inactivation processes are much shorter than those used in either the MNT or the BR models. It is debatable whether the slow component of this current, $i_{Ca,s}$ is present in Purkinje fibre, and has not been included in the model. The fast component, $i_{Ca,f}$, of this current was divided into the individual ion movements of Ca^{2+} , K^+ and where necessary Na^+ .

$$i_{Ca,f} = df(i_{si,Ca} + i_{si,K} + i_{si,Na}) \quad (4.81)$$

where constant field formulations for the individual ion movements were used. The shorter time constants give rate constants for the gating variables as

$$\begin{aligned} \alpha_d &= 30 \frac{V_m + 24}{1 - \exp(-(V_m + 24)/4)} \\ \beta_d &= 12 \frac{V_m + 24}{\exp((V_m + 24)/10) - 1} \\ \alpha_f &= 6.25 \frac{V_m + 34}{\exp((V_m + 34)/4) - 1} \\ \beta_f &= \frac{50}{1 + \exp(-(V_m + 34)/4)} \end{aligned} \quad (4.82)$$

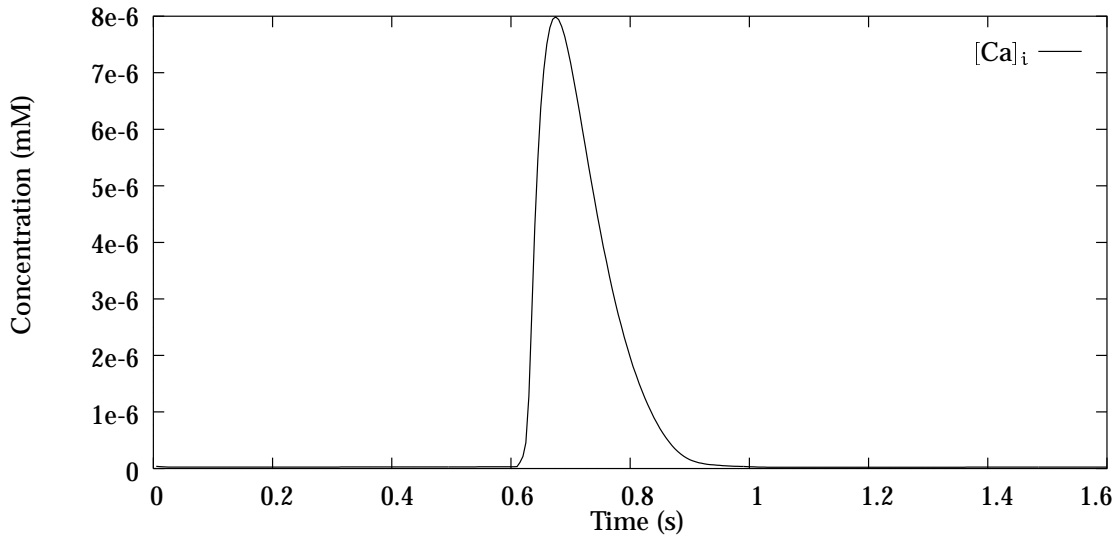


FIGURE 4.30: Changes in intracellular calcium concentration as determined by the DFN model.

Ion concentrations

Additionally, the DFN model attempted to quantify the changes in several ion concentrations, as well as the $[Ca]_i$ of earlier models.

1. Intracellular sodium concentration

The model of change in $[Na]_i$ is defined as the sum of the various sodium currents divided by the intracellular fluid volume:

$$\frac{d[Na]_i}{dt} = -(i_{na} + i_{b,Na} + i_{f,Na} + i_{si,Na} + 3i_p + \frac{n_{NaCa}}{n_{NaCa} - 2} i_{NaCa}) / V_i F \quad (4.83)$$

where V_i is the intracellular fluid volume.

2. Intracellular calcium concentration

Changes in $[Ca]_i$ were first modelled in the BR model, and this process has been taken one step further in the DFN model, although this model still provides only a simple model of calcium movement within the cell. The Ca^{2+} is assumed to be sequestered by the sarcoplasmic reticulum, and the amount stored here is $[Ca]_{up}$. Some fraction of the calcium is transferred to a release store in the junctional SR ($[Ca]_{rel}$) before being released into the intracellular space, this release being induced

by calcium. The concentration of calcium in each of these various stores is modelled, together with the transfer between the calcium sites and the Ca^{2+} transfer across the cell membrane via the other ionic currents. These seem to be the minimum assumptions required to model the calcium transient.

The associated currents are defined as

$$\begin{aligned} i_{\text{up}} &= \alpha_{\text{up}}[\text{Ca}]_i(\overline{[\text{Ca}]_{\text{up}}} - [\text{Ca}]_{\text{up}}) - \beta_{\text{up}}[\text{Ca}]_{\text{up}} \\ i_{\text{tr}} &= \alpha_{\text{tr}}p([\text{Ca}]_{\text{up}} - [\text{Ca}]_{\text{rel}}) \\ i_{\text{rel}} &= \alpha_{\text{rel}}[\text{Ca}]_{\text{rel}}\left(\frac{[\text{Ca}]_i^r}{[\text{Ca}]_i^r + K_{m,\text{Ca}}}\right) \end{aligned} \quad (4.84)$$

where $\overline{[\text{Ca}]_{\text{up}}}$ is the maximum value of $[\text{Ca}]_{\text{up}}$ and is set to 5 mM, r is the number of Ca^{2+} ions assumed to bind to the release site (usually 2), and p is governed by a first order HH-type equation with rate constants identical to those for f (Equation (4.82)) but slowed by a factor of 10. $K_{m,\text{Ca}}$ is usually set to 0.001 mM. The α parameters are determined from time constants measured for the movement of calcium from one space to another.

This results in the change in concentrations being given by

$$\begin{aligned} \frac{d[\text{Ca}]_{\text{up}}}{dt} &= (i_{\text{up}} - i_{\text{tr}})/2V_{\text{up}}F \\ \frac{d[\text{Ca}]_{\text{rel}}}{dt} &= (i_{\text{tr}} - i_{\text{rel}})/2V_{\text{rel}}F \\ \frac{d[\text{Ca}]_i}{dt} &= -(i_{\text{si},\text{Ca}} + i_{\text{b},\text{Ca}} - \frac{2i_{\text{NaCa}}}{n_{\text{NaCa}} - 2} + i_{\text{up}} - i_{\text{rel}})/2V_iF \end{aligned} \quad (4.85)$$

where $V_{\text{up}} = 0.05V_i$ is the volume of the uptake stores (approximately 5% of the total intracellular volume) and $V_{\text{rel}} = 0.02V_i$ is the volume of the release stores. The change in concentration of intracellular Ca^{2+} is shown in Figure 4.30.

3. Extracellular potassium concentration

Assuming a homogeneous K^+ concentration in a three-compartment model, the change in extracellular potassium is given by

$$\frac{d[\text{K}]_c}{dt} = -P([\text{K}]_c - [\text{K}]_b) + i_{m,\text{K}}/V_eF \quad (4.86)$$

where $[\text{K}]_b$ is the bulk extracellular K^+ concentration, P is the rate constant for exchange (between 0.2 and 1 s^{-1} , V_e is the extracellular space volume, and the total

potassium membrane flux $i_{m,K}$ is given by

$$i_{m,K} = i_{K,1} + i_K + i_{f,K} + i_{si,K} + i_{b,K} - 2i_p \quad (4.87)$$

4. Intracellular potassium concentration

This is related to the total K^+ membrane flux.

$$\frac{d[K]_i}{dt} = -i_{m,K}/V_i F \quad (4.88)$$

where V_i is the volume of the intracellular space.

Extensions to the model

The DFN model was subsequently altered and extended, firstly to describe the behaviour of the SA node (Noble and Noble 1984) and later to the ionic processes observed within rabbit atrial cells (Hilgemann and Noble 1987). The Hilgemann model significantly extended the DFN model in terms of the movement of Ca^{2+} within the cell, and particularly in relation to the uptake and release through the sarcoplasmic reticulum.

4.1.8 Luo-Rudy I Model

The Luo and Rudy (1991) model is the next significant update to the BR mammalian ventricular model. It is known as the Luo-Rudy I (LR-I) model because it is the first of the two Luo-Rudy models.

The ionic current I_{ion} is the sum of six different currents: i_{Na} , a fast sodium current; i_{si} , a slow inward current; i_K , a time-dependent potassium current; i_{K1} , a time-independent potassium current; i_{Kp} , a plateau potassium current; and i_b , a time-independent background current.

1. i_{Na} : *Fast Sodium Current*. The LR-I model adopts the same activation (m) and inactivation (h) gate variables as the EJ model, and also incorporates a slow

inactivation gate (j) as suggested by the BR model. The sodium current has the form

$$i_{Na} = \overline{g_{Na}} m^3 h j (V_m - E_{Na}) \quad (4.89)$$

where $\overline{g_{Na}}$ is the maximum conductance of the sodium channel (given as $23 \text{ mS} \cdot \text{cm}^{-2}$), and E_{Na} is the reversal potential of the channel (which they set to 54.4 mV). The m and h gates have identical rate constant coefficients to those given above in Equation (4.61) except that α_m has an additional factor of 0.1 in the denominator in order to provide a realistic activation threshold for this current in a mammalian ventricular cell. The slow inactivation gate j rate constant coefficients are given by

$$\alpha_j = \begin{cases} 0 & \text{if } V_m \geq -40 \text{ mV} \\ \frac{-1.2714 \times 10^5 \exp(0.2444 V_m) - 3.474 \times 10^{-5} \exp(-0.04391 V_m)}{1 + \exp(0.311(V_m + 79.23))} (V_m + 37.78) & \text{if } V_m < -40 \text{ mV} \end{cases}$$

$$\beta_j = \begin{cases} \frac{0.3 \exp(-2.535 \times 10^{-7} V_m)}{(1 + \exp(-0.1(V_m + 32)))} & \text{if } V_m \geq -40 \text{ mV} \\ \frac{0.1212 \exp(-0.01052 V_m)}{(1 + \exp(-0.1378(V_m + 40.14)))} & \text{if } V_m < -40 \text{ mV} \end{cases} \quad (4.90)$$

2. i_{si} : *Slow Inward Current*. This current is the same as in the BR model, which has the form

$$i_{si} = \overline{g_{si}} d f (V_m - E_{si}) \quad (4.91)$$

where E_{si} is given by

$$E_{si} = 7.7 - 13.0287 \ln([Ca]_i) \quad (4.92)$$

The rate constants d and f are governed by the rate constants in Equation (4.57). The concentration of intracellular calcium is governed by

$$\frac{d([Ca]_i)}{dt} = -10^{-4} i_{si} + 0.07(10^{-4} - [Ca]_i) \quad (4.93)$$

and the concentration is measured in units of mMol.

3. i_K : *Time-dependent Potassium Current*. This channel is controlled by a time dependent activation gate (X) and a time independent inactivation gate (X_i), neither of which are dependent on $[K]_o$.

$$i_K = \overline{g_K} X X_i (V_m - E_K) \quad (4.94)$$

where the maximum conductance of the potassium channel $\overline{g_K}$ is dependent on $[K]_o$ and is given by

$$\overline{g_K} = 0.282 \sqrt{[K]_o/5.4} \quad (4.95)$$

X_i is the inward rectification parameter, and is given by

$$X_i = \begin{cases} \frac{2.837(\exp(0.04(V_m+77))-1)}{((V_m+77)\exp(0.04(V_m+35)))} & \text{if } V_m > -100\text{mV} \\ 1 & \text{if } V_m \leq -100\text{mV} \end{cases} \quad (4.96)$$

The rate constants for X are governed by the same equations as for the MNT and BR models and are given in Equation (4.42).

4. i_{K1} : *Time-independent Potassium Current*. This channel contains a single inactivation gate (K1) whose time constant is small enough that it can be approximated by its steady-state value $K1_\infty$.

$$i_{K1} = \overline{g_{K1}} K1_\infty (V_m - E_{K1}) \quad (4.97)$$

where the maximum conductance of the potassium channel $\overline{g_{K1}}$ is given by

$$\overline{g_{K1}} = 0.6047 \sqrt{[K]_o/5.4} \quad (4.98)$$

and the reversal potential E_{K1} is given by

$$E_{K1} = \frac{RT}{F} \ln \left(\frac{[K]_o}{[K]_i} \right) \quad (4.99)$$

The rate constants for K1 are given by

$$\alpha_{K1} = \frac{1.02}{(1 + \exp(0.2385(V_m - E_{K1} - 59.215)))} \quad (4.100)$$

$$\beta_{K1} = \frac{0.49124 \exp(\frac{V_m - E_{K1} + 5.476}{12.45}) + \exp(\frac{V_m - E_{K1} - 594.31}{16.2})}{1 + \exp(-0.5143(V_m - E_{K1} + 4.753))}$$

and the steady-state value $K1_\infty$ is given by

$$K1_\infty = \frac{\alpha_{K1}}{\alpha_{K1} + \beta_{K1}} \quad (4.101)$$

5. i_{Kp} : *Plateau Potassium Current*. This current has been created in order to describe the contribution of a time independent $[K]_o$ -insensitive channel at plateau potentials.

$$i_{Kp} = 0.0183 Kp (V_m - E_{Kp}) \quad (4.102)$$

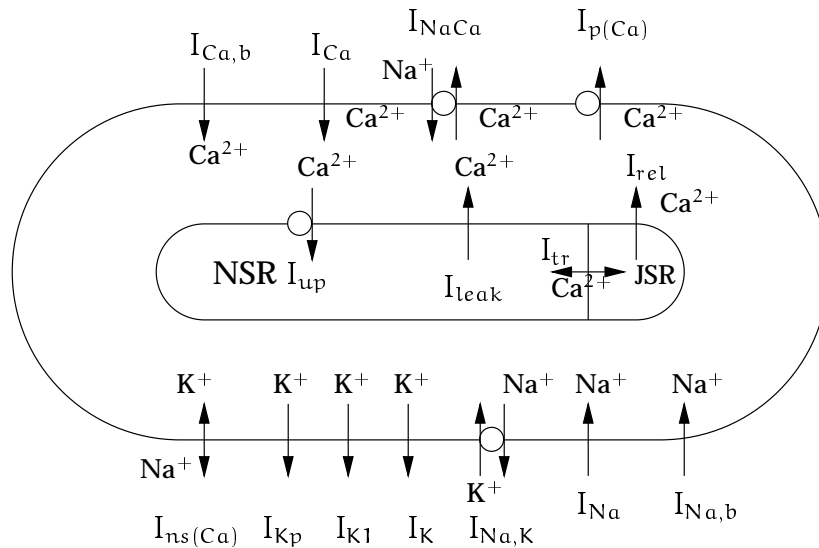


FIGURE 4.31: Schematic diagram of the LR-II model of ionic currents, pumps and exchangers (derived from Luo and Rudy (1994a, Fig. 1)). The sarcoplasmic reticulum (SR) is divided into two compartments: the network SR (NSR) and the junctional SR (JSR).

where $E_{Kp} = E_{K1}$, and

$$Kp = \frac{1}{1 + \exp\left(\frac{7.488 - V_m}{5.98}\right)} \quad (4.103)$$

6. i_b : *Background Current*. This is an additional current which contributes at plateau potentials.

$$i_b = 0.03921(V_m + 59.87) \quad (4.104)$$

4.1.9 Luo-Rudy II Model

A subsequent pair of papers by Luo & Rudy (1994a; 1994b) further developed the LR-I model by addressing some of the issues which were not investigated in the original model. In particular the LR-II model incorporates a more thorough description of the processes which regulate $[Ca]_i$ and the movement of Ca^{2+} through the cell and to and from the sarcoplasmic reticulum. The various currents that comprise the LR-II model are summarised in Table 4.1.9, and show the gate variables associated with each

	Currents	Gates		Ions	Comments
		Activ.n	Inact.n		
1)	i_{Na}	$\{m^3\}$	$\{h, j\}$	Na^+	Fast Na^+ channel
2)	$i_{Ca,t} = i_{Ca+}$ $i_{Ca,Na} + i_{Ca,K}$	$\{d\}$	$\{f, f_{Ca}\}$	Ca^{2+}, Na^+, K^+	L-type Ca^{2+} channel $f_{Ca} \sim 1/(1 + ([Ca]_i)^2)$
3)	i_K	$\{X^2\}$	$\{X_i\}$	K^+	delayed rectifier; $g_{max} \sim \sqrt{[K]_o}$ x_i is V_m -dependent only
4)	i_{NaCa}			Na^+, Ca^{2+}	$3Na^+:Ca^{2+}$ exchanger
5)	$i_V = i_{K1} + i_{Kp} + i_{p(Ca)} + i_{Na,b} + i_{Ca,b} + i_{NaK}$ i_{K1} i_{Kp} $i_{p(Ca)}$ $i_{Na,b}$ $i_{Ca,b}$ i_{NaK}	$\{K_1\}$		K^+ K^+ Ca^{2+} Na^+ Ca^{2+} Na^+, K^+	total time-independent current inward rectifier; $g_{max} \sim \sqrt{[K]_o}$ plateau K^+ channel Ca^{2+} pump in sarcolemma background Na^+ leakage background Ca^{2+} leakage ATP-dep. $3Na^+:2K^+$ pump
6)	$i_{ns(Ca)} = i_{ns,Na} + i_{ns,K}$			Na^+, K^+	non-specific Ca^{2+} activated
7)	Ca^{2+} cycling i_{rel} i_{up} i_{leak} i_{tr}			Ca^{2+} Ca^{2+} Ca^{2+} Ca^{2+}	CICR from JSR to myoplasm Ca^{2+} uptake from myoplasm to NSR Ca^{2+} leak from NSR to myoplasm Ca^{2+} transfer from NSR to JSR

TABLE 4.5: Description of the ionic currents defined by the LR-II model.

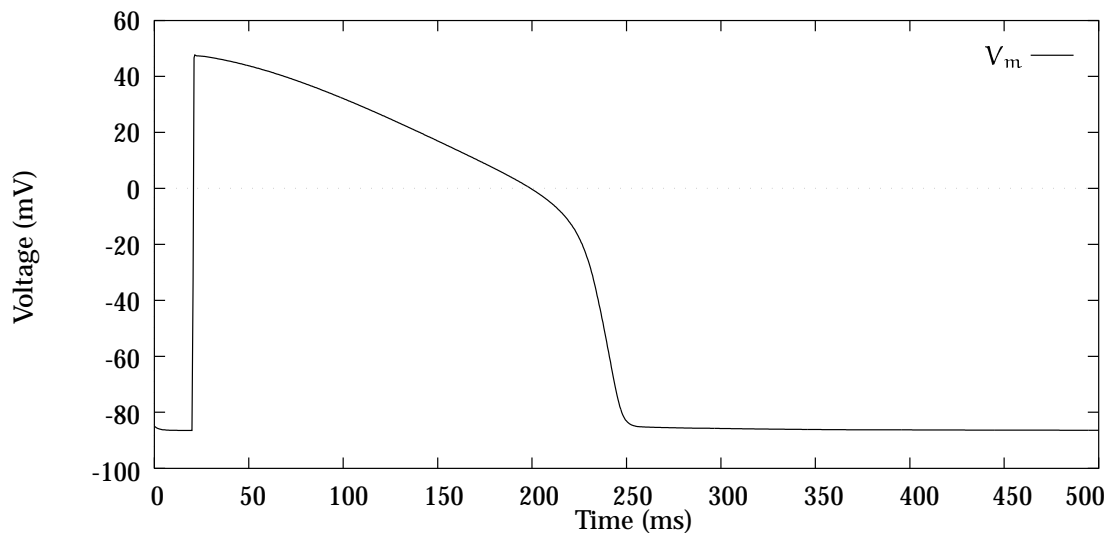


FIGURE 4.32: Action potential from the LR-II model definition.

current and the ions which are involved. A schematic describing the ionic currents defined by the LR-II model is drawn in Figure 4.31. Henry Liu, an undergraduate student at Auckland University, implemented this second Luo-Rudy model as part of an assessed project, and subsequently discovered that the equations provided in the papers were incomplete, and after some dialogue with the authors the model still required some intelligent predictions to be made in order to obtain a reasonable solution. Using values for constants as defined in the paper together with some help from the authors resulted in the ventricular action potential graphed in Figure 4.32.

Ionic currents in the sarcolemma

The full equations for all of the ionic currents will not be given here, but rather a brief discussion of each current which indicates how it differs from the previous LR-I model. The full equations may be found in Luo and Rudy (1994a).

1. i_{Na} : *Fast Na⁺ current*. The formulation of this current is identical to that in the earlier model in that it describes three gate variables (m , h and j) with identical rate constants, except that the maximum conductance has decreased to compensate for the increased reversal potential due to a lower $[Na]_i$ which matches observed values in more recent experiments.

2. $i_{Ca,t}$: *Ionic currents through the L-type Ca^{2+} channel.* This current is the sum of three individual currents relating to the passage of Ca^{2+} , Na^+ and K^+ ions through this channel in a manner similar to the i_{si} current of the DFN model. The channel is permeable to these three ions in the ratio of 2800:3.5:1 respectively, and therefore the largest individual current is i_{Ca} . The model also adds a second inactivation gate f_{Ca} in addition to the standard activation gate d and inactivation gate f . The kinetics of these gates also differs from any previous model to match with recent experimental data.
3. i_K : *Time-dependent K^+ current.* This current now includes an X^2 dependence on the activation gate which was suggested as necessary in the earlier model, but was unable to be successfully incorporated until the i_{Ca} current was properly formulated. The X_i inactivation gate is present, however both gates have new kinetics.
4. i_{NaCa} : *Na^+ - Ca^{2+} exchanger.* This current has a new formulation from the original in the DFN model which corrects several deficiencies in its dependence on the various ions.
5. i_{K1} : *Time-independent K^+ current.* This current is identical to the original except that, again because of the accurately formulated i_{Ca} , the maximum conductance can be increased slightly to a more realistic level.
6. i_{Kp} : *Plateau K^+ current.* Identical to the LR-I model.
7. $i_{p(Ca)}$: *Sarcolemmal Ca^{2+} pump.* An additional mechanism for removing Ca^{2+} from the cell to help maintain a low $[Ca]_i$ at rest.
8. $i_{Na,b}$: *Na^+ background current.* Similar to the background sodium current in the DFN model.
9. $i_{Ca,b}$: *Ca^{2+} background current.* The same as for the DFN model except for a difference in the maximal conductance.
10. i_{NaK} : *Na^+ - K^+ pump.* This is reformulated from the equations in the DFN model to correctly simulate the voltage dependence of this current on the level of $[Na]_o$.

The previous six currents are combined into a single time-independent, purely voltage-dependent current called i_V , which is the equivalent of $i_{K1(T)}$ from the LR-I model.

11. $i_{ns(Ca)}$: *Non-specific Ca^{2+} -activated current*. This current describes a channel which is activated by Ca^{2+} , but is permeable to only Na^+ and K^+ .

It is important to note that the i_{to} chloride-based current has not been included in this model, presumably still due to its poorly understood mechanisms.

Calcium fluxes in the SR

A much more sophisticated model of calcium movement to and from (and within) the SR has been developed for this model which is substantially different from the calcium transport model formulated in the DFN model. It includes an additional current i_{leak} which describes the leakage for Ca^{2+} from the NSR to the myoplasm as well as a detailed model of the process of calcium-induced calcium release.

In addition, the model begins to define the Ca^{2+} buffers in the myoplasm, though apparently the definition of the kinetics of these parameters (troponin and calmodulin) is incomplete.

Enhancements to the Luo-Rudy II Model

Zeng, Laurita, Rosenbaum and Rudy (1995) recently updated the LR-II model to incorporate a number of additional refinements determined following the earlier paper. There were four main enhancements to the model:

1. The time-dependent K^+ current i_K was shown to be composed of two distinct component currents. i_{Kr} ("rapid") is a fast activation current incorporating both a time-dependent activation gate X_r and a time-independent inactivation gate R in order to approximate the fast inactivation process of this channel, and the inward-rectification property which it has. i_{Ks} ("slow") has similar characteristics to the original i_K with a squared dependence on the activation gate X_s , but as neither

inward rectification nor inactivation of this gate were observed, there is no time independent inactivation gate.

2. The maximal conductance of the plateau K^+ current was altered slightly to conform to recent experiments.

3. In addition to the currents through the L-type Ca^{2+} channel, a T-type Ca^{2+} current $i_{Ca(T)}$ was added, which is a low-threshold fast inactivation calcium current. It has a squared dependence on the activation gate b and linear dependence on the inactivation gate g .

4. An analytical expression was derived to compute Ca^{2+} buffering in the junctional SR, and in the cytosol under steady state conditions.

The authors do note in the paper that the results generated are specific to the guinea-pig ventricular cells, and cannot be extrapolated to other animals, as the contribution of each of the various currents is markedly different.

4.2 Simplified Ionic Current Models

In the above biophysically motivated models, empirical formulae have been fitted to experimental data in an attempt to define an equation which will exactly replicate the features of the measured voltage clamp data. This results in a large number of complicated formulae and a lot of flexibility in their response to variations in cellular properties such as concentrations or cell size. This flexibility can be traded for computational speed by formulating *simplified* models which use a few equations to describe the gross features of activation and recovery. These simplified models usually only have a single variable and equation which models the recovery process together with an function of the transmembrane potential providing a model of activation.

A simplified model must at least describe the following features to some extent:

Excitability The mechanism by which a stimulus which exceeds some threshold

value initiates an action potential.

Refractoriness The fact that the heart cannot be reexcited immediately after an action potential. A subsequent fully normal action potential can usually not be initiated until well after the membrane regains its resting potential.

Restitution The dependence of action potential duration on the recovery time. If the time between action potentials is shorter than the second APD will also be shorter.

Dispersion The dependence of wavefront speed on recovery time. Again, the wavefront will slow if it is travelling into more recently recovered tissue.

The simplified models defined below model each of these features in varying ways and with differing levels of success. Naturally, none of them describe the processes as well as a physiological model does. The models are still very useful because of their smaller size and greater speed, but cannot be used to model the effect of chemical or physiological changes to the system.

4.2.1 Polynomial Models

The starting point for many of the simplified models is a polynomial function, usually a cubic. The suitability of polynomial functions for modelling cardiac activity is discussed in a paper by Hunter, McNaughton and Noble (1975) in which various polynomial models are compared to Hodgkin-Huxley-type equations.

A single polynomial function on its own provides a crude model of membrane depolarisation, but doesn't describe any features of repolarisation, such as changes in refractory period. It is therefore only useful for studies of activation or propagation, but cannot be used to study reentry or other multiple excitation phenomena. A cubic is often used for modelling propagation because of its simplicity, especially in comparing with eikonal models which specify only activation time.

The polynomial function is defined so that it crosses the zero line at three distinct points. These three characteristic voltages are the resting potential of the cell

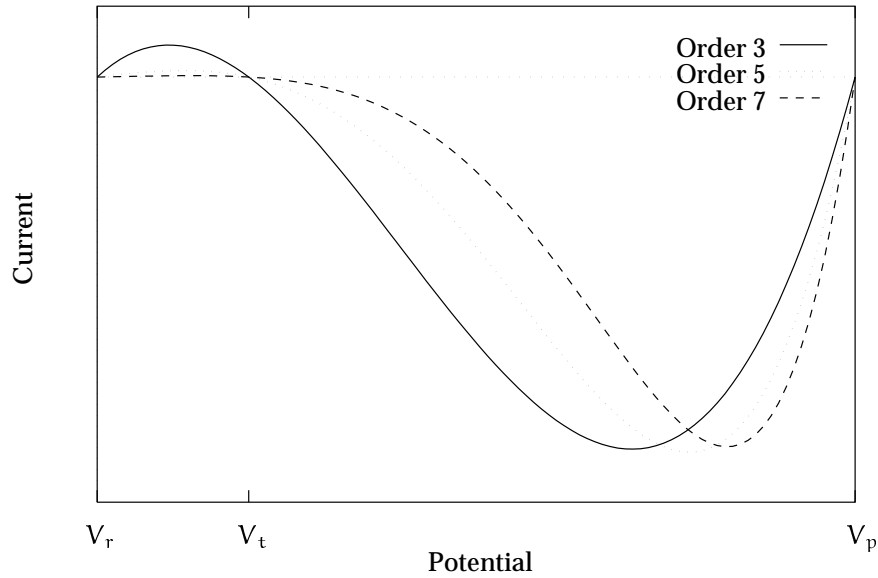


FIGURE 4.33: Form of the polynomial models. The higher order models are scaled to give approximately the same negative peak current as the cubic model.

membrane V_r , the threshold potential V_t , and the peak or plateau potential V_p . Without loss of generality, we can rescale all potentials to be with respect to the resting potential, in effect shifting the curve so that the resting potential is at zero millivolts. The simplest and most common polynomial model is an order three (cubic) equation of the form

$$I_{\text{ion}(O_3)} = \bar{g}_m V_m \left(1 - \frac{V_m}{V_t}\right) \left(1 - \frac{V_m}{V_p}\right) \quad (4.105)$$

where \bar{g}_m has dimensions of conductance ($\text{mS} \cdot \text{cm}^{-2}$), and is the slope of the cubic at the origin, but also scales the entire function.

The cubic model can be extended to use higher order functions, in particular functions of order five or seven. The formulation of these models is

$$I_{\text{ion}(O_5)} = \bar{g}_m V_m \left(1 - \left(\frac{V_m}{V_t}\right)^2\right) \left(1 - \left(\frac{V_m}{V_p}\right)^2\right) \quad (4.106)$$

and

$$I_{\text{ion}(O_7)} = \bar{g}_m V_m \left(1 - \left(\frac{V_m}{V_t}\right)^3\right) \left(1 - \left(\frac{V_m}{V_p}\right)^3\right) \quad (4.107)$$

which also both have zeros at the same threshold and peak potentials as shown in Figure 4.33.

A piecewise-linear approximation to this cubic form may also be taken by specifying the derivatives of the function as an angle at the characteristic voltages. Kogan, Karplus, Billett, Pang, Karagueuzian and Khan (1991) describes this in terms of a FitzHugh-Nagumo (FHN) model.

There are two assumptions which are made when transforming a complete model (such as the Beeler-Reuter or Luo-Rudy model) to a simplified form, and these are summarised in Karpoukhin, Kogan and Karplus (1994). The first assumption is that the activation gate variables m and h are changing rapidly enough that they immediately reach their steady state values. This assumption results in a decrease in the maximal rate of depolarisation. The second assumption assumes that there are no time-independent components of the outward current, which results in changes in the early part of the repolarisation phase of the action potential. In their paper, Karpoukhin et al. derive a general form of a simplified model from the Noble model based on the above two assumptions, which reduces the complete model to

$$C_m \frac{dV_m}{dt} = -I_{inw}(V_m) - \left(\frac{Y}{Y_B} \right)^k I_{outw}(V_m) \quad (4.108)$$

$$\tau_Y(V_m) = Y_\infty(V_m) - Y$$

where I_{inw} is an inward current corresponding to Equation (4.26) and I_{outw} is an outward current corresponding to Equations (4.27) and (4.28). Y is the generalised recovery variable, and the parameters Y_B and k control the APD and the shape of the action potential during repolarisation. The authors then consider the following models in terms of this general equation, from which each can be derived.

4.2.2 FitzHugh-Nagumo Model

One of the simplest activation models that incorporates a recovery process was developed several decades ago by FitzHugh(1961) in the United States, Nagumo in Japan, and Bonhoeffer in Germany, and has become known as the FHN model (Winfree 1990a). This extends the cubic model described above with the addition of a recovery variable.

The FHN model has been written in a number of different forms (Winfree 1990a; Winfree 1991; Rogers and McCulloch 1994a). For this model, the transmembrane

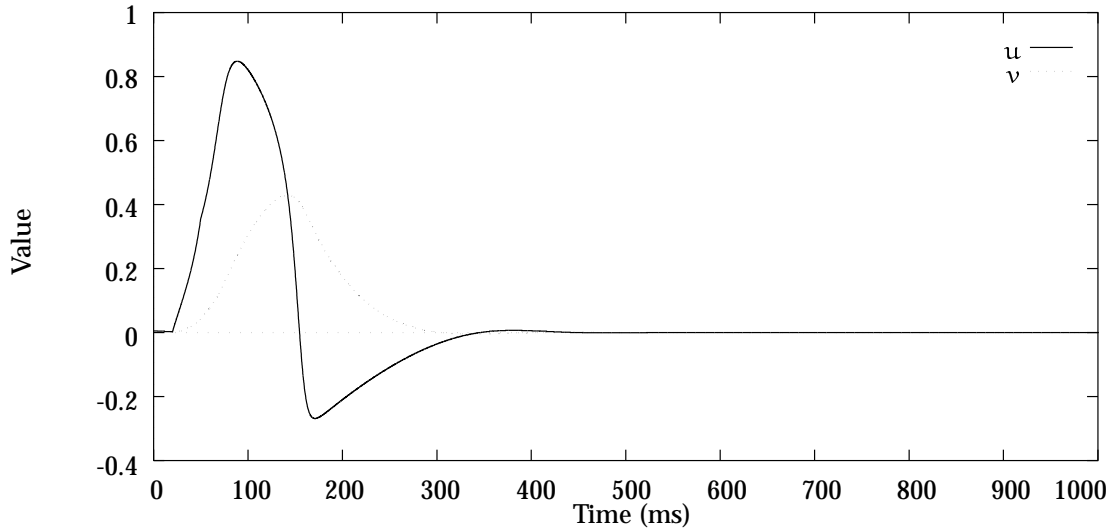


FIGURE 4.34: Action potential generated by the FitzHugh-Nagumo model and shape of the recovery variable time course.

potential is often normalised so that it lies between zero and one using the relation

$$u = \frac{V_m - V_{rest}}{V_{plateau} - V_{rest}} \quad (4.109)$$

where the resting and plateau potentials are as in the cubic ionic equation definition above and u is the normalised potential. The most useful form of the FHN model for application to the bidomain equation is given by Keener (1988) in which he defines the ionic current as

$$I_{ion(FHN)} = c_1 u(u - \alpha)(1 - u) - c_2 v \quad (4.110)$$

where c_1 and c_2 are the excitation rate and excitation decay constants respectively. The activation portion is again a cubic with zeros at 0, α and 1. α is the activation threshold value and lies between 0 and $\frac{1}{2}$, with typical values of between 0.1 and 0.15. The recovery variable v is updated by the equation

$$\frac{dv}{dt} = b(u - dv) \quad (4.111)$$

where b and d are the recovery rate and recovery decay constants respectively. The resulting form of the action potential and the recovery variable is shown in Figure 4.34.

Rogers and McCulloch (1994a) have proposed an extension to the standard FHN

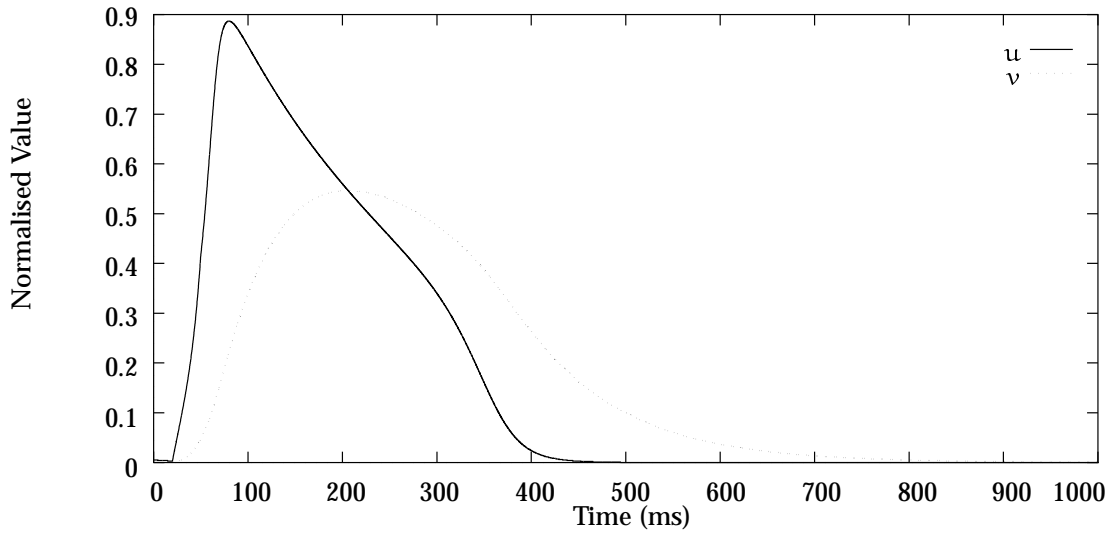


FIGURE 4.35: Action potential generated by the FitzHugh-Nagumo model with Rogers and McCulloch (1994a) extensions. The recovery variable is also shown.

model in which they rewrite the ionic current as

$$I_{\text{ion(FHNR)}} = c_1 u(u - \alpha)(1 - u) - c_2 uv \quad (4.112)$$

The rationale for this change is to remove the undershoot of the transmembrane potential at the end of the action potential as is shown in the graph generated from this equation in Figure 4.35.

Aliev and Panfilov (1996) have further updated this form of the FHN equation by modelling the change of the recovery variable as

$$\begin{aligned} \frac{dv}{dt} &= \epsilon(u, v)(-v - ku(u - a - 1)) \\ \epsilon(u, v) &= \epsilon_0 + \mu_1 \frac{v}{u + \mu_2} \end{aligned} \quad (4.113)$$

where ϵ_0 , μ_1 , μ_2 and k are constants. The rationale for this was to provide a more realistic restitution period and allow for reentrant phenomena.

Other modifications are made to the model by Kogan et al. (1991) in an attempt to modify the restitution curve of the model so that the time course of recovery is slowed down and the model exhibits some degree of APD shortening for successive stimuli.

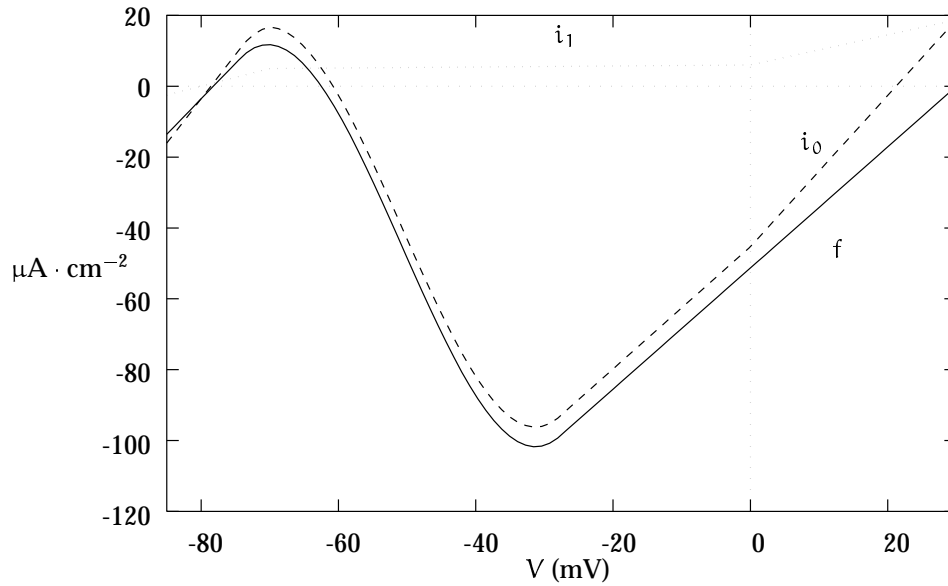


FIGURE 4.36: Form of the functions i_0 and i_1 in the Van Capelle-Durrer model.

4.2.3 Van Capelle-Durrer Model

The van Capelle-Durrer (VCD) model is another simplified model which was developed independently from the FHN model, yet also follows the same generalised formula.

Original model

The basis for the VCD model was proposed by van Capelle and Durrer (1980) as a simple model that displays some of the crucial features of propagation required for the study of focal tachycardias and circus movement tachycardias. It uses only two variables, the transmembrane potential V_m and an excitability parameter Y . From their equations we can write the ionic current as

$$I_{\text{ion(VCD)}} = -Yi_1 - (1 - Y)i_0 \quad (4.114)$$

Y is updated according to

$$\frac{dY}{dt} = \frac{1}{\tau}(Y_{ss} - Y) \quad (4.115)$$

where T is the time constant of the activation/inactivation process. The other functions Y_{ss} , i_0 and i_1 are given by

$$\begin{aligned}
 Y_{ss} &= \begin{cases} 0 & \text{if } V_m < -80 \text{ mV} \\ 1 & \text{if } V_m > -60 \text{ mV} \\ (V_m + 80)/20 & \text{otherwise} \end{cases} \\
 i_1 &= \begin{cases} 5 + 0.5(V_m + 70) & \text{if } V_m < -70 \text{ mV} \\ 6 + 0.425V & \text{if } V_m > 0 \text{ mV} \\ 5 + (V_m + 70)/70 & \text{otherwise} \end{cases} \\
 i_0 &= f + i_1 \\
 f &= \begin{cases} 7.84 + 2(V_m + 74.3) & \text{if } V_m < -74.3 \text{ mV} \\ -98.84 + 1.71(V_m + 27.8) & \text{if } V_m > -27.8 \text{ mV} \\ a_f V_m^3 + b_f V_m^2 + c_f V_m + d_f & \text{otherwise} \end{cases}
 \end{aligned} \tag{4.116}$$

$$\begin{aligned}
 \text{where} \quad a_f &= 3.837854 \times 10^{-3} \\
 b_f &= 0.584649 \\
 c_f &= 25.32834 \\
 d_f &= 235.6256
 \end{aligned}$$

For a normal activation the action potential and time course of Y take the form shown in Figure 4.37.

Modifications to the original model

Modifications to the VCD model have been made by Garfinkel (1994) which aim to make the model more realistic. In particular, it increases the value of \dot{V}_{max} to be more in line with observed values, and it provides an alternative set of parameters which change the APD slightly in order to mimic an ischemic condition. In order to achieve this, they make the following changes:

1. Change C to a more realistic one-tenth of its original value.
2. Change f to $f^* = Kf$ where $K = 4$ (this increases \dot{V}_{max}).

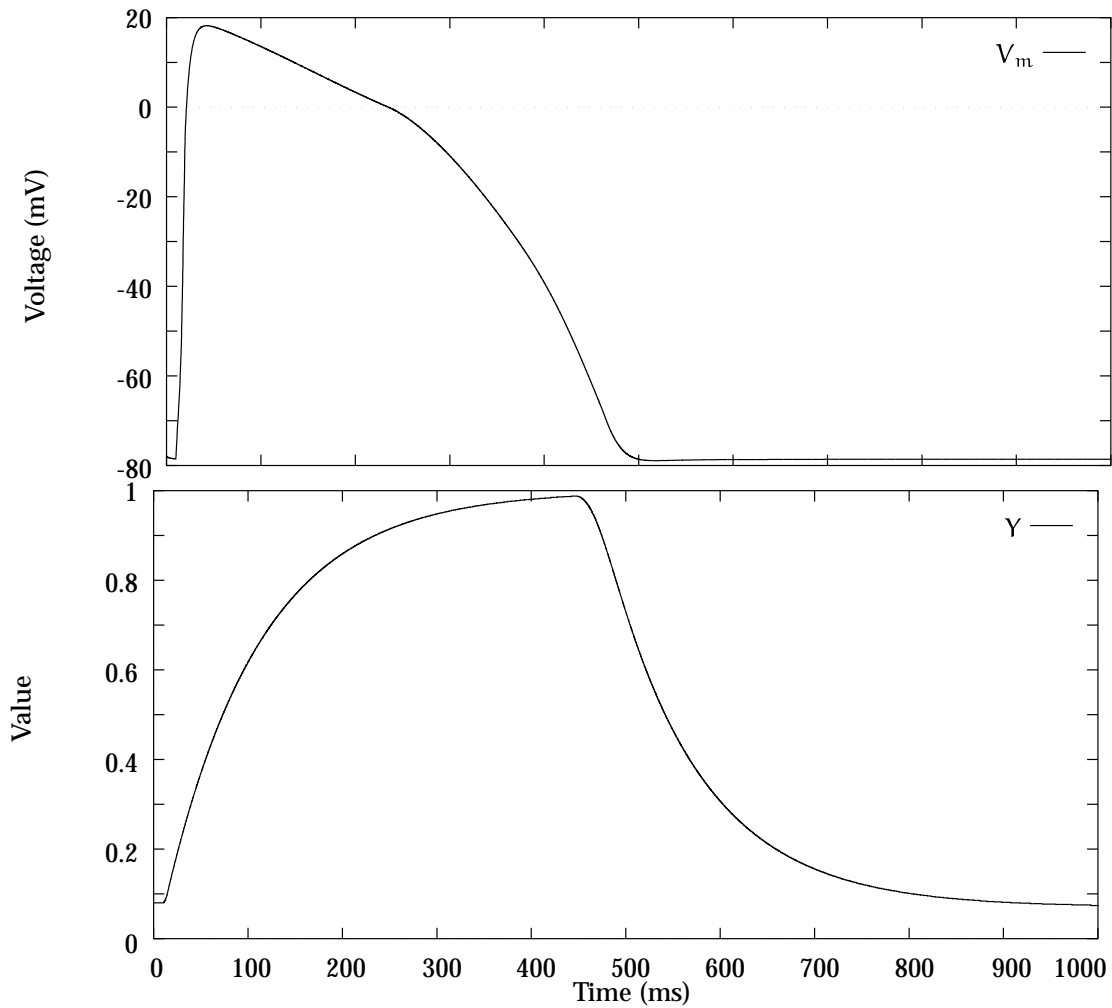


FIGURE 4.37: Form of the action potential and recovery variable as generated by the VCD model.

3. Change T to T^* where

$$T^* = \begin{cases} T_1 & \text{if } \dot{Y} \geq 0 \\ T_2 & \text{if } Y > Y_{lim} \\ T_3 & \text{otherwise} \end{cases}$$

which changes the APD and gives restitution to the action potential. Y_{lim} is given as 0.85.

4. Change i_1 to

$$i_1^* = \begin{cases} i_1 & \text{if } \dot{V} > 0 \\ (APDC)i_1 & \text{if } \dot{V} < 0 \end{cases}$$

APD	112 ms	209 ms
T_1	0.33	0.5
T_2	0.066	0.1
T_3	3.31	3.0
APDC	2	1

TABLE 4.6: Parameter constants for normal tissue (APD = 209 ms) and ischemic tissue (APD = 112 ms)

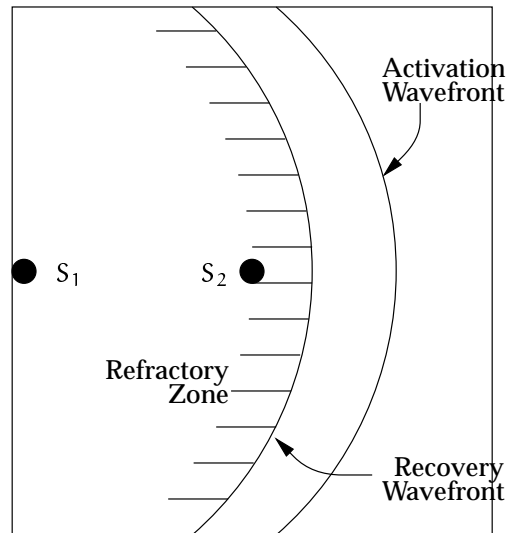


FIGURE 4.38: “ S_1 - S_2 ” stimulus protocol as defined by Garfinkel (1994).

which alters the APD under ischemic conditions.

Values are given in Table 4.6 for a normal APD of 209 ms and an “ischemic” condition of 112 ms. With these modifications to the VCD model and using the parameter values given, spiral waves can be induced for the “ischemic” case, but not for the values given for “normal” tissue. Multiple waves can be created with multiple stimuli, but even the “ischemic” condition does not lead to a severely fractionated state with many small spirals.

They give an “ S_1 - S_2 ” stimulus protocol which is similar to an experimental protocol in order to produce spiral waves. S_1 is a single short stimulus as shown in Figure 4.38 which produces a single wave. S_2 is another single stimulus of much greater current, and is delivered in the refractory zone behind the first wave. Timing and placement

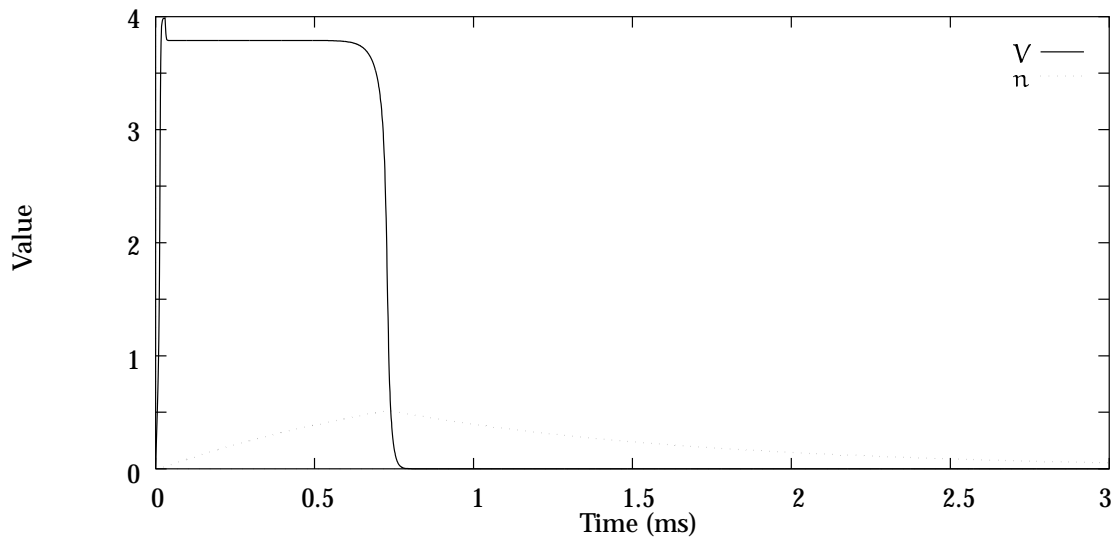


FIGURE 4.39: Characteristic action potential form generated by the Karma model for small C_m and large M .

of this stimulus is critical, and this produces a pair of spiral waves in ischemic tissue only. Further stimuli in similar positions at the back of these spirals produce additional spirals.

4.2.4 Karma Model

The model proposed by Karma (1993) is a simplification of the original Noble model which has, according to Karpoukhin et al. (1994), three essential properties of the Noble model that are not in the original FHN model:

1. The maximal change in transmembrane potential ($\frac{dV_m}{dt}$) is insensitive to the change of the slow gate variable n when repeatedly excited.
2. The fast repolarisation period is much longer than the fast depolarisation period.
3. When repeatedly excited, there is an alternans in the APD.

The model contains two variables E which is a scaled potential, and the recovery variable n , where the ionic current is given as

$$I_{\text{ion}} = -V_m + \left[A - \left(\frac{n}{n_B} \right)^M \right] [1 - \tanh(V_m - 3)] \frac{V_m^2}{2} \quad (4.117)$$

and the change in recovery variable n is given by

$$\frac{\partial n}{\partial t} = H(V_m - 1) - n \quad (4.118)$$

where $H(x)$ is the standard Heaviside step function, and $A = 1.5415$, M and n_B are constants. M controls the wavefront sensitivity, and in the limit, where $C_m \ll 1$ and $M \gg 1$, the front velocity is independent of n and approaches a step function. The parameter n_B controls the APD of an isolated pulse which generally increases with n_B . Typical values for these parameters are $M = 30$ and $n_B = 0.507$. With these parameters, a typical action potential is shown in Figure 4.39 together with the shape of the recovery variable.

Chapter 5

The Collocation Model

Cardiac activation models based on the bidomain framework as derived in Chapter 3 are described mathematically by a set of coupled partial differential equations and require a time-stepping integration technique which updates the values of state variables at all points throughout the solution domain at each time step. There are several such techniques which have been developed for solving general sets of partial differential equations, but each has some disadvantages for this particular problem. These techniques are called *discretisation* techniques because they break the global problem down into a number of smaller problems by discretising (partitioning or subdividing) the solution domain into a number of smaller (still coupled) regions and formulating the equations within each region. Because of this process, the continuous partial differential equations are not solved exactly, and the behaviour of the solution may be somewhat different depending on whether the solution is calculated in a continuous or discrete sense (Keener 1987; Keener 1988). The other issue is that a continuous differential equation may not be the best model of propagation because it does not model the discontinuous cellular structure of cardiac muscle, and it may be necessary to develop a discontinuous partial differential equation (Plonsey and Barr 1987) in order to model the cell-to-cell propagation delays more accurately. However, recent papers by Trayanova and Pilkington (1993) have shown that, for a field stimulation, the effects caused by including a model of cell-to-cell coupling is negligible in terms of the overall activation solution, and a continuum model which does not specifically account for individual cells, though incorporates the junctional resistance in the local

conductivity tensor, is a reasonable assumption.

Some of the features of cardiac propagation, and especially of reentrant behaviour, are different to those observed in a continuous excitable media such as the Belousov-Zhabotinsky chemical reagent (Agladze et al. 1994). This gives sufficient justification for using a discretisation technique, though care must be taken not to include additional numerical artifacts in the solution process.

5.1 Existing Solution Techniques

There are three main numerical techniques which are used to integrate a set of coupled differential equations over a defined geometry – the finite difference method, the finite element method and the boundary element method. Each technique has advantages and disadvantages for the cardiac activation problem, and the first two have been fairly widely used. The boundary element method is not suitable for the activation problem for reasons explained later. This section outlines some of the previous use of the other two methods, and shows that, because of problems which they have in different areas, neither of them are ideally suited to the cardiac electrical problem. A new technique is then proposed which overcomes the deficiencies of previous techniques.

5.1.1 The finite difference method

The *finite difference method* is a well established discretisation technique for solving general classes of partial differential equations on a regular grid of solution points, and has been applied to the cardiac activation equations in many studies. The finite difference method constructs a grid of solution points over the domain of interest as shown in a two-dimensional example in Figure 5.1. In this example an irregular domain is covered with a regular grid of solution points at which the activation equations will be satisfied exactly. In a similar way the time-dependent component is discretised into a number of *time steps* and at each time step the equations are incrementally solved. The domain boundary is approximated on the

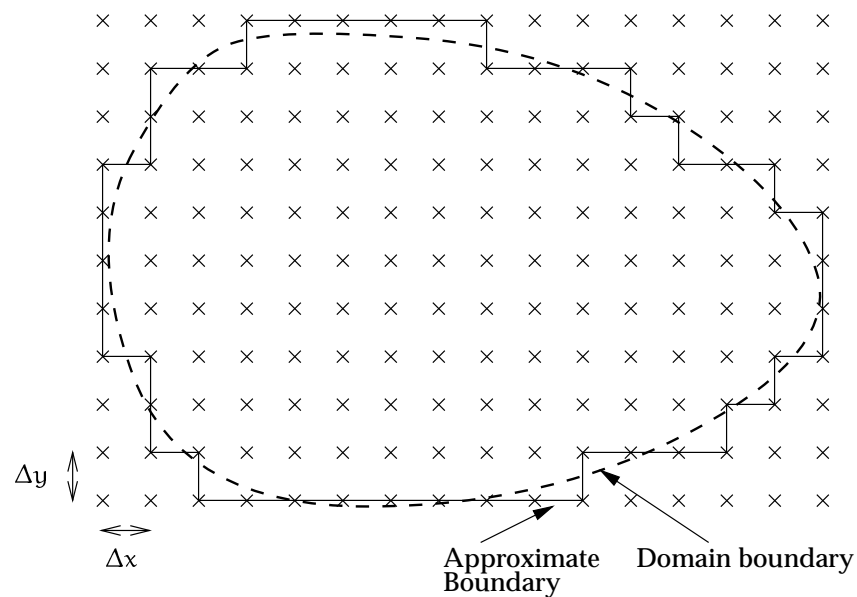


FIGURE 5.1: Two-dimensional finite difference grid defined to cover an irregular domain. Note that solution points do not lie on the true boundaries, but an approximate rectilinear geometry is defined. Some solution points are not contained within the region of interest.

grid of solution points, often by determining which points are within the domain and taking the external boundary of those points. The finite difference formulation approximates each partial derivative by a *finite difference* formed from a truncated Taylor's series expansion of the variable in terms of values at neighbouring points. This approximation is accurate to within some truncation error dependent upon the spacing between solution points Δx and the time step Δt . Solution techniques based upon the finite difference method are the easiest to construct and solve, and consequently the finite difference method is the most frequently used technique for solving cardiac activation equations.

There are two related forms of the finite difference method which determine the way in which the differential equations are integrated. The most common of these is called *explicit finite differences* in which a forward difference formula is used such that the value of a variable at a given time is determined explicitly from the values of that point and neighbouring points at the previous time step, and each solution point may be updated independent of all other points. This method has the advantage that it is computationally simple and fast but it requires a very small time increment in order for the solution to remain stable and accurate. Various Euler and Runge-

Kutta methods and other predictor-corrector techniques are used to perform the time integration. Keener (1988) defines one- and two-dimensional explicit finite difference schemes using a FitzHugh-Nagumo activation model to investigate the mechanism for the formation of reentrant waves of excitation in anisotropic media. Papers by Kogan *et al.* (1991; 1992) illustrate the solution of their modified FHN model over a two-dimensional 128×128 finite difference grid on a massively parallel computer using an explicit finite difference scheme with a Runge-Kutta-2 integration in order to look at restitution and unidirectional block due to narrow pathways. In order to develop a stable solution they required an integration time step size of 0.025 time units, where each time unit corresponded to 2 ms. One such model which solved for 500 time units required about 6.5 minutes of computing time on a Connection Machine 2¹ using 16,384 processing elements. Courtemanche and Winfree (1991) construct an Euler finite difference technique which is used on a 400×400 point grid with a grid spacing of $\Delta x = 0.25$ mm and a time step of $\Delta t = 0.025$ ms. The more advanced ionic model of Beeler and Reuter was used, and the solutions were performed on a CRAY-YMP supercomputer², with 400 ms of simulated activity requiring 30 minutes of computational time. Panfilov and Holden (1993) defines a two-dimensional technique which solves the van Capelle-Durrer equations using an explicit Euler scheme on grids of up to 100×100 points. A three-dimensional simulation of a scroll ring was rewritten in the cylindrical polar coordinate system, but due to the cylindrical symmetry of this particular investigation, the problem becomes a two-dimensional problem with a modified Laplacian operator.

The alternative finite difference technique is called *implicit finite differences* in which a central difference formula is used and the resulting algebraic equations are implicitly coupled at the new time step. This means that the new value of a variable at one point is additionally dependent on the new values at neighbouring points, resulting in a dependent set of linear equations. Using an appropriate solution technique results in a solution which is stable for any time step Δt , and therefore larger time steps may be taken during periods in which the values of the variables are not changing rapidly. By incorporating a scheme for *temporal adaption* this can be taken advantage of, and the size of each time step can be computed so that the most accurate and efficient solution is obtained. The disadvantage with an implicit

¹Thinking Machines Corp.

²Cray Research Inc.

METHOD	T_S	N	T_{CPU}	V_{peak}	θ
EM	6	3,001	1,359	14.20	0.535
EM-DTAR	6	3,001	558	13.60	0.542
IM	6	115	1,021	13.89	0.543
EB	6	3,001	1,762	13.84	0.542
IB	6	115	3,840	13.89	0.543
EM	500	250,000	238,520	16.65	0.506
SM	500	2,546	4,848	16.60	0.506
IM	500	179	4,502	16.26	0.504

TABLE 5.1: Comparison of finite difference formulations (adapted from Pollard et al. (1993, Table 2)). T_S = simulation time (ms). N = number of iterations. T_{CPU} = total CPU time (s). V_{peak} = peak transmembrane potential (mV). θ = conduction velocity (ms^{-1}). Methods: “E” – Explicit, “S” – Semi-implicit, “I” – Implicit, “M” – Monodomain, “B” – Bidomain.

formulation is that the solution matrices are large (though banded) and require more computational time to construct and solve.

Pollard et al. (1993) compare explicit and implicit solution techniques, together with a *semi-implicit* method which alternates explicit and implicit expressions in the x and y directions at each time step in order to improve the stability of the explicit method without the more considerable overhead of a fully implicit scheme. They constructed an 80×80 point grid with isotropic conduction and used the ionic current model defined by the Ebihara-Johnson equations to describe activation and the Beeler-Reuter equations to describe the repolarisation. An IBM RS/6000³ workstation was used in the comparison, and both monodomain and bidomain activation models were simulated for 6 ms using the Ebihara-Johnson ionic current model, and monodomain repolarisation defined by a combined Ebihara-Johnson/Beeler-Reuter membrane model for a time period of 500 ms. For the explicit technique, a fixed time step of $2 \mu s$ was used in order to maintain stability, but the time step was allowed to vary for the implicit and semi-implicit formulations. Their results (summarised in Table 5.1) show that there is little difference in the solution values (as measured by the peak transmembrane potential and the computed conduction velocity) between

³International Business Machines Corp.

the various finite difference implementations. Substantial differences do exist in the solution times, where the explicit method is similar or faster for a short simulation of activation only, but requires much more computing time for a longer simulation of activation and repolarisation. The implicit method takes advantage of the fact that the solution variables are changing slowly during the repolarisation phase and therefore a larger time step can be used. An explicit method can be speeded up by using a *spatially adaptive* technique to restrict computation to points close to the activation wavefront. This is shown in the above simulation results by the line “EM-DTAR”, where DTAR is an acronym for Dynamic Tracking of the Active Region. A similar method is described later in Section 5.3.4.

5.1.2 The finite element method

An alternative solution method for solving a system of differential equations is the *finite element method* which has been widely used in engineering problems involving a complex geometry. However, the evaluation of element integrals for the Galerkin method on a structured mesh is a relatively much more expensive process and probably explains why the finite element method has found little application yet in modelling myocardial activation. The finite element method (which is discussed in more detail later in this chapter) discretises the region into small areas or volumes (rather than the points used in finite differences) and approximates the solution from nodal values over these *elements* using interpolation functions or *basis functions*. Due to this interpolation between nodes, a finite element mesh can accurately represent the nature of a complex geometry by defining nodes on the boundary of the region, and using automatic mesh generation to create the internal nodes. The finite element method has not been used in modelling cardiac activation to any large extent, mainly due to the difficulties in constructing such a formulation, and the computational expense in evaluating the integral equations and assembling and solving the large matrices generated by the Galerkin finite element technique. Smith and Cohen (1984) claims to use a low order finite element model but in fact their method resembles a cellular automata type model with no evaluation of the differential equations. Sepulveda, Roth and Wikswo (1989) use a finite element mesh consisting of almost 1000 eight-noded quadrilateral and six-noded triangular elements meshed from almost 3000 nodes, and solve the anisotropic bidomain equations over a two-dimensional quarter circle. Their results show excellent agreement with analytic

solutions with less than a 1% error at all nodes. Unfortunately they give no indication of the computational effort required for the solution. A review paper by Miller and Henriquez (1990) discusses the general use of finite element techniques in the analysis of different forms of bioelectric phenomena, with mention made of cardiac activation models to that date, and show that finite elements have not been used significantly in this field. They have been quite successful in solving other bioelectric problems, particularly in their ability to accurately represent the geometry, though most models use only low order linear or quadratic basis functions for interpolation.

A more comprehensive finite element based formulation is described by Rogers and McCulloch (1994a) which constructs a high order finite element representation of the geometry. In this model the finite element equations are generated by using a collocation method which satisfies the equations exactly at a set of points, whereas the traditional Galerkin method solves the equations by minimising an integrated error. This results in a faster assembly of the solution matrices which are in turn much sparser than Galerkin generated matrices. Given an optimum placing of the nodal points, the collocation method produces results which are comparable with the Galerkin method. A problem with the collocation approach is that fewer equations are generated than are required to satisfy the number of degrees-of-freedom of the problem, and complex boundary conditions are difficult to incorporate. These problems have been overcome by using a Galerkin approach to generate additional equations to satisfy the boundary degrees-of-freedom. Such a method is easily applied to two- and three-dimensional problems. Results presented so far have shown only application to simple two-dimensional meshes (Rogers and McCulloch 1994a; 1994b). The method was implemented on a DECstation 5000/200 workstation⁴ and a Cray Y-MP 8/864 supercomputer⁵ with a transparent socket link between the two machines. For a 10×10 element mesh using a modified FitzHugh-Nagumo model of the membrane kinetics with a model of the anisotropic fibre direction fields and conductivities, assembly of the finite element matrices took approximately 2 seconds on the workstation, factorising the matrices required 5.6 seconds and integration of the equations for a sufficient time to allow a wave to propagate through the mesh required 38 seconds. On the Cray supercomputer, the factorisation and integration times reduced to 1.2 seconds and 2.6 seconds,

⁴Digital Equipment Corp.

⁵Cray Research Inc.

respectively.

5.1.3 The need for a new technique

Other traditional solution techniques based on integral equations such as the *boundary element method* are not suitable to use for this problem due to the non-uniform anisotropy of the tissue and the inhomogeneity of the electrical structures, which the boundary element method is unable to deal with. Both finite difference and finite element methods are shown to work, though there are advantages and disadvantages with each. A finite difference formulation of the differential equations is simple to construct, and the solution of each iteration tends to be very fast. The method defines a grid of solution points over a region, and holds parameters and unknowns at each of these points. In general, a grid with even spacings between solution points is required, which means that it is difficult to account for the complexity of the geometry of the solution domain. It also makes it difficult, if not impossible, to obtain a solution for a deforming domain, such as will occur in whole heart activation models combined with models of the mechanical behaviour. Finite element models are conceptually more difficult to construct than finite difference models, because they solve for an unknown potential over an area or volume rather than simply at a point. This can also be a disadvantage for cardiac problems as the steep slope of the action potential means that there can be a sharp discontinuity in potential at a point, where the finite element method would try to smooth this out. Additionally, when using a Galerkin finite element technique, the effect of a change at one point in the mesh is instantly applied to all other points in the mesh given an implicit integration procedure (for an explicit integration scheme the effect is propagated by one node every time step). In problems such as mechanical deformation this is what happens physically, but in the cardiac activation process a change in potential has only a local effect. The collocation finite element approach overcomes these two difficulties. Finite element models have the advantage that they can easily model a complex geometry, and therefore could be applied to a deforming region, and the model by Rogers and McCulloch (1994a) could support this although they have not chosen to do so. This would require a re-assembly and factorisation of the matrices for each change in the geometry, which may be computationally significant.

There are several distinctive features of the cardiac activation problem which need to be adequately addressed in any model.

- *The heart has a complex shape, and measurements of the location of ventricular wall boundaries (especially the endocardial surfaces) is difficult* — Accurate measurements must be made of the cardiac geometry and the location of important structures, and incorporated into the model. The mathematical description of the geometry should be fitted as accurately as possible to the measured data.
- *Ventricular tissue has a branching interconnected network of fibres and sheets which continually vary in direction and branching ratios throughout the wall* — The orientation of the ventricular microstructural axes must be measured at a large number of points throughout the heart and an accurate model fitted to this data. It will be used in the activation model to compute a orthogonal description of the local conductivity at each point.
- *During the activation and repolarisation process the tissue may deform, changing the geometry and the orientation of the microstructure* — The model needs to be able to cope with a deforming geometry governed by the equations of large deformation elasticity theory so that state variables are tracked at material points in the heart rather than at fixed points in space.
- *The nature of ionic movements within the cell and the cell membrane is still only partially understood, with various simplified and biophysically based models of ionic behaviour providing different levels of accuracy* — An appropriate ionic current model for a given problem should be able to be used according to the accuracy required and the computational time available, and the solution process not tied to one particular model but able to incorporate new models as they are developed.
- *Cellular activation has a very small space constant, potentially smaller than cellular dimensions, and a very small time constant due to the fast rate constants of the gating variables in the activation currents* — In order to be computationally tractable, a model needs to incorporate available space-averaging and time-averaging techniques to reduce the size of the problem.

Because of these constraints, a new method for solving partial differential equations

has been developed which is specifically tailored towards addressing the issues involved in the cardiac activation problem. This method is called a *Collocation-Derived Finite Difference method* because it solves the transmembrane equation evaluated at distinct points, and draws on strengths of both the finite difference and finite element techniques described above. The finite element method is used to efficiently describe the cardiac geometry and microstructure, and is the most suitable method for describing these quantities for two reasons. Firstly, a finite element mesh is easy to fit to experimental measurements of geometry, and provide accurate interpolation of microstructural information. Secondly, models of mechanical deformation most often use the finite element method for solving the resulting system of equations.

In order to provide a local behaviour with a small space constant the activation equations are not solved using the finite element method, but a non-uniform regular finite difference grid is defined from the finite element mesh at *material points* and a collocation method resembling explicit finite differences is used to solve the monodomain equations. This has the advantage of using a fast finite difference based solution scheme which does not smooth out the solution over a volume, yet the grid is defined by the geometry of the problem and will track any geometrical deformation because the solution points remain attached to the same physical material point during deformation. If the second extracellular equation is also to be solved for, then another more appropriate technique is used. The description of cardiac geometry and microstructure comes from the most accurate source (Le Grice 1992), and the ionic current model can be chosen from any of those listed in Chapter 4 according to the features which are required to be modelled.

This method is described in the rest of this chapter by firstly outlining the finite element method, and then detailing how the collocation scheme is imposed on this framework.

5.2 The Finite Element Method

The finite element method was developed as a technique for solving a large range of engineering-related problems for which some mathematical model was defined.

It has found particular application in the field of continuum mechanics, solving problems associated with such things as heat conduction, structural behaviour, elasticity, fluid flow and many other fields. The finite element method works by discretising the domain of the problem into a number of smaller elements and approximating the continuous mathematical model in each of these discrete elements by using a simple interpolation function.

5.2.1 Notation

The description of vector and tensor quantities in this chapter is through the use of index notation and the Einstein summation convention. A good reference on the form and application of index notation is found in Kikuchi (1986). The Einstein summation convention states that where an index appears exactly twice in an equation, then the variables are implicitly summed over a range defined either by the context of the equation or by explicitly stating it. Most often the range is defined by three-dimensional geometry, and thus the index steps from one to three. Where summation over a range is not required for a pair of indices, parentheses “()” are used surrounding these indices. There is also no summation if an index is repeated more than twice, or if two or more pairs of repeated indices are present in each multiplication. In the following examples, the index notation is on the left and the expanded form is on the right. In this equation

$$\begin{aligned} y_i x^i &= \sum_{i=1,3} y_i x^i \\ &= y_1 x^1 + y_2 x^2 + y_3 x^3 \end{aligned}$$

the index i is implicitly summed over for the values of 1, 2 and 3. Similarly,

$$\begin{aligned} x_{k(l)}^\alpha y_{j(l)}^k &= \sum_{k=1,3} x_{k(l)}^\alpha y_{j(l)}^k \quad (\text{no implicit summation}) \\ &= x_{1l}^\alpha y_{jl}^1 + x_{2l}^\alpha y_{jl}^2 + x_{3l}^\alpha y_{jl}^3 \quad (\text{no implicit summation}) \end{aligned}$$

where the index k is summed over, but neither of the non-repeated indices α and j nor the parenthesised index l are summed over. Arabic letters are generally used for indices related to a reference coordinate system, and Greek letters are used for indices that refer to a local material coordinate system.

5.2.2 Basis functions

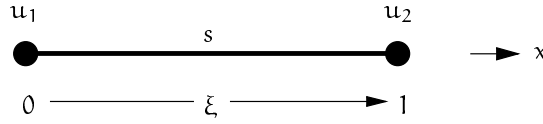
Given some domain Ω over which some set of equations is to be solved, the finite element method approximates these continuous functions by discretising the domain. Let Ω be divided into a number of elements, where Ω_e is a typical element. The element is constructed by joining a set of points, called the *nodal points* of the element, and the number and position of these *nodes* depends on the type of element used. The sequence of nodes in an element define the connectivity.

In order to approximate the function over an element Ω_e , the functions are interpolated between the nodes. Special interpolation functions called *basis functions* are used to interpolate some function or field variable over Ω_e from values specified at the nodes of the element. The field variable or function may be any quantity of interest, most often geometric variables (such as x_i coordinates) or solution variables (such as potential or temperature or $[Ca]_i$). Basis functions also have the alternate names *interpolation functions* or *shape functions*.

Basis functions can be functions of any form, but are specially chosen with certain desirable properties. In this thesis, all basis functions are defined by sets of polynomial functions, distinguished only by the order of the polynomials. Low order basis functions are used where there is little variation in a quantity between nodes, and higher order functions are used when the interpolation is required to be more accurate, or where there are large spatial gradients in the quantities of interest. Further explanation can be found in Oden (1972).

Linear Lagrange basis functions

The simplest basis function is a *linear Lagrange* basis function which provides a linear interpolation between nodes. Consider the one-dimensional element with arc-length s shown in Figure 5.2 which has some scalar quantity u defined on it, such that $u = u_1$ at node 1 at the left hand end and $u = u_2$ at node 2. A normalised measure of distance along the element is introduced, called ξ , which is defined such that $\xi = 0$ at node 1 and $\xi = 1$ at node 2. The mapping between the global x coordinate and the local ξ coordinate is determined by the arc-length s of each element, and the

FIGURE 5.2: A one-dimensional element with nodal quantities u_1 and u_2 .

mapping is defined by

$$\frac{dx}{d\xi} = s \quad (5.1)$$

and therefore

$$\xi = \frac{d\xi}{dx}x \quad (5.2)$$

$$x = \frac{dx}{d\xi}\xi \quad (5.3)$$

where $\frac{d\xi}{dx} = \frac{1}{s}$ is the inverse of $\frac{dx}{d\xi}$. A linear interpolation $u(\xi)$ of u along the element is defined as

$$u(\xi) = \Psi_1 u_1 + \Psi_2 u_2 \quad (5.4)$$

with basis functions (or *weighting functions*) Ψ_1 and Ψ_2 . These weighting functions are defined so that $u(\xi)$ is satisfied exactly at the two end nodes, i.e. $u(0) = u_1$ and $u(1) = u_2$, and therefore $\Psi_1 = 1$ at node 1 and 0 at node 0, and vice versa for Ψ_2 .

$$\Psi_1 = 1 - \xi, \quad \frac{d\Psi_1}{d\xi} = -1 \quad (5.5)$$

$$\Psi_2 = \xi, \quad \frac{d\Psi_2}{d\xi} = 1 \quad (5.6)$$

These weighting functions are the *linear Lagrange basis functions*.

Basis functions for domains of higher order dimensionality may be constructed by taking the tensor product of one-dimensional basis functions. For example, a two-dimensional element has four nodes as shown in Figure 5.3, and therefore a set of four *bilinear* basis functions needs to be constructed where Ψ_n is one at node n and zero at the other three nodes. The interpolation of a variable u is given by

$$u(\xi_1, \xi_2) = \Psi_1(\xi_1, \xi_2)u_1 + \Psi_2(\xi_1, \xi_2)u_2 + \Psi_3(\xi_1, \xi_2)u_3 + \Psi_4(\xi_1, \xi_2)u_4 \quad (5.7)$$

where the four bilinear basis functions are

$$\begin{aligned} \Psi_1(\xi_1, \xi_2) &= (1 - \xi_1)(1 - \xi_2) & \Psi_2(\xi_1, \xi_2) &= \xi_1(1 - \xi_2) \\ \Psi_3(\xi_1, \xi_2) &= (1 - \xi_1)\xi_2 & \Psi_4(\xi_1, \xi_2) &= \xi_1\xi_2 \end{aligned} \quad (5.8)$$

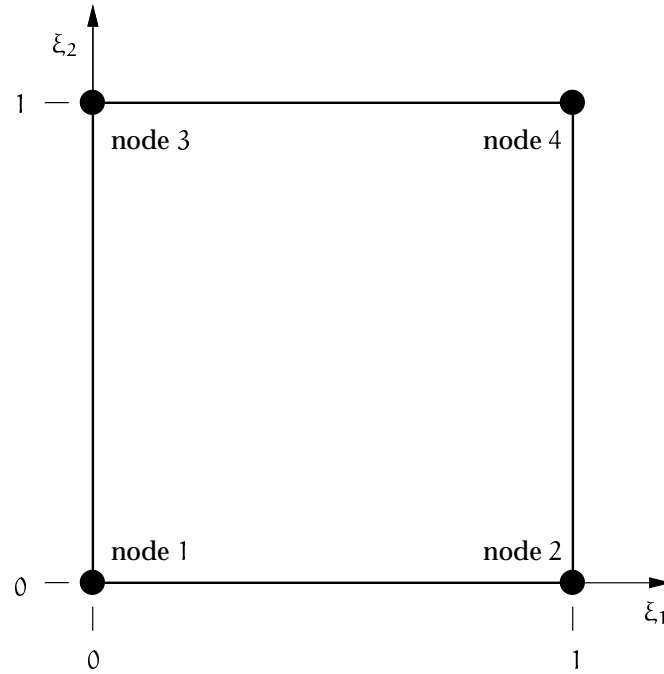


FIGURE 5.3: Bilinear element

Three-dimensional basis functions are defined in the same way. For example a trilinear basis function has 8 nodes with basis functions

$$\begin{aligned}
 \Psi_1(\xi_1, \xi_2, \xi_3) &= (1 - \xi_1)(1 - \xi_2)(1 - \xi_3) & \Psi_2(\xi_1, \xi_2, \xi_3) &= \xi_1(1 - \xi_2)(1 - \xi_3) \\
 \Psi_3(\xi_1, \xi_2, \xi_3) &= (1 - \xi_1)\xi_2(1 - \xi_3) & \Psi_4(\xi_1, \xi_2, \xi_3) &= \xi_1\xi_2(1 - \xi_3) \\
 \Psi_5(\xi_1, \xi_2, \xi_3) &= (1 - \xi_1)(1 - \xi_2)\xi_3 & \Psi_6(\xi_1, \xi_2, \xi_3) &= \xi_1(1 - \xi_2)\xi_3 \\
 \Psi_7(\xi_1, \xi_2, \xi_3) &= (1 - \xi_1)\xi_2\xi_3 & \Psi_8(\xi_1, \xi_2, \xi_3) &= \xi_1\xi_2\xi_3
 \end{aligned}
 \tag{5.9}$$

if the nodes are numbered most quickly in the ξ_1 direction and most slowly in the ξ_3 direction.

If the variable of interest varies more than linearly over the domain, there are several options. One is to subdivide the domain into multiple elements, each which may be of differing lengths, and interpolate linearly within each element. Figure 5.4 shows an example one-dimensional problem where the domain has been subdivided into three elements of unequal length. A solution variable u is defined over the domain, with nodal values as shown in Table 5.2. Element Ω_1 maps global values of u_1 and u_2 onto local values u_1 and u_2 , and then according to Equation (5.4) the linear

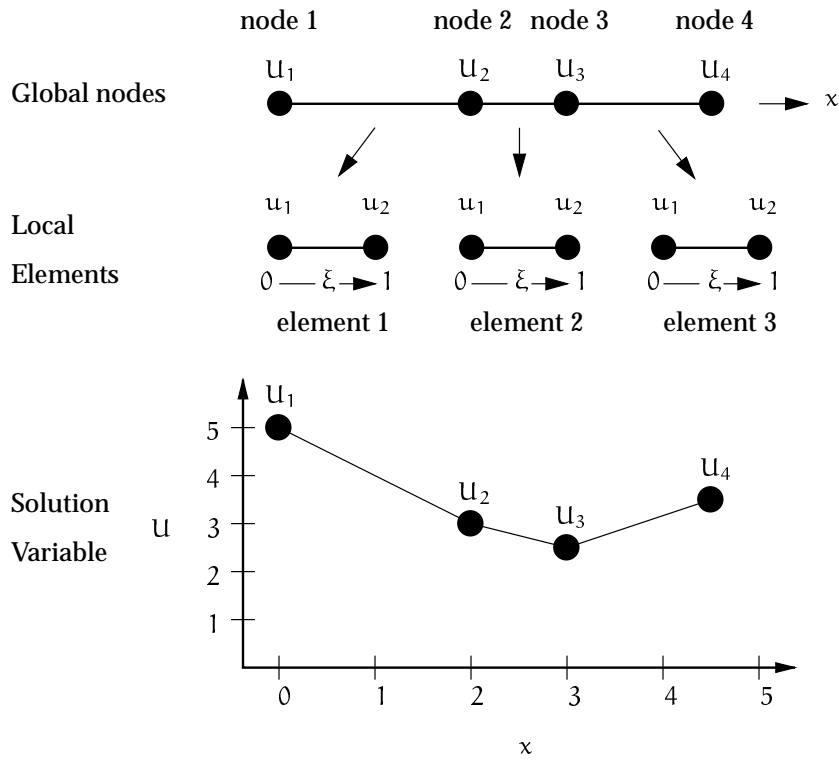


FIGURE 5.4: Three one-dimensional linear elements with linear Lagrange basis functions applied to the solution variable U .

Node	Position (x)	U
1	0	5
2	2	3
3	3	2.5
4	4.5	3.5

TABLE 5.2: Nodal values of the solution variable U .

interpolation of u within the element becomes

$$u(\xi) = 5(1 - \xi) + 3\xi \quad (5.10)$$

and from this we can compute the value of U at any point within element 1 by transforming to the ξ -coordinates using Equations (5.1) and (5.2), where the arc-length of element 1 is $s = 2$. For example, the value of U at $x = 1$ corresponds to the value of $u(\xi = 1/2)$ which, according to Equation (5.10) is

$$\begin{aligned} u(\xi = 0.5) &= 5(1 - 0.5) + 3(0.5) \\ &= 4 \end{aligned} \quad (5.11)$$

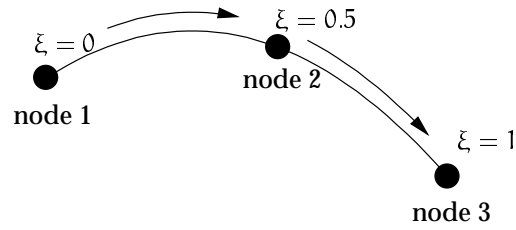


FIGURE 5.5: Quadratic element definition.

as can be seen from the graph at the bottom of Figure 5.4. Similarly, we can construct expressions for each of the other elements, and thus have an interpolation of u at all points in the domain. Note that u is continuous throughout the domain, due to the fact that nodal values are common to neighbouring elements. Continuity of the solution variable is known as C^0 continuity.

In some cases it is sensible to use higher order basis functions rather than linear functions. This reduces the number of elements required, and increases the accuracy of the interpolation, though the equations used are somewhat more complex. There are two other basis functions which have been used in this work. The first are *quadratic Lagrange basis functions*, which are similar to the linear Lagrange functions, and the second are called *cubic Hermite basis functions*, and have a different form with advantages over Lagrange bases.

Quadratic Lagrange basis functions

Higher order Lagrangian bases are constructed by adding more nodes to each element, and applying the same rules as for constructing the linear basis. Therefore, in a *quadratic* basis, an element is constructed as shown in Figure 5.5 with three nodes at $\xi = 0$, $\xi = 0.5$ and $\xi = 1$. There are three corresponding basis functions Ψ_1 , Ψ_2 and Ψ_3 , where Ψ_n is one at node n and zero at the other two nodes. This gives equations of the form

$$\Psi_1 = (1 - \xi)(1 - 2\xi) \quad \frac{d\Psi_1}{d\xi} = 4\xi - 3 \quad (5.12)$$

$$\Psi_2 = 4\xi(1 - \xi) \quad \frac{d\Psi_2}{d\xi} = 4 - 8\xi \quad (5.13)$$

$$\Psi_3 = \xi(2\xi - 1) \quad \frac{d\Psi_3}{d\xi} = 4\xi - 1 \quad (5.14)$$

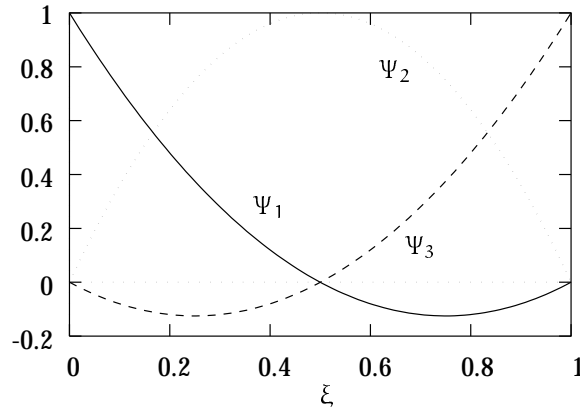


FIGURE 5.6: Quadratic Lagrange basis functions Ψ_1 , Ψ_2 and Ψ_3

which are also graphed in Figure 5.6. The quadratic interpolation of a field variable u over the element is given by

$$u(\xi) = \Psi_1 u_1 + \Psi_2 u_2 + \Psi_3 u_3 = \Psi_n u_n \quad (5.15)$$

which once again has only C^0 continuity between elements.

Two-dimensional *biquadratic* or three-dimensional *triquadratic* basis functions are constructed by taking the tensor product of the one-dimensional basis functions in a similar manner to that shown earlier for linear basis functions. The biquadratic basis functions are given in Equation (5.16), where the nodal positions are defined as in the diagram in Figure 5.16b.

$$\begin{aligned} u(\xi_1, \xi_2) &= \Psi_n u_n \\ &= \Psi_1(\xi_1)\Psi_1(\xi_2)u_1 + \Psi_2(\xi_1)\Psi_1(\xi_2)u_2 \\ &\quad + \Psi_3(\xi_1)\Psi_1(\xi_2)u_3 + \Psi_1(\xi_1)\Psi_2(\xi_2)u_4 \\ &\quad + \Psi_2(\xi_1)\Psi_2(\xi_2)u_5 + \Psi_3(\xi_1)\Psi_2(\xi_2)u_6 \\ &\quad + \Psi_1(\xi_1)\Psi_3(\xi_2)u_7 + \Psi_2(\xi_1)\Psi_3(\xi_2)u_8 \\ &\quad + \Psi_3(\xi_1)\Psi_3(\xi_2)u_9 \end{aligned} \quad (5.16)$$

Higher order Lagrange basis functions may be constructed with increasing numbers of nodes, but this quickly becomes an inefficient way of interpolating over a domain, because all Lagrange functions are only C^0 -continuous (values are continuous, but derivatives are not).

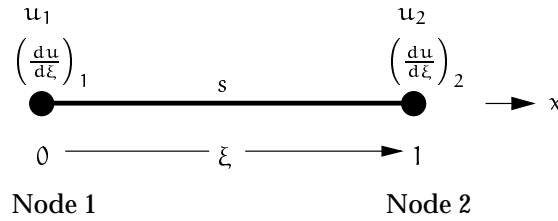


FIGURE 5.7: Cubic one-dimensional element, defining both the value and derivative of the variable at each node.

Cubic Hermite basis functions

A more useful basis function provides not only a continuous interpolation between elements, but also defines continuous derivatives, which is especially useful when defining geometrical surfaces. This C^1 -continuous behaviour is obtained by using *cubic Hermite basis functions* which are a new class of basis functions. Cubic Hermite functions require only two nodes per element, but both the value and derivative of the field variable are specified at each node.

Consider a one-dimensional element Ω_e as in Figure 5.7 which has nodes at $\xi = 0$ and $\xi = 1$. In order to interpolate values of some field variable u over Ω_e using a cubic Hermite basis, four nodal quantities are required. The first two are the values of u at each node as for Lagrangian bases, and are written as u_1 and u_2 . Additionally, the derivative of u with respect to the local element coordinate ξ must be defined at each node, and are denoted by $\left(\frac{du}{d\xi}\right)_1$ and $\left(\frac{du}{d\xi}\right)_2$ at nodes 1 and 2 respectively.

The cubic Hermite interpolation of u within the element is then given using four basis functions

$$u(\xi) = \Psi_1^0 u_1 + \Psi_2^0 u_2 + \Psi_1^1 \left(\frac{du}{d\xi}\right)_1 + \Psi_2^1 \left(\frac{du}{d\xi}\right)_2 \quad (5.17)$$

where Ψ_1^0 is associated with the value of u at node 1, Ψ_2^0 with the value at node 2, Ψ_1^1 with the derivative of u at node 1, and Ψ_2^1 with the derivative at node 2. Thus the superscript refers to the type of basis function, and the subscript refers to the “local” node as before. These basis functions have the following properties: Ψ_n^0 is equal to one at node n and equal to zero at node $1 - n$. $\frac{d\Psi_n^0}{d\xi}$ is zero at both nodes so that it does not weight the derivatives. For the basis multipliers of the derivatives at each node, Ψ_n^1 is zero at both nodes, and $\frac{d\Psi_n^1}{d\xi}$ is one at node n and zero at the other node.

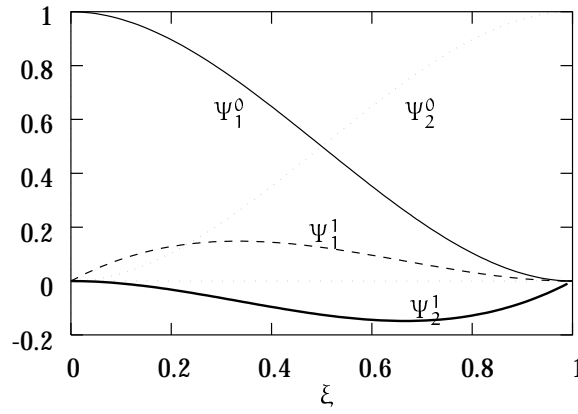


FIGURE 5.8: Cubic Hermite Basis Functions.

This gives rise to the equations given in Equation (5.18) and plotted in Figure 5.8.

$$\Psi_1^0 = 1 - 3\xi^2 + 2\xi^3 \quad \frac{d\Psi_1^0}{d\xi} = -6\xi + 6\xi^2 \quad (5.18)$$

$$\Psi_2^0 = \xi^2(3 - 2\xi) \quad \frac{d\Psi_2^0}{d\xi} = 6\xi - 6\xi^2 \quad (5.19)$$

$$\Psi_1^1 = \xi(\xi - 1)^2 \quad \frac{d\Psi_1^1}{d\xi} = 3\xi^2 - 4\xi + 1 \quad (5.20)$$

$$\Psi_2^1 = \xi^2(\xi - 1) \quad \frac{d\Psi_2^1}{d\xi} = 3\xi^2 - 2\xi \quad (5.21)$$

One difficulty arises when using cubic Hermite basis functions in practice, and this relates to the derivative of the solution at the nodes. If neighbouring elements have different arc lengths, then the value of $\left(\frac{du}{d\xi}\right)_n$ will be different in each element for the same node. It is more useful to define a global nodal derivative with respect to the arc-length $\left(\frac{du}{ds}\right)_n$, and then use

$$\left(\frac{du}{d\xi}\right)_{\Omega_e, n} = \left(\frac{du}{ds}\right)_n \left(\frac{ds}{d\xi}\right)_{\Omega_e, n} \quad (5.22)$$

where $\left(\frac{ds}{d\xi}\right)_{\Omega_e, n}$ is an element *scale factor* which describes the mapping between s and ξ , at node n for element Ω_e . This enforces continuity on $\frac{du}{ds}$ between elements which is more useful practically.

Two-dimensional cubic Hermite basis functions can be constructed using a similar method as used for the Lagrange functions, except that the cubic Hermite basis

requires the four quantities listed in Equation (5.23) to be defined at each node, totalling 16 nodal parameters per element.

$$u, \quad \frac{\partial u}{\partial \xi_1}, \quad \frac{\partial u}{\partial \xi_2} \quad \text{and} \quad \frac{\partial^2 u}{\partial \xi_1 \partial \xi_2} \quad (5.23)$$

The last term is a second-order cross-derivative term which is additionally required in order to maintain derivative continuity with respect to the ξ -coordinates. The full bicubic Hermite interpolation of a quantity u is given in Equation (5.24) using the nodal parameters and the one-dimensional basis functions.

$$\begin{aligned} u(\xi_1, \xi_2) = & \Psi_1^0(\xi_1)\Psi_1^0(\xi_2)u_1 + \Psi_2^0(\xi_1)\Psi_1^0(\xi_2)u_2 \\ & + \Psi_1^0(\xi_1)\Psi_2^0(\xi_2)u_3 + \Psi_2^0(\xi_1)\Psi_2^0(\xi_2)u_4 \\ & + \Psi_1^1(\xi_1)\Psi_1^0(\xi_2) \left(\frac{\partial u}{\partial \xi_1} \right)_1 + \Psi_2^1(\xi_1)\Psi_1^0(\xi_2) \left(\frac{\partial u}{\partial \xi_1} \right)_2 \\ & + \Psi_1^1(\xi_1)\Psi_2^0(\xi_2) \left(\frac{\partial u}{\partial \xi_1} \right)_3 + \Psi_2^1(\xi_1)\Psi_2^0(\xi_2) \left(\frac{\partial u}{\partial \xi_1} \right)_4 \\ & + \Psi_1^0(\xi_1)\Psi_1^1(\xi_2) \left(\frac{\partial u}{\partial \xi_2} \right)_1 + \Psi_2^0(\xi_1)\Psi_1^1(\xi_2) \left(\frac{\partial u}{\partial \xi_2} \right)_2 \\ & + \Psi_1^0(\xi_1)\Psi_2^1(\xi_2) \left(\frac{\partial u}{\partial \xi_2} \right)_3 + \Psi_2^0(\xi_1)\Psi_2^1(\xi_2) \left(\frac{\partial u}{\partial \xi_2} \right)_4 \\ & + \Psi_1^1(\xi_1)\Psi_1^1(\xi_2) \left(\frac{\partial^2 u}{\partial \xi_1 \partial \xi_2} \right)_1 + \Psi_2^1(\xi_1)\Psi_1^1(\xi_2) \left(\frac{\partial^2 u}{\partial \xi_1 \partial \xi_2} \right)_2 \\ & + \Psi_1^1(\xi_1)\Psi_2^1(\xi_2) \left(\frac{\partial^2 u}{\partial \xi_1 \partial \xi_2} \right)_3 + \Psi_2^1(\xi_1)\Psi_2^1(\xi_2) \left(\frac{\partial^2 u}{\partial \xi_1 \partial \xi_2} \right)_4 \end{aligned} \quad (5.24)$$

In addition, the scaling factors need to be specified for each ξ direction according to the arc lengths s_1 and s_2 , together with a cross-derivative scale factor. In order to ensure C^1 continuity across element boundaries these scaling factors are required to be nodally based (Bradley, Pullan and Hunter 1997), and in general are chosen to be the average of adjacent arc lengths so that the ξ coordinate is most evenly spaced. Further explanation can be gained from Hunter, Smail, Nielsen and Grice (1996).

Mixed basis functions

It is often useful to take combinations of the various basis functions in order to interpolate a quantity of interest most accurately and efficiently. For example, a quantity may vary quickly in the ξ_3 direction, but slowly in the ξ_1 and ξ_2 directions.

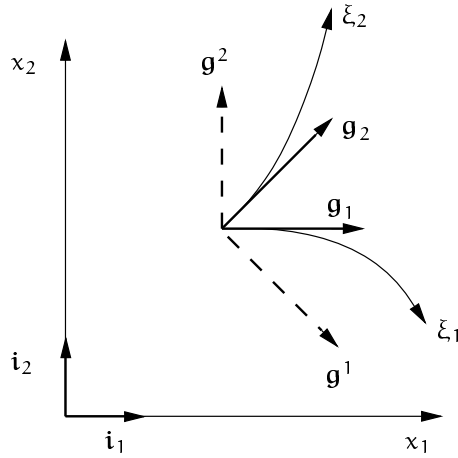


FIGURE 5.9: Curvilinear ξ_i -coordinate system defined using finite elements.

This is efficiently represented using linear Lagrange interpolation in the first two directions and cubic Hermite interpolation in the third, and is constructed by taking the tensor product of the bilinear Lagrange basis functions described in Equation (5.8) together with a cubic Hermite basis function (Equation (5.18)). This basis is conveniently referred to as a bilinear-cubic basis function.

5.2.3 Base vectors

A finite element is described in terms of local ξ_i -coordinates, using some set of basis functions $\Psi_n(\xi_1, \xi_2)$ which require the definition of n nodes per element. Using these basis functions, we can generalise an interpolation such as Equation (5.4) to an arbitrary number of dimensions k , and derive a mapping from ξ_i -space to x_k -space

$$x_k(\xi_i) = \Psi_n(\xi_i)x_k^n \quad (5.25)$$

where x_k^n is the x_k coordinate for node n of the element, and an implicit summation is used over the number of nodes. This mapping defines a curvilinear coordinate system such as the two-dimensional example shown in Figure 5.9. This two-dimensional mapping using the bilinear basis functions defined in Equation (5.8) is determined by Equation (5.25) as

$$x_1(\xi_1, \xi_2) = \Psi_1(\xi_1, \xi_2)x_1^1 + \Psi_2(\xi_1, \xi_2)x_1^2 + \Psi_3(\xi_1, \xi_2)x_1^3 + \Psi_4(\xi_1, \xi_2)x_1^4 \quad (5.26)$$

$$x_2(\xi_1, \xi_2) = \Psi_1(\xi_1, \xi_2)x_2^1 + \Psi_2(\xi_1, \xi_2)x_2^2 + \Psi_3(\xi_1, \xi_2)x_2^3 + \Psi_4(\xi_1, \xi_2)x_2^4 \quad (5.27)$$

We will use this two-dimensional mapping to define further quantities related to the local coordinate system, although all quantities generalise easily to three (or more) dimensions as required. Flugge (1972) presents a more thorough derivation of the various quantities.

Covariant base vectors \mathbf{g}_1 and \mathbf{g}_2 tangent at a point to the element coordinates ξ_1 and ξ_2 are defined by

$$\mathbf{g}_i = \frac{\partial x_k}{\partial \xi_i} \mathbf{i}_k \quad (5.28)$$

and locally define the coordinate system. Using the finite element mapping in Equation (5.25) then the relationship between global coordinates and local coordinates is

$$\frac{\partial x_k}{\partial \xi_i} = \frac{\partial \Psi_n}{\partial \xi_i} x_k^n \quad (5.29)$$

A set of *contravariant base vectors* \mathbf{g}^i are defined to be orthogonal to \mathbf{g}_i by

$$\mathbf{g}^i \cdot \mathbf{g}_j = \delta_j^i \quad (5.30)$$

and are an alternative measure of the local coordinates as shown in Figure 5.9. Note that \mathbf{g}^1 is orthogonal to \mathbf{g}_2 and vice versa.

Figure 5.10 shows a vector quantity \mathbf{u} which may be defined relative to the local coordinate system by either using contravariant components u^i relative to the covariant base vectors \mathbf{g}_i , or by using covariant components u_i relative to the contravariant base vectors \mathbf{g}^i

$$\mathbf{u} = u^i \mathbf{g}_i = u_i \mathbf{g}^i \quad (5.31)$$

5.2.4 Metric tensors

The relationship between covariant and contravariant components of a vector is given by the *metric tensor* which is a measure of the incremental physical distance associated with the ξ_i -coordinates. Covariant and contravariant components of the symmetric metric tensor are obtained from the inner products of the base vectors by

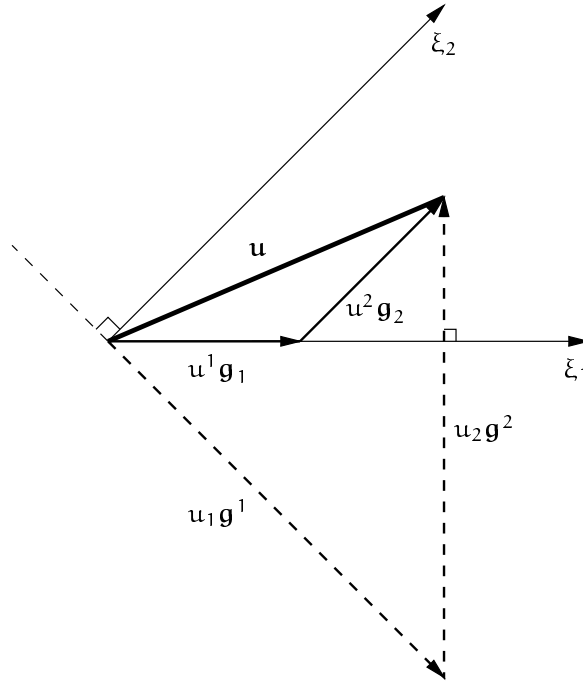


FIGURE 5.10: Description of a vector u in terms of vector components and base vectors.

the equations

$$g_{ij} = \mathbf{g}_i \cdot \mathbf{g}_j = \frac{\partial x_k}{\partial \xi_i} \frac{\partial x_k}{\partial \xi_j} \quad (5.32)$$

$$g^{ij} = \mathbf{g}^i \cdot \mathbf{g}^j = \frac{\partial \xi_i}{\partial x_k} \frac{\partial \xi_j}{\partial x_k}$$

This gives the relationship between between the covariant and contravariant components of a vector u as

$$u^i = g^{ij} u_j \quad \text{and} \quad u_i = g_{ij} u_j \quad (5.33)$$

and similarly the relationship between forms of the base vectors is given by

$$\mathbf{g}^i = g^{ij} \mathbf{g}_j \quad \text{and} \quad \mathbf{g}_i = g_{ij} \mathbf{g}_j \quad (5.34)$$

The metric tensor derives its name from measuring the physical distance ds^2 associated with incremental changes $d\xi^1$ and $d\xi^2$ in the ξ_i -coordinates

$$\begin{aligned} ds^2 &= dx_k dx_k = g_{ij} d\xi^i d\xi^j \\ &= g_{11} d\xi^1 d\xi^1 + g_{12} d\xi^1 d\xi^2 + g_{21} d\xi^2 d\xi^1 + g_{22} d\xi^2 d\xi^2 \end{aligned} \quad (5.35)$$

For skewed cartesian ξ_i -coordinates subtending an angle α , this reduces to the cosine rule for triangles

$$(ds)^2 = (d\xi^1)^2 + (d\xi^2)^2 + 2 \cos \alpha d\xi^1 d\xi^2 \quad (5.36)$$

5.2.5 Measures of curvature

The partial derivative of a scalar quantity u with respect to the ξ_j -coordinate is $\frac{\partial u}{\partial \xi_j}$ irrespective of the nature of the coordinate system. However, the partial derivative of a vector \mathbf{u} is dependent upon the coordinate system and must consider the change of the base vectors with the ξ_j -coordinate. The covariant and contravariant forms are

$$\begin{aligned} \frac{\partial \mathbf{u}}{\partial \xi_j} &= \frac{\partial u^i \mathbf{g}_i}{\partial \xi_j} = \frac{\partial u^i}{\partial \xi_j} \mathbf{g}_i + u^i \frac{\partial \mathbf{g}_i}{\partial \xi_j} \\ &= \frac{\partial u_i \mathbf{g}^i}{\partial \xi_j} = \frac{\partial u_i}{\partial \xi_j} \mathbf{g}^i + u_i \frac{\partial \mathbf{g}^i}{\partial \xi_j} \end{aligned} \quad (5.37)$$

where $\frac{\partial \mathbf{g}_i}{\partial \xi_j}$ and $\frac{\partial \mathbf{g}^i}{\partial \xi_j}$ are vector quantities. The components of this vector projected onto the base vectors \mathbf{g}_k are called *Christoffel symbols* and denoted Γ_{ij}^k by the relationship

$$\frac{\partial \mathbf{g}_i}{\partial \xi_j} = \Gamma_{ij}^k \mathbf{g}_k \quad (5.38)$$

and are a measure of the curvature of the ξ_j -coordinates. If the ξ_j -coordinates are rectangular cartesian, then the base vectors are constant and orthogonal, and these partial derivatives and the Christoffel symbols are all identically zero.

Substituting Equation (5.38) into Equation (5.37) gives

$$\begin{aligned} \frac{\partial \mathbf{u}}{\partial \xi_j} &= \frac{\partial u^i}{\partial \xi_j} \mathbf{g}_i + u^i \Gamma_{ij}^k \mathbf{g}_k \\ &= \left(\frac{\partial u^k}{\partial \xi_j} + u^i \Gamma_{ij}^k \right) \mathbf{g}_k \\ &= u^k |_{,j} \mathbf{g}_k \end{aligned} \quad (5.39)$$

where

$$u^k |_{,j} = \frac{\partial u^k}{\partial \xi_j} + u^i \Gamma_{ij}^k \quad (5.40)$$

are called the *covariant derivatives* of u^k . Using a comma to denote partial differentiation, we can write

$$u_{,j} = u^k|_j g_k \quad \text{where} \quad u^k|_j = u^k_{,j} + u^i \Gamma_{ij}^k \quad (5.41)$$

Alternatively, using the contravariant base vectors and the covariant components of u , we have

$$u_{,j} = u_i|_j g^i \quad \text{where} \quad u_i|_j = u_{i,j} - u_k \Gamma_{ij}^k \quad (5.42)$$

The Christoffel symbols can be calculated by taking the inner product of $g_{i,j}$ with the contravariant base vectors g^k

$$\Gamma_{ij}^k = g_{i,j} \cdot g^k \quad (5.43)$$

where

$$g_{i,j} = \Gamma_{ij}^k g_k = \frac{\partial^2 x_k}{\partial \xi_i \partial \xi_j} \mathbf{i}_k \quad (5.44)$$

Note that the partial derivative of a scalar is identical to its covariant derivative $u_{,i} = u|_i$. Also, the metric tensor may be used to define the *contravariant derivative* as $u|^i = u|_j g^{ij}$.

5.2.6 Reference coordinate systems

The nodal points of a finite element mesh need to be defined with respect to some reference coordinate system. In order to efficiently define the nodal positions one of a variety of coordinate systems can be used.

The rectangular cartesian coordinate system

In two dimensions (2D), orthogonal rectilinear axes x and y are defined, and an additional orthogonal axis z is defined in three dimensions (3D). In the cardiac model which we use, the axes are defined so that the x -axis coincides with the central axis of the heart and passes through the intersection of the aortic and mitral valve rings, and through the apex of the left ventricle, and is therefore defined to be positive in the downwards vertical direction. The y -axis passes through the centre of the right ventricle, and the z -axis is defined to be orthogonal to those two.

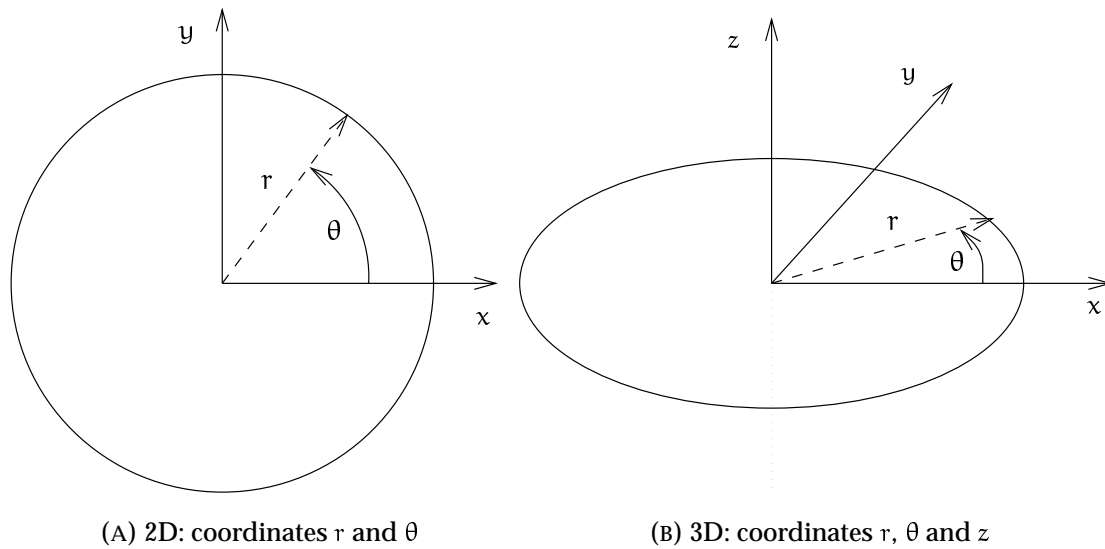


FIGURE 5.11: Definition of the cylindrical polar coordinate system.

The cylindrical polar coordinate system

A 2D cylindrical polar coordinate system defines each point in terms of a radius r and an angle θ . These values are related to the rectangular-cartesian (r.c.) values by the equations

$$\begin{aligned} r &= \sqrt{x^2 + y^2} \\ \theta &= \tan^{-1} \left(\frac{y}{x} \right) \end{aligned} \quad (5.45)$$

and inversely

$$\begin{aligned} x &= r \cos \theta \\ y &= r \sin \theta \end{aligned} \quad (5.46)$$

In 3D, a linear z axis identical to that in r.c. coordinates is added, and the geometrical representation of both 2D and 3D is shown in Figure 5.11. When used in modelling the heart, because of the orientation of the heart with respect to the cartesian coordinate system, the x -axis is vertical, and therefore the mapping

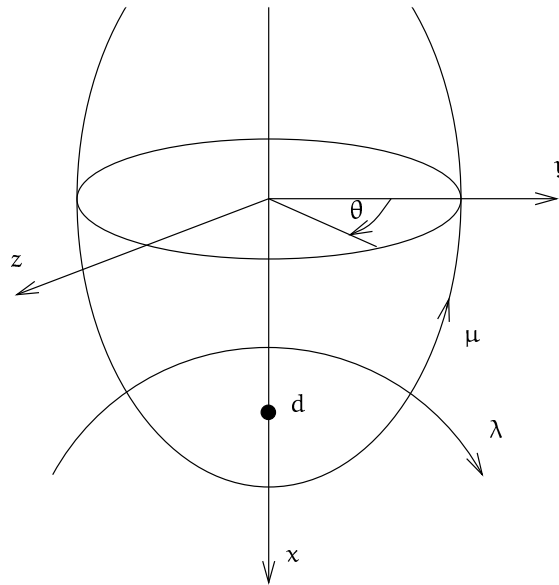


FIGURE 5.12: The cardiac prolate spheroidal coordinates (λ, μ, θ) in relation to the r.c. coordinates (x, y, z) , where d is the focus of the prolate spheroid.

between cartesian coordinates (x, y, z) and the polar coordinates (x, r, θ) is given by

$$\begin{aligned} x &= x \\ y &= r \cos \theta \\ z &= r \sin \theta \end{aligned} \tag{5.47}$$

The prolate spheroidal coordinate system

It is more convenient to use a prolate spheroidal coordinate system (as shown in Figure 5.12) when modelling cardiac geometry. This is because a reasonable first order approximation (a confocal ellipsoid) to the left ventricle may be obtained with a single element. Accurate solutions to simple problems are easy to compare to analytic solutions to verify the accuracy on simple meshes that are a similar shape to the cardiac model. In addition, the problem of fitting a surface to measured data points is simplified if the fit is performed in prolate spheroidal coordinates, and becomes a linear problem rather than the much more complicated non-linear fit in r.c.

coordinates. The prolate spheroidal coordinate system defines a curvilinear radius λ and two angles μ and θ . The relationship between prolate-spheroidal coordinates (λ, μ, θ) and r.c. coordinates (x, y, z) is given by:

$$\begin{aligned}x &= d \cosh \lambda \cos \mu \\y &= d \sinh \lambda \sin \mu \cos \theta \\z &= d \sinh \lambda \sin \mu \sin \theta\end{aligned}\tag{5.48}$$

where “d” is the focus position on the x-axis, λ is the radius, and μ and θ are angles as shown. Two additional benefits of this system become obvious. Firstly, it becomes possible to use lower order basis functions for describing the parameters μ and θ while still retaining a high order cubic Hermite basis for λ which varies much more over the surface. Secondly, the focus parameter d provides a convenient means of scaling the overall size of a heart.

5.2.7 Material coordinates

The nature of the cardiac microstructure is inherently orthotropic and inhomogeneous. Equations describing activation contain terms which depend on the local conductivity tensor, and therefore a model of the local microstructural orientations is required. The definition of the diffusion term in the bidomain equations assumes that conductivity can be specified in particular directions within the tissue.

The heart model which is used incorporates a set of three axes which reflect the microstructural orientation at any point in the ventricular myocardium. These define a tensor quantity $\frac{\partial v_j}{\partial x_i}$ which describes the change in material parameters with respect to the reference coordinate system. These are the direction cosines of the *material coordinates* at a given point.

One-Dimensional Elements

For one-dimensional elements, there is no concept of a directional conductivity, and the propagation direction is aligned with the element. Thus the direction cosine simply relates the element orientation to the global (x, y, z) coordinate system.

For elements defined in rectangular cartesian coordinates, the direction cosines are

$$\frac{\partial v_1}{\partial x_i} = \frac{\frac{\partial x_i}{\partial \xi_1}}{\sqrt{\sum_j \left(\frac{\partial x_j}{\partial \xi_1}\right)^2}} \quad (5.49)$$

The cylindrical-polar coordinate system defines coordinates in the (r, θ, z) space as given by Equation (5.46) and the coordinate derivative transformation is given by

$$\begin{aligned} \frac{\partial x}{\partial \xi_1} &= \frac{\partial r}{\partial \xi_1} \cos \theta - r \sin \theta \frac{\partial \theta}{\partial \xi_1} \\ \frac{\partial y}{\partial \xi_1} &= \frac{\partial r}{\partial \xi_1} \sin \theta + r \cos \theta \frac{\partial \theta}{\partial \xi_1} \\ \frac{\partial z}{\partial \xi_1} &= \frac{\partial z}{\partial \xi_1} \end{aligned} \quad (5.50)$$

and the same equations above are used as for the r.c. case.

Two-Dimensional Elements

For two-dimensional elements, we can introduce the concept of a fibre angle α . This is defined at each point within the geometry as the angle at which the fibres are aligned relative to the local ξ coordinates. The local element $\xi_{1,2}$ coordinates are oriented at an angle ϕ to the global (x, y) coordinate system where

$$\phi = \tan^{-1} \left(\frac{\partial y}{\partial \xi_1} / \frac{\partial x}{\partial \xi_1} \right) \quad (5.51)$$

and the direction cosines come from the projection of the sum of these angles onto the global (x, y) coordinates:

$$\frac{\partial v}{\partial x_i} = \begin{bmatrix} \cos(\alpha + \phi) & \sin(\alpha + \phi) & 0 \\ -\sin(\alpha + \phi) & \cos(\alpha + \phi) & 0 \\ 0 & 0 & 0 \end{bmatrix} \quad (5.52)$$

By definition, the two directions are orthogonal while in an undeformed state, but as the material deforms, the material coordinates may become skewed.

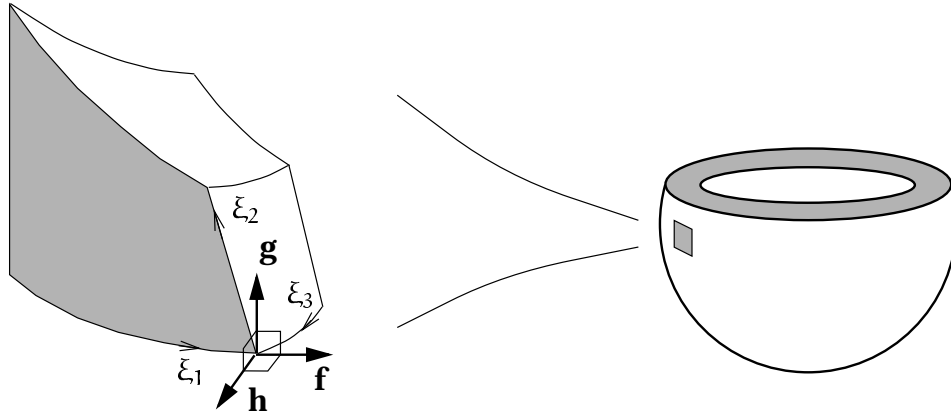


FIGURE 5.13: Definition of the wall coordinate system vectors ($\mathbf{f}, \mathbf{g}, \mathbf{h}$) with respect to the finite element material coordinates (ξ_1, ξ_2, ξ_3).

Three-Dimensional Elements

In order to describe cardiac microstructural information it is necessary to define two coordinate systems. The first is the *microstructural material coordinate system* which is defined by the orientation of the fibres and sheets at a point in the myocardium. The coordinate system is represented by the base vectors ($\mathbf{a}, \mathbf{b}, \mathbf{c}$), where \mathbf{a} is the *fibre axis* and is defined to be aligned with the local fibre direction, \mathbf{b} is the *sheet axis* and lies perpendicular to the fibre axis in the plane of the sheet, and \mathbf{c} is the *sheet-normal axis* defined to be normal to the plane of the sheet. Therefore, by definition, the microstructural material coordinate system is defined to be orthonormal in the undeformed reference state (equivalent to zero ventricular transmural pressures) though under deformation the axes are in general non-orthogonal.

The second coordinate system is the *wall coordinate system* defined by orthonormal base vectors ($\mathbf{f}, \mathbf{g}, \mathbf{h}$) which are defined in terms of finite element material coordinates (ξ_1, ξ_2, ξ_3) as shown in Figure 5.13. The ξ_i coordinates are in general non-orthogonal, but it is more useful to define other properties with respect to an orthonormal system. The first vector \mathbf{f} is defined to coincide with the local ξ_1 coordinate direction at a point. The second vector \mathbf{g} lies within the (ξ_1, ξ_2) tangent plane and is perpendicular to \mathbf{f} , and not necessarily aligned with ξ_2 . The last vector \mathbf{h} is defined to be normal to both \mathbf{f} and \mathbf{g} as $\mathbf{h} = \mathbf{f} \times \mathbf{g}$ to ensure that the wall vectors are orthonormal and form the basis of a right-handed coordinate system.

A series of three successive coordinate rotations of $(\mathbf{a}, \mathbf{b}, \mathbf{c})$ specifies the transformation of the microstructural material components of the fibrous-sheet vectors into wall coordinates.

Firstly, $(\mathbf{a}, \mathbf{b}, \mathbf{c})$ are rotated about the fibre vector, \mathbf{a} , into $(\mathbf{a}, \mathbf{b}', \mathbf{c}')$ where \mathbf{b}' lies in the (ξ_1, ξ_2) -coordinate plane. The angle between \mathbf{b} and \mathbf{b}' is referred to as the *sheet angle*, γ . A positive sheet angle represents a right-handed (anti-clockwise) rotation about \mathbf{a} from \mathbf{b}' to \mathbf{b} . The associated coordinate transformation is expressed mathematically in Equation (5.53).

$$\begin{bmatrix} \mathbf{a} \\ \mathbf{b}' \\ \mathbf{c}' \end{bmatrix} = \begin{bmatrix} 1 & 0 & 0 \\ 0 & \cos \gamma & -\sin \gamma \\ 0 & \sin \gamma & \cos \gamma \end{bmatrix} \begin{bmatrix} \mathbf{a} \\ \mathbf{b} \\ \mathbf{c} \end{bmatrix} \quad (5.53)$$

Secondly, $(\mathbf{a}, \mathbf{b}', \mathbf{c}')$ is rotated about the \mathbf{b}' axis into $(\mathbf{a}', \mathbf{b}', \mathbf{h})$ as \mathbf{a}' now also lies in the (ξ_1, ξ_2) -coordinate plane. The angle between \mathbf{a} and \mathbf{a}' is referred to as the *imbrication angle*, β . A positive imbrication angle depicts an anti-clockwise rotation from \mathbf{a}' to \mathbf{a} about \mathbf{b}' . Equation (5.54) defines the coordinate transformation.

$$\begin{bmatrix} \mathbf{a}' \\ \mathbf{b}' \\ \mathbf{h} \end{bmatrix} = \begin{bmatrix} \cos \beta & 0 & -\sin \beta \\ 0 & 1 & 0 \\ \sin \beta & 0 & \cos \beta \end{bmatrix} \begin{bmatrix} \mathbf{a} \\ \mathbf{b}' \\ \mathbf{c}' \end{bmatrix} \quad (5.54)$$

Lastly, $(\mathbf{a}', \mathbf{b}', \mathbf{h})$ is rotated about \mathbf{h} into $(\mathbf{f}, \mathbf{g}, \mathbf{h})$. The angle between \mathbf{a}' and \mathbf{f} is referred to as the *fibre angle*, α . This coordinate rotation is defined in Equation (5.55).

$$\begin{bmatrix} \mathbf{f} \\ \mathbf{g} \\ \mathbf{h} \end{bmatrix} = \begin{bmatrix} \cos \alpha & -\sin \alpha & 0 \\ \sin \alpha & \cos \alpha & 0 \\ 0 & 0 & 1 \end{bmatrix} \begin{bmatrix} \mathbf{a}' \\ \mathbf{b}' \\ \mathbf{h} \end{bmatrix} \quad (5.55)$$

In a mathematical model the fitted microstructural directions are stored with respect to the finite element coordinate system so that they deform appropriately under ventricular deformation, and it is useful to construct the microstructural material vectors at any given point from these. This is achieved by firstly constructing the wall vectors, $(\mathbf{f}, \mathbf{g}, \mathbf{h})$, from the finite element material coordinates, (ξ_1, ξ_2, ξ_3) , and subsequently transforming $(\mathbf{f}, \mathbf{g}, \mathbf{h})$ into $(\mathbf{a}, \mathbf{b}, \mathbf{c})$ using interpolated fibre (α), imbrication (β) and sheet (γ) angles. Equation (5.56) defines this coordinate

transformation, which consists of the inverse operations to those described in Equations (5.53)–(5.55), performed in reverse order.

$$\begin{bmatrix} \mathbf{a} \\ \mathbf{b} \\ \mathbf{c} \end{bmatrix} = \begin{bmatrix} 1 & 0 & 0 \\ 0 & \cos \gamma & \sin \gamma \\ 0 & -\sin \gamma & \cos \gamma \end{bmatrix} \begin{bmatrix} \cos \beta & 0 & \sin \beta \\ 0 & 1 & 0 \\ -\sin \beta & 0 & \cos \beta \end{bmatrix} \begin{bmatrix} \cos \alpha & \sin \alpha & 0 \\ -\sin \alpha & \cos \alpha & 0 \\ 0 & 0 & 1 \end{bmatrix} \begin{bmatrix} \mathbf{f} \\ \mathbf{g} \\ \mathbf{h} \end{bmatrix} \quad (5.56)$$

This brief outline is expanded more fully in a paper by Le Grice et al. (1994) and further again by Hunter, Smaill, Nielsen and Grice (1996) and Nash (1998).

5.3 Definition of the Collocation-Derived Finite Difference Method

This finite element framework, which has been developed in the previous sections, is useful for describing the geometry of a problem. However, as has been outlined in Section 5.1.3, the finite element method is not an ideal scheme for solving the activation equations. This has led to the development of a new technique which is called a *Collocation-Derived Finite Difference method*. This method is based upon a finite element framework, but possesses some advantages over it. The collocation method uses a finite element mesh to accurately describe the geometry of the solution domain, and to solve equations of motion when a deforming model is required. A grid of solution points is defined on top of the mesh, and collocation equations satisfy the equations exactly at these collocation points. Where a bidomain model is being solved for, a finite element formulation is used for the additional equation. In this section the formulation of the collocation method is described, and for illustration purposes a simple four element two-dimensional mesh is used.

5.3.1 Collocation point definition

The collocation grid is constructed using the basis functions which describe the finite element mesh. Each grid point is defined at some ξ_i position within an element, and

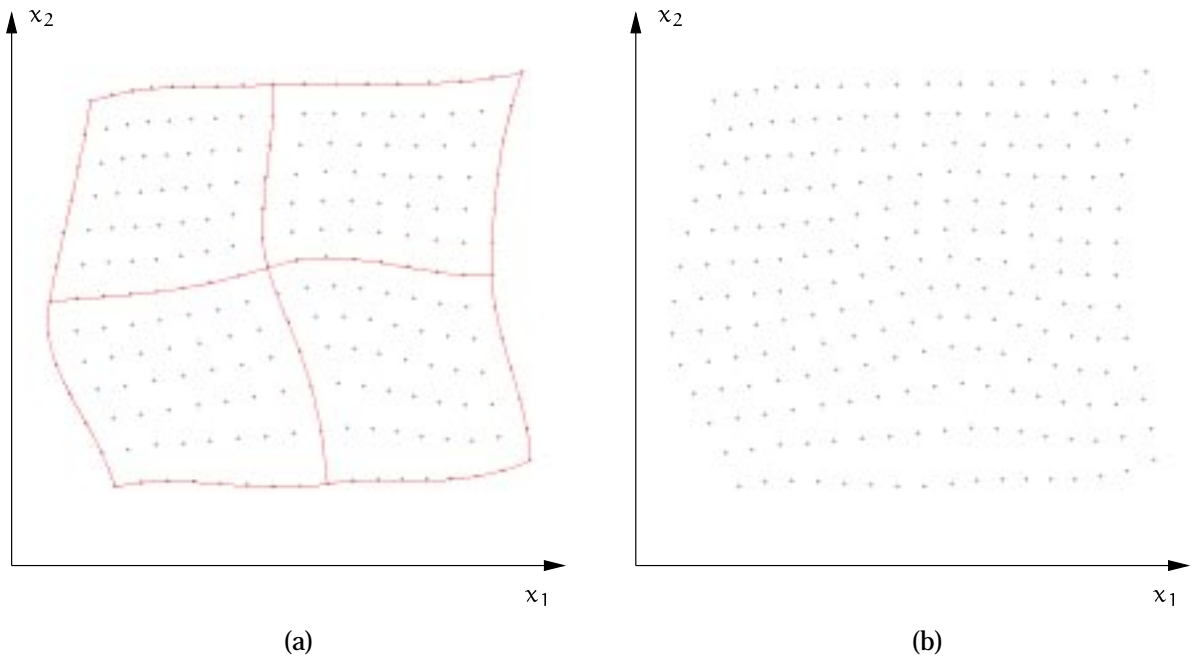


FIGURE 5.14: Creation of collocation points at even ξ spacings from a finite element mesh. (a) 9 grid points are defined in the ξ_1 direction, and 7 points in the ξ_2 direction within each element. (b) The collocation grid - a curvilinear regular grid with uneven spacing of grid points.

local metric values are obtained from the element basis functions at that point. Either Equation (3.11) or Equation (3.12) can be solved for on any regularly connected grid with arbitrary spacing between grid points, though all grid points must lie within the finite element mesh. For convenience, we place the grid points at equal ξ_i spacings as shown in Figure 5.14. A necessary condition is that we have a regularly connected grid which is one in which each grid point (except a boundary point) has a set of unique neighbouring points in each of the ξ_i directions.

As shown in Figure 5.14, a different number of grid points may be defined in each ξ_i direction, in this case 9 points in the ξ_1 direction and 7 points in the ξ_2 direction, totalling 221 grid points in this four element mesh. Note that although points are defined on element boundaries ($\xi = 0, 1$) duplicate points from neighbouring elements are removed so that there are no coincident grid points.

The microstructural fibre orientation is defined over the mesh, as shown in

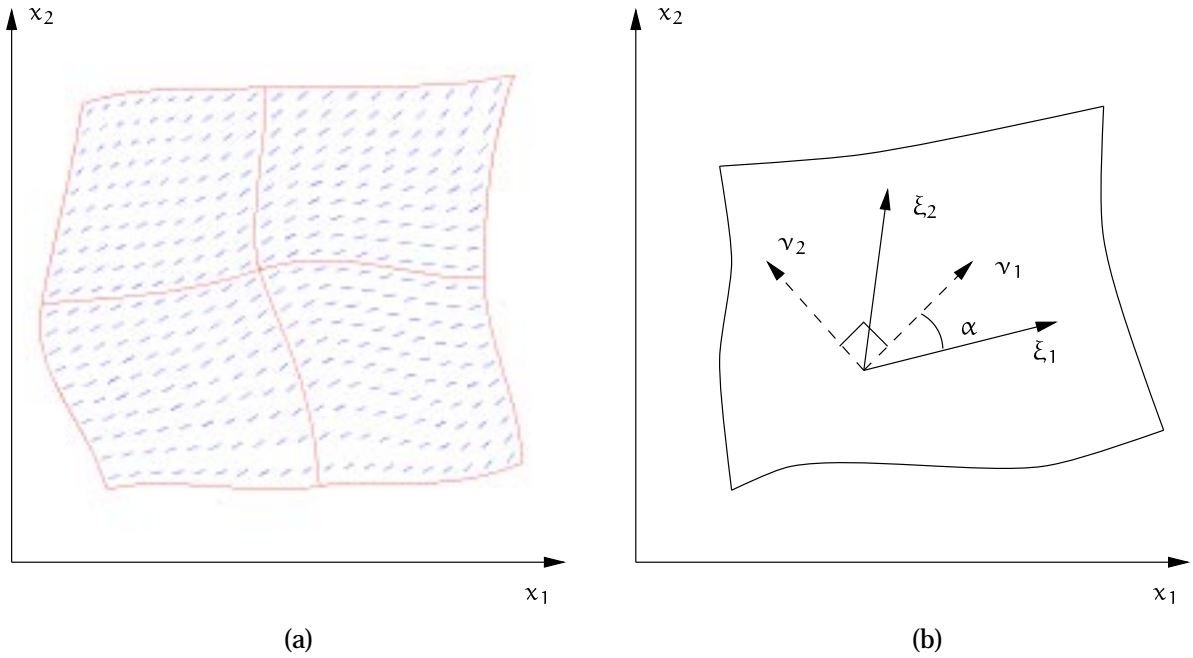


FIGURE 5.15: Definition of material coordinates from fibre direction. (a) Fibre directions interpolated from nodal values using basis functions. (b) Local material coordinates ν_1 aligned with local fibre direction and ν_2 defined orthogonal to ν_1 .

Figure 5.15a. For the mesh illustrated, a fibre angle of 10° is defined at the lower left corner, 35° at the lower right corner, 30° at the upper left and 47° at the upper right. The fibre angle α is defined relative to the ξ_1 coordinate as shown in Figure 5.15b. Local material coordinates are defined at all collocation points by interpolating the nodal values using the element basis functions. ν_1 is aligned with the fibre direction, and ν_2 is defined to be orthogonal to ν_1 in the global (x_1, x_2) -coordinate system. In three dimensions, ν_2 is aligned with the sheet direction (still orthogonal to ν_1), and ν_3 is defined to be orthogonal to both ν_1 and ν_2 . The conductivity tensor σ is assumed to be diagonal in the material coordinate system, i.e. the principal directions of conductivity are the material axes. The tensor therefore has three components: σ_f in the fibre direction, σ_s in the sheet direction, and σ_c in the sheet-normal (or cross-sheet) direction.

The metric quantities g_{ij} , g^{ij} and Γ_{ij}^k are computed from the values of $\frac{\partial x_k}{\partial \xi_i}$ at each point. The grid is regularly connected, so that every point has eight neighbours in two dimensions and 26 neighbours in three dimensions, but, unlike a conventional

finite difference scheme, the spacing between grid points may be irregular or skewed.

5.3.2 Solution method

This grid of collocation points provides the framework on which the bidomain equations, Equations (3.9) and (3.11), may be solved. The collocation scheme for solving Equation (3.11) is described first, and is essentially the same if the problem is formulated as a monodomain problem, with all references to the extracellular potential being ignored. The solution of Equation (3.9) uses a different approach, and is discussed in Section 5.3.2.

Equation (3.11) may be rewritten as

$$\nabla \cdot (\sigma_i \nabla (V_m + \phi_e)) = A_m \left(C_m \frac{\partial V_m}{\partial t} + I_{ion} \right) - I_s \quad (5.57)$$

and therefore, for simplicity, this section is written so that it refers to both the bidomain and monodomain formulations with the symbol u used to refer to the potential, such that $u = V_m + \phi_e$ for the bidomain formulation and $u = V_m$ for the monodomain formulation. The left hand side of the equation is referred to as the diffusion term as its form is the same as that of a diffusion equation. Due to only a single conductivity being used in either case, that of the intracellular domain, the conductivity tensor in this section will be referred to simply as σ in order to reduce the number of subscripts required.

This conductivity is defined as a diagonal tensor defined in terms of microstructural material coordinates, that is, a conductivity is specified in the fibre direction, and additional conductivity values defined in orthogonal directions in the undeformed state, one in the plane of the sheet, if working with a three-dimensional preparation, one in a direction orthogonal to the first two. These microstructural axes are not required to be aligned with the elemental ξ coordinates, and under deformation the material axes may become non-orthogonal. If we use the symbol σ'_{β}^{α} to represent the diagonal conductivity tensor defined in terms of the microstructural axes (where α and β range over the number of material axes), then the mapping from the material

coordinates to the local ξ coordinates is given by

$$\sigma_k^i = \frac{\partial \xi_i}{\partial v^\alpha} \frac{\partial v_\beta}{\partial \xi_k} \sigma_{\beta}^{\prime \alpha} \quad (5.58)$$

where σ_k^i is in general a fully populated matrix, and where i and k range over the number of elemental material coordinates.

In addition, the full conductivity tensor σ_k^i may vary with ξ_j over the domain, and this variation needs to be accounted for in the computation of the diffusion term. Using the metric components defined in Section 5.2.4 this term is rewritten as

$$\begin{aligned} \nabla \cdot (\sigma \nabla u) &= (\sigma_k^i u_{,i})_{,j} g^{jk} \\ &= [(\sigma_k^i u_{,i})_{,j} - \Gamma_{kj}^l (\sigma_l^i u_{,i})] g^{jk} \\ &= (\sigma_{k,j}^i u_{,i} + \sigma_k^i u_{,ij} - \Gamma_{kj}^l \sigma_l^i u_{,i}) g^{jk} \end{aligned} \quad (5.59)$$

and in this form, it is defined in terms of the material coordinates, and is therefore independent of the reference coordinate system, and of changes in geometry due to deformation or contraction.

Combining Equations (5.57) and (5.59) and rearranging results in an equation for the incremental change in transmembrane potential at a point given some small time step Δt

$$\Delta V_m = \frac{\Delta t}{C_m} \left(-I_{ion} + \frac{1}{A_m} [(\sigma_{k,j}^i u_{,i} + \sigma_k^i u_{,ij} - \Gamma_{kj}^l \sigma_l^i u_{,i}) g^{jk} + I_s] \right) \quad (5.60)$$

where the metric values and diffusion tensor values and derivatives can be computed once for a given geometry, and only the first and second derivatives of the potential u must be computed at each time-step.

The metric values required (Γ_{kj}^l and g^{jk}) are computed using Equations (5.32) and (5.43) from the basis function information defined by the finite element mesh, and this is one of the reasons for deriving the collocation grid from a finite element mesh. The local derivative of σ_k^i with respect to ξ_j is computed by taking first order finite differences about a point, in a similar way to Equation (5.61). Using this method, different conductivities may be specified at each point, allowing for easy definition of cardiac tissue exhibiting some degree of activation block.

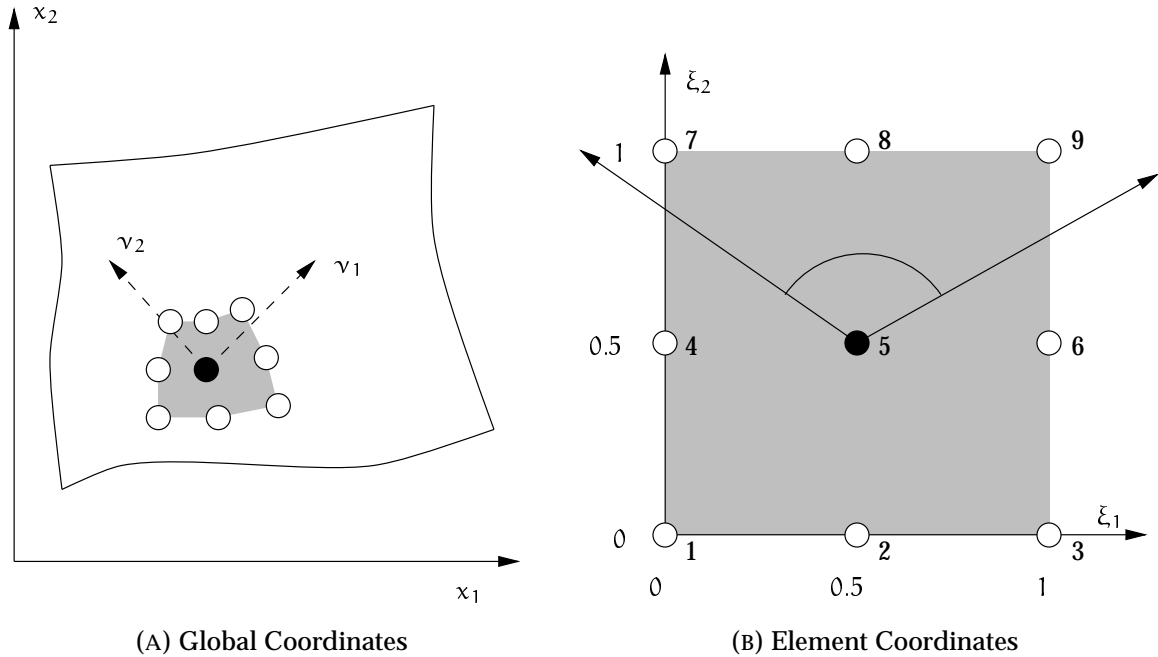


FIGURE 5.16: From the 9 neighbouring collocation points shown in (a), a local biquadratic element is defined in (b).

Collocation scheme

Because of the irregular spacing within the grid, a traditional finite difference scheme will not work with the collocation grid. However, we can apply the method illustrated in Figure 5.16. At some collocation point not on the boundary of the grid (an *internal* collocation point, shown shaded in black as point 5 in Figure 5.16a), we take the eight neighbours of that point and form a 9-noded finite element centred on that point as shown in Figure 5.16b, and use biquadratic basis functions Ψ_n as defined in Equation (5.16). This local element is not the same as the finite element from which the collocation grid was derived, but is used simply to discretise Equation (5.60) at a point. For a three-dimensional grid, we take the 26 neighbours and use triquadratic basis functions to form a local triquadratic element, but the procedure is identical. Note that the microstructural axes, which were defined to be orthogonal in the global coordinate system, become non-orthogonal in the local element coordinates.

Using this biquadratic element, we can compute the derivatives $u_{,i}$ and $u_{,ij}$ required

for Equation (5.60). The equations for the central point are

$$\begin{aligned}
 u_{5,1} &= u_6 - u_4 \\
 u_{5,2} &= u_8 - u_2 \\
 u_{5,11} &= 4(u_6 - 2u_5 + u_4) \\
 u_{5,22} &= 4(u_8 - 2u_5 + u_2) \\
 u_{5,12} &= u_9 - u_7 - u_3 + u_1
 \end{aligned} \tag{5.61}$$

These computations are equivalent to taking finite differences about point 5 in the local coordinate system. Using an explicit forward Euler solution scheme, Equation (5.60) is solved at a given time step for all internal collocation points. Computationally, the most expensive term to calculate at each step is the ionic current I_{ion} , which may be chosen from any of the ionic current models presented in Chapter 4.

The size of the time step is governed by the stability criterion for the explicit Euler solution technique used. As shown by Pollard et al. (1993) the stability threshold for this method is proportional to

$$\Delta t \propto (\Delta x^2 + \Delta y^2 + \Delta z^2)^{-1} \tag{5.62}$$

which places severe restrictions on Δt when a high spatial resolution is required. Use of a semi-implicit technique significantly improves the stability threshold and is a possibility for use where a high density of collocation points is desired. Other methods will give even better convergence, though at some expense of the computational time. Multigrid solution methods are an obvious choice, with other possible techniques including a wavelet solution method.

Boundary conditions

Values at grid points on the boundary of the domain are solved for using a separate technique to that used for the interior points due to the fewer neighbouring points. The intracellular domain is effectively surrounded by a non-conducting medium, and therefore a *no-flux* or *Neumann* boundary condition is applied at each point on the boundary of the domain. In the solution process, the boundary points are updated at each time step after new values for all the internal points have been computed. For an orthogonal geometry, the no-flux boundary condition can be

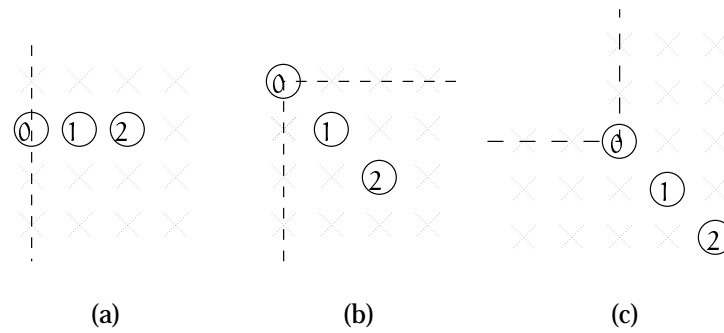


FIGURE 5.17: No-flux boundary condition implementation. Point 0 is the boundary point and points 1 and 2 are the internal points as given in Equation (5.63). (a) Edge boundary condition. (b) and (c) 2D corner boundary conditions.

written as

$$u_0 = \frac{4u_1 - u_2}{3} \quad (5.63)$$

where grid point 0 is the boundary point and grid points 1 and 2 are internal points perpendicular to the boundary at point 0 as shown in Figure 5.17. This approach generalises to three dimensions with more possible variations of the number of neighbouring points. Current may be applied at the boundary by defining a specific flux rather than enforcing zero flux.

When the solution domain is non-orthogonal, Equation (5.63) does not exactly give zero flux on the boundary. In a more general case, the no-flux condition is derived as

$$\begin{aligned} 0 &= \frac{\partial u}{\partial \mathbf{n}} \\ &= \nabla u \cdot \mathbf{n} \\ &= u|_i n^i \\ &= u_{,i} n^i \end{aligned} \quad (5.64)$$

where $\mathbf{n} = n^i g_i$ is the vector normal to the boundary. Any error introduced by using the approximation given in Equation (5.63) is present at a boundary point only as the wavefront passes that point, and is proportional to the skew in the geometry; that is, the angle between the elemental ξ direction and the normal \mathbf{n} . A worst-case situation exists when a step wavefront is moving directly along a boundary at 1 grid point per iteration, and for a severe skew of 45° , the boundary value computed using Equation (5.63) leads or lags the wavefront by a single time step. Additionally, the previous time step (in which u_1 is zero and u_2 is maximal) results in a maximum 33%

error. At all other times the value calculated from the simplified boundary condition is accurate. All simulations performed for this thesis would exhibit smaller errors than this worst-case scenario, and Equation (5.63) has been used to describe the no-flux boundary condition in all instances.

Integrating the bidomain equation

The above methods are sufficient to solve the monodomain formulation, however the complete bidomain model contains an additional equation, Equation (3.9), which is quasi-static rather than time-dependent. It is possible to solve the complete system of equations (the transmembrane equation and the extracellular equation: Equations (3.9) and (3.11) respectively) as a coupled system, as is done by Pollard et al. (1993), using an explicit or implicit solution technique. We chose not to couple the equations together in order to retain more flexibility in the methods by which the equations were solved and the time-scales appropriate to each equation. In this case, the extracellular equation is being considered to be an *update* equation which updates the extracellular potential to match the computed transmembrane potential. The equation is solved subsequent to the transmembrane equation, and therefore the left hand side of Equation (3.9) is already known. It can therefore be rewritten as a Poisson equation

$$\nabla \cdot ((\sigma_i + \sigma_e) \nabla \phi_e) = f \quad (5.65)$$

where the source term on the right hand side

$$f = \nabla \cdot (\sigma_i \nabla V_m) \quad (5.66)$$

is known.

In many cases, the solution of the activation wavefront position and the value of the transmembrane potential is unchanged whether or not the extracellular potential is computed. This allows us to only compute the extracellular potential when it is required, which is a good reason for not coupling the two equations together. One of the main requirements for the extracellular potential is that it provides the source for a model describing the electric field within a torso and on the body surface. This model is often solved using either a finite element method or a boundary element

method, or a combination of both (Pullan, Bradley and Hunter 1993*b*; Pullan, Bradley and Hunter 1993*a*), for the governing Laplace's equation in three dimensions

$$\nabla^2 \phi_o = 0 \quad (5.67)$$

Because the geometry of the bidomain problem is defined already using a finite element mesh, our initial intention was therefore to use the finite element technique (Zienkiewicz and Taylor 1994) as the solution method for the extracellular potential. This would provide an easy coupling to the torso model, and in fact the solution for the extracellular and the extramyocardial domains could be achieved using a single coupled solution process. The implementation of this method is relatively straightforward, and the bidomain equation could be solved using a 3 Gauss point per ξ direction integration scheme. However, it was soon realised that the extracellular potential varies on the same scale as the transmembrane potential as they are in fact related by their second derivatives, and the resolution of finite elements required would need to be much greater than needed for defining the collocation grid. This is an inefficient use of resources for this problem, and negates much of the philosophy behind using only as many finite elements as needed to describe the mechanical deformation of the geometry, and constructing a collocation scheme from that.

The alternative is to use another solution technique which is more applicable at the small scales needed. An obvious choice is the *multigrid* technique (Briggs 1987) which is a very fast iterative solution technique which uses a hierarchy of grid point refinements to approximate the solution and reduce the errors as it moves through a range of grid densities. The Poisson equation is particularly suited to a multigrid technique, and we have found in other studies that anisotropic conductivities of the order of 10:1 do not pose a problem. This technique has the advantage that the same set of grid points used to solve the monodomain equation may be used in the solution of the bidomain equation.

The main concern which dictated the method which we used at this time was the ease of coupling to the extramyocardial solution (or torso solution). The solution scheme we use for this problem is a combined finite element-boundary element scheme (Pullan et al. 1993*b*; Pullan et al. 1993*a*), and therefore coupling to a finite element bidomain solution scheme for the extracellular potential was much more convenient. Using this method, the extracellular and extramyocardial potentials could be solved for simultaneously using a coupling between different solution

regions. Coupling a multigrid scheme to the boundary element scheme would be much more difficult, but there are advantages in terms of spatial resolution which the multigrid scheme provides, and this will need to be considered in the future.

5.3.3 Tracking a deforming geometry

There are many instances when a deforming geometry becomes part of the problem, due either to an imposed deformation or due to the contraction process. This deformation is easily tracked (or computed) using the finite element mesh, using appropriate equations to describe the deformation. The collocation grid is then redefined from the new nodal positions according to the same original mesh, in the same way as described in Section 5.3.1, along with new measures of the metric variables. Because the finite element nodes are affixed to material points, the new position of each collocation point corresponds with the same material point prior to the deformation, and therefore the state variables carried at that point apply to the same physical region of tissue. The material coordinates may change as a result of the deformation, which means that the relationship of the diffusion tensor to material coordinates must be updated. In general the mechanical deformation occurs on a much slower time scale than the electrical activation, and therefore the equations describing contraction need to be solved less regularly. There needs to be a balance in the relative solution times between keeping the mechanical deformation accurate, and redefining the collocation grid and geometrical information. Because different techniques are used for each model, the two sets of computations are essentially independent, allowing the freedom to choose an appropriate time scale for each.

5.3.4 Dynamic tracking of the active region

One of the disadvantages of using an explicit collocation scheme is that a solution must be generated at every time step for every solution point, and the time step needs to be quite small in order for the solution to be stable. During the cardiac activation process, only a small number of points are active at any one time, and therefore computational time is wasted on points which do not change. Barr and

Plonsey (1984) proposed a scheme called Dynamic Tracking of the Active Region (DTAR) in which they only solve for points which are already active, or may become active in the next time step. A point may become active if it has a neighbour whose potential exceeds some preset value above the resting potential (0.1 mV for example), or if current is injected at that point. The conditions under which points are removed from the solution domain are less clearly specified, and depend on the ionic current model used. Usually this will be when the potential has resumed a steady value, and any ionic currents or recovery variables have returned to their resting value.

The DTAR scheme is implemented here by initially only solving at points where current is injected. After each time step, the currently active points are scanned, and if their potential exceeds the preset value, then all neighbours of that point are added to the list of active points. The point is then flagged so that it will not be scanned again. This particular scheme does not allow reentrant wavefronts to be tracked, but in most cases where a reentrant wave is propagating, a large number of the solution points are active at any one time, and the computational overhead of tracking the active points outweighs any savings from computing fewer points.

Chapter 6

Two-Dimensional Activation using the Collocation Method

It is important that the solution technique used to solve the activation equations is both accurate and fast, and that it incorporates descriptions of the features (such as a varying fibre field) that are properties of ventricular myocardium. In addition, the particular model which we chose to use sought to satisfy another requirement, namely that it should be easy to integrate the activation model into a larger, global model of cardiac function which incorporates such features as models of mechanical deformation in the myocardium and electric field in the torso cavity, and models of other important processes which may be added in the future. This chapter uses a series of simple examples to illustrate the suitability of the collocation technique to achieve these requirements for problems in two dimensions.


Section 6.3 begins with some simple examples using a monodomain model on a square membrane, and performs simulations using a variety of solution geometries, ionic current models, fibre orientations and conductivity ratios. It is shown that the method is convergent with both decreasing spatial and temporal resolution. Section 6.4 extends the models to show the behaviour of the technique for reentrant waves occurring as a result of multiple stimuli. In Section 6.5 the monodomain formulation is extended to a full bidomain model, and the solution of the extracellular equation is illustrated. The process is then shown for a simple example involving coupling the activation model to a model of the electrical field

in the body cavity. Another application is shown in Section 6.6 in which a one-dimensional network of fibres is used to activate a two-dimensional region, in an initial concept model of the activity of the Purkinje fibre network. Finally, Section 6.7 uses an optimisation technique which makes use of the activation model in order to interpret experimental results by determining tissue conductivities based on electrode recordings.

In Chapter 7, solutions are given for a variety of three-dimensional geometries, including an anatomically accurate model of ventricular myocardium. Electromechanical coupling is explored in Chapter 8 where the activation model is coupled to a simple model of mechanical deformation. Firstly a weakly coupled system shows the wave propagating in a mesh which is being externally deformed, and then a stricter coupling is shown in which the contraction of the membrane is in response to the activation of the tissue by the wavefront.


6.1 Accompanying Movie Files

All of the simulations presented in the following three chapters have either two-dimensional or three-dimensional geometries, and are, by the nature of the problem, time dependent. This three- and four-dimensional output is difficult to reproduce on two-dimensional sheets of paper, and three main forms of output are used. For solutions in which a single wavefront activates a two-dimensional domain, then a map of contours of activation time represents the passage of the wavefront. For reentrant waves and solutions on three-dimensional geometries, the results are shown in two forms. Firstly, the time sequence is represented in this thesis as a time series of snapshots of the domain showing the transmembrane potential at each interval. In these cases, the images begin at the top left, and the time sequence increases left-to-right in rows.

Even this representation makes it somewhat difficult to determine the activation characteristics, and so some of the examples are additionally reproduced in movie format on the accompanying CD, and, at least temporarily, on the World Wide Web. These are represented by a small icon () together with a filename. The filename specifies the name of the directory and the name of the file, where the directory is

relative to a base directory. The CD is written in ISO-9660 format, and is readable on Macintosh, IBM-PC compatible and Unix systems. For each system the base directory is: “/CDROM/” under Unix, “D:\” on a PC (where “D” is the CDROM drive) and “MOVIES” on a Macintosh. On the WWW the base directory is given by the URL “<http://www.esc.auckland.ac.nz/People/Students/Sands/Thesis/Movies/>” and is accessible using Netscape or any similar Web browser with a password available from the author (g.sands@auckland.ac.nz). The contents of the movie files is documented using an HTML interface, and may be accessed from the CD or through the Web by pointing a browser to movies.htm.

The movies are available in several formats, and many of the files are large. All of the movies were initially generated as Silicon Graphics Movie format files, and are on the Web in a compressed version of this form (extension “.mv.gz”). These files have been compressed using gzip which is freely available. These files can only be played on SGI workstations using their built-in movie player, movieplayer. Two standard formats have been used for portability – the MPEG¹ format and the Quicktime² format, for which viewers are freely available for most modern computers. On the accompanying CD, the movies are reproduced at its original resolution (which ranges upwards from 400 × 400 pixels) with file extensions of “.mpg”. This is larger than the standard MPEG format, and consequently some viewers may have difficulty with these resolutions, and so the movie is additionally available on the Web in the standard 320 × 240 resolution with file extensions “.mpv”. Although the MPEG format is significantly lossy, and does especially poorly at compressing computer generated movies, it generally produces the smallest files, hence its use. The CD also contains the movies in the Quicktime format with extension “.mov”, and scaled to a standard size of 640 × 480.

Table 6.1 shows the location of the available files for an example movie denoted by  square/epicard. Several utility programs are also included on the CD and on the Web. An Stuffit-encoded archive of Sparkle, an MPEG player for the Macintosh is located in the macutils/ directory, and MPEG and Quicktime archives for IBM-compatible PCs running Windows (3.1 or 95) are in the winutils/ directory. Source code for two Unix viewing programs is located in the unix/ directory.

¹<http://www.mpeg.org/index.html/>

²<http://quicktime.apple.com/>

IBM-PC Compatible

D:\square\epicard.mpg

D:\square\epicard.mov

Macintosh

MOVIES:square:epicard.mpg

MOVIES:square:epicard.mov

Unix

/CDROM/square/epicard.mpg

/CDROM/square/epicard.mov

World Wide Web<http://www.esc.auckland.ac.nz/People/Students/Sands/Thesis/Movies/square/epicard.mpg><http://www.esc.auckland.ac.nz/People/Students/Sands/Thesis/Movies/square/epicard.mpv><http://www.esc.auckland.ac.nz/People/Students/Sands/Thesis/Movies/square/epicard.mv.gz><http://www.esc.auckland.ac.nz/People/Students/Sands/Thesis/Movies/square/epicard.mov>

TABLE 6.1: Location of movie files for the example file description square/epicard.

6.2 The CMISS Solution Environment

A set of computer subroutines has been written which define the equations describing the bidomain model and the various activation models, and implement the collocation method for solving them. These routines have been coded in Fortran 77, and are integrated into a larger, general purpose program called CMISS³ which has been developed over many years by a number of people in our research group at the University of Auckland. According to the WWW page, CMISS is

... a mathematical modelling environment that allows the application of finite element analysis, boundary element and collocation techniques to a variety of complex bioengineering problems. It consists of a number of modules including a graphical front end with advanced 3D display and modelling capabilities, and a computational backend that may be run remotely on powerful workstations or supercomputers.

Many existing routines were used in the development of these examples, particularly those dealing with finite element mesh generation and mechanical deformation solution, and the collocation routines which have been written for this problem are

³<http://www.esc.auckland.ac.nz/Groups/Bioengineering/CMISS/>

designed to be integrated with these other routines.

The majority of examples were solved on a Digital Alphastation 200 4/233⁴ which is a 233 MHz Alpha-based workstation running VMS V6.1. A new, high performance supercomputer was installed at the University of Auckland towards the end of the work done for this thesis, and some of the larger three dimensional problems were solved on this new computer. The supercomputer is an SGI Power Challenge⁵ comprising 16 MIPS R10000 CPU units, each with 2 Mb of secondary cache running at 195 MHz, with 2 Gb of physical memory.

The code presented some unique difficulties when being adapted to run on multiple processors. At each time step, the use of the explicit finite difference method means that computations at each solution point are independent, and therefore the total computations are easily divided among the processors which are available. However, the computational time required for a single time step at each collocation point is very small, on the order of 0.01 s, and the overhead required for partitioning the problem over multiple processors dominates the solution time for a small number of collocation points. For a problem using approximately 16000 collocation points, the speedup in going from one processor to two results in a speed increase by a factor of 1.74. Further increasing the number of processors to four, eight and sixteen results in speed increase factors of 3.04, 4.88 and 6.63 respectively. For this reason, solution times are given solely for simulations run on the Alpha workstation in the format 5m36s (CPU) according to the number of minutes and seconds of CPU time used. Solution speeds are also indicated in terms of collocation point iterations per second (cpi/s) where a speed of 1 cpi/s states that one iteration of one collocation point takes one second of CPU time to solve.

6.3 Single Stimulus Activation

In this section, the results of a number of simple test problems are shown which illustrate the flexibility of the collocation solution method and demonstrate its suitability and accuracy. Each problem is derived from the previous by making

⁴Digital Equipment Corp.

⁵Silicon Graphics Inc.

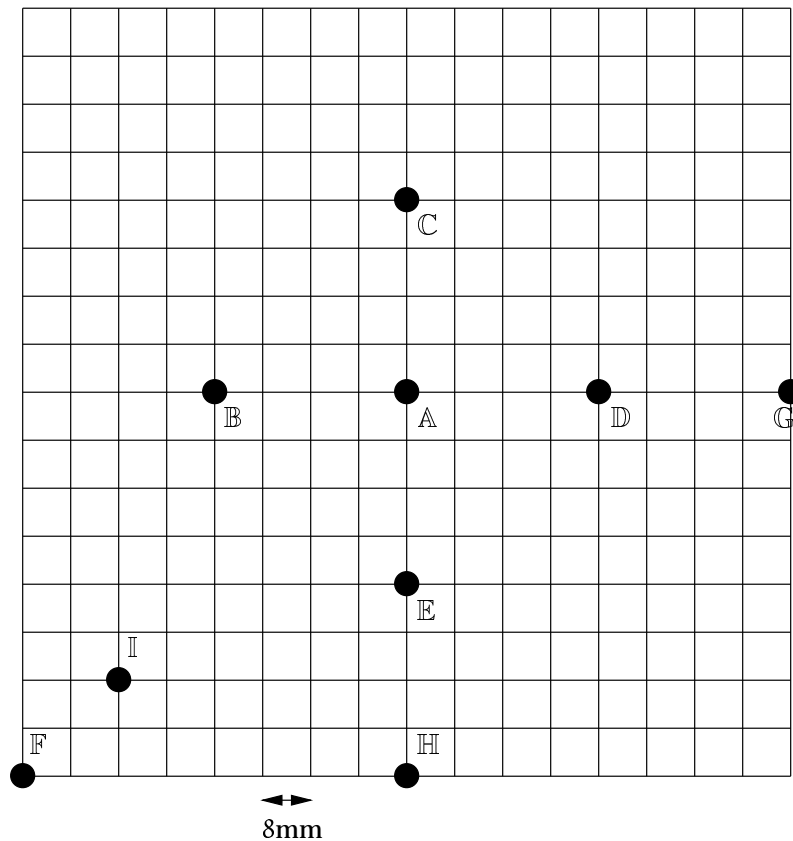


FIGURE 6.1: Solution points on square membrane used as an example.

small changes, and the results show the effect of that change.

6.3.1 The initial problem

The solution domain for the problem consists of a square, two-dimensional finite element mesh with 16 elements in each direction. Each element is a square with a side-length of 8 mm, and therefore the entire domain covers $128 \times 128 \text{ mm}^2$ with 256 elements and 289 nodes. The square mesh is shown in Figure 6.1, and several points are labelled with names A to I. In some parts of the examples shown further on, these points are used as references for either initial conditions or solutions. An extended linear Lagrange basis specifies a 9×9 gauss point scheme within each element, which results in a collocation grid of $129 \times 129 = 16641$ collocation points at a regular 1 mm spacing. A monodomain solution is considered on a homogeneous, isotropic domain, i.e. $\sigma_f = \sigma_s$. A cubic equation is used to describe the ionic model

Parameter	Value
C_m	10 nF · mm ⁻²
A_m	200 mm ⁻¹
$\sigma_{f,s}$	1 mS · mm ⁻¹
V_{rest}	-85 mV
$V_{threshold}$	-75 mV
$V_{plateau}$	15 mV
$\overline{g_m}$	4×10^{-3} mS · mm ⁻²

TABLE 6.2: Values of the constants for an isotropic domain and a cubic ionic current model.

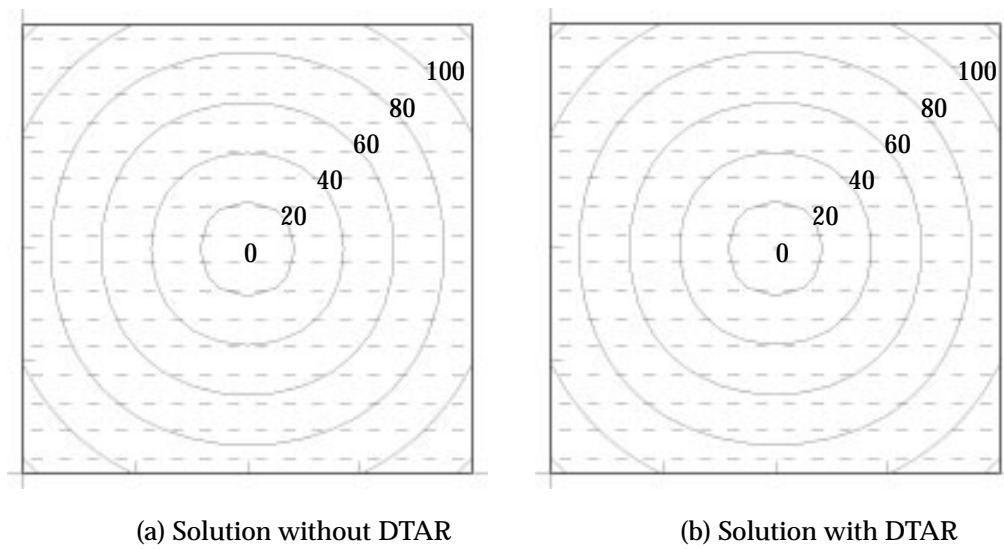


FIGURE 6.2: Isochronal contours of activation time on a isotropic square mesh using a cubic ionic current model. (a) Dynamic tracking (DTAR) not used. (b) DTAR used.

(see Equation (4.105) on page 113), with parameters as given in Table 6.2. The initial conditions specify a single pulse of amplitude $0.1 \text{ mA} \cdot \text{mm}^{-3}$ and duration 1 ms to be applied at a collection of 9 collocation points centred on point \mathbb{A} in the centre of the mesh. More than one collocation point is activated in order that the applied current does not immediately leak away from the stimulus site. Zero-flux boundary conditions are applied for all points on the boundary. An explicit collocation scheme with a time step of $\Delta t = 0.1 \text{ ms}$ is used to solve for the transmembrane potential V_m for a total of 150 ms.

Isochronal contour lines describing the activation time are shown in Figure 6.2a, and as expected the resulting wavefront propagation is circular from the stimulus point. For the purpose of these comparisons, the activation time for a collocation point is defined as the time at which that point experiences the largest depolarising change in V_m . The solution for 1500 iterations was achieved in 6m33s (CPU) which translates to 63,515 collocation point iterations per second (cpi/s). In order to obtain the contour lines, a finite element field was fitted to the resulting point values of activation time using the bilinear elements which defined the solution domain. The RMS (root mean square) error for this fit was 0.208 ms.

6.3.2 Use of DTAR

The second example is identical to the first, except that in this case an algorithm known as DTAR (see Section 5.3.4) has been used to solve only the points contained within an “active” region near the wavefront. The variation from resting potential before a neighbouring point was included in the solution process was set to 0.1 mV, and a collocation point was removed from the solution once its transmembrane potential attained a value within 0.01 mV of the plateau potential. The resulting isochronal contours are plotted in Figure 6.2b and show no apparent difference from those of the standard solution. The difference in activation time between the DTAR and non-DTAR solutions at every collocation point in the mesh is no greater than 0.1 ms, which is the resolution due to the time step. The total solution time is 1m41s (CPU) which required 1244 iterations until all points were removed from the solution process. This translates into an effective speed of 205,000 cpi/s, or a 3.2-fold increase in solution speed. A maximum number of 3200 collocation points were in the solution process at any one time step, and the extra time was used in housekeeping for the DTAR method. The RMS error in fitting the activation field was again 0.208 ms.

6.3.3 Convergence

As with any model, a number of assumptions need to be made at various stages of the solution. The following sections examine the assumptions required in the

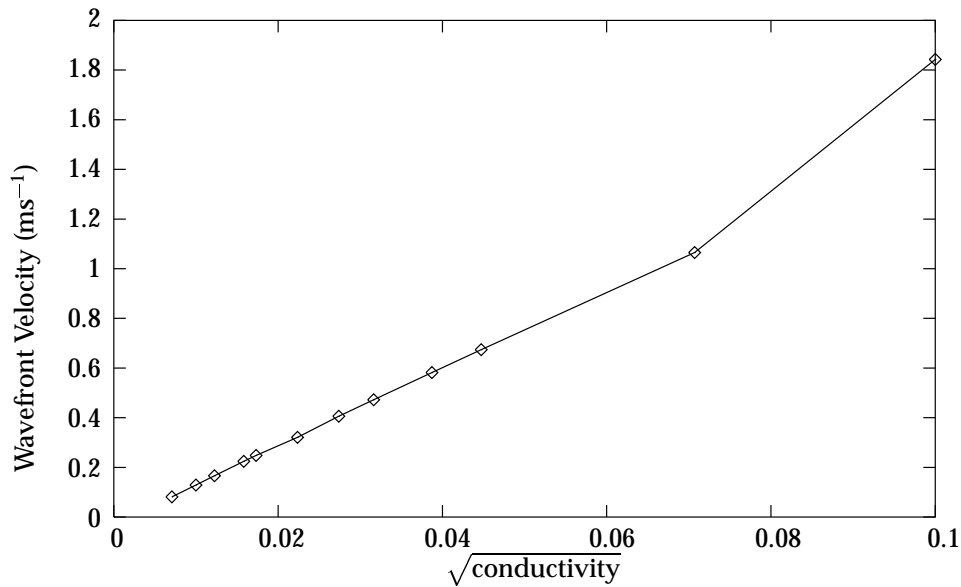


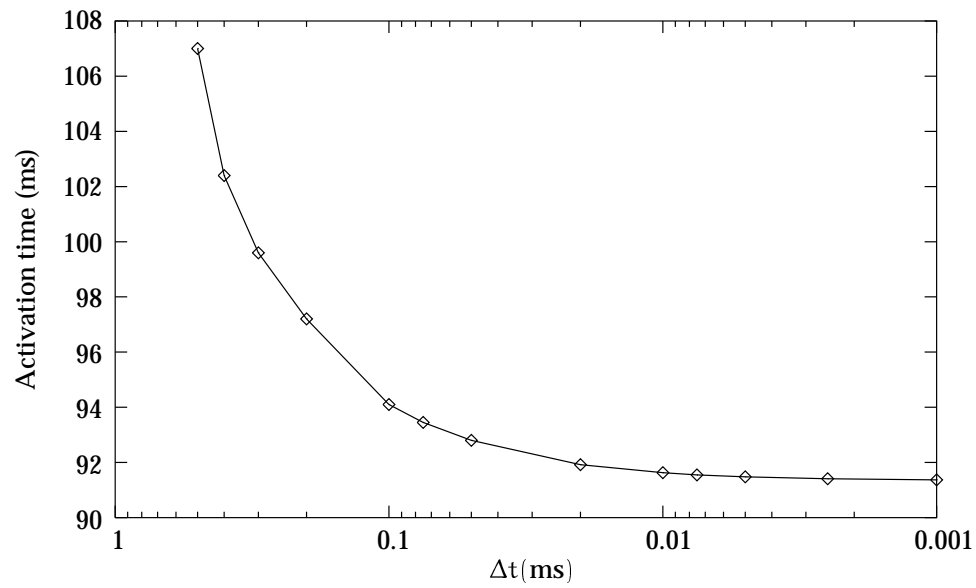
FIGURE 6.3: Correlation between wavefront velocity and the square root of the conductivity

numerical implementation of the model relating to the trade-off between a fully converged solution and the computational time required to solve to that level.

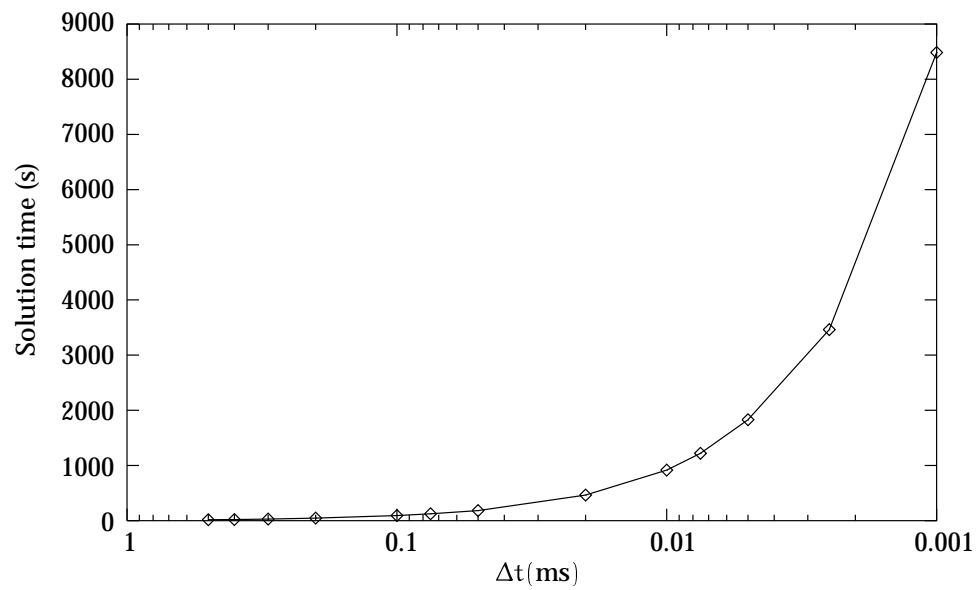
One important aspect of convergence to check is that the wavefront velocity is proportional to the square root of the conductivity. The above non-DTAR model was used with an isotropic conductivity tensor ranging between $0.05 \text{ mS} \cdot \text{mm}^{-1}$ and $10 \text{ mS} \cdot \text{mm}^{-1}$. The resulting correlation between the square root of the conductivity and the wavefront velocity is shown in Figure 6.3, where a linear relationship is demonstrated for all except the final value. This value of $10 \text{ mS} \cdot \text{mm}^{-1}$ is outside the range of conductivities which are used (0.1 to $2.0 \text{ mS} \cdot \text{mm}^{-1}$), and is in error solely because of the time step used. Reducing this time step maintains the linear relationship for this conductivity also.

6.3.4 Size of time step

For the explicit solution technique, there is an upper limit for the time step Δt beyond which the solution of the equations is unstable. For values of Δt below this maximum, the collocation method should converge to more accurate values



(A) Activation Time



(B) Solution Time

FIGURE 6.4: Influence of change in time step on (a) the activation time at a point, and (b) the time required for solution.

as the time step decreases. In order to determine this, we stimulate at point \mathbb{A} as above, and measure the time at which the wavefront reaches some other point. In this case, we choose to use point \mathbb{I} (at coordinates (16, 16) on the leading diagonal) because it is relatively far from the stimulus, but away from the boundary so that any possible boundary effects will not influence the results. A series of simulations were performed in which the time step varied from $\Delta t = 0.5$ ms down to $\Delta t = 0.001$ ms. The activation time of point \mathbb{I} , in milliseconds, is plotted against the value of the time step in Figure 6.4a, and shows that the solution converges quickly as the time step reduces. This increase in accuracy from a small time step is at the cost of CPU time required for the solution as Figure 6.4b shows, where the solution CPU times are measured in seconds. The other simulations in this thesis are performed with time steps mostly in the range of 0.01 ms to 0.1 ms depending on the collocation grid spacing.

6.3.5 Resolution of collocation points

It is a more difficult problem to examine convergence resulting from an increase in collocation point density. Increasing the spatial resolution of the solution points changes the solution in two main ways. Firstly, the current density injected into the domain decreases if the current size and number of stimulation points both remain the same. Secondly, a time step which produces a converged result for one grid point spacing, as shown in the previous section, will give a less converged solution at a higher grid point resolution. This is due to the fact that the maximum allowable time step is governed by the stability criterion (Equation (5.62)) for the explicit Euler solution method.

For these reasons, if the spatial resolution is increased while either or both of the temporal resolution and the stimulus current remain the same, then the solution of the equations begins to diverge at very high solution point densities. In order to address these issues, the following problem was constructed.

It seems that a solution of one-dimensional propagation gives us enough information about the accuracy of the problem, and this is effectively achieved by using a line stimulus which bisects the solution domain through point \mathbb{A} . The isotropic domain ensures that the resulting wave remains planar throughout the mesh. Once

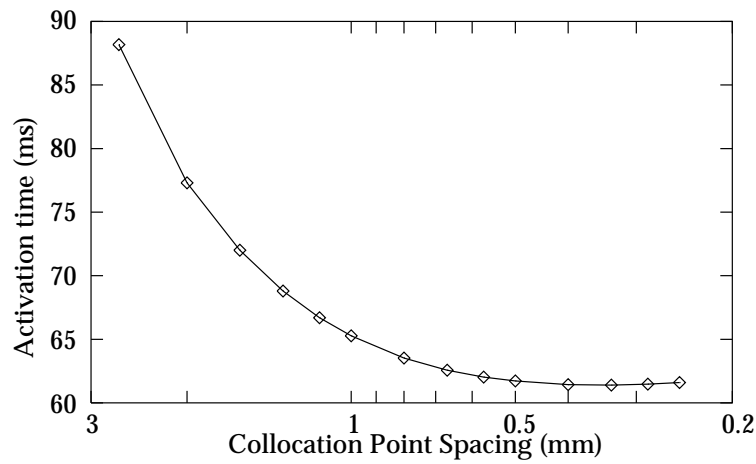
again the activation time is measured at point II and compared for a range of collocation point spacings. In order to compensate for the changes caused by a change in spatial resolution, the time step and the stimulus intensity are altered. The time step is changed so that $\Delta t \propto \Delta x^2$ and the current so that $I_{app} \propto (\Delta x^2)^{-1}$. Therefore, for a decrease in Δx by a factor of 2, the time step decreases by a factor of 4 and the stimulus current increases by a factor of 4.

The results of this problem are presented in Figure 6.5, where the first two graphs show the change in solution time at point II with a variation in spatial resolution for both the simplified cubic equation, and the more realistic Beeler-Reuter equation. The last pair of graphs show the relationships between Δx and the two other input variables, Δt and I_{app} . For the cubic equation the solution has seemed to converge, until the final two data points, represented by spacings of 0.288 and 0.25 mm respectively. The results show a slight increase ($\sim 0.3\%$ at the final point) in the computed activation time over those spacings. If the value of the applied current is increased further for this last example, this has little effect on the computed solution time ($< 0.1\%$ for a 2.5 times increase in I_{app}), while an additional decrease in Δt has a marginally greater effect (a decrease in Δt to 0.0005 gives a 1.5% change in the computed activation time). The Beeler-Reuter model is much slower to converge than the cubic model, and at the finest resolution it has converged to only about 1%.

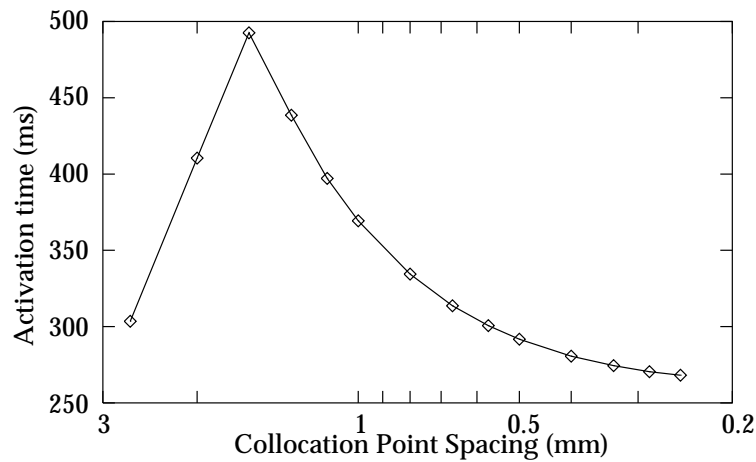
6.3.6 Convergence implications

Section 6.3.4 shows that the explicit solution technique for the equations generated using the cubic ionic current model in a monodomain context converges as the solution time-step is reduced. Other ionic current models show a similar rate and degree of convergence. Section 6.3.5 shows that both the cubic ionic model and the Beeler-Reuter ionic model converge as the spacing between collocation points is reduced, though the BR solution is much slower to converge, and considerable computational solution time is required at high collocation resolutions.

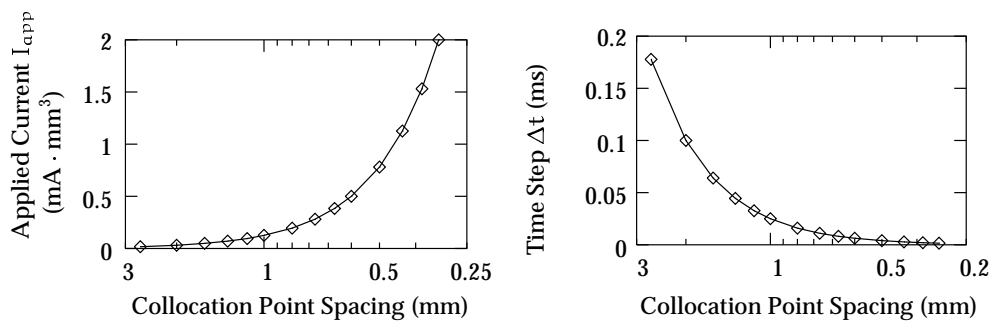
Because of this exponential relationship between the resolution of the time and space variables in the solution, and the computational solution time required, many of the following examples have parameters chosen for their solution which are not fully converged. In a number of cases in which the result looks slightly different



(A) Convergence for cubic model



(B) Convergence for Beeler-Reuter model



(C) Input Variables

FIGURE 6.5: Change in computed activation time at point II with change in spatial resolution.

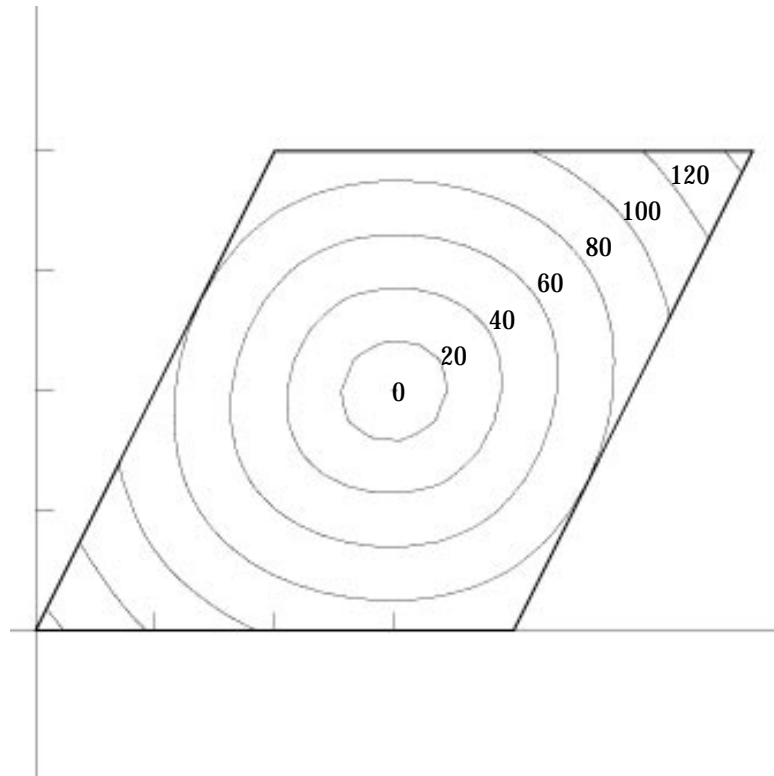


FIGURE 6.6: Contours of activation time for a trapezoidal mesh.

from what would be expected in a fully converged solution, the result has been resolved using smaller values of either Δt or Δx , or both. In every case looked at, the solution has indeed become as expected, demonstrating that the underlying models are accurate.

6.3.7 Non-orthogonal geometry

In order to check that the metric tensors correctly specified the distortion of geometry between collocation points, a trapezoidal mesh provides a skewed geometry. The resulting mesh contained the same number of elements as in the previous examples, but the top of the mesh was shifted by half its width, i.e. 64 mm. The same parameters and initial conditions were used, and DTAR was employed. The solution required 1467 iterations which took 1m55.7s (CPU) and the resulting isochrones of the activation time are shown in Figure 6.6. These isochrones are almost exactly circular, with the slight elongation in the direction of the long axis due to the extreme

distortion, which is substantially greater than would normally occur.

6.3.8 Anisotropy with a constant fibre angle

The original square mesh was modified to include a constant 0° fibre angle at all points throughout the domain. The conductivities were modified such that the ratio between them was 5:1. The conductivities used were $\sigma_f = 1 \text{ mS} \cdot \text{mm}^{-1}$ and $\sigma_s = 0.2 \text{ mS} \cdot \text{mm}^{-1}$. Isochronal contours of activation time for this setup are plotted in Figure 6.7a. The mesh took just over 240 ms to fully activate. When the fibre angle was changed to a constant 45° the ellipsoidal pattern was similar, but aligned with the new fibre axes as shown in Figure 6.7b. In this case, the mesh required only 220 ms to fully activate.

The next pair of diagrams show the activation patterns as the conductivity ratio is changed. Both examples have a constant fibre angle of 30° . For the diagram on the left in Figure 6.8a the conductivities are the same as above. The right-hand diagram of Figure 6.8 shows the contours for a 10:1 conductivity ratio which uses conductivities of $\sigma_f = 1.5 \text{ mS} \cdot \text{mm}^{-1}$ and $\sigma_s = 0.15 \text{ mS} \cdot \text{mm}^{-1}$. The fibre conductivity was increased so that the mesh was fully activated in approximately the same time, though the greater elongation of the ellipses can still be seen.

6.3.9 Point stimulus with varying fibre angle

The next pair of simulations use the material properties defined above with a domain which includes a varying fibre angle. In Figure 6.9a the fibre angle varies linearly from 10° at the top and bottom edges of the mesh to a maximum of 90° in the centre of the mesh. The second example on the right, the fibre angle varies linearly from 50° along the lower edge through 90° in the centre to 130° along the top edge of the mesh. In each example, the domain was activated in the centre, and the ratio of conductivities was 10:1 with values as given in the previous example. The RMS errors in fitting the contour fields of activation time were 0.56 ms and 0.52 ms respectively. As expected, the contour lines follow the fibre directions as the wavefront propagates most quickly in these directions.

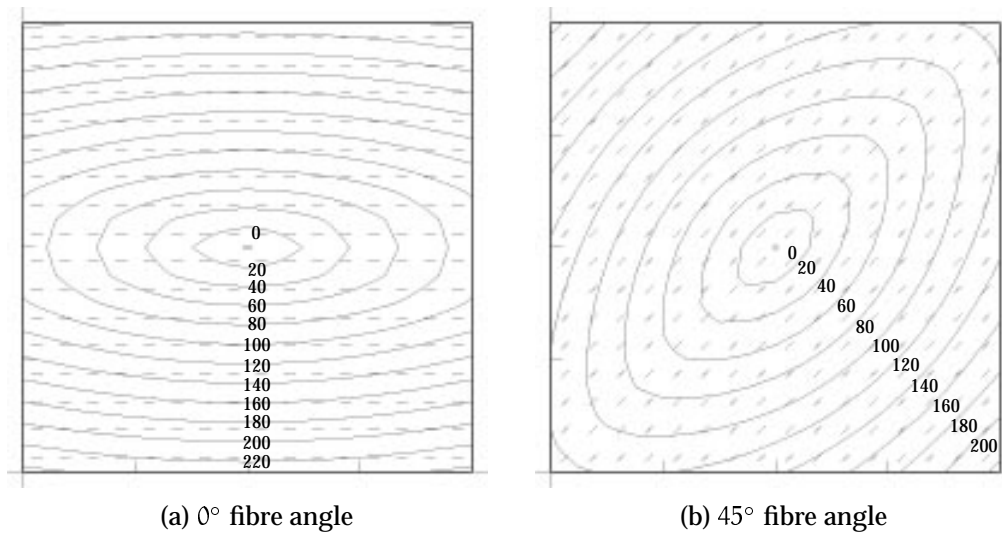


FIGURE 6.7: Contours of activation time for a constant fibre angle and anisotropic conductivities. (a) 0° fibre angle. (b) 45° fibre angle.

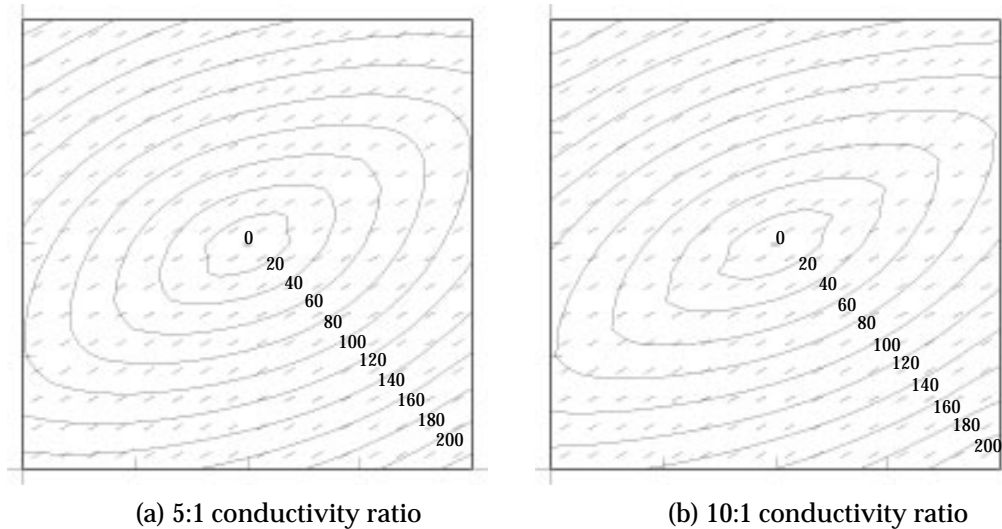


FIGURE 6.8: Contours of activation time for a constant 30° fibre angle and varying anisotropic conductivities. (a) 5:1 conductivity ratio. (b) 10:1 conductivity ratio. The fibre conductivity is greater in the 10:1 case than in the 5:1.

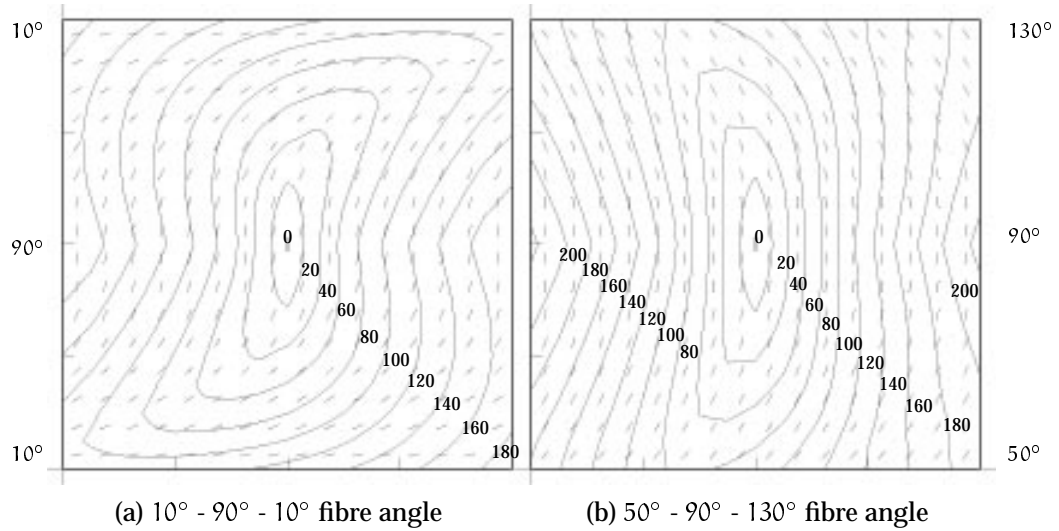


FIGURE 6.9: Contours of activation time for a constant conductivity ratio and varying fibre angles. (a) The fibre angle varies from 10° through 90° and back to 10° from bottom to top throughout the mesh. (b) The fibre angle varies from 50° through 90° to 130° .

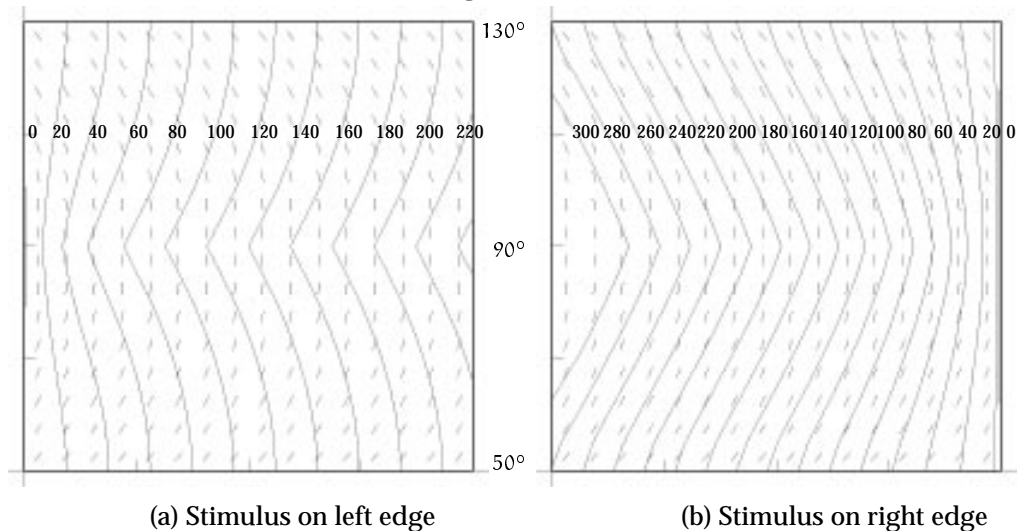


FIGURE 6.10: Contours of activation time showing the effect of fibre curvature on wavefront propagation. (a) Line stimulus on the left hand edge of the mesh (TA Propagation). (b) Line stimulus on the right hand edge of the mesh (TW Propagation).

6.3.10 Line stimulus with varying fibre angle

Using the second of the above meshes, we can investigate the effect of fibre curvature on wavefront propagation. Figure 6.10 shows the activation isochrones of two stimuli to the domain, the first from the left and the second from the right. Rogers and McCulloch (1994b) discuss this phenomenon and define two terms to describe the direction of propagation. The propagation against the fibre curvature shown in Figure 6.10a is called *TA* (Transverse Against) propagation, and the alternate is termed *TW* (Transverse With) propagation. The results shown here confirm the conclusions of Rogers and McCulloch who show that the *TA* wave propagates up to 65% more quickly than the corresponding *TW* wave. In this case here, the *TA* wave (left stimulus) activated the entire domain in 245 ms, and was 40% faster than the *TW* (right edge) activation which took 345 ms. The RMS errors in fitting the contour fields of activation time were 0.23 ms and 0.34 ms respectively.

6.3.11 Using the FitzHugh-Nagumo model

A number of ionic current models have been implemented which integrate with the collocation activation model. The simplest change from the cubic model is the FitzHugh-Nagumo model (see Section 4.2.2). The FHN model was used with parameters given in Table 6.3 and gave identical results whether or not the DTAR algorithm was used, with point \mathbb{F} in the lower left corner being activated 118.5 ms after a central stimulus for each technique. The non-DTAR solution required 7m20s (CPU) to achieve 1500 iterations, which is 56,768 cpi/s. This indicates that the computation required for the FHN model is approximately 11% greater than that for the cubic model. While the non-DTAR solution rate was constant at 29 s per 100 iterations, the DTAR solution varied between 4s (CPU) and 38s (CPU) per 100 iterations, showing the computational overhead of up to 25% required by the DTAR method. The effective solution rate for the DTAR technique was 75,649 cpi/s, which is considerably slower than the cubic solution, and is due to the additional time each point is active due to the recovery processes.

Activation time isochrones are drawn in Figure 6.11a and a colour plot showing the transmembrane potential at 50 ms is drawn in the right hand side of the same figure.

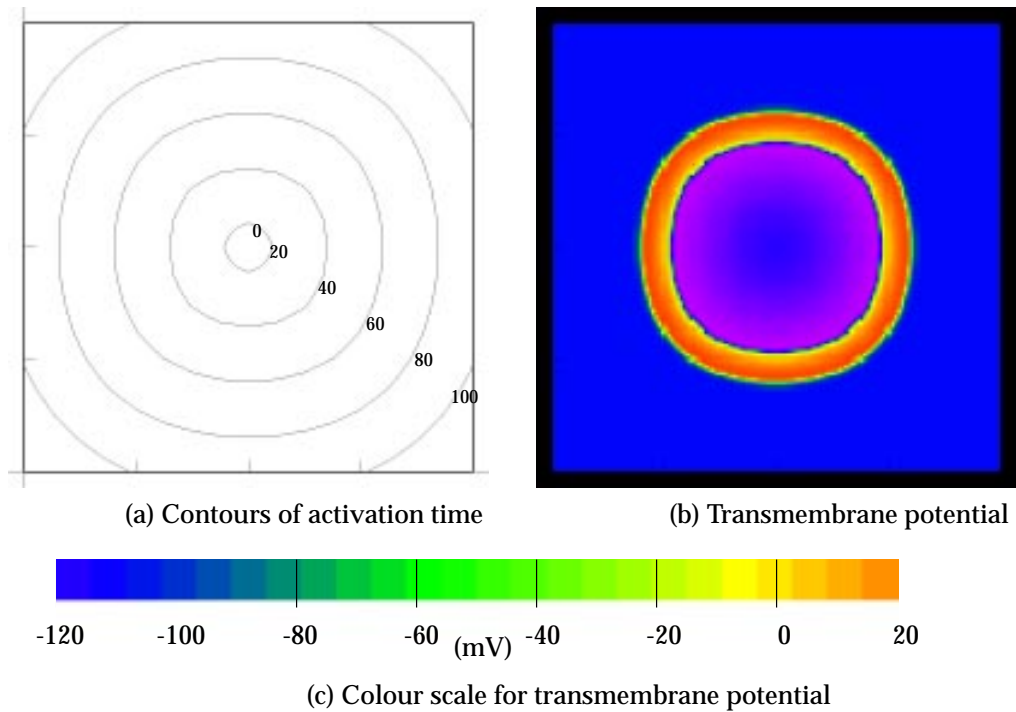


FIGURE 6.11: Isotropic activation of a square using the FHN ionic current model. (a) Contours of activation time. (b) Value of the transmembrane potential at $t = 50$ ms. (c) The colour scale for the transmembrane potential.

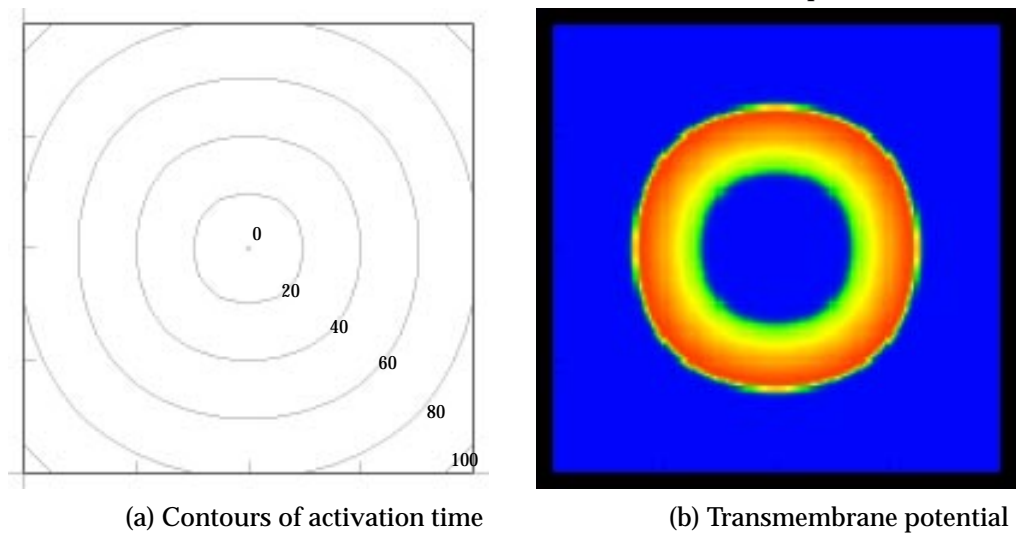


FIGURE 6.12: Isotropic activation of a square using the modified Rogers-FHN ionic current model. (a) Contours of activation time. (b) Value of the transmembrane potential at $t = 50$ ms.

Parameter	Value	
C_m	10	$\text{nF} \cdot \text{mm}^{-2}$
A_m	200	mm^{-1}
$\sigma_{f,s}$	1	$\text{mS} \cdot \text{mm}^{-1}$
V_{rest}	-85	mV
$V_{\text{threshold}}$	-75	mV
V_{plateau}	15	mV
c_1	6×10^{-3}	
c_2	5×10^{-3}	
b	0.02	
d	1	

TABLE 6.3: Values of the constants for an isotropic domain and the FitzHugh-Nagumo ionic current model.

Figure 6.11c shows the colour scale used in this and subsequent figures involving transmembrane potential. The RMS error for the contour field was 0.301 ms.

The FHN model with Rogers-McCulloch modifications

The identical problem was solved using the form of the FHN model developed by Rogers and McCulloch (1994a) which has a shorter recovery process due to the lack of undershoot of the transmembrane potential. The difference in activation times at the furthest corner of the mesh was negligible (0.1 mV) depending on whether or not DTAR was used. Figure 6.12 shows activation contours and a colour map of the potential at $t = 50$ ms, with an RMS error on the contour fit of 0.178 ms. A complete activation using the DTAR technique took 4m8s (CPU) to complete 1440 iterations, with an estimated 96,508 cpi/s. The non-DTAR solution took 7m16s (CPU) for 1500 iterations, which is almost identical to the original FHN model.

Parameter	Value	
C_m	2.5	$\text{nF} \cdot \text{mm}^{-2}$
A_m	200	mm^{-1}
$\sigma_{f,s}$	1	$\text{mS} \cdot \text{mm}^{-1}$
T	5	

TABLE 6.4: Values of the constants for an isotropic domain and the van Capelle-Durrer ionic current model.

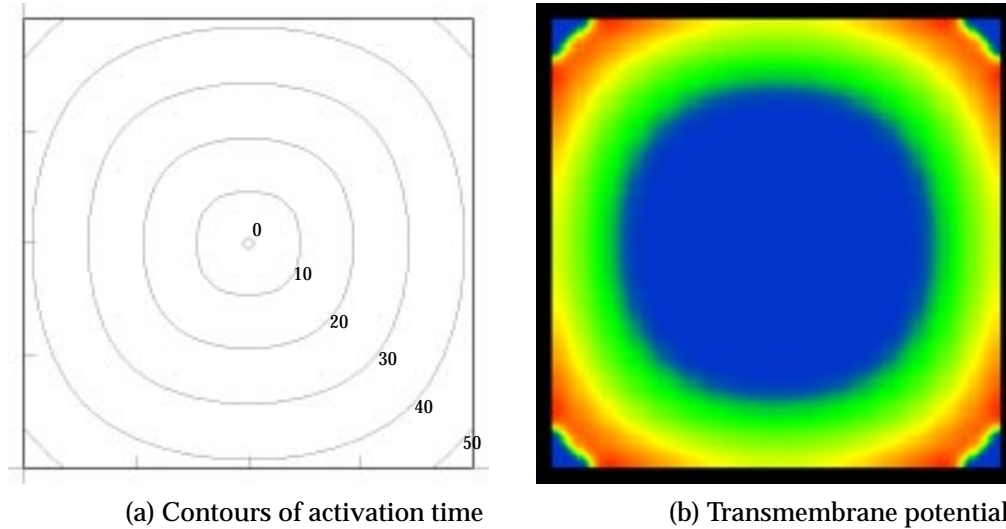


FIGURE 6.13: Isotropic activation of a square using the modified van Capelle-Durrer ionic current model. (a) Contours of activation time. (b) Value of the transmembrane potential at $t = 50$ ms.

6.3.12 Using the van Capelle-Durrer model

The van Capelle-Durrer (VCD) model (see Section 4.2.3) was also employed on the isotropic square domain, with the parameters given in Table 6.4. The modified form of this equation was used, with parameters as defined in Table 4.6 for “ischemic” conditions. Using these parameters and conditions, the solution took 8m5s (CPU) for 1500 iterations, which is 51,467 cpi/s, and about 20% slower than the cubic model. An efficient algorithm for removing points from the DTAR active list had not been formulated, and therefore the DTAR model ran about 15% slower than the non-DTAR model. Activation isochrones are drawn in Figure 6.13a with a RMS on the field fit of 0.105 ms, and a complete activation of the mesh in 53 ms. The second

diagram shows the transmembrane potential at $t = 50$ ms, at which point the mesh is almost entirely activated. The reason for using this particular modified version of the VCD model is that it is designed to facilitate the creation of reentrant spiral waves.

6.3.13 Biophysically-based models

The next stage of activation modelling involves using a biophysically based ionic current model to describe the membrane kinetics, such as one of those presented in Section 4.1. One of the simpler models relating to ventricular tissue is the Beeler-Reuter model (Section 4.1.4), and this was implemented in the activation model, together with options for sodium kinetics described either by Ebihara and Johnson (Section 4.1.5) or by Drouhard and Roberge (Section 4.1.6) in addition to the standard Beeler-Reuter model of the sodium current.

The standard isotropic example used throughout this chapter was solved using the BR model. The nature of the BR model defines an action potential (Figure 4.14) which is considerably longer than a FHN or VCD action potential. Therefore in order to view an entire action potential (including recovery) on the mesh at a single time instant, the conductivities were reduced by a factor of ten to a value of $0.15 \text{ mS} \cdot \text{mm}^{-1}$. Other constants were defined as in Table 4.4, except that the membrane capacitance was defined to be the same as used in the above examples. A full solution of the activation totalled 19000 iterations at 0.1 ms time step increments, and required 216m40s (CPU). This is equivalent to 24,321 cpi/s which is less than half the speed of the VCD model, and just over a third of the speed of the cubic model. A large portion of this additional time is due to the computation of exponents for the rate equations which were determined as required. A quicker method would be to compute the values once only, and store them in a lookup table for later use. Solutions using the DTAR method were, as in earlier examples, indistinguishable from the full solution.

Activation isochrones are drawn at 100 ms intervals in the left-hand diagram in Figure 6.14, and on the right is a map of transmembrane potential throughout the mesh at $t = 500$ ms, with the same ranges on colour shadings as above.

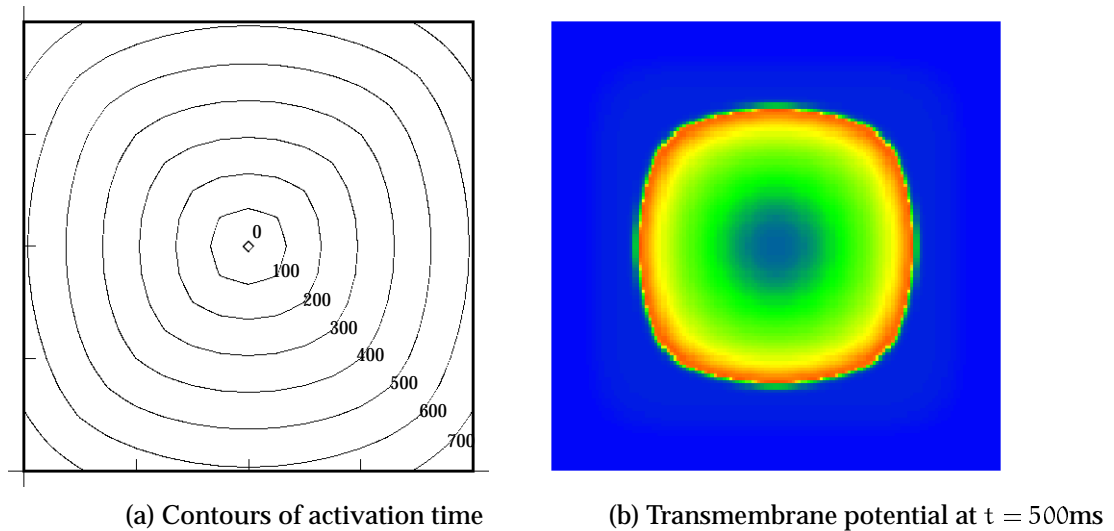


FIGURE 6.14: Isotropic activation of a square using the Beeler-Reuter ionic current model. (a) Contours of activation time. (b) Colour field of the value of the transmembrane potential at $t = 500$ ms.

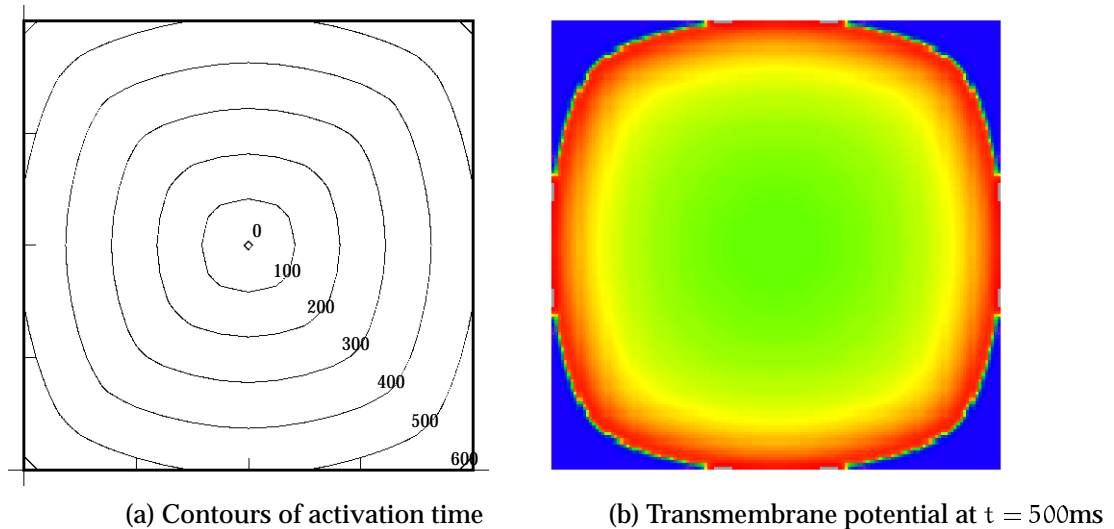


FIGURE 6.15: Isotropic activation of a square using the Beeler-Reuter ionic current model with sodium current modifications by Drouhard and Roberge. (a) Contours of activation time. (b) Colour field of the value of the transmembrane potential at $t = 500$ ms (with range of -120 mV to 40 mV).

The same example was repeated using the BR-DR model (Section 4.1.6) which varies from the above only in the implementation of the sodium current. The constants used were as above, except that the sodium conductance ($\overline{g_{Na}}$) and sodium reversal potential (E_{Na}) were changed to match the values given in the original paper by Drouhard and Roberge (1987). Similar plots of activation time and potential are shown in Figure 6.15 with the only difference being a range of -120 mV to 40 mV on the colour map of membrane potential at $t = 500$ ms.

6.4 Reentrant Waves from Multiple Stimuli

Using some of the ionic current models with certain parameters, it is possible to generate reentrant waves, either by setting appropriate initial conditions (of potential and other state variables) or by defining appropriate stimuli on an initially quiescent region. The latter approach is preferred because it is potentially reproducible in an experimental situation. In general, these waves are constructed by using two stimuli. The first excites the region, and then a second stimulus is added during the refractory period of the first activation wave, which allows for re-stimulus in a single direction only.

In this section, the van Capelle-Durrer equation is used with the modifications described in Section 4.2.3 for ischemic behaviour (producing shorter APD and therefore a greater possibility for a self-sustaining reentrant wave). Because we use the VCD model for these simulations the DTAR algorithm is not employed, but even if a different ionic current model had been used it would still be unwise to use DTAR as most of the points are active at any one time, and the housekeeping procedures would increase rather than decrease the total solution time. An example is also shown using the Beeler-Reuter ionic model and incorporates a more physiologically reasonable restitution period.

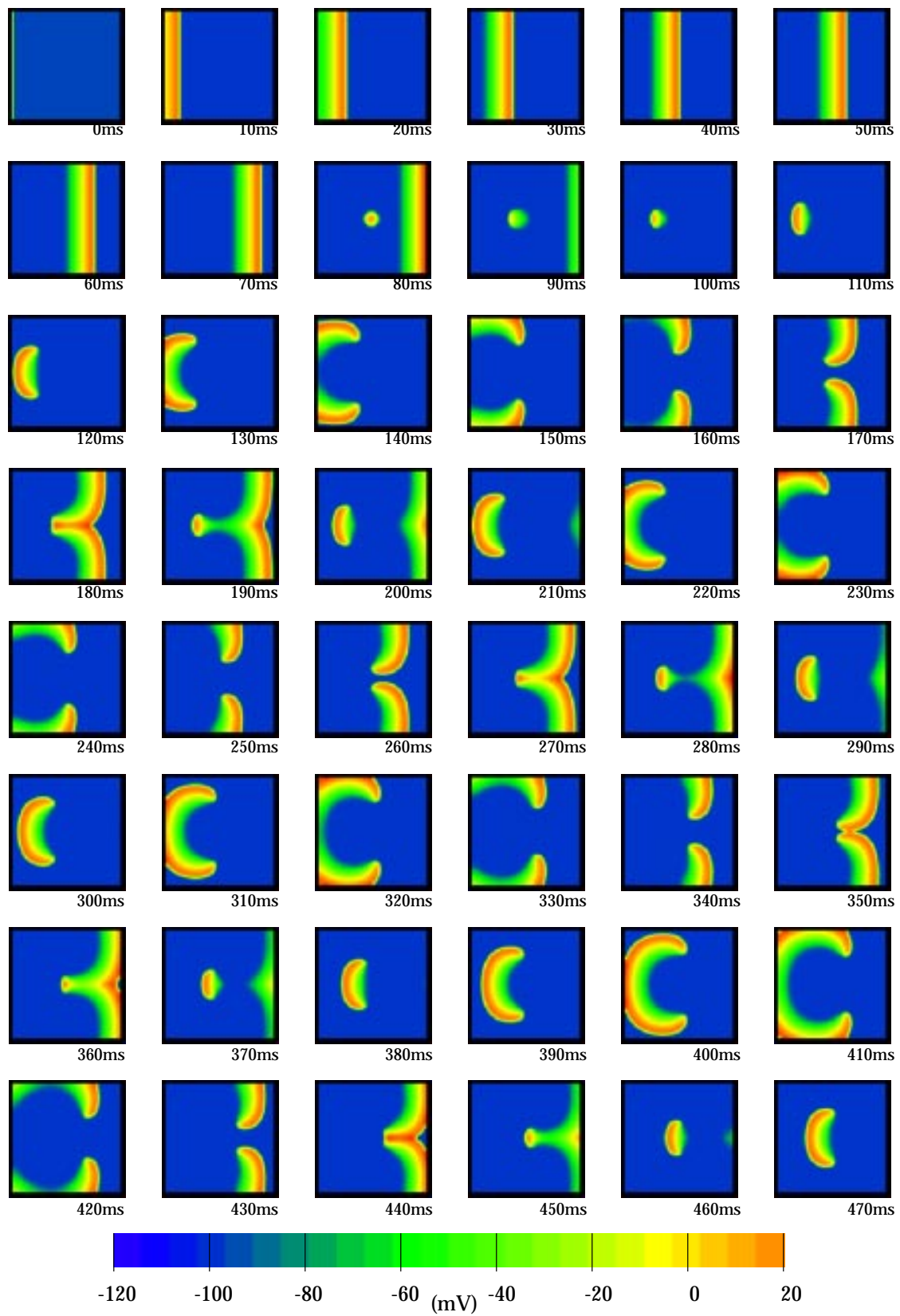




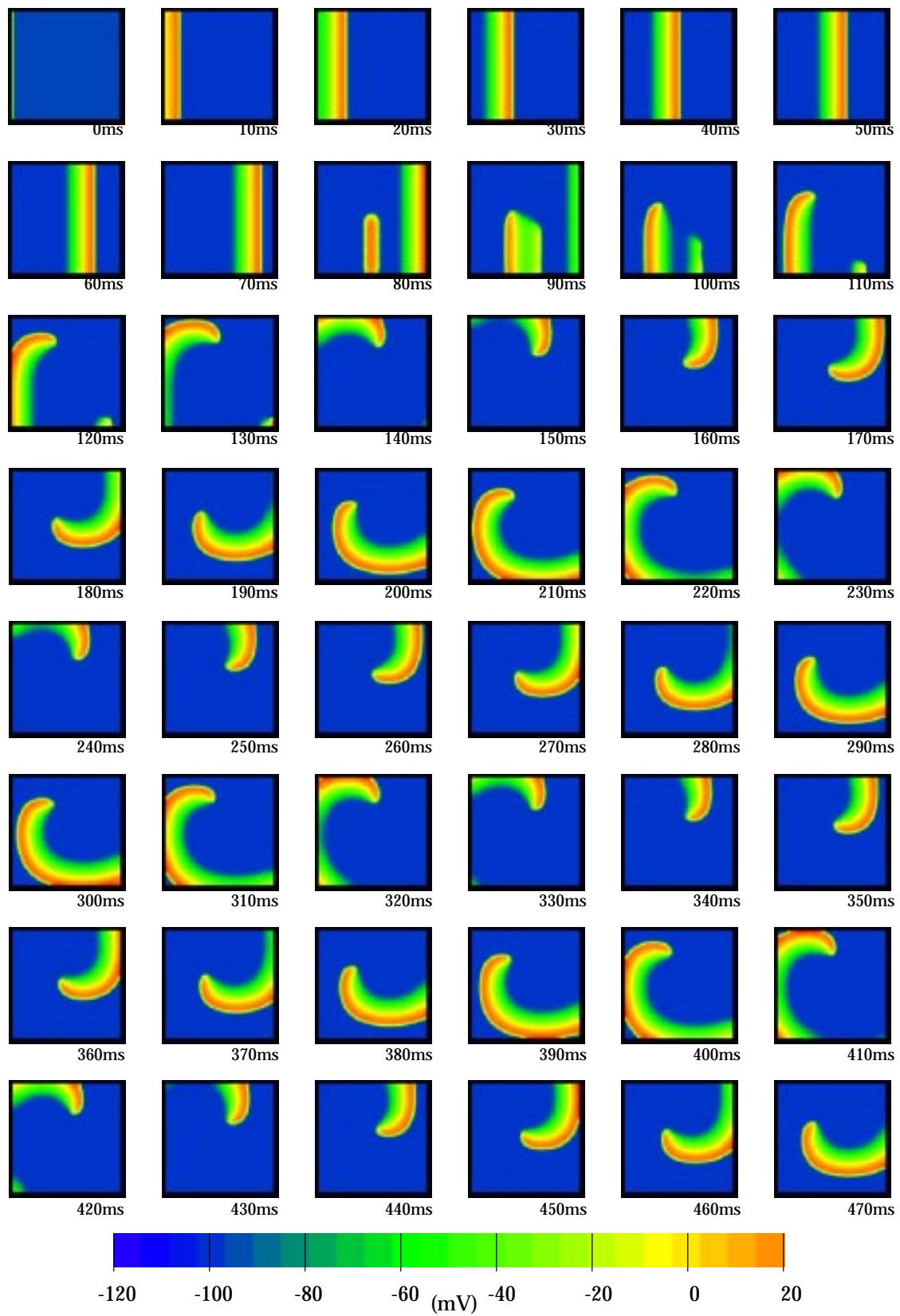
FIGURE 6.16: Symmetric spiral waves produced from a point stimulus.

6.4.1 Point re-stimulus

The first example defines an isotropic square mesh as used above, with the same VCD model and parameters as defined in Section 6.3.12. An initial plane wave is initiated along the left hand edge of the mesh at $t = 0$ ms with a stimulus as above of duration 1 ms and amplitude $0.1 \text{ mA} \cdot \text{mm}^{-3}$. A second stimulus of duration 1 ms and amplitude $0.5 \text{ mA} \cdot \text{mm}^{-3}$ is made at $t = 75$ ms at a group of 9 collocation points surrounding point \mathbb{A} . Due to the isotropy of the material and the precise timing of the second stimulus to lie within the restitutive period of the first wave as it passes this point, a pair of symmetric spiral waves are initiated. A time series showing the development of the spiral waves is shown in Figure 6.16.  reentry/vcdisopt Note the unidirectional block caused by the recovering tissue in frames $t = 80 - 110$ ms, and the collision of the wavefronts in frame $t = 180$ ms. If the second stimulus is initiated 5 ms earlier, then no propagated wave results, as the region surrounding the second stimulus has not recovered enough to support reactivation, and a 5 ms delay in the second stimulus produces bi-directional propagation, and the (near) circular wavefront propagates throughout the domain and then dies. The spiral waves have a period of just under 90 ms. As expected for an isotropic medium and an ionic model based on a cubic-type activation, the paths of the wavetips of the spiral waves are almost exactly circular.

6.4.2 Line re-stimulus

A single spiral wave can be generated if the second stimulus is a line, rather than a point. In this example a line of points between point \mathbb{A} and point \mathbb{H} is used as the re-stimulus line, with the second stimulus again being at $t = 75$ ms with an amplitude of $0.5 \text{ mA} \cdot \text{mm}^{-3}$. This produces a single spiral wave as shown in Figure 6.17.  reentry/vcdisoln As above, the second stimulus has a magnitude of $0.5 \text{ mA} \cdot \text{mm}^{-3}$, and is applied at $t = 75$ ms for a duration of 1 ms. In an isotropic domain such as this, the stimulus produces a single rotating spiral whose tip traces a stationary circular path. Note that a partial wave is initiated (frames 90 ms to 130 ms) propagating behind the first wavefront. Because it is propagating into recovering tissue, it propagates more slowly than the other second wave, reaching the external boundary after 50 ms, whereas the spiralling wave reaches the boundary after 35 ms.

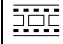
FIGURE 6.17: Spiral wave produced from a line stimulus between Δ and \mathbb{H} .

The partial wave quickly dies out. Again, the path traced by the wavetip of the spiral is circular, and the cycle period is around 90 ms, as in the previous example.

6.4.3 Reentry and anisotropy

A number of factors influence the shape and passage of reentrant waves, including anisotropic material parameters and a deforming geometry. This section briefly considers the effect of varying fibre orientations on spiral waves. Each example is similar to the previous example, except that the initial activation wave is propagated from the right hand edge of the domain. In each case, the stimulus has an amplitude of $0.5 \text{ mA} \cdot \text{mm}^{-3}$ and a duration of 1 ms, though the application time of the stimulus varies. A conductivity ratio of 2:1 is used with conductivities of $\sigma_f = 1 \text{ mS} \cdot \text{mm}^{-1}$ and $\sigma_s = 0.5 \text{ mS} \cdot \text{mm}^{-1}$. The VCD model is again used with all other material constants being the same as in Table 6.4.

Constant fibre orientation

The fibres are aligned to be constantly horizontal throughout the mesh, and with the wave initially propagating along the fibre direction, the second stimulus is applied slightly earlier than above at $t = 70 \text{ ms}$ in order to lie within the restitutive zone. The resulting spiral wave is shown in Figure 6.18.  reentry/vcdconst The wavetip now traces a slightly elliptical path aligned with the fibre direction, and the spiral period is substantially lengthened to about 180 ms due to the slower propagation across the fibres.

A similar example using a constant 30° fibre angle throughout the mesh produces a similar result, though the ellipse traced by the wavetip is rotated so that the long axis is aligned with the fibre direction.

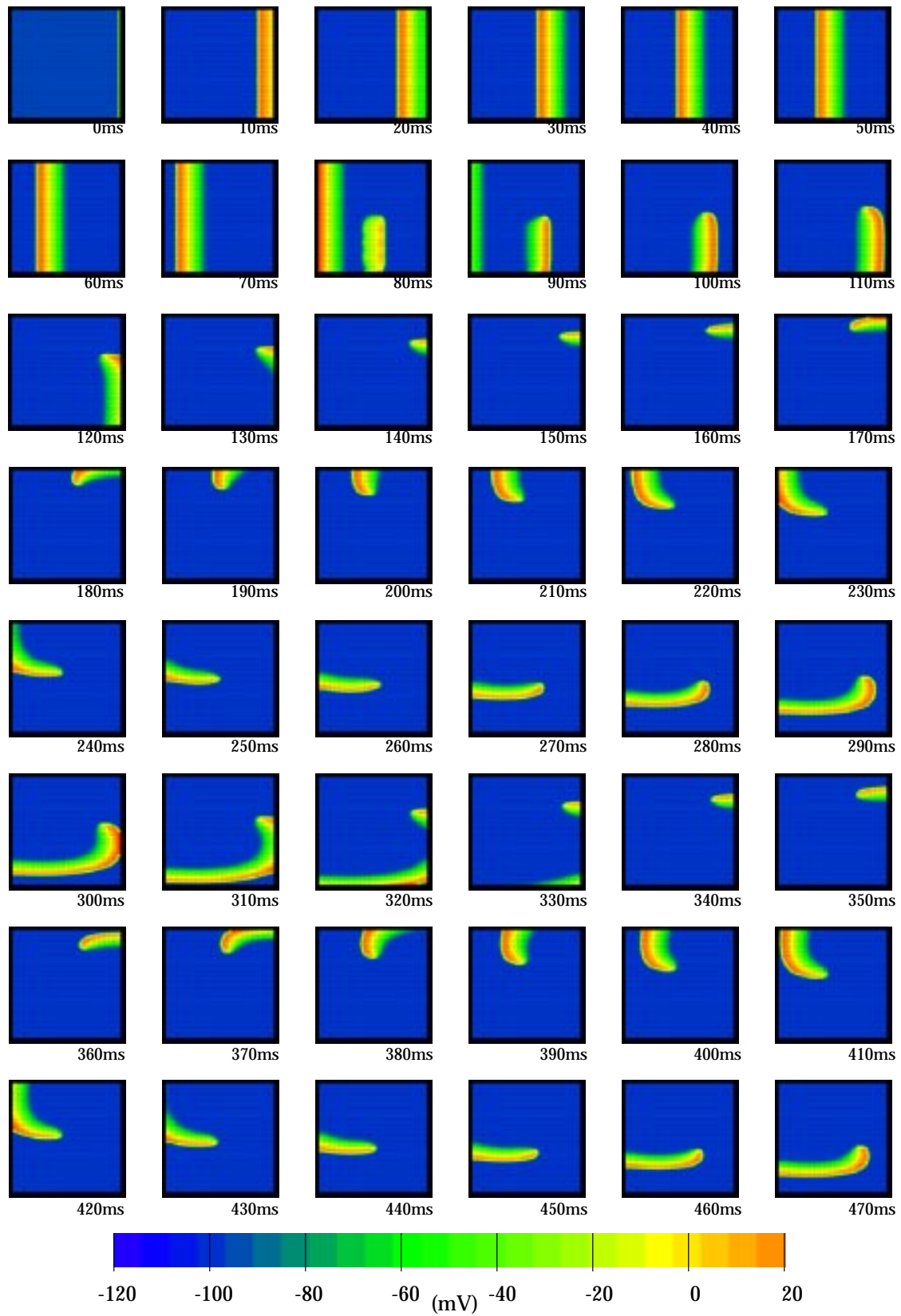


FIGURE 6.18: A constant fibre orientation causes the path of the spiral tip to elongate.

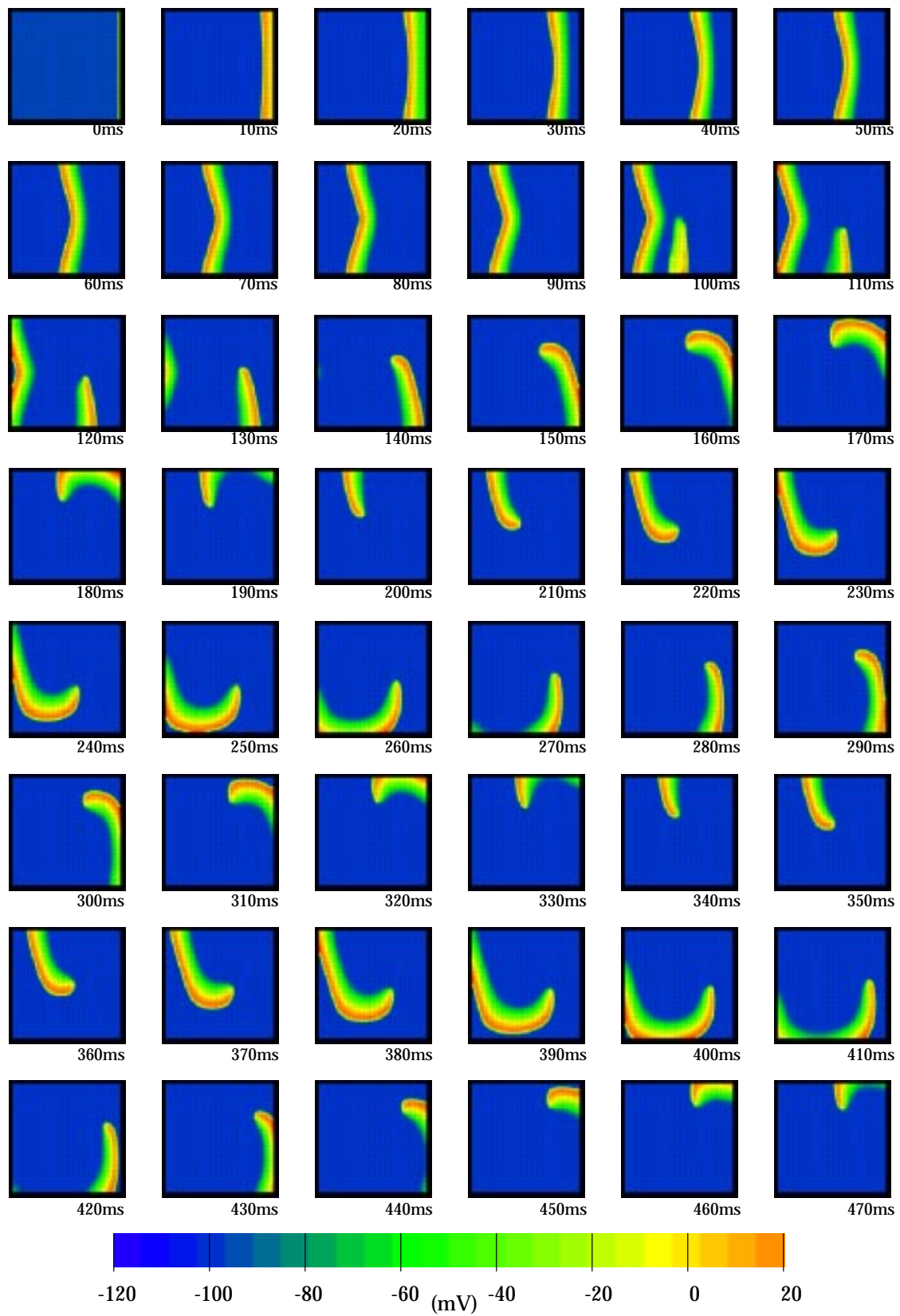

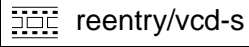


FIGURE 6.19: Spiral wave propagation in a curved fibre field.

Curved fibre orientation

The fibre direction changes from 50° at the bottom of the domain to 130° at the top, in the same pattern used in the simulation in Figure 6.9b. The initial wave is propagating across the fibre direction and is therefore slower, which means that the second stimulus is applied later at $t = 90$ ms. The resulting spiral wave is shown in Figure 6.19.  With this orientation of the fibre direction, the ring about which the wavetip is circling drifts to the right.

S-shaped fibre orientation

For this example we use again the fibre field shown in Figure 6.9a which is 10° at the top and bottom of the domain and varies linearly through an angle of 90° in the centre of the mesh. In this case the appropriate time for the second stimulus to be applied is at $t = 75$ ms, which results in the spiral wave shown in Figure 6.20.  This shows the wavefront deforming in shape because of the varying anisotropy, but the wavetip follows an almost stationary path, drifting only very slowly to the left.

Beeler-Reuter model

Reentrant phenomena are described more accurately using a biophysical ionic current model, due to the additional variables which help to describe the repolarisation of the membrane, and model the refractory processes and membrane restitution. The Beeler-Reuter model is used here in an almost identical scenario to the previous example, with the same fibre field. Due to the fact that this model has a considerably longer action potential than either the FHN or VCD models, the same conductivities as above would have resulted in the wave being active over the whole region simultaneously, and there is no time at which a second stimulus could be applied to cause a reentrant wave. In order to produce a wavefront with a shorter spatial length the conductivities were reduced to $\sigma_f = 0.2 \text{ mS} \cdot \text{mm}^{-1}$ and $\sigma_s = 0.1 \text{ mS} \cdot \text{mm}^{-1}$ while maintaining the above-used 2:1 conductivity ratio.

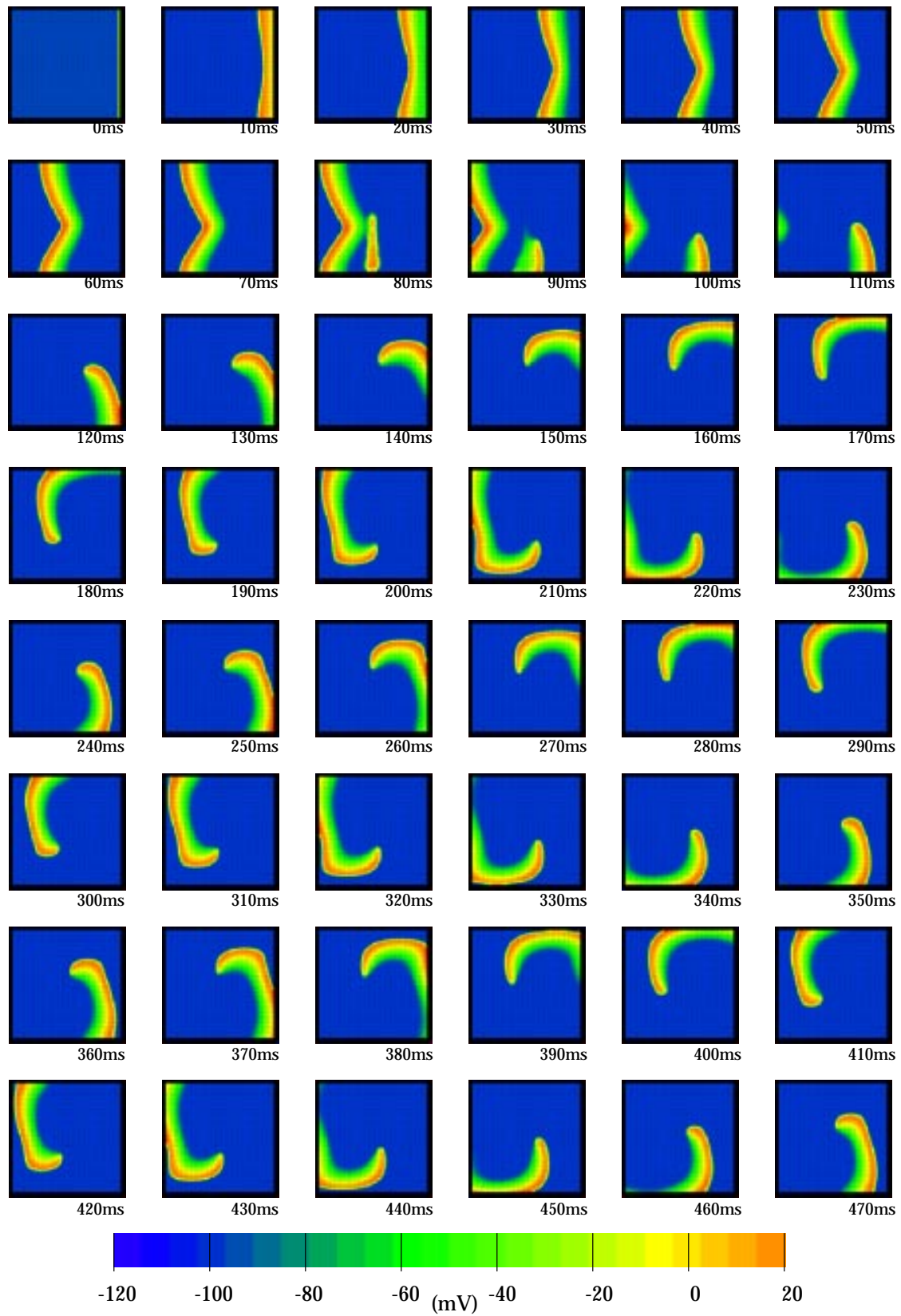


FIGURE 6.20: Spiral wave propagation in an S-shaped fibre field.

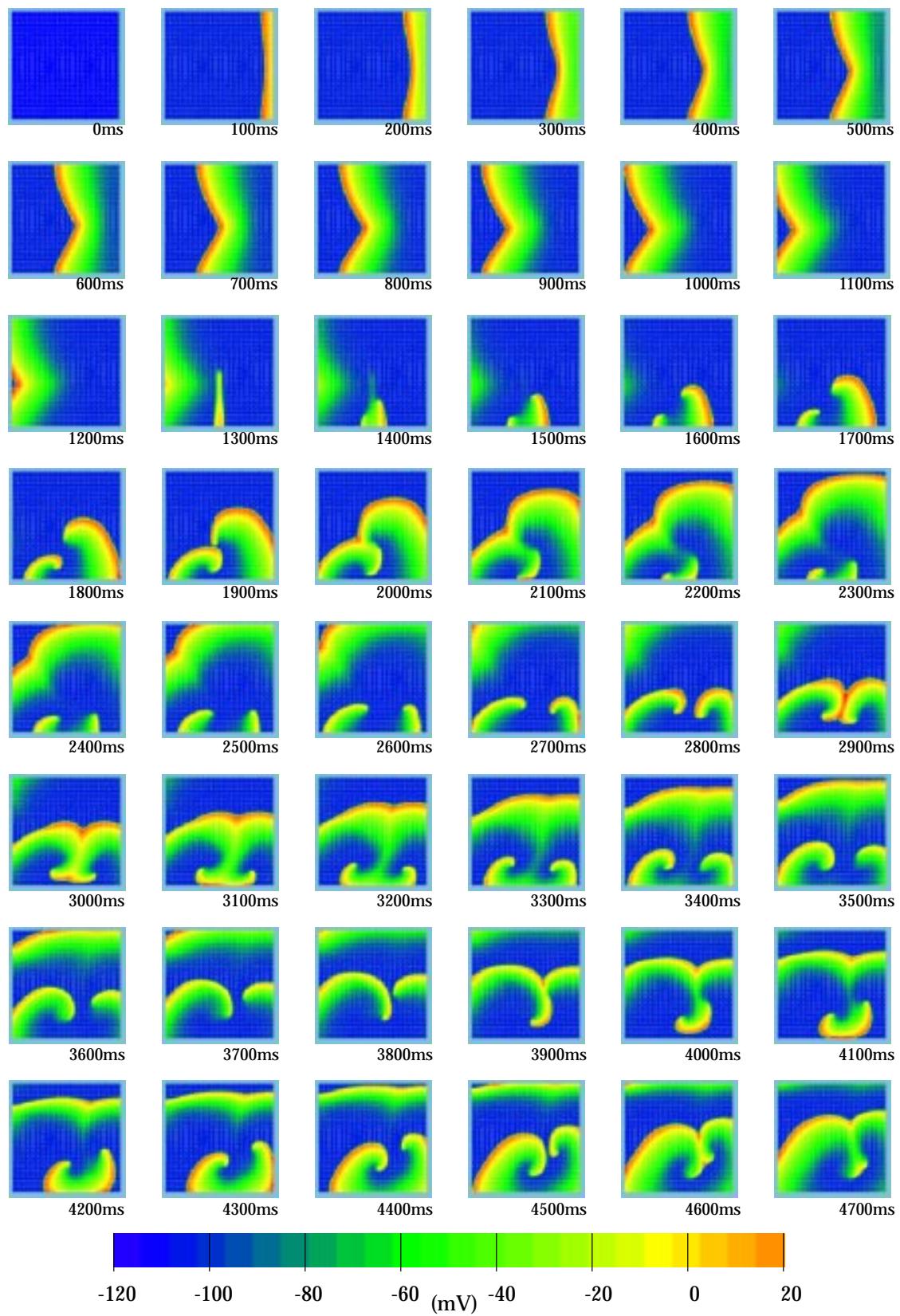


FIGURE 6.21: Spiral wave propagation in an S-shaped fibre field using the Beeler-Reuter ionic current model.

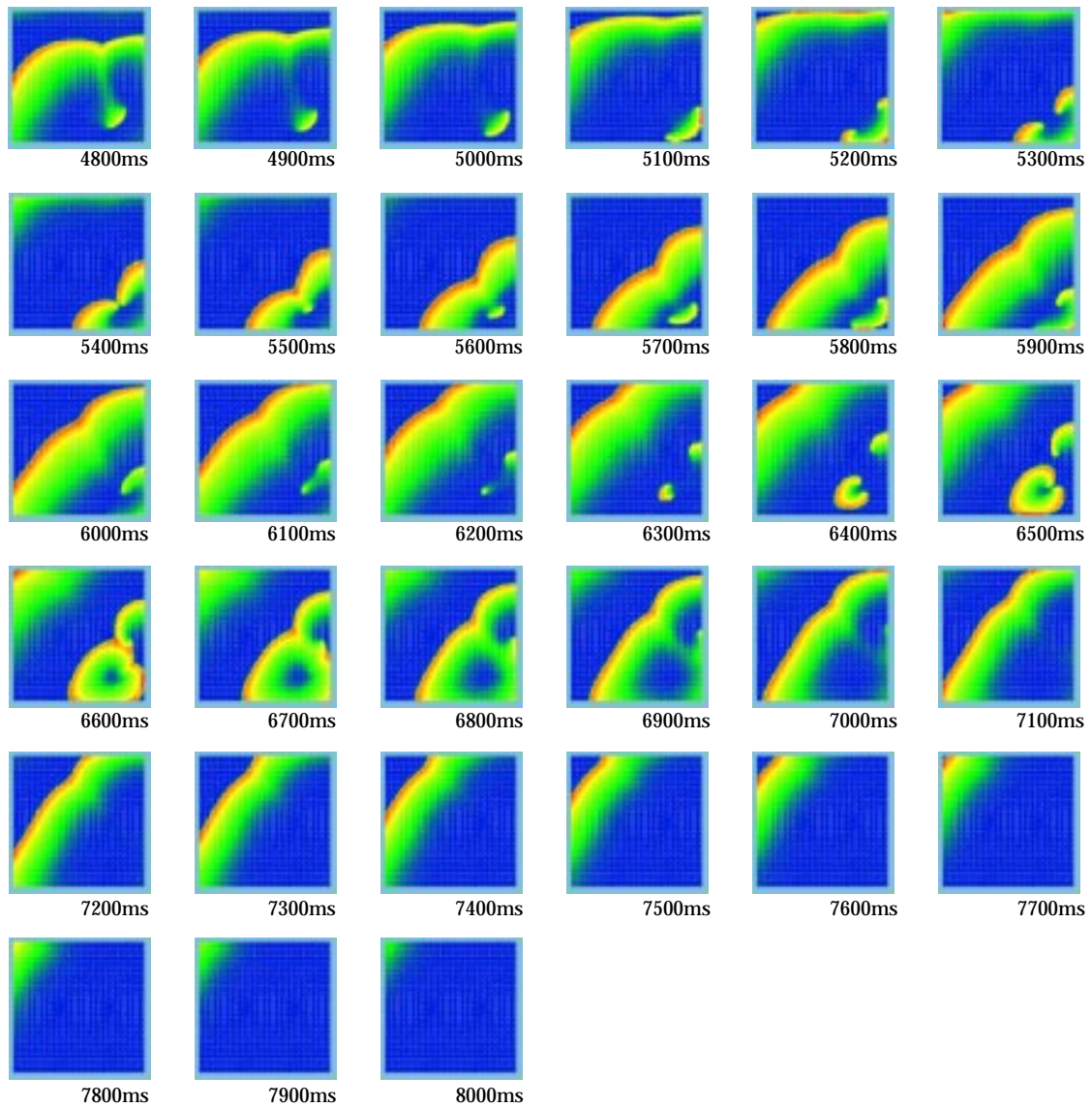
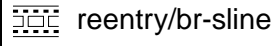


FIGURE 6.22: Previous figure continued

A similar activation protocol to the VCD model example above is employed, in which the right-hand edge of the mesh is stimulated with a $0.1 \text{ mA} \cdot \text{mm}^{-3}$ pulse for 1 ms, followed by a stimulus to the lower half of the centre line with a magnitude of $0.2 \text{ mA} \cdot \text{mm}^{-3}$ for a period of 4 ms. Due to the nature of the wave on the anisotropic domain it was difficult to determine a time for the second stimulus which would produce a single rotating wave, and the most appropriate stimulus time was at $t = 1250 \text{ ms}$. The resulting activation is shown in a time sequence in Figures 6.21 and 6.22, and in the following analysis, the frames are referred to for convenience as frames 0 through 80 with each frame being at 100 ms increments.

 Each frame of the movie required approximately 13m (CPU) to compute and draw on the Alpha workstation.

Following the second stimulus, a pair of resulting waves can be observed in frame 14. The smaller wave, propagating to the left, propagates more slowly than the other wave due to it travelling into less-recovered tissue. The left-hand wave reaches the left-hand boundary in frame 20, whereas the other wave has reached the opposite boundary by frame 18. The interactions of the multiple wavefronts can be clearly seen in the subsequent frames. The influence of the waves meeting in the centre of the domain (as in frames 29 and 30) is shown in the subsequent passage of the right hand wave in frames 33 to 38 in a vertical fashion, without entering that central zone. The cause of the final extinction of the wave is shown in frames 60 to 62 where a small portion of the wave becomes separated from the rest, and this single dot behaves as a point stimulus, producing a final wave which travels throughout the entire domain.

6.5 Using The Bidomain Model

In some situations a measure of the extracellular potential is required, and therefore it is necessary to solve the coupled system of bidomain equations (Equations (3.9) and (3.11)). Modelling of the potential field generated in the torso and on the body surface is one such example, in which the models are coupled across the epicardial surface through the extracellular potential to the extramyocardial potential. Alternatively, an electric field may be applied in the extracellular space as a means of stimulating the myocardium, and the coupling to the transmembrane

potential is through the extracellular equation. This is a common method of applying a stimulus in an experimental situation.

The initial approach to solving the extracellular equation made the assumption that the extracellular potential is both small relative to the transmembrane potential, and that it is relatively smooth. Using this assumption, the solution method was to solve the extracellular equation using the finite element method on the mesh from which the collocation grid had been generated. This gave the spatial resolution of the extracellular equation to be approximately 5 to 10 times greater than required for the transmembrane equation. The solutions using this method were ill-converged, and developed a divergent oscillation.

This lack of convergence is because the extracellular potential has spatial gradients of the same order as the transmembrane potential. While the above assumption is true for the potential measured some distance from the cell membrane, it is certainly not true at the scale on which the bidomain equations are constructed. Therefore the extracellular equation needs to be solved on the same scale as the transmembrane equation.

6.5.1 The coupled bidomain model

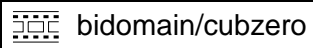

There are a number of possible solution methods for solving the coupled bidomain equations. The most elegant would be to use a solution technique based on the same collocation points used for the transmembrane solution, and one possible approach would be the use of a multigrid technique. The disadvantage to this technique is that it would be difficult to couple the extracellular potential across the myocardial boundary to a model of the field potential in the torso which, in our case, uses a combination of finite elements and boundary elements. Because of this restriction, the extracellular solution in this thesis uses a highly refined finite element mesh and the finite element technique to solve the equation. This is an inefficient method, and consumes unnecessarily large amounts of computer memory.

The series of simulations on which we determined the effectiveness of the bidomain model used a plane wave propagation across a square mesh as used in the previous problems. With isotropic conductivities, this approximates the solution of a one-

dimensional core conductor model. This meant that the mesh needed to be refined in one direction only, reducing the memory requirements. The mesh used had 64 elements in the x direction (in which the wavefront was propagating) and 16 elements in the y direction along which there were not large spatial gradients.

Two ionic current models were used. First, the cubic model tested simply the effect of activation on the wavefront, and subsequently the FHN model examined the effect of both activation and recovery. For the each model, an isotropic conductivity of $1 \text{ mS} \cdot \text{mm}^{-1}$ was used for the intracellular domain. The extracellular conductivity was 5 times this value, at $5 \text{ mS} \cdot \text{mm}^{-1}$. This would give a maximum value of ϕ_e as about $\frac{1}{5}$ of the range of values of ϕ_i , or about $\pm 20 \text{ mV}$. All other material parameters had the same values to those defined in Tables 6.2 and 6.3 for these two ionic models. In addition, two sets of boundary conditions were applied to the extracellular domain.

Zero boundary conditions

The first set of boundary conditions specify that the extracellular potential is zero on all external boundaries. This is equivalent to placing tissue in a bath of highly conducting solution. The resulting time sequence is shown in Figure 6.23  for the cubic model and in Figure 6.24  for the FHN model. These figures show a series of snapshots of the solution domain, with potential field maps of both the transmembrane and extracellular potentials at each time step. The transmembrane potential (on the left) varies between -90 mV and 20 mV , and the extracellular potential varies between -20 mV and 20 mV as shown in the colour scales along the bottom of each figure. Contour lines drawn on the extracellular field maps are at 2 mV intervals. Frames are shown at 5 ms intervals in rows from top to bottom.

For the cubic model under this set of boundary conditions, the extracellular potential forms a negative “cone” in front of the wavefront and a positive “cone” behind it. The potential values are heavily influenced by the boundary conditions, and the potential difference across the wavefront remains at less than 20 mV throughout the activation.

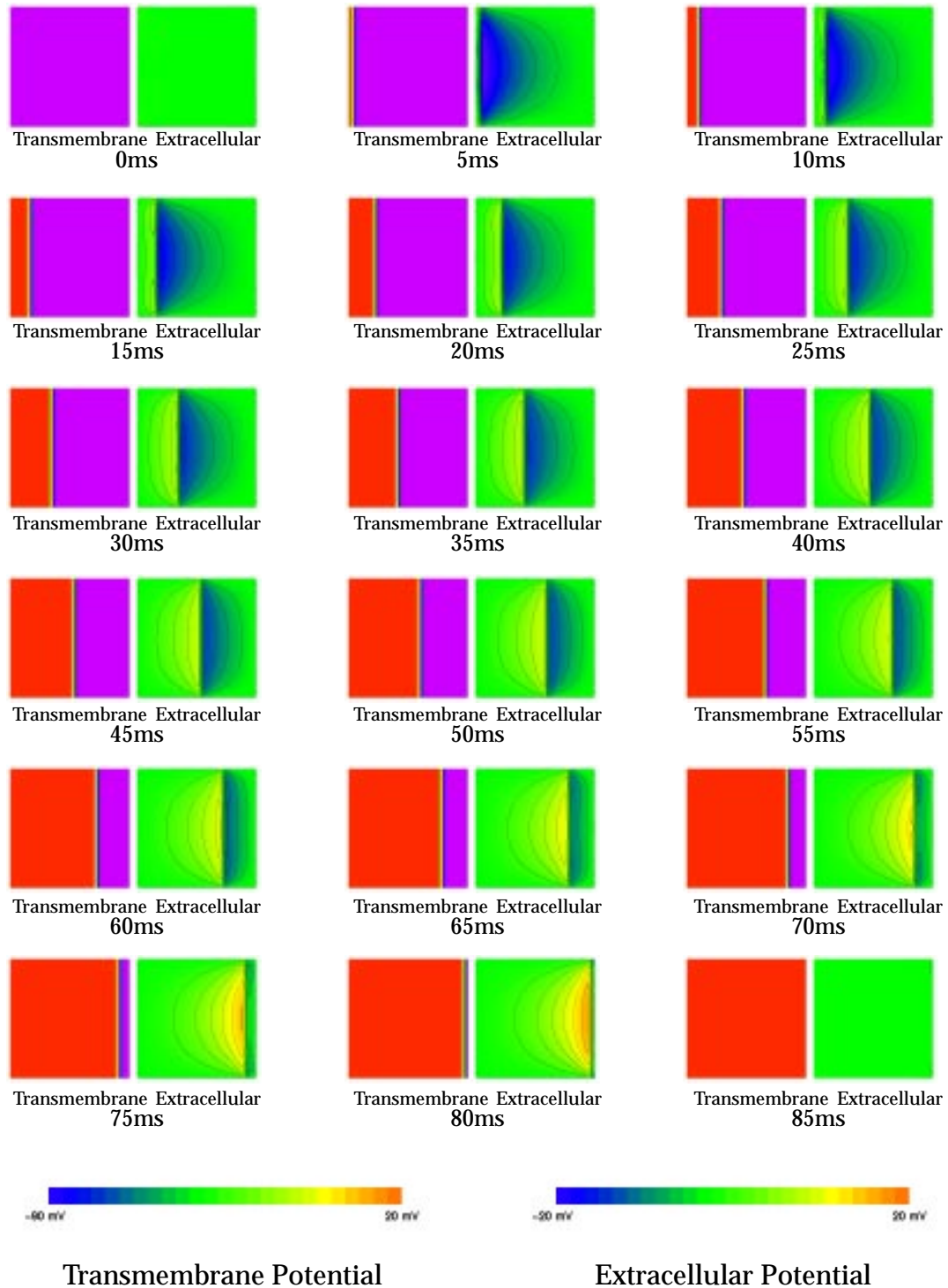


FIGURE 6.23: Plane wave stimulation using the cubic ionic equation in the bidomain model. The extracellular potential is fixed to zero on all boundaries.

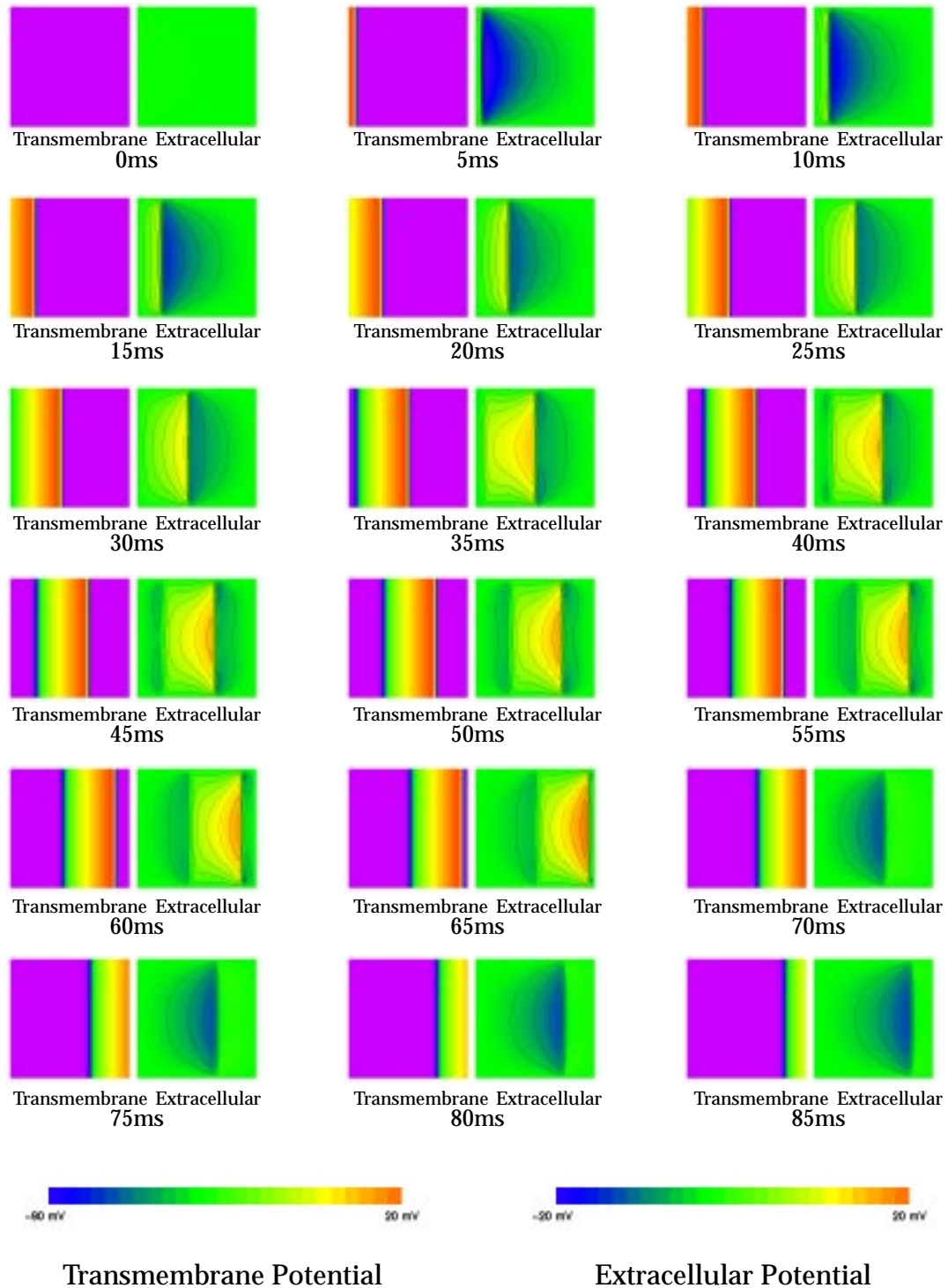
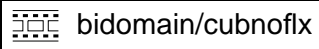


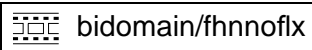
FIGURE 6.24: Plane wave stimulation using the FHN ionic equation in the bidomain model. The extracellular potential is fixed to zero on all boundaries.

The FHN model produces a very similar picture, with a negative extracellular potential in front of the wavefront, a positive potential during the wavefront and then a negative one again in the region which the wavefront has passed through.

For each model, the one-dimensional approximation is most valid along the horizontal centre line of the mesh, although the values are greatly influenced by the boundary conditions. As expected, the action potential velocity is not changed whether or not the extracellular potential is computed.

No-flux boundary conditions

The second set of boundary conditions again specify a zero potential on the left and right edges of the mesh, but specify a no-flux boundary condition on the extracellular potential on the top and bottom edges. This provides a solution which gives a better approximation of one-dimensional propagation, as can be seen for the cubic model in Figure 6.25  and for the FHN model in Figure 6.26

.

In these figures, the isopotential contour lines are vertical, and the extracellular potential is again negative before the wavefront, and positive while the transmembrane potential is high.

The degree of resolution of the finite mesh that was required for the extracellular equation, and the amount of computer memory that was needed to store the information, made it too difficult to construct a similar mesh that would allow for an arbitrary stimulus, or for changes in the anisotropies of each domain. These studies will be possible when a more appropriate solution method is implemented for the extracellular equation.

In both the above examples, the boundary conditions required on the extracellular domain impose a significant constraint on the shape and behaviour of the final solution. Ideally, the extracellular solution should not be constrained at all, though a technique for doing so was not implemented for this thesis.

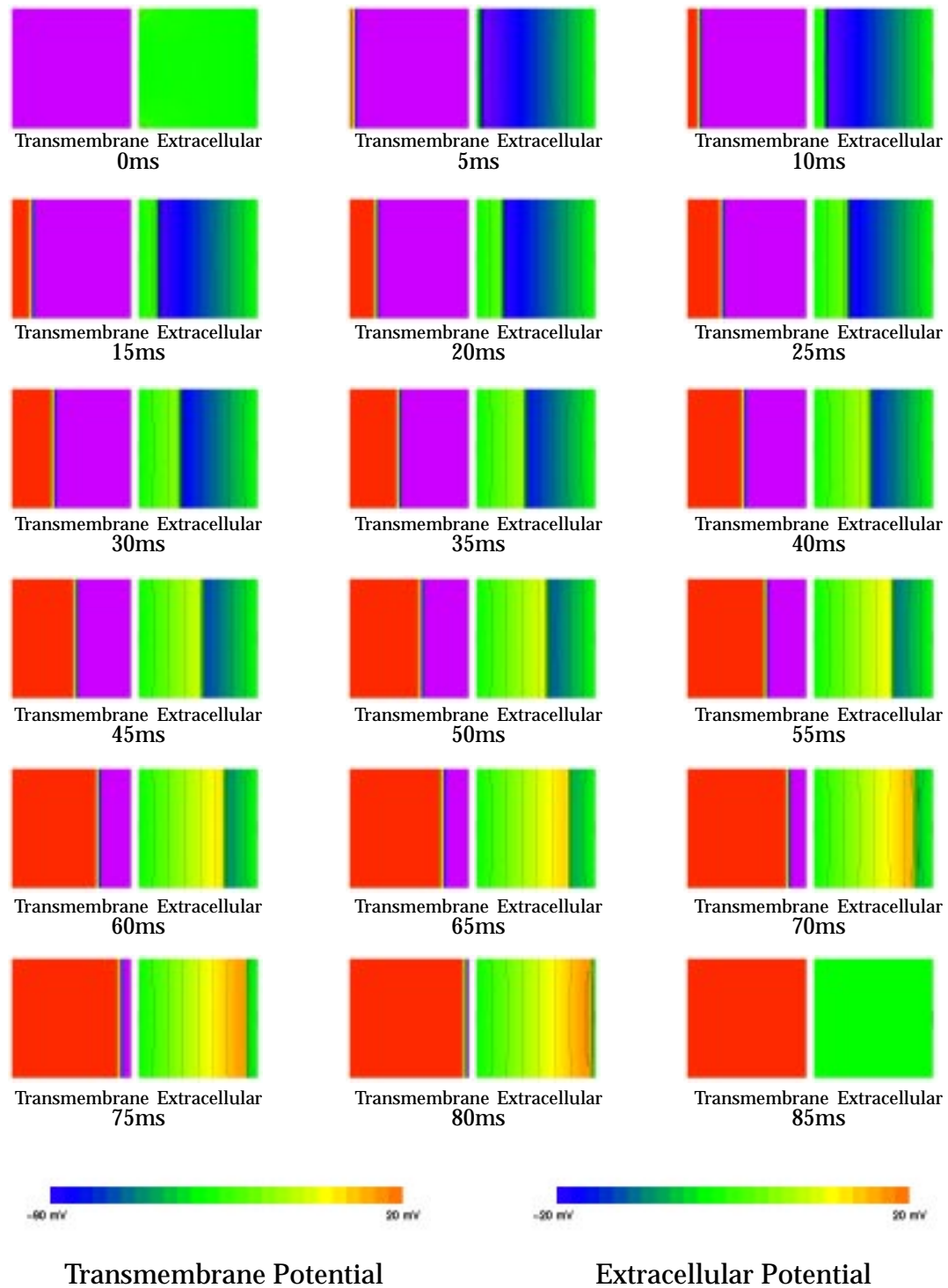


FIGURE 6.25: Plane wave stimulation using the cubic ionic equation in the bidomain model. The extracellular potential is fixed to zero on the left and right boundaries, and a no-flux boundary condition is applied to the top and bottom boundaries.

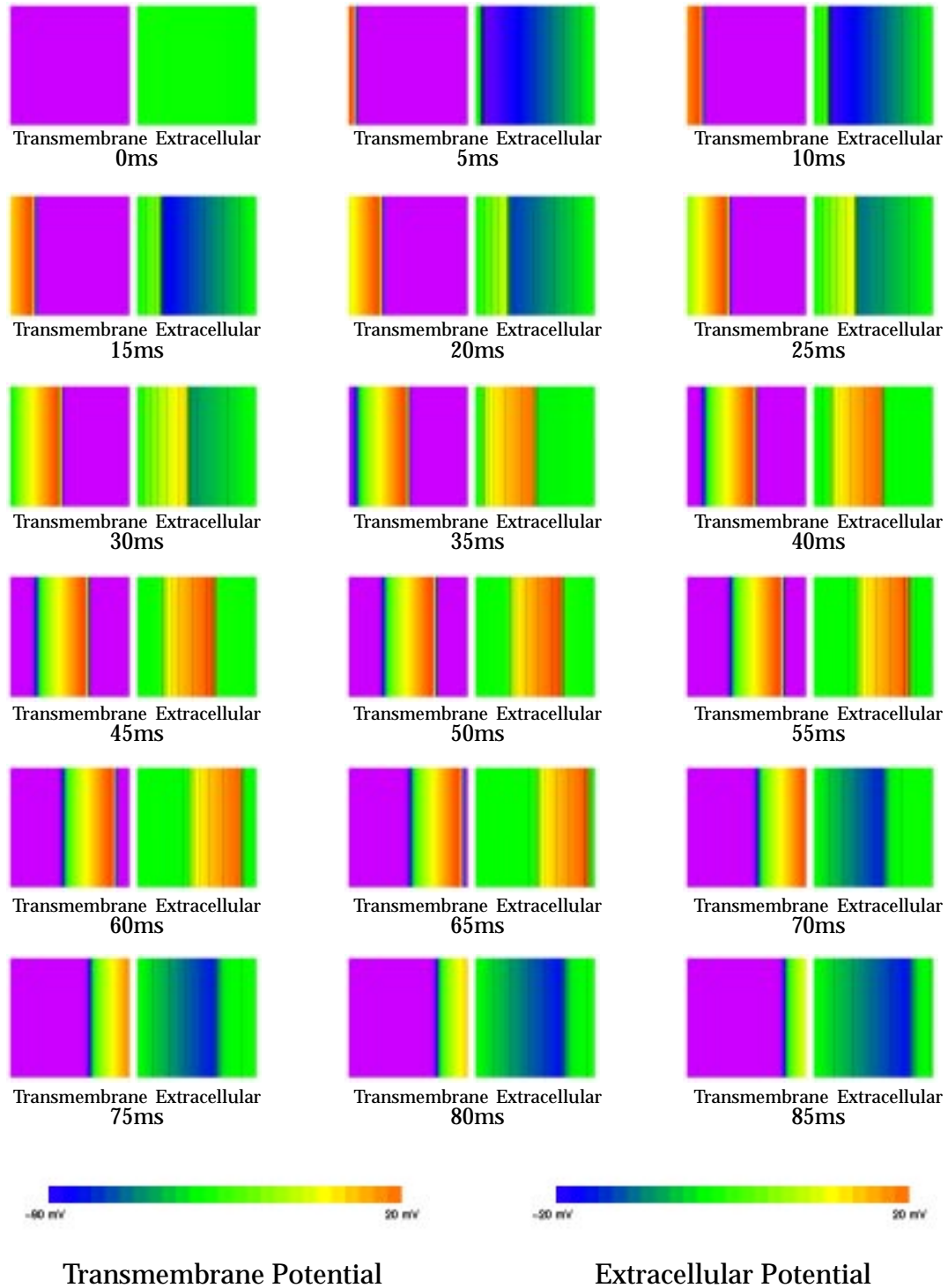


FIGURE 6.26: Plane wave stimulation using the FHN ionic equation in the bidomain model. The extracellular potential is fixed to zero on the left and right boundaries, and a no-flux boundary condition is applied to the top and bottom boundaries.

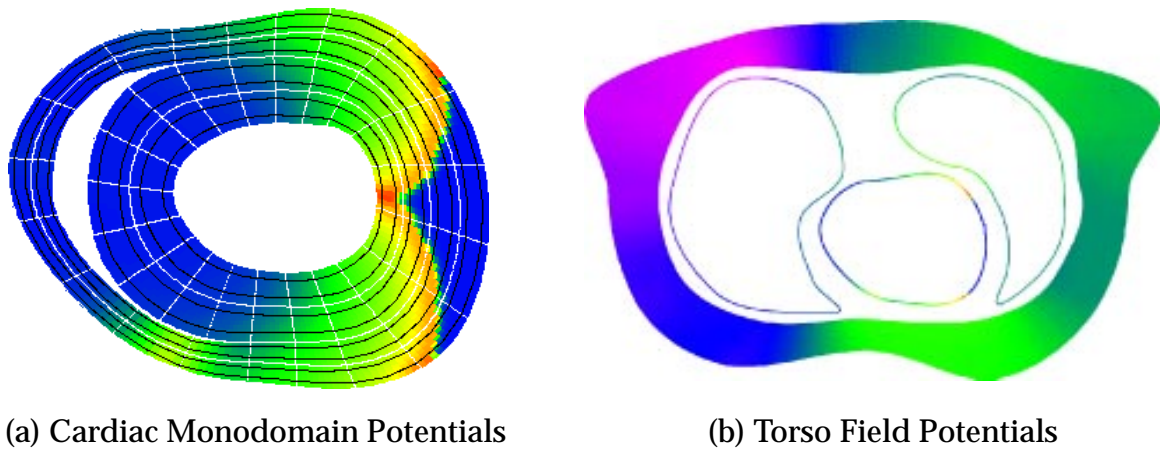


FIGURE 6.27: Partially coupled bidomain model.

6.5.2 Coupling to a torso model

Because of the difficulty in this implementation of the bidomain model of coupling the extracellular solution to a torso model, this process has not been completed. The process is, however, shown to be feasible in the following example in which the monodomain potential is computed at a single time step, and used as the input to a model of the torso potential. This example was constructed solely to demonstrate proof of concept.

The cardiac geometry used is the same as defined for a later example in Section 8.2.5, in which the initial epicardial position is taken from an MRI scan. The solution in the cardiac region is as described in this section, and at 75 ms the geometry and transmembrane potential have reached the stage shown in Figure 6.27a. The geometry and transmembrane potential on the epicardium at this time instant is used as the input for the torso model.

The torso model was created by digitising key regions from the same MRI image, and fitting finite element and boundary element meshes to the digitised points. The lungs are meshed using 8 boundary elements for each lung, and the regions characterised by fat and skeletal muscle are meshed using a total of 24 finite elements. The epicardial surface is meshed by 160 boundary elements which correspond to the lines between grid points located on the epicardial boundary of the finite elements used for the activation model. Conductivities are assigned in

each domain, and in this case are homogeneous and isotropic throughout the cavity, with a conductivity of $0.1 \text{ mS} \cdot \text{mm}^{-1}$. The potentials within the torso are solved for using a coupled finite element-boundary element method, resulting in the map of potentials shown in Figure 6.27b, where the colour scale of torso potentials is the same as for the cardiac map.

The method by which this solution was achieved is inefficient, and is not suitable for obtaining a large number of these coupled solutions for a complete activation process. Both the solution method for the extracellular bidomain equation, and the interface to the extramyocardial torso activation equation need to be improved so that useful results may be obtained.

6.6 Purkinje Fibre Network

This section shows only the very first stage of an ongoing study into the mechanisms by which the Purkinje fibre network activates the ventricular myocardium. This model builds on the work done in this thesis, and is being performed by a fellow graduate student, Martin Buist.

Using a simple algorithm for determining the structure of a branching tree, a four-generation, one-dimensional finite element mesh is constructed using a Monte Carlo method (Wang, Bassingthwaight and Weissman 1992) with varying branching angles and branch lengths as drawn in Figure 6.28. Grid points are defined along the fibre elements, and also in the two-dimensional “tissue” mesh, which in this example measures 10mm square. In this example, 9 grid points are used in each ξ -direction in each region. The regions are coupled at fibre endpoints using a simple algorithm which links the grid point at the end of the fibre to its closest neighbour in the two-dimensional mesh. Because of the high density of grid points in the tissue, the greatest distance between coupled points is less than 0.06mm, and this distance is not considered significant.

A constant fibre field at a 0° angle to the mesh is defined in the tissue, and an anisotropic conductivity tensor is used with a 5:1 conductivity ratio. The values used are $\sigma_f = 0.2 \text{ mS} \cdot \text{mm}^{-1}$ and $\sigma_s = 0.04 \text{ mS} \cdot \text{mm}^{-1}$. The Purkinje

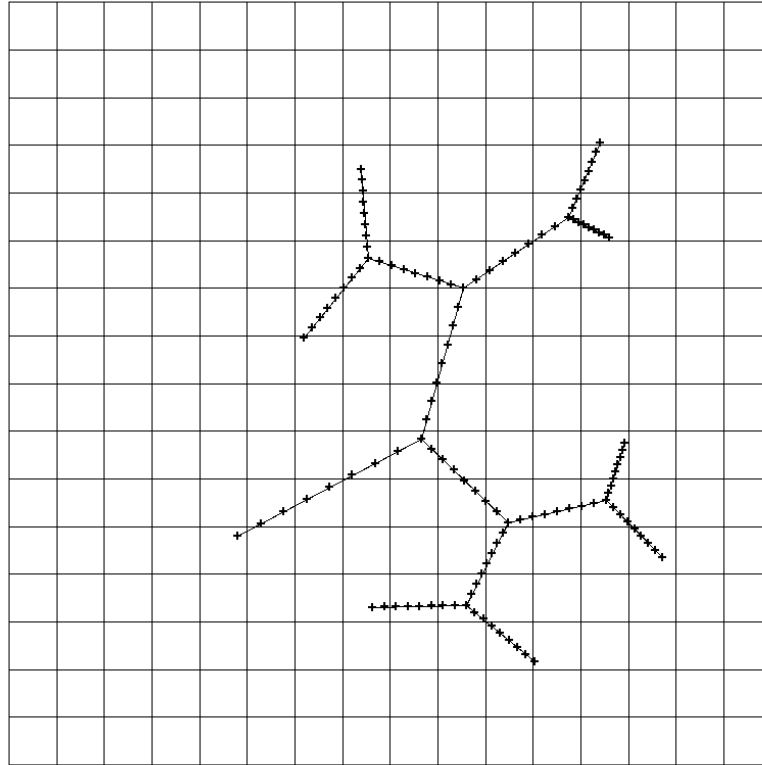
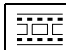


FIGURE 6.28: Purkinje fibre mesh with defined grid points, and the two-dimensional tissue.

fibres are given a slightly greater conductivity of $\sigma = 0.5 \text{ mS} \cdot \text{mm}^{-1}$. The cubic activation-only ionic current model is used with the same parameters as in previous examples. The primary endpoint of the Purkinje network is activated with a 2ms pulse of $0.5 \text{ mA} \cdot \text{mm}^{-3}$. The resulting activation wave is drawn in Figure 6.29.

 purkinje/tree-51

As the movie sequence shows, the initial stimulus conducts at a constant velocity through the fibre network, and activates at eight discrete points on the tissue surface at slightly different times, depending on the length of the fibre to that point. This causes an activation wave on the tissue which spreads over the entire block very quickly.

There are many other examples which can be investigated using the activation model within this structural context. Issues such as bundle branch block, partial block, or unidirectional block can easily be modelled, and an ionic current model which is

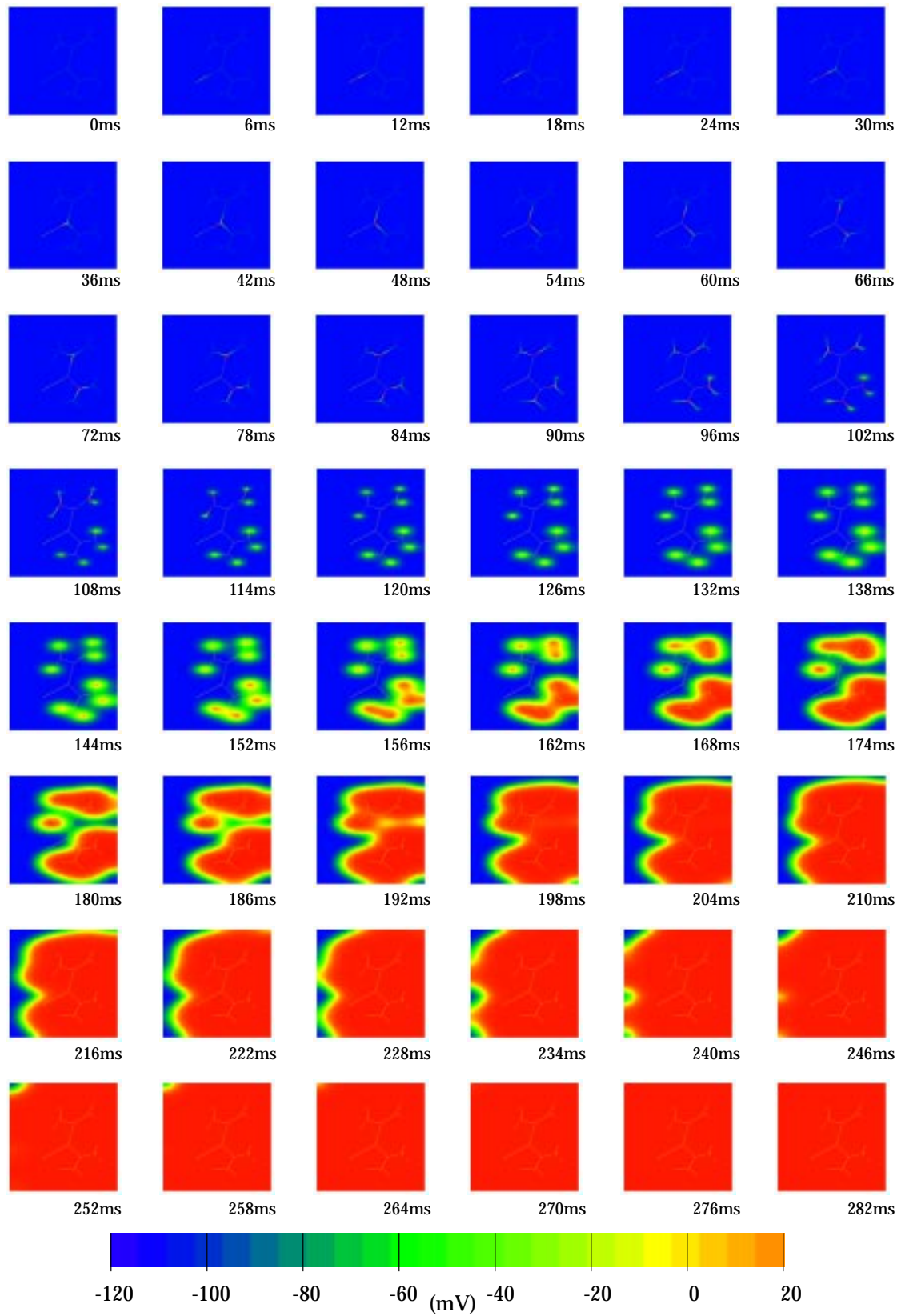


FIGURE 6.29: Purkinje fibre network activates two-dimensional myocardium.

targeted to the Purkinje fibre network (such as the DFN model) can be used in this region only.

6.7 Optimisation of Material Parameters

Most experimental research and clinical diagnosis in the field of cardiac activation is performed on an empirical basis, and computer modelling is not often used. This is for two main reasons: firstly that it is difficult to adequately describe the experimental or clinical situation in mathematical terms, and secondly that the model is usually very slow to compute. There is, at this stage, more potential for a model to be used on previously collected data where the solution time is not critical.

One particular example for which this model has been used is in determining the anisotropic conductivities in a small region of tissue based on electrode recordings of membrane potential. The modelling uses data from an experiment performed at Cedars Sinai Medical Center by Peng Chen on canine myocardium. 509 surface electrodes were arranged in a rectangular fashion as shown in Figure 6.30 and placed on the epicardial surface of an excised canine heart. The electrodes are placed at 1 mm spacing in 24 rows of 21 electrodes plus several additional electrodes at the bottom. A stimulus is applied near electrodes **148,169,190** and **211** which are at the upper left hand edge of the region. The activation and resulting epicardial potentials were recorded on the EMAP⁶ acquisition and analysis system (see Section 2.4) configured with 512-channels, and sampled at 1 kHz.

Some of the resulting signals are shown in Figure 6.31, and the quality of the signals ranges from excellent to poor. A poor signal may result from a bad electrical connection or movement during acquisition. The signals are manually checked to eliminate poor quality signals and the activation time at each remaining electrode is automatically determined using a gradient method which finds the largest absolute change in potential. These values are used to fit a field map of activation times, shown in Figure 6.32, for which the colour range is from 0 ms to 70 ms and the individual electrode activation times are overlaid. Missing numbers on the plot indicate that the electrodes have been removed from the field fit. The average

⁶Electrophysiological MAPPING system developed by the University of Auckland and M.I.T.



FIGURE 6.30: Electrode layout configuration for material parameter optimisation problem, with 1.6 mm spacing between each electrode in both the x and y directions.

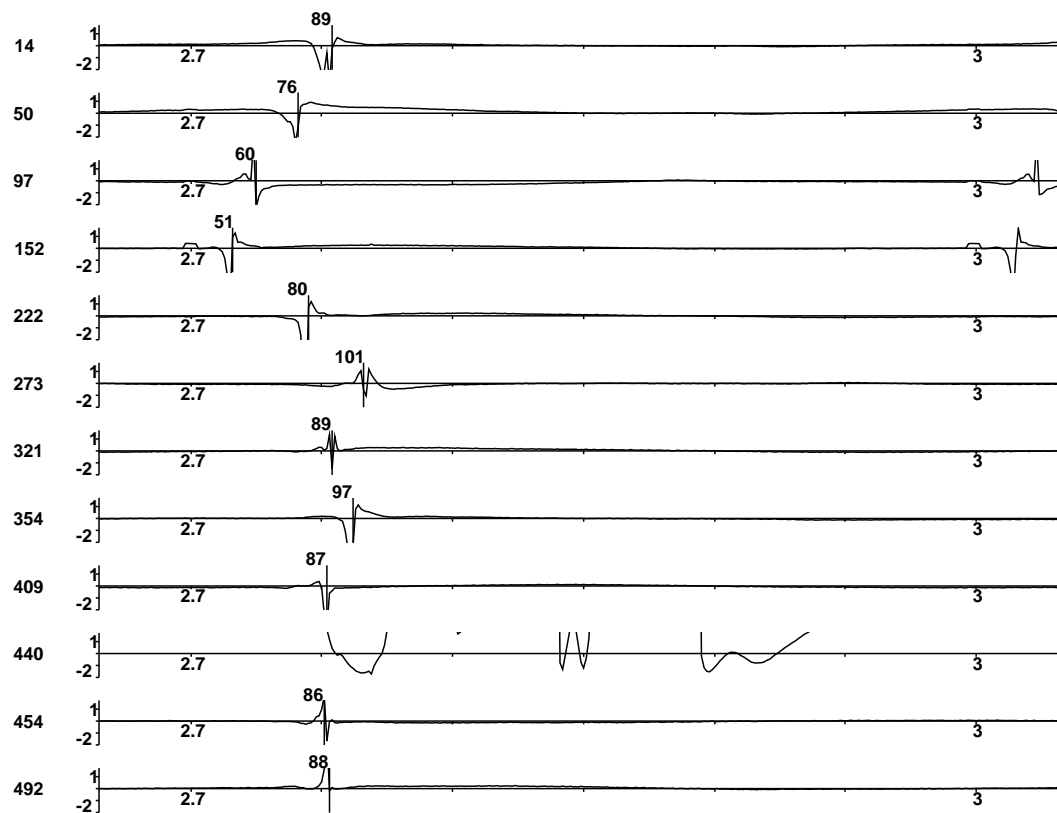


FIGURE 6.31: Several electrode recordings. Electrode **440** was rejected because of a poor recording.

absolute error of the fit is 0.8044 and the maximum absolute error is 9.139, where times are fitted in milliseconds. A few facts may be gleaned from this map. Electrode **97** has an activation time (22 ms) which is significantly smaller than those surrounding it, however the signal from that electrode is well-formed and there is no reason to doubt it, as can be seen in Figure 6.31. An electrode which is activated much later than those surrounding it is electrode **321**, with a similar distortion of the field. Other than these two electrodes, the field has a very reasonable fit to the data and is relatively smooth. Contour lines on this field are drawn in 1 ms and 5 ms increments in Figure 6.33.

Based solely on this level of output it is difficult to manually determine conductivities, and therefore an automatic optimising method is developed. A rectangular domain is defined which covers the electrodes and this domain measures 36 mm wide by 42 mm high, and is subdivided into 378 finite elements, each 2 mm \times 2 mm. A 9×9 extended Lagrange basis function is defined in each element which con-

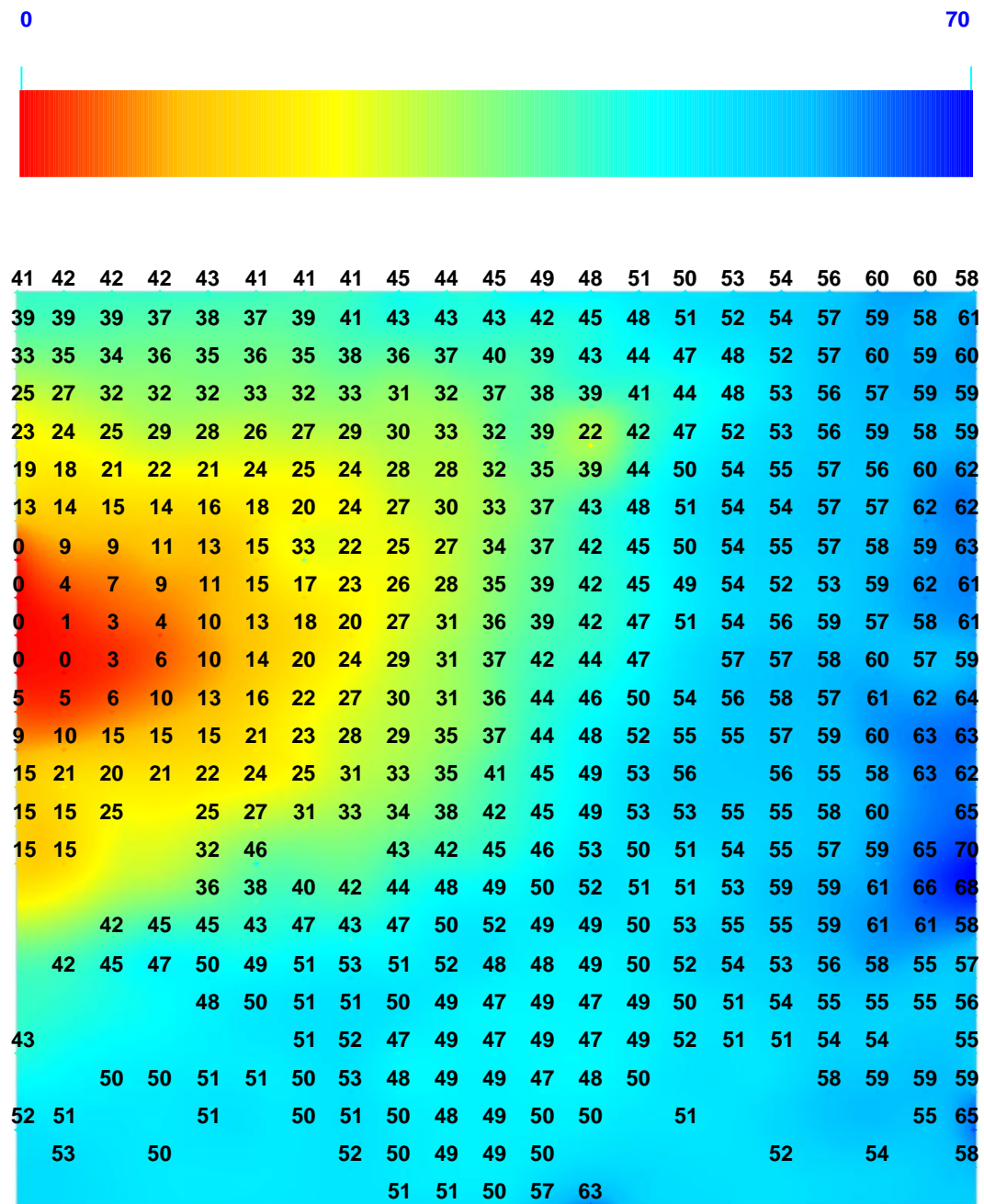


FIGURE 6.32: Field map showing activation time throughout the region based on recorded electrode activation.

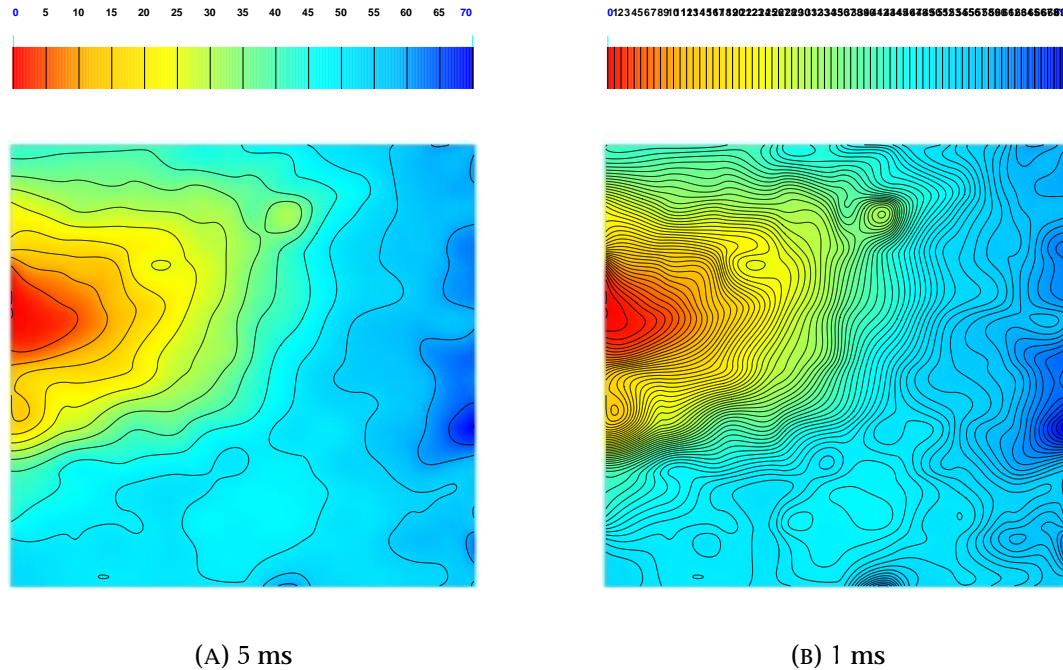


FIGURE 6.33: Field maps of activation time with overlaid contour lines at (a) 5 ms increments and (b) 1 ms increments.

constructs a grid of 24505 collocation points at 0.25 mm spacings. An stimulus region is defined consisting of groups of collocation points surrounding the 4 activating electrodes. Because this problem is solely concerned with activation time, a simple cubic model of the ionic currents is used, and the material parameters used are the same as defined in Table 6.2 for the above problems using a cubic model. The fibre angle is not known within the tissue, but based upon the fitted maps of activation time, a constant fibre angle of 0° is used throughout the domain.

The solution of the problem requires the use of a nonlinear optimising technique such as Levenberg-Marquardt or sequential quadratic programming (Bard 1974), and in this case we use specifically the `E04UPF` routine from the NAG library (NAG 1993) which is designed to minimise an arbitrary smooth sum of squares problem subject to constraints using a sequential quadratic programming method. Initially, a set of approximate conductivities is estimated, and the activation problem is solved. We consider a residual to be the difference in activation time between an electrode and its nearest collocation point, and compute a residual for each electrode. The average distance between an electrode and its nearest collocation

point is 0.1 mm, with a maximum distance of 0.14 mm. There are 461 electrodes remaining in the problem, and therefore the optimiser requires the estimation of 922 objective Jacobian elements at each gradient evaluation. The optimiser must determine derivatives of the problem, that is, how the residuals change as the conductivities vary. This cannot be computed analytically, and the optimiser must compute the derivatives using a finite difference technique which involves solving the problem for small changes in conductivity. Because of this, the solution is very slow, as a number of activation problems need to be solved at each time step in order to establish a search direction and step length for the optimisation.

The bounds set on the material conductivities are

$$0.2 \times 10^{-3} \leq \sigma_f \leq 0.6 \times 10^{-3} \quad (6.1)$$

$$0.1 \times 10^{-3} \leq \sigma_s \leq 0.4 \times 10^{-3} \quad (6.2)$$

and these bounds were determined approximately from the map. The optimiser required 12 major iterations which involved 11 computations of the gradient and 49 evaluations of the function by solving an activation problem. The value of the conductivities estimated by the optimiser was $\sigma_f = 0.49187 \times 10^{-3}$ and $\sigma_s = 0.32288 \times 10^{-3}$, with the sum of squared residuals at these values of 1.96×10^4 . The final nonlinear objective value was 9801.9. The optimisation required 321m40s (CPU), or almost $5\frac{1}{2}$ hours. The resulting map of activation time from the optimised parameters is shown in Figure 6.34 with the colour scale ranging from 0 ms to 90 ms. Overlaid on this are the electrode activation times as data points coloured according to their magnitude. Where the fit is accurate, the colours should be the same as the underlying map, and large residuals can easily be seen.

The optimised conductivities give a conductivity ratio of only 1.5:1 which is much smaller than commonly observed in cardiac tissue. Figure 6.34 shows that, initially, the computed wavefront is ahead of the data points (the green points in the blue region), and then later the wavefront is behind the actual activation (the yellow points in the red region). Looking at the contour plots in Figure 6.33 makes it easy to see why this is the case, as approximately the first 40 ms is fairly constant in terms of propagation, and then the rest of the region is activated fairly quickly. This could be explained by the fact that the two-dimensional map that is measured is in fact only the surface of a three-dimensional section of ventricular wall. After about 20 ms the wavefront has reached the endocardial surface and spreads out quickly over the surface through the Purkinje fibre network, and therefore the rest of the epicardium

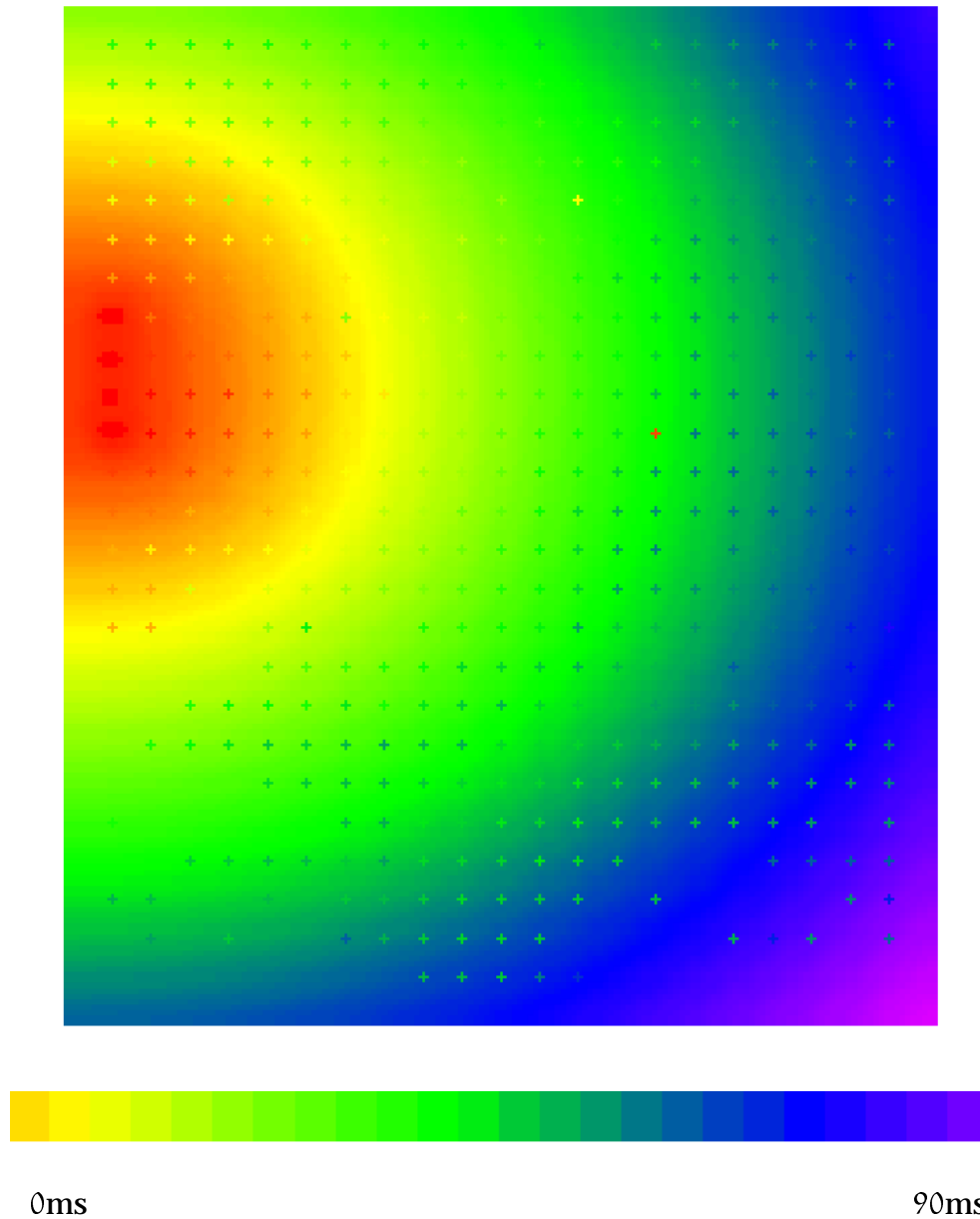


FIGURE 6.34: Field map showing activation time using computed material conductivities of $\sigma_f = 0.49187 \times 10^{-3}$ and $\sigma_s = 0.32288 \times 10^{-3}$. Measured activation times from electrodes are drawn as data points on the same colour scale. The scale ranges from 0 ms to 90 ms.

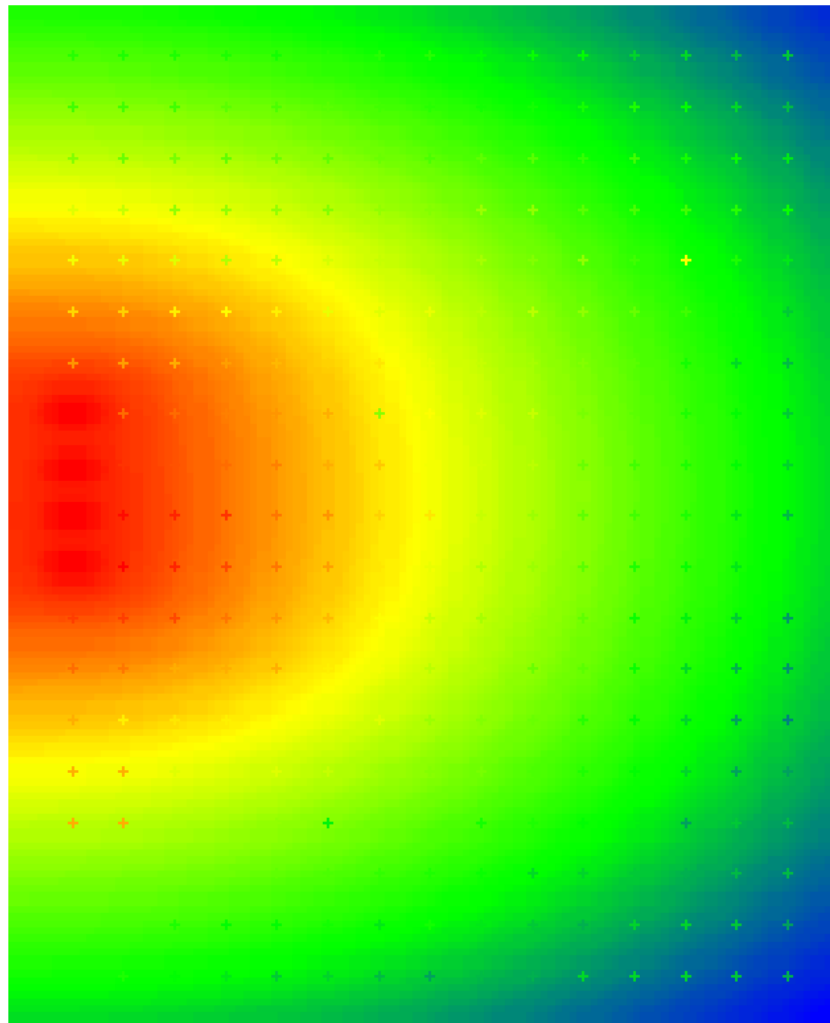
is quickly activated another 20 ms later. This indicates that a better prediction of the true conductivities may be achieved if just the top left corner of signals is modelled on a smaller finite element mesh, and the three-dimensional effect is minimised.

The first 15 columns and 19 rows of electrodes are used in this second optimisation, which is the rectangle cornered by electrodes **1** and **393**. 272 acceptable electrodes remain in this region. A smaller finite element mesh covers this area, with 208 elements in total covering 26 mm \times 32 mm, and giving 13545 collocation points. The same material parameters and initial conditions are used, and the bounds on the conductivities are also the same.

This second problem solved much more quickly than the first, and resulted in substantially different optimised values for the conductivities. The solution took 168m10s (CPU), and took 17 iterations of the nonlinear solver. This included 16 gradient evaluations and 50 solutions of the activation problem. Approximately 1m40s (CPU) were required for each solution of the activation problem, comprising around 50% of the total solution time, and therefore the time is split evenly between the optimiser and the activation model.

The resulting optimised values for the conductivities were $\sigma_f = 0.43023 \times 10^{-3}$ and $\sigma_s = 0.16493 \times 10^{-3}$. These values give a conductivity ratio of 2.6:1 which is within the range of experimentally measured values. The resulting field map is shown in Figure 6.35, and the measured electrode activation times are much more closely matched to the optimised field. The sum of squared residuals is much smaller at 5473, and the nonlinear objective value decreased from 11214 at the start of the optimisation to a value of 2736.3. Some of the decrease in these values over the previous optimisation comes from the fewer number of electrodes used in this case.

Although the optimised values seem to fit the measured data reasonably well, there are several improvements which would be possible to make. Firstly, the estimated fibre angle may not be accurate. This would be easily overcome by having a photograph of the activation region which shows the fibre directions, and these can easily be incorporated into the finite element model, and thereby into the collocation grid. Attempting to optimise a varying fibre field as well as the conductivities would be extremely slow, and even a constant fibre angle would require a much greater computational time. Secondly, the method is slow, with most of the solution



0ms

90ms

FIGURE 6.35: Field map showing activation time on the upper right hand corner of the previous problem using new optimised material conductivities of $\sigma_f = 0.43023 \times 10^{-3}$ and $\sigma_s = 0.16493 \times 10^{-3}$. Measured activation times from electrodes are drawn as data points on the same colour scale. The scale ranges from 0 ms to 90 ms.

time being taken with repeated solution of the activation problem. Because only activation time is required, a better approach may be to solve an eikonal equation (Colli Franzone, Guerri and Rovida 1990) which determines only the activation time of each point. Thirdly, no account has been taken of the electrotonic spread of the activation wave from the initial stimulation point to neighbouring regions which may cause the wavefront to seem to travel quickly near the stimulus, but more slowly a few millimetres away from it. This possible effect could be tested for by removing from the optimisation a number of points close to the stimulus and resolving for the conductivities.

Chapter 7

Three Dimensional Collocation Solutions

The nature of the collocation method defines a solution method which is essentially identical for domains defined in one, two or three dimensions. One-dimensional propagation occurs in the central septal bundle and through the Purkinje fibre network as illustrated in Section 6.6. Ventricular propagation is three-dimensional, and this chapter presents results obtained both in simple three-dimensional domains, and in an anatomically accurate model of the ventricular geometry. Atrial propagation is also three-dimensional, though some preliminary studies by an undergraduate student has considered the thickness of the atrial wall to be sufficiently small such that the propagation can be modelled as a two-dimensional activity.

The main difference in a three-dimensional solution is the nature of the material coordinate vector γ_i which now has three principal directions. Three forms of the conductivity tensor exist in a three-dimensional domain. An *isotropic* tensor contains, as before, the same conductivity in all directions. A *transversely isotropic* conductivity tensor specifies one conductivity in the fibre direction, and the conductivity is the same (and usually smaller) in all directions normal to the fibre axis. The most general form of the tensor is an *orthotropic* conductivity tensor in which a separate value of the conductivity is defined in each of the three directions defined by the fibre, sheet and sheet-normal axes. These material axes are related to the element coordinates

through a series of transformations defined by the fibre angle, the sheet angle and the imbrication angle as defined in Section 5.2.7.

Once the geometry and microstructure have been defined, then the process by which the collocation equations are constructed and solved is similar to the two-dimensional examples in Chapter 6.

7.1 Activation in a Cube

This series of examples demonstrates the collocation method in a simple three-dimensional domain. A cube is constructed with sides of length 8 mm and 33 collocation points along each side, totalling 35937 collocation points. The resulting grid is regularly spaced with points at 0.25 mm intervals. The domain is activated by either a stimulus at a cluster of 27 points in the centre of the domain, or at a cluster in one corner. The central stimulus requires $0.2 \text{ mA} \cdot \text{mm}^{-3}$ for a period of 1 ms, whereas the corner stimulus only requires $0.1 \text{ mA} \cdot \text{mm}^{-3}$ because the effect of the no-flux boundary condition on the nearby edges is to allow propagation in fewer directions, increasing the available current. A timestep of $\Delta t = 0.02 \text{ ms}$ is used.

The cubic model is used first to demonstrate three-dimensional activation, with parameters as used above in Section 6.3.1, except for the values of the conductivity tensor. For each of the first three pairs of examples, the fibre axis is aligned with the x -axis (in the diagrams which are drawn, this is normal to the right-hand face of the cube), sheet axis is aligned with the y -axis (vertically through the top face), and the sheet-normal axis runs in the direction of the z -axis (normal to the left-hand face).

7.1.1 Isotropic activation

The first pair of activations use an isotropic conductivity tensor for which the conductivity in each direction is $\sigma = 0.1 \text{ mS} \cdot \text{mm}^{-1}$. A colour field showing activation times is drawn in Figure 7.1 for both stimulus protocols.

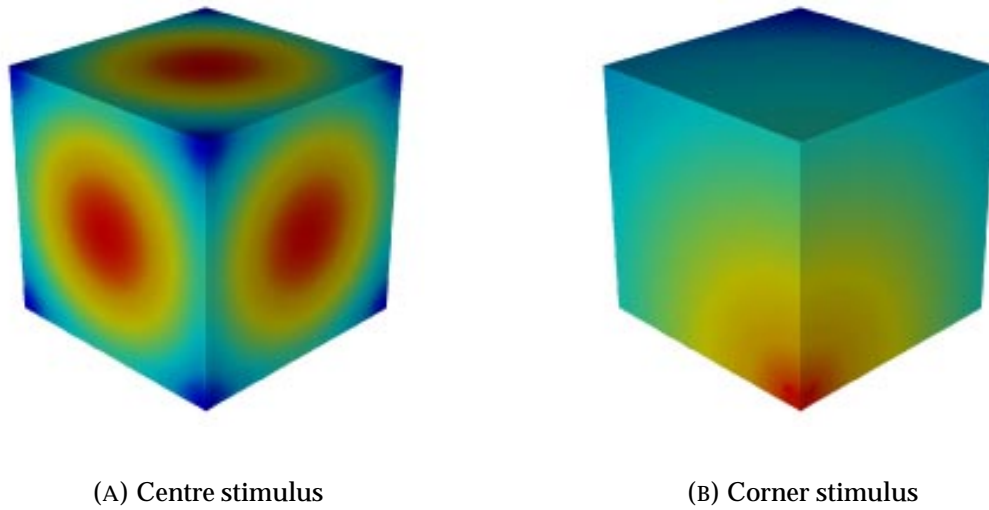


FIGURE 7.1: Activation in a cube with an isotropic conductivity tensor. Red represents earliest activation, and blue represents latest.

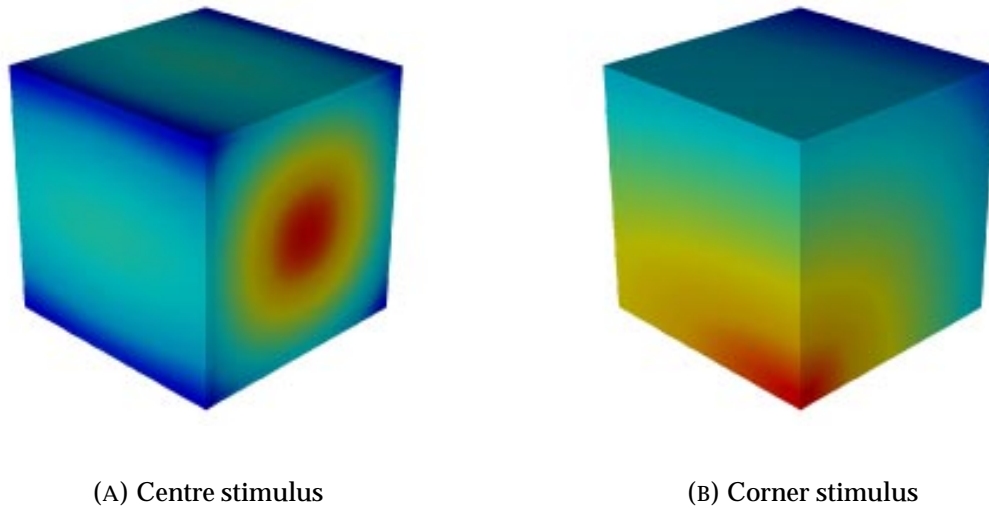


FIGURE 7.2: Activation in a cube with a transversely isotropic conductivity tensor. Red represents earliest activation, and blue represents latest.

For the central stimulus, as expected, the wave forms a spherical shape within the domain, and the wavefront reaches the external boundary first at the centre of each face, and activation appears to spread outwards across each surface in a circular fashion from each central point as the sphere continues to expand. The earliest activation on the outside surface is at 22.1 ms, and the latest occurs at 32.7 ms at the corners of the domain. The colour range for the plot in Figure 7.1a displays red at 22.1 ms through to blue at 32.7 ms.

The corner stimulus also produces circular wavefronts on each face, with the furthestmost corner from the initial stimulus being activated at 58.0 ms. The colour ranges on the plot in Figure 7.1b displays red at 0.0 ms through to blue at 58.0 ms.

7.1.2 Transversely isotropic conductivities

The second pair of activations define a transversely isotropic conductivity tensor, for which the fibre conductivity remains the same as above ($\sigma_f = 0.1 \text{ mS} \cdot \text{mm}^{-1}$), and the sheet and cross-sheet conductivities are reduced by a factor of 5 to $\sigma_{s,c} = 0.02 \text{ mS} \cdot \text{mm}^{-1}$. The resulting wave forms an ellipsoid with a circular cross-section along the fibre axis, and an elliptical cross-section along the other major axes.

This change in the conductivity ratio causes the activation wave to propagate more quickly along the fibre direction than it did in the previous example because less current is transmitted in other directions due to the lower conductivities. For the central stimulus, this results in the earliest activation time on the surface being reduced to 17.4 ms, while the latest activation is correspondingly delayed to 58.2 ms at the four corners of the cube. The resulting map of activation times is shown in Figure 7.2a with the colour range being defined between these two values.

Figure 7.2b shows the corresponding activation map for a stimulus in the corner, with the latest activation time now being 113.1 ms at the diagonally opposite corner. An elliptical cross-section can be seen on the left-hand face, and a circular cross-section on the right.

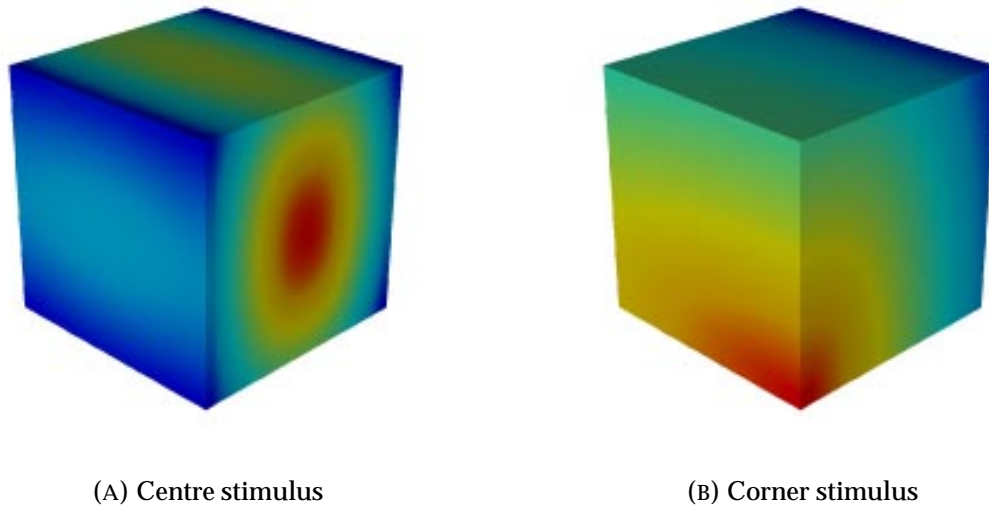


FIGURE 7.3: Activation in a cube with an orthotropic conductivity tensor. Red represents earliest activation, and blue represents latest.

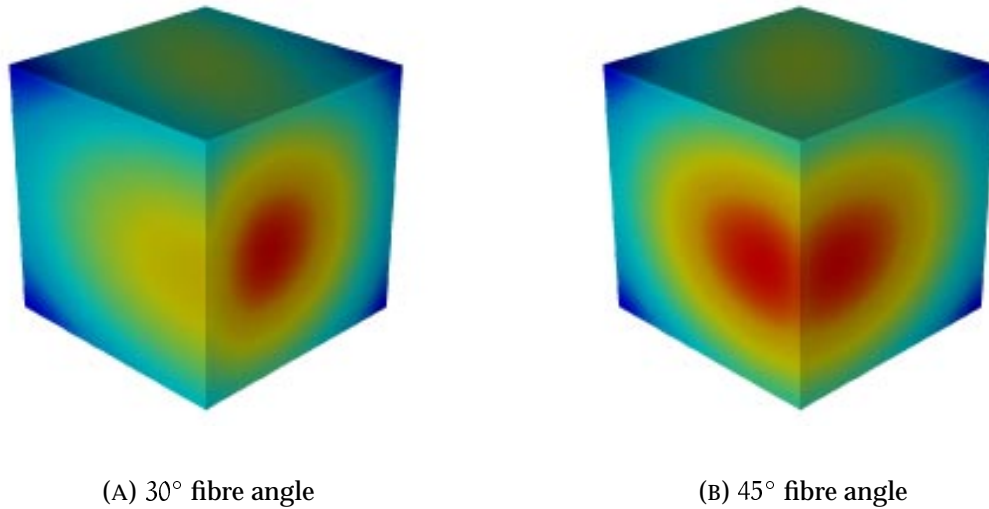


FIGURE 7.4: Rotation of the fibre angle throughout the cube causes the activation pattern to change. Red represents earliest activation, and blue represents latest.

7.1.3 Orthotropic conductivities

The third pair of activations define an orthotropic set of conductivities in which the fibre conductivity is the same as before, the sheet conductivity is one quarter of that and the sheet-normal conductivity is one half of that again. The actual values used are $\sigma_f = 0.1 \text{ mS} \cdot \text{mm}^{-1}$, $\sigma_s = 0.025 \text{ mS} \cdot \text{mm}^{-1}$ and $\sigma_c = 0.0125 \text{ mS} \cdot \text{mm}^{-1}$. The wavefront resulting from this stimulus produces an ellipsoid which has an elliptical cross-section through every axis.

The activation field from a central stimulus is shown in Figure 7.3a with the earliest activation on the right hand surface at 17.2 ms, and the latest activation occurs at the corners at 66.0 ms. The field is coloured between these values. The wavefront is only marginally faster along the fibre direction than it was in the previous example, but the wavespeed in the sheet-normal direction is markedly slower.

A corner stimulus as shown in Figure 7.3b shows elliptical wavefronts on the two faces adjacent to the stimulus, and the opposite corner activates after 129.0 ms.

7.1.4 Variation in fibre angle

The final pair of simulations show the results of orthotropic activation on a mesh for which the fibre angle has been rotated, which alters the angle of the fibre-sheet plane. Figure 7.4a shows the result of a 30° rotation and Figure 7.4b illustrates a 45° rotation, both examples having a central stimulus. For the first example, the surface activation times range from 19.6 ms through to 58.7 ms, and the 45° example ranges from 23.2 ms through to 57.8 ms at the corners.

7.1.5 A reentrant scroll wave

A reentrant wave is initiated in the cube by a similar method to those which created a spiral wave in two dimensions. The FHN ionic current model is used as a simple model of activation and recovery. For this simulation, an isotropic conductivity tensor was used with a value of $\sigma = 0.01 \text{ mS} \cdot \text{mm}^{-1}$, which is much smaller than

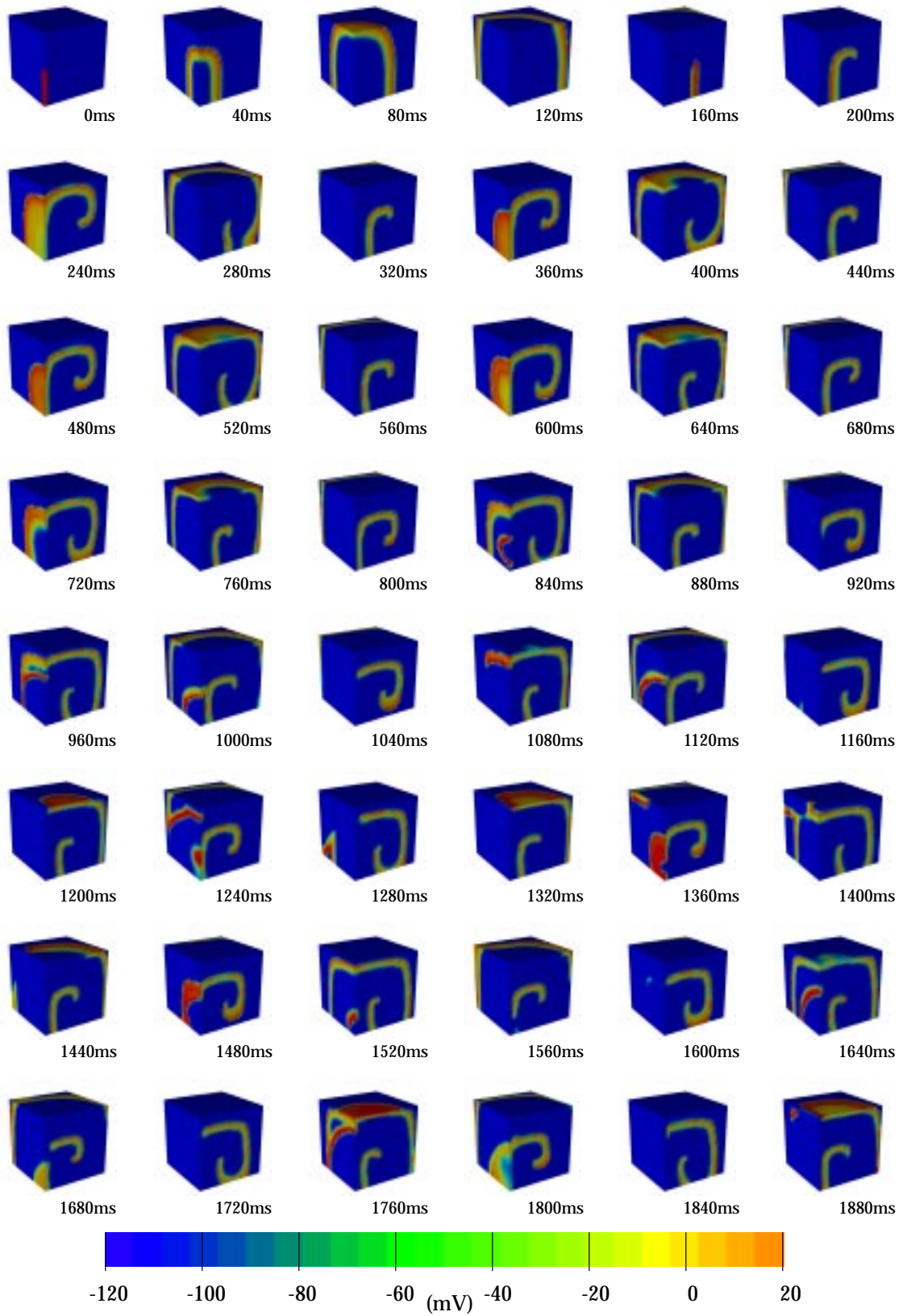


FIGURE 7.5: Transmembrane potential on cube surface resulting from an internal scroll wave generated using the FHN model.

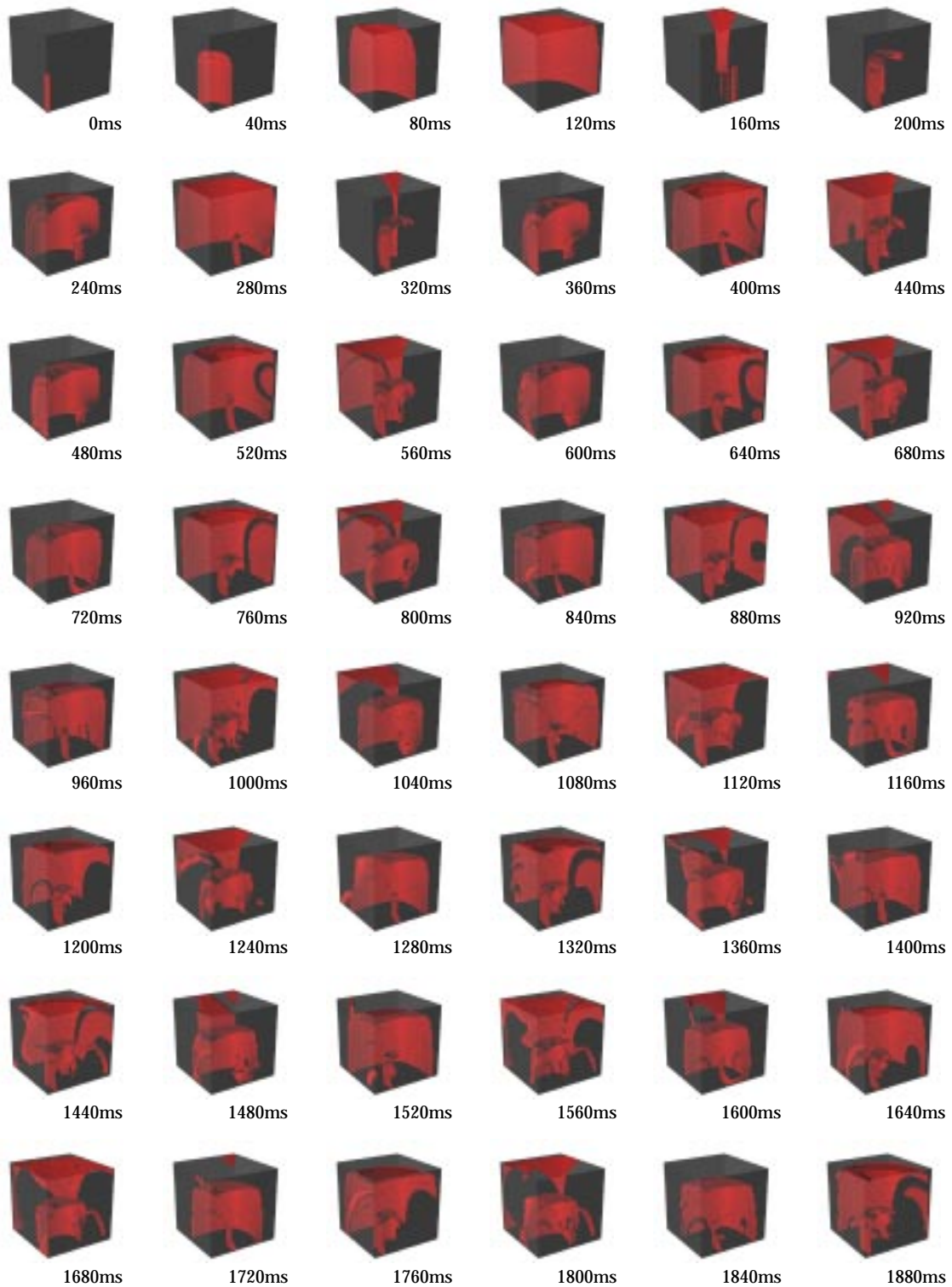
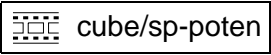
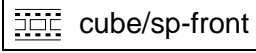
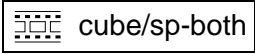


FIGURE 7.6: Scroll wave wavefront is approximately drawn by defining surfaces where $V_m = -5$ mV.

usual in order to allow the reentrant wave to develop within the limited confines of the cube. The resulting wavefront is represented in two figures. Figure 7.5  shows the transmembrane potential on the surfaces of the cube nearest to the activating stimuli. Figure 7.6  shows the cube from the same vantage point, but with transparent walls to show the internal movement of the activation wavefront. The position of the wavefront is approximately defined by constructing a surface through all points where the transmembrane potential is $V_m = -5$ mV. This leads to a doubling of the surface on either side of the spike of the action potential, though the pair of surfaces are close together. Where the action potential peaks short of the -5 mV threshold value, the wavefront appears to have “holes” in it, though this is only an artifact of the graphical surface generation. Both movies are combined into a single movie in .

Two stimuli are used to construct the reentrant wave in a similar way to those defined in two dimensions. The initial stimulus is applied along one half of a corner edge, as shown in the first frame of each of the movies. The magnitude of this stimulus is $1 \text{ mA} \cdot \text{mm}^{-3}$ and it lasts for 1 ms. The fifth frame of the series, at 160 ms, shows the cube just after the application of the second stimulus. This second stimulus is applied for 15 ms from $t = 140$ ms with a magnitude of $1.1 \text{ mA} \cdot \text{mm}^{-3}$. As seen in Figure 7.6 the stimulus extends into the cube by approximately one quarter of its width. This stimulus initiates a spiral on the right-hand surface as shown in the remaining frames in Figure 7.5, but the activity beneath the surface is more complex, as shown both by the change in transmembrane potential on the left-hand surface in this figure, and the internal movement of the wavefront in the subsequent figure.

7.2 A Finite Element Model of Ventricular Anatomy

We now solve the activation equations on an anatomically accurate domain defining ventricular myocardium. The mathematical model describing this domain is concerned only with ventricular geometry and microstructure, and does not model the atria, or any internal conducting pathways. The anatomical finite element model of the left and right ventricles consists of two quantitative fields — the ventricular geometry, and the fibrous-sheet structure orientations throughout the ventricular

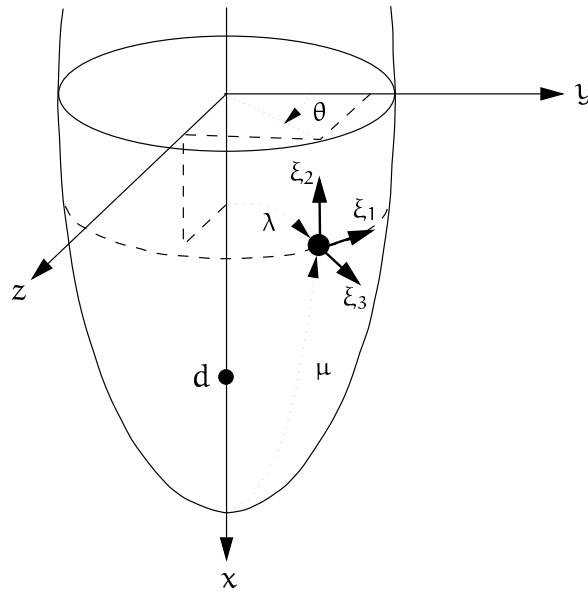


FIGURE 7.7: The finite element material coordinates (ξ_1, ξ_2, ξ_3) for the ventricular model.

myocardium. The latter is naturally split into the muscle fibre and sheet orientation fields as outlined in Section 5.2.7. Each field has been fitted using least squares techniques based on the finite element method (Nielsen et al. 1991), using data collected from careful anatomical studies of canine hearts (LeGrice 1992).

7.2.1 Ventricular geometry

The first set of field variables to be defined at the nodes of the finite element mesh are the geometric coordinates (λ, μ, θ) . We use a prolate spheroidal coordinate system (see Section 5.2.6) rather than rectangular cartesian coordinates because the prolate spheroid provides a good initial approximation to ventricular boundary geometry and therefore reduces the required number of nodal parameters. The finite element material coordinates ξ_1 , ξ_2 and ξ_3 (see Section 5.2.2), are chosen to lie in the circumferential, longitudinal (apex-to-base) and transmural (through wall) directions, respectively (refer to Figure 7.7). Note that the ξ_1 -coordinate increases in the opposite direction to that of θ to ensure that (ξ_1, ξ_2, ξ_3) is a right handed coordinate system.

To describe the complex shape of the endocardial and epicardial surfaces the model uses bicubic Hermite interpolation for the radial coordinate, λ , in the (ξ_1, ξ_2) -wall plane and linear Lagrange interpolation for λ in the transmural ξ_3 -direction, or in other words, λ is represented using bicubic Hermite/linear Lagrange interpolation. This provides smoothly continuous ventricular boundary surfaces. In contrast, μ and θ are described using trilinear Lagrange functions as there is little to be gained by using higher order basis functions in any of the ξ_i -directions.

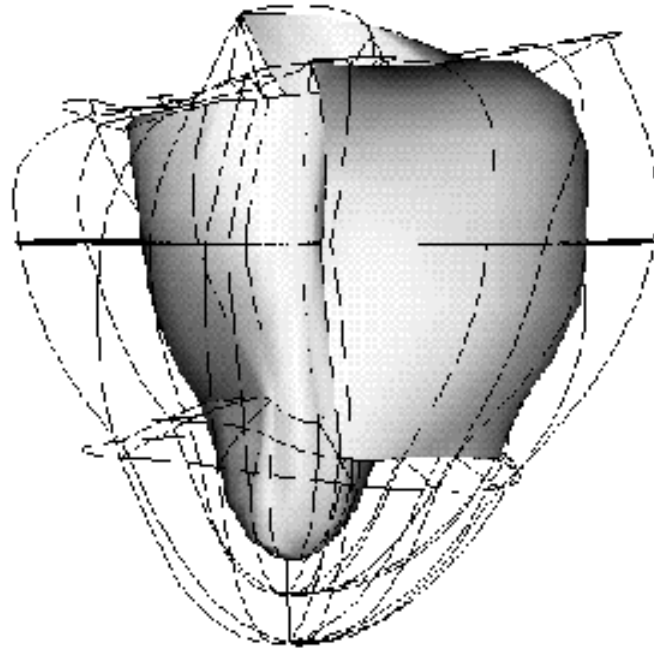
Using these interpolation schemes, the model uses 60 three-dimensional elements connecting 99 nodes to accurately represent the geometry of the ventricles. Figure 7.8 shows the outlines of the element configuration, with endocardial and epicardial surfaces separately shaded.

There are ten elements in the circumferential direction and three levels of elements in the longitudinal direction. The model is comprised of two layers of elements — the inner layer encompasses the septal wall and inner portions of the left ventricular free wall, while the outer layer of elements makes up the right ventricular free wall and the outer portions of the left ventricular free wall.

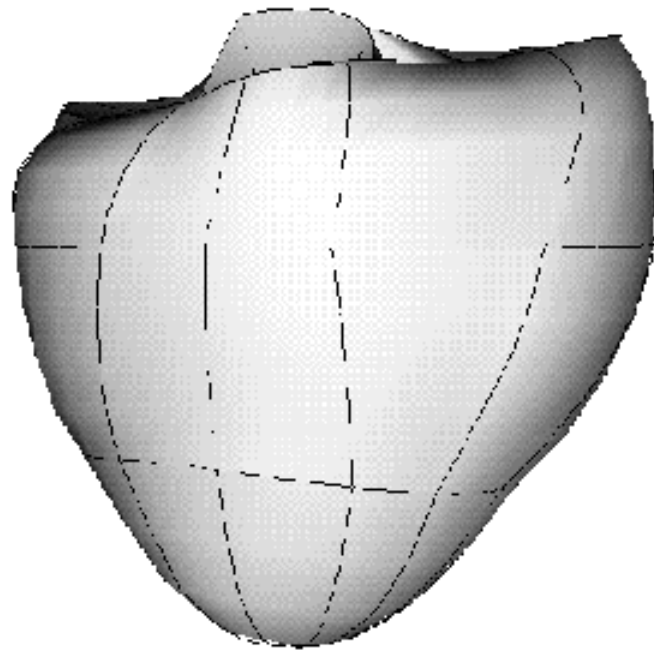
7.2.2 Myocardial fibre orientations

To model the muscle fibre orientations, it is assumed here that the fibres lie in (ξ_1, ξ_2) -coordinate planes so that they are tangential to the endocardial and epicardial surfaces. This is reasonable throughout the ventricular myocardium except at the left ventricular apex where the fibres spiral from epicardium to endocardium. Throughout this model, the fibre angle is defined with respect to the ξ_1 -coordinate which is directed along θ coordinate lines and increases as θ decreases (see Figure 7.9). The fibre angle at any point in the model is given by an interpolation of fibre field parameters defined at the same nodal positions used to define the ventricular geometry.

The basis functions used to interpolate the fibre angle within an element are chosen to reflect the extent of the spatial variation of fibre orientation. Generally, fibre orientations rotate steeply in the transmural direction and so cubic Hermite interpolation is used for the ξ_3 -coordinate. In contrast, fibre orientations generally

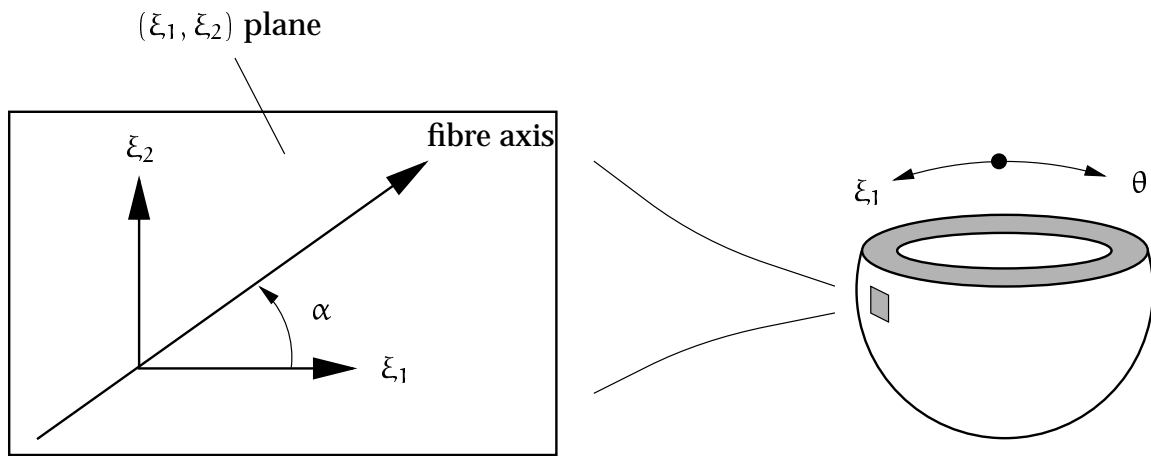


(A) Endocardium



(B) Epicardium

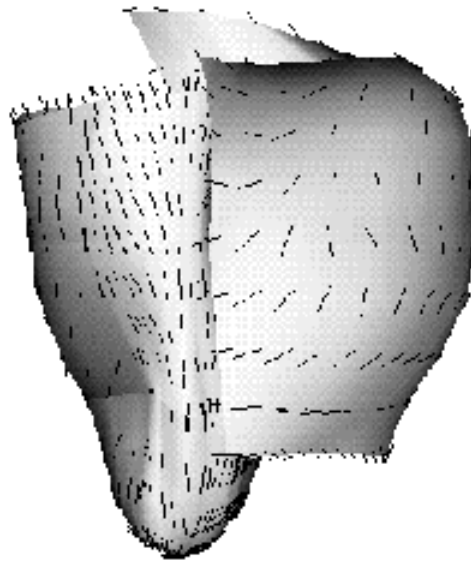
FIGURE 7.8: Finite element model of the ventricular wall geometry.

FIGURE 7.9: The fibre angle, α .

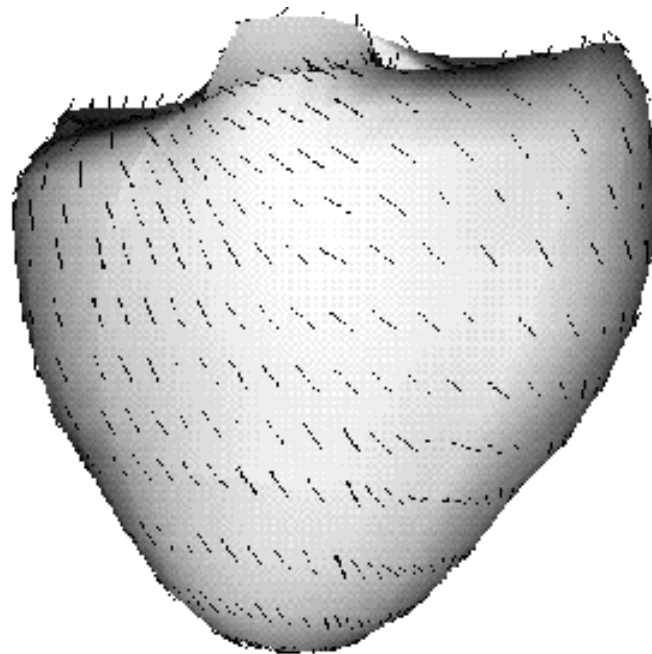
vary more slowly in the plane of the wall, thus requiring only linear Lagrange interpolation in the ξ_1 and ξ_2 directions. Figure 7.10 shows line segments on the endocardial and epicardial surfaces that are aligned with the local fibre orientation.

Special attention is required at the junction of the left and right ventricular free walls and the ventricular septum. In the right ventricular free wall, fibre orientation typically varies from -60° at the epicardium to $+90^\circ$ at the endocardium, whereas in the septal wall the fibre angle ranges from approximately -90° at the right ventricular endocardium to around $+80^\circ$ at the left ventricular endocardium. Thus on either side of the right ventricular border, the principal angle for endocardial fibres with a common orientation differs by 180° . In addition, there is a discontinuity in fibre angle due to the merging of right ventricular free wall and septal fibres with left ventricular fibres. To accommodate these abrupt changes in fibre orientation three versions of the fibre angle (plus arc-length derivatives) are stored at each of the nine nodes at the junction between the left and right ventricular walls. There is one version of the fibre angle for the right ventricular free wall, one for the septal wall and one for the adjacent left ventricular free wall. Errors due to these discontinuities have been localised by using smaller elements at these sites.

This model uses 234 degrees of freedom (90 nodes with 2 DOF/node and 9 nodes with 6 DOF/node) to fit the fibre field and provides an accurate and efficient representation of the experimentally measured fibre orientation field since the fitting and measurement errors are of a similar magnitude (Nielsen et al. 1991). Moreover, it has been demonstrated that there is a high level of consistency between fitted



(A) Endocardium



(B) Epicardium

FIGURE 7.10: Fibre orientations at the ventricular surfaces.

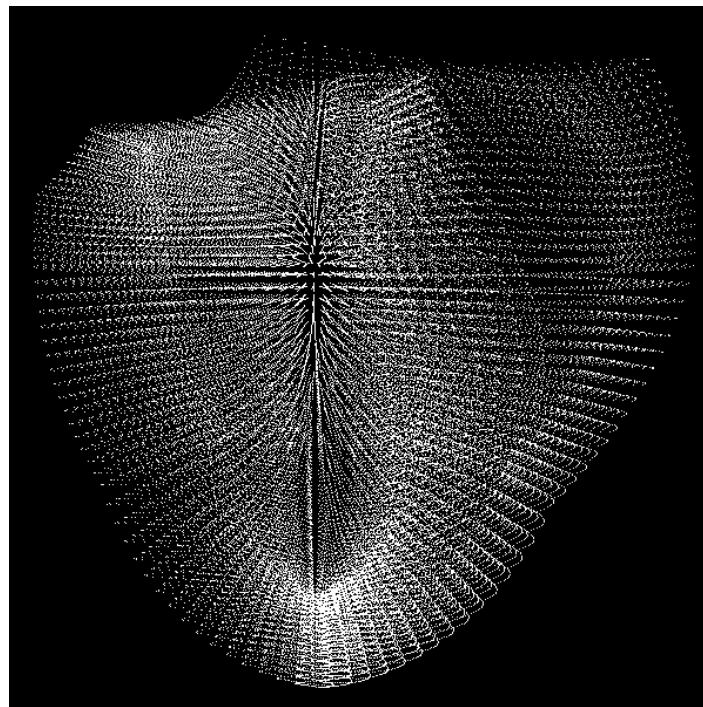


FIGURE 7.11: 66303 collocation points make up the grid from the ventricular finite element mesh.

fibre orientation fields in different hearts, defined relative to their measured and fitted geometry (Grice, Smaill and Hunter 1993). It is worth noting that this model shows significant changes in the transmural variation of fibre orientation at different ventricular sites.

7.3 Ventricular Activation

A refinement of the finite element mesh described in the previous section is used as the solution domain for a series of activation simulations. The above mesh is refined once in the ξ_2 -direction (represented by the coordinate μ) to give 120 elements and 195 nodes, and a collocation scheme using $9 \times 9 \times 9$ collocation points within each element is applied to this mesh, giving a total of 66303 collocation points within the mesh, as shown in Figure 7.11. This section compares the activation patterns through the ventricles depending on the nature of the conductivities, and to clearly highlight this, a standard endocardial stimulus is not used. A localised point stimulus gives a

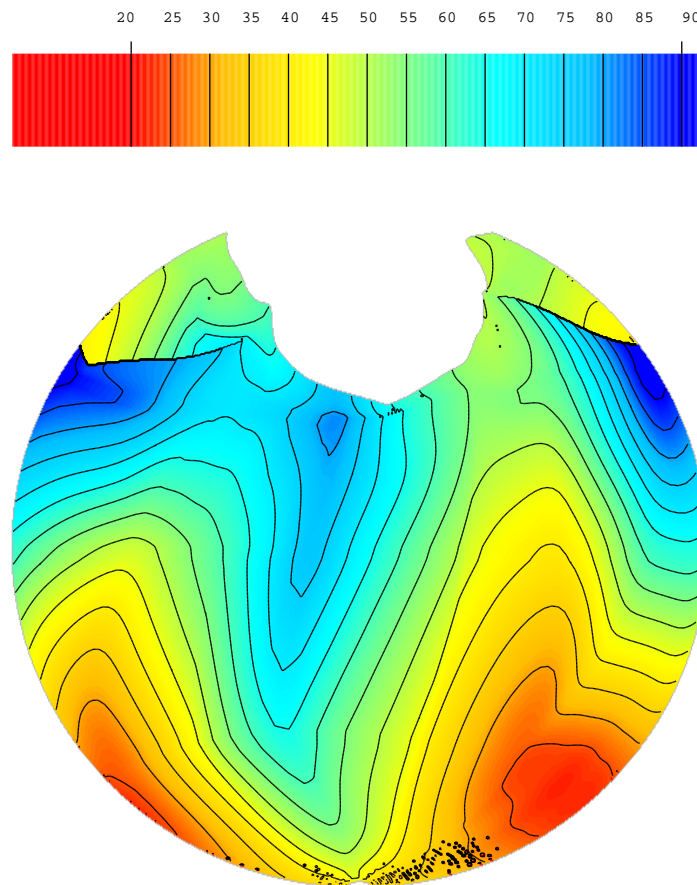


FIGURE 7.12: Epicardial activation time is shown using a Hammer projection for an isotropic ventricular model.

clearer picture of the effect of the fibre and sheet microstructure, and a small cluster of points is chosen which are located on the left ventricular septal wall near the apex.

The FitzHugh-Nagumo model is used with the Rogers modifications in each of the three simulations, and the model parameters are the same as are used in Section 6.3.11, except for the conductivities. The first simulation determines the wavefront propagation through an isotropic domain, the second considers the microstructure to be transversely isotropic, and the third simulation examines the effect of defining an orthotropic microstructure.

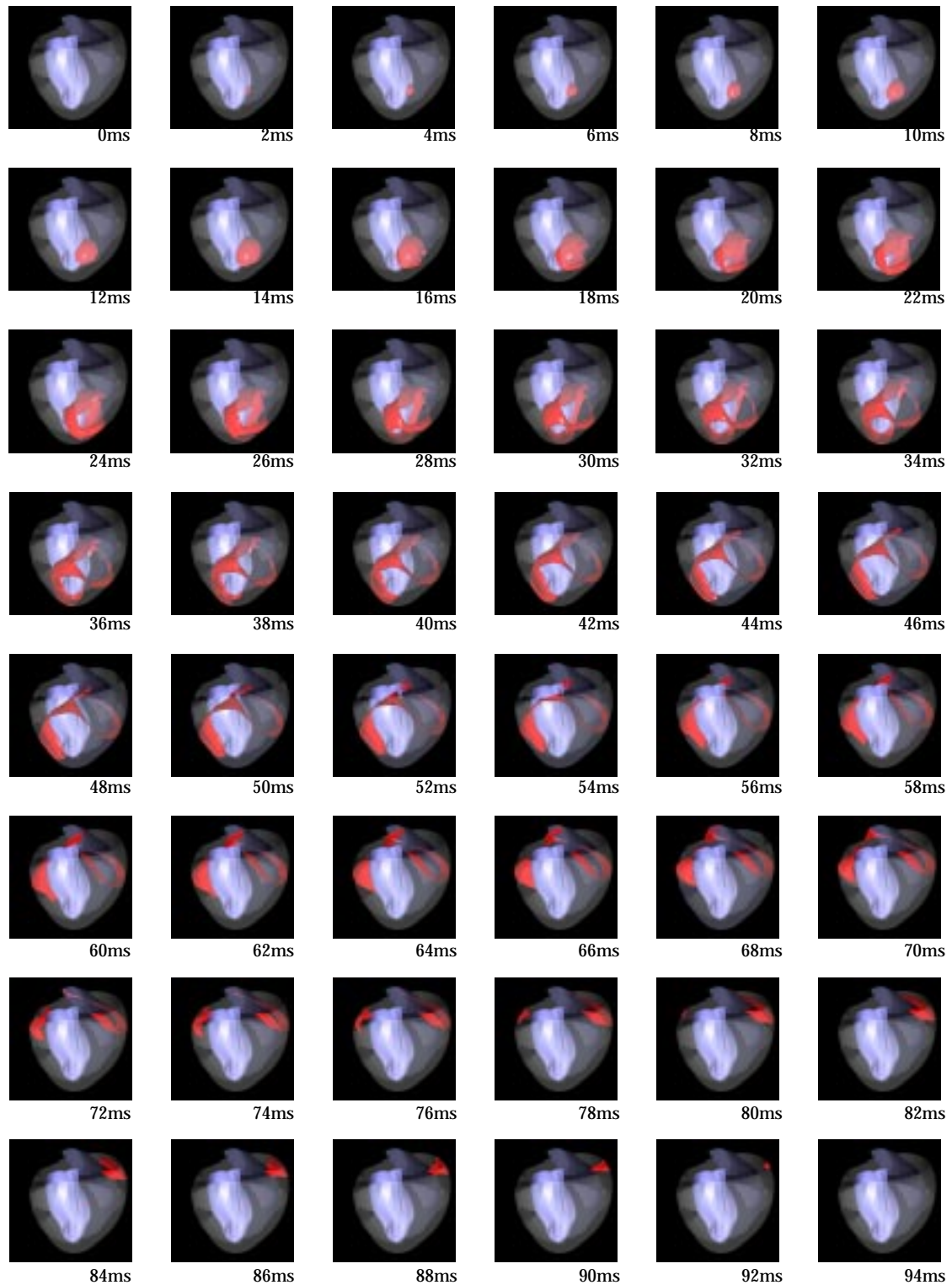


FIGURE 7.13: Activation in an anatomically accurate model of the ventricles using isotropic conductivities.

7.3.1 Isotropic conductivities

The first example defines an isotropic conductivity tensor to be $\sigma = 1.0 \text{ mS} \cdot \text{mm}^{-1}$ in the direction of each of the three principal axes. The activation time on the epicardial surface is shown using a Hammer projection in Figure 7.12. The definition of the Hammer projection is explained in Appendix A. The two regions at the top of the map, where there is a sharp discontinuity in the potential, are in fact projections of the RV septal wall where it extends beyond the epicardial surface, and as such, are unrelated to the rest of the diagram. A movie has also been created which shows the animation of the wavefront moving across the epicardial surface [heart/hapispot](#), but the individual frames have not been reproduced in the thesis. A time series shows the movement of the wavefront through the myocardium at 2 ms time increments in Figure 7.13 [heart/hapiswav](#) for which the wavefront position is determined from the activation times of the internal collocation points.

The initial spread from the activation point is within the septum, and epicardial breakthrough is on the apical RV wall at about 21 ms. From this point the activation spreads throughout the ventricular wall, and final activation is near the basal ring in the centre of the RV at approximately 93 ms.

7.3.2 Transversely isotropic conductivities

The above conductivity is maintained in the fibre direction, but this example reduces the conductivity in the directions normal to the fibre axis by a factor of 5, so that $\sigma_{s,c} = 0.2 \text{ mS} \cdot \text{mm}^{-1}$ in the sheet and sheet-normal directions, giving a 5:1 conductivity ratio. Epicardial activation time is drawn in Figure 7.14, and the movie showing the potential on the epicardium is in [heart/haptrpot](#). The resulting activation wavefront is shown at 4 ms time increments in Figure 7.15 [heart/haptrwav](#).

Due to the fibre directions within the ventricular wall, which are in general circumferential, the activation wave takes considerably longer to reach the epicardium. Initial epicardial breakthrough is very close to the apex, and aligned approximately with the anterior LV-RV boundary, with the activation time delayed to approxi-

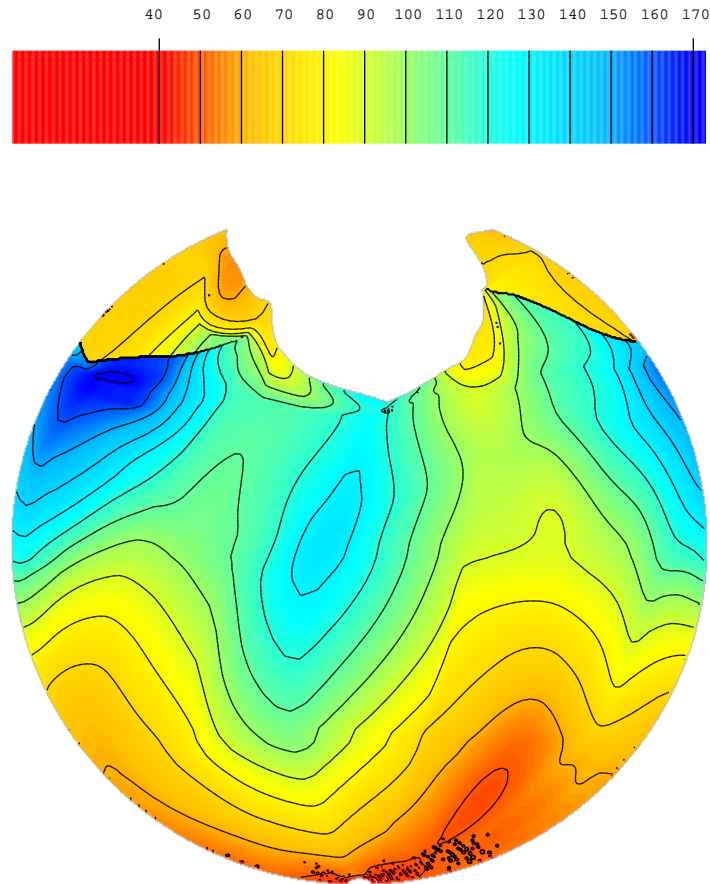


FIGURE 7.14: Epicardial activation time is shown using a hammer projection for a transversely isotropic ventricular model.

mately 40 ms. The point of final epicardial activation has moved towards the posterior RV at the basal ring, with a final activation time of approximately 172 ms.

7.3.3 Orthotropic conductivities

There are not yet any experimental studies which quantify the ratios for an orthotropic conductivity tensor, and it is at this stage uncertain as to whether or not any variation in transverse conduction needs to be implemented in an activation model. Given these uncertainties, it is difficult to make predictions regarding the effect of incorporating a fully orthotropic description of the cardiac microstructure. This section changes the conductivity in the sheet-normal direction

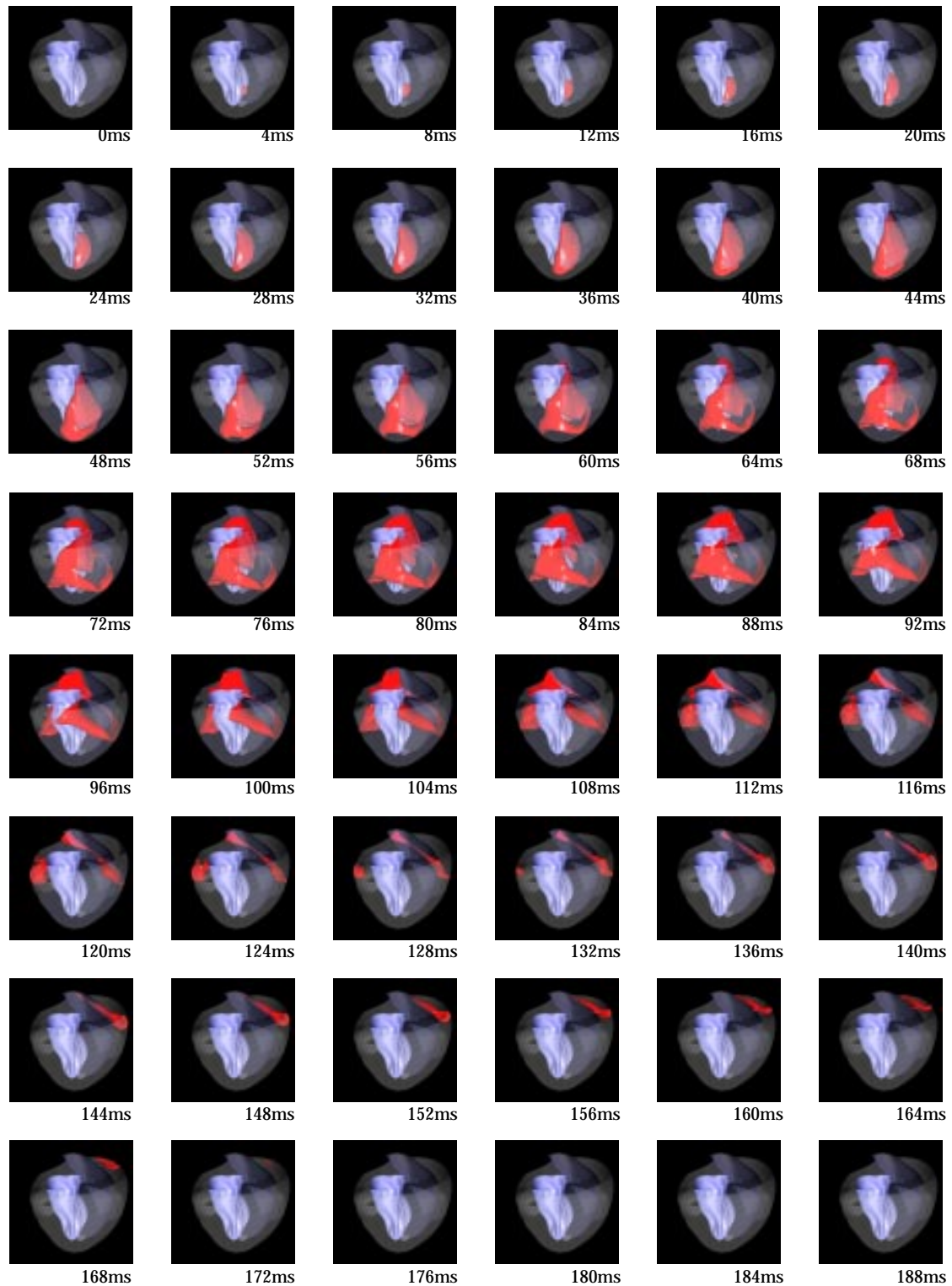


FIGURE 7.15: Activation in an anatomically accurate model of the ventricles using transversely isotropic conductivities.

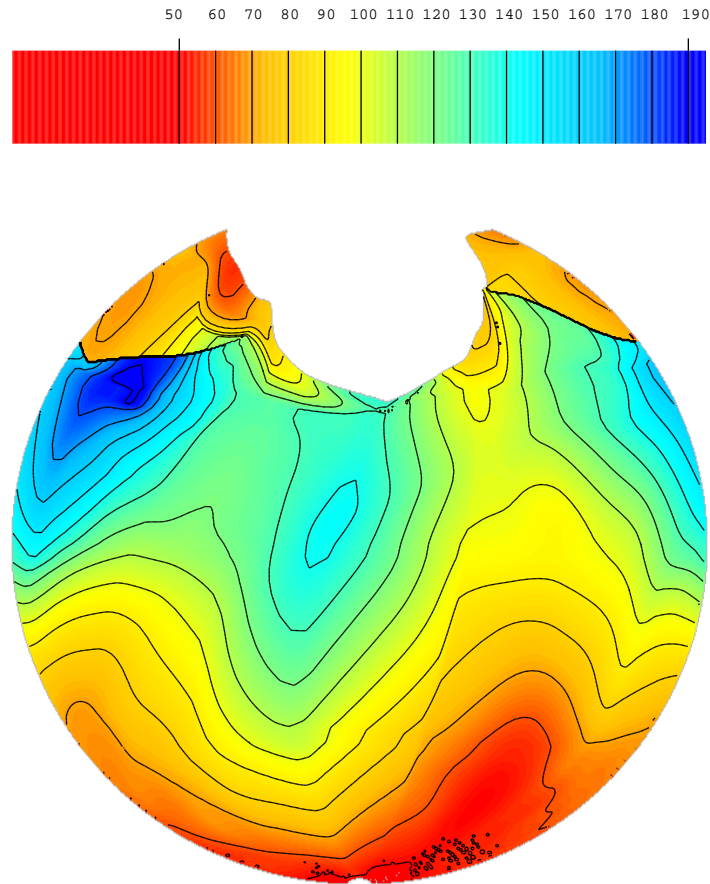


FIGURE 7.16: Epicardial activation time is shown using a hammer projection for an orthotropic ventricular model.

by only a factor of 2 over that used in the previous section so that any variation can be obviously seen as being due to the nature of the microstructure rather than the extreme values of the conductivities. This results in the conductivity tensor comprising values in a 10:2:1 ratio, where the values used are $\sigma_f = 1.0 \text{ mS} \cdot \text{mm}^{-1}$, $\sigma_s = 0.2 \text{ mS} \cdot \text{mm}^{-1}$ and $\sigma_c = 0.1 \text{ mS} \cdot \text{mm}^{-1}$. Illustration of the activation times is drawn in Figure 7.16, and shows a slightly different pattern from the previous two. The associated movie of the epicardial transmembrane potential is in the movie [heart/haporpot](#), and the corresponding passage of the wavefront is shown in Figure 7.17 [heart/haporwav](#).

The total activation time is slightly slower again, as would be expected, with initial epicardial breakthrough at approximately 48 ms, and final at around 195 ms. The initial breakthrough is spread more evenly over the apical region, with the main

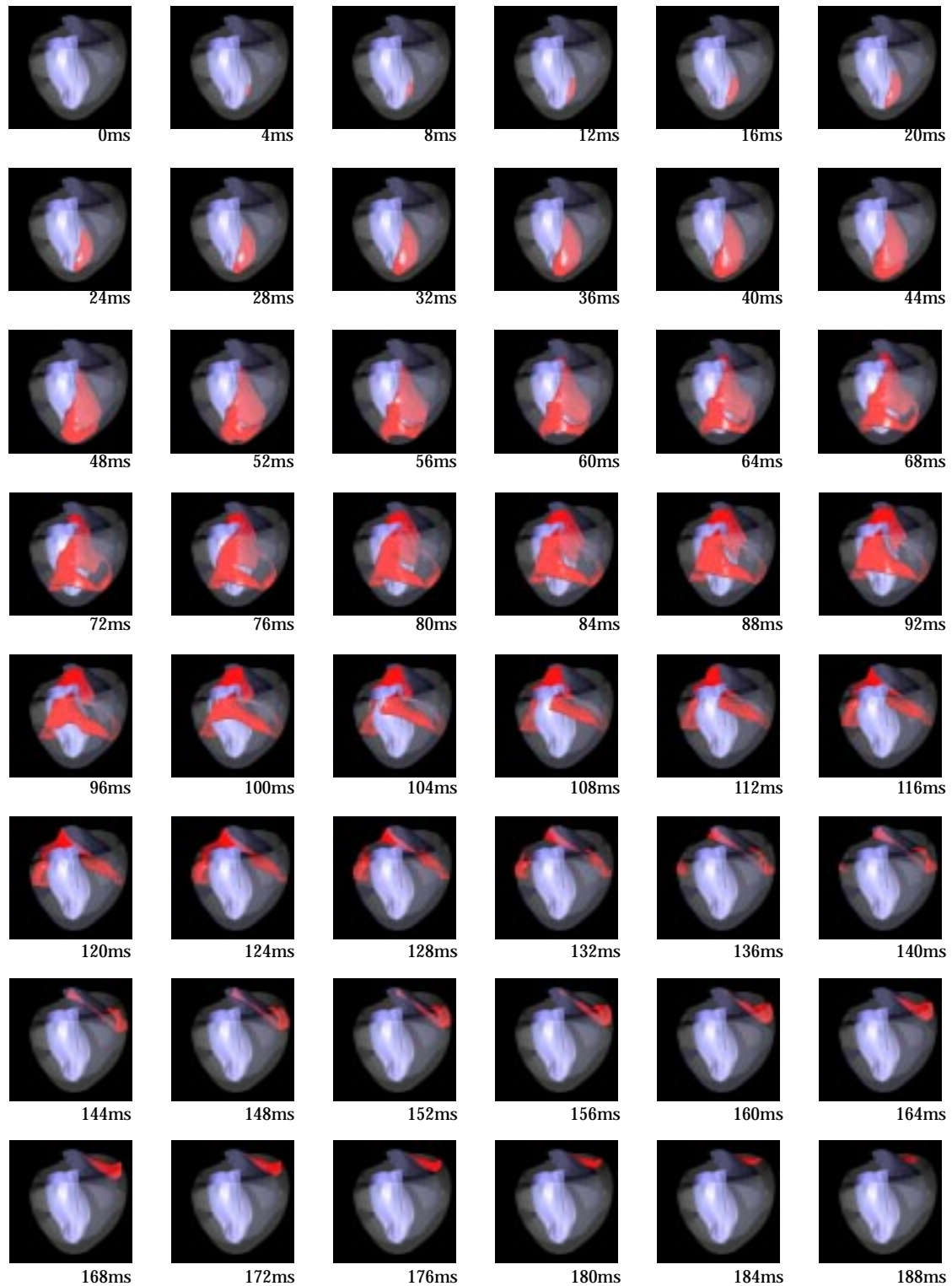


FIGURE 7.17: Activation in an anatomically accurate model of the ventricles using orthotropic conductivities.

initial thrust being towards the anterior edge of the LV. The activation shown at the top of the picture is a projection of the RV septal wall where it extends beyond the epicardial surface, and therefore is not relevant to the discussion, except to note that it also is activated somewhat earlier than in the previous two examples. The final activation is again confined to a region on the posterior RV basal ring.

Chapter 8

Coupled Electromechanics

In the process of cardiac activation, there are mechanical processes at work in the cardiac tissue, which influence and are influenced by the electrical processes. In spite of the large-scale deformation which occurs in a heartbeat, the mechanical deformation is ignored in most activation models. The collocation method described in this thesis has been designed to be easily integrated with a model of deformation, and this section illustrates the flexibility of the method in an electromechanically coupled problem.

There is a two-way interaction between electrical and mechanical processes. Electromechanical coupling describes the influence of electrical activity on the mechanical deformation, and occurs because the depolarisation of the membrane causes calcium to be released from the sarcoplasmic reticulum within the cell, and this acts on the actin and myosin myofilaments causing the cell to contract. In a normal heart, the wavefront from one heartbeat has propagated through the ventricles without reactivating any portion of the tissue, and the contraction does not affect wavefront propagation (though it may affect the recovery process). Mechanoelectrical coupling is the influence of contraction on the excitation wave, and if a reentrant loop is formed, such that the subsequent wavefronts pass through pre-excited tissue, then the muscle may have a deformed geometry and microstructure, and these wavefronts will almost certainly propagate with a different speed, and perhaps direction. It has been seen for some time that mechanical changes can initiate electrophysiological changes by a process known

as contraction-excitation coupling or mechanoelectrical (ME) feedback (Penefsky and Hoffman 1963; Lab 1982; Lerman, Burkhoff, Yue and Sagawa 1985; Kohl, Kamkin, Kiseleva and Noble 1994), and a summary of the concepts is found in Lab (1991). Some recent papers have proposed the existence of *stretch-activated* ion channels (Bustamante, Ruknudin and Sachs 1991; Hagiwara, Masuda, Shoda and Irisawa 1992; Sigurdson, Ruknudin and Sachs 1992; Ruknudin, Sachs and Bustamante 1993) which alter the membrane potential through the transfer of ions when the membrane is stretched.

To whatever extent the electromechanical coupling occurs, there needs to be a greater ability to include it in models of cardiac activity, especially in the investigation of reentrant behaviour. The first stage is to show that the collocation method works correctly given a deforming geometry, and this is discussed in Section 8.1 in which there is only mechanoelectrical coupling (without stretch activated channels) and no electromechanical coupling. Following this, we use a simple coupling and contraction model to allow the membrane to deform in response to the stimulus wave.

8.1 Weakly-Coupled Electromechanics

A *weakly-coupled* electromechanical system is one for which there is minimal coupling between the two processes. In this example the only effect is the influence of path-length changes and material axis deformations caused by the movement of the tissue. A deformation is imposed on the geometry, and the change in material axes is defined by a finite element model of membrane theory finite elasticity for an incompressible medium which uses a pole-zero representation of the forces generated along material axes (Hunter, Nash and Sands 1996). This geometric deformation defines a change in the location of collocation points, which track material positions as they move, and a change in the material axes and therefore conductivities at the point.

A similar smaller problem was developed for Hunter, Nash and Sands (1996) to show propagation in a deforming membrane, and first published there.

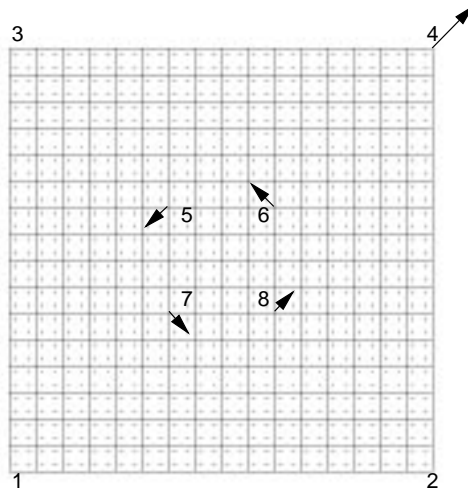


FIGURE 8.1: Definition of the square membrane showing fibre angle variation. Proposed displacements are shown as arrows.

We outline here a simple example designed to show the ability of this collocation scheme to solve the activation equations on a deforming region. Figure 8.1 shows the initial geometry, which is initially exactly the same as the problem defined above in Section 6.4.3 with an S-shaped fibre orientation.

The following deformation is applied to the mesh. Point 1 is fixed in both x and y , although the mesh is able to rotate about this point. Point 2 is fixed in y and point 3 is fixed in x , meaning that these two points are constrained to remain on the coordinate axes. Point 4 is defined to move by 0.3 mm in both x and y directions at each load step, and points 5 to 8 move by 0.15 mm in a diagonal fashion as shown by the arrows in Figure 8.1 at each load step. 50 load steps were precomputed using the finite element program with the convergence criterion being that the sum of solution vector increments has fallen below 10^{-4} mm and that the ratio of unconstrained residuals to constrained residuals has also fallen to less than 10^{-4} . The deformation of the mesh is computed using a large deformation model of the membrane mechanics using an orthotropic constitutive law, and taking into account the defined fibre directions. The final mesh at 50 load steps is shown in Figure 8.2, with the computed deformed fibre orientations shown on the right hand side of the figure.

In the undeformed mesh, the conductivity tensor is diagonal because the local

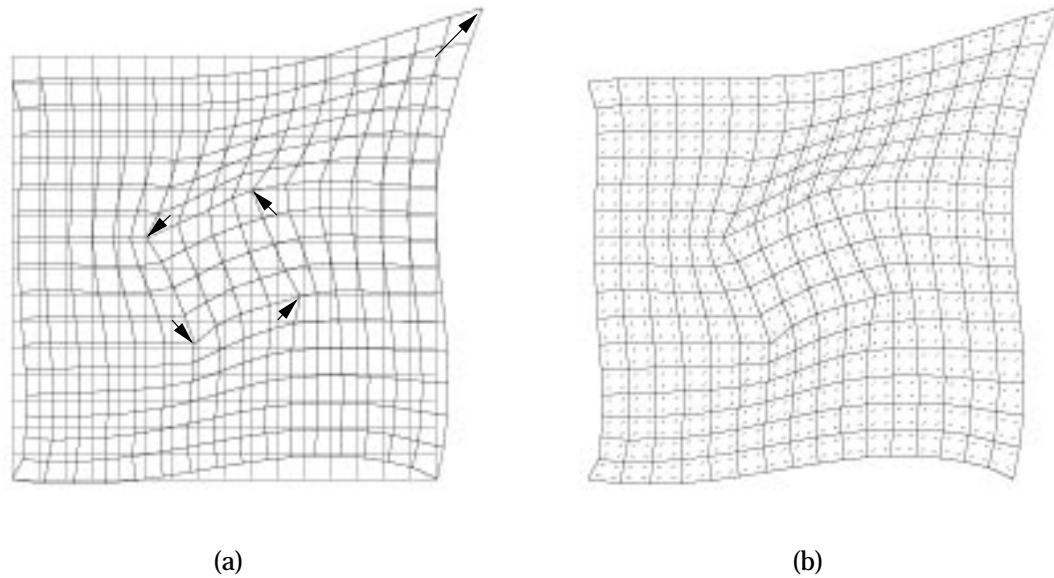
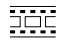


FIGURE 8.2: (a) Deformed mesh, with undeformed mesh shown using dotted lines. The imposed deformation is shown as arrows of displacement. (b) Deformed finite element mesh showing orientation of deformed fibre directions.

material coordinates are by definition orthogonal, but it becomes more non-diagonal as the stretch distorts the membrane, and thus changes the mapping from material coordinates to global coordinates. The precomputed load steps are applied at 10 ms intervals throughout the activation process, and the local metric tensors and conductivities are updated for each solution point at their new positions. The stimulus protocol used is the same as for the VCD example described for Figure 6.20 in Section 6.4.3. The resulting spiral wave is presented in the time series in Figure 8.3.

 reentry/vcdweak

In comparing this sequence with that shown in Figure 6.20 for the similar non-deforming setup, we notice one main difference. The rotation time for the spiral wave has decreased from about 110 ms for the non-deforming mesh to around 70 ms. This is solely because the central portion of the mesh is being rotated in the same direction as the spiral wave is propagating. If the central rotation was in the opposite direction to the spiral wave rotation, we would expect a corresponding increase in the rotation time.

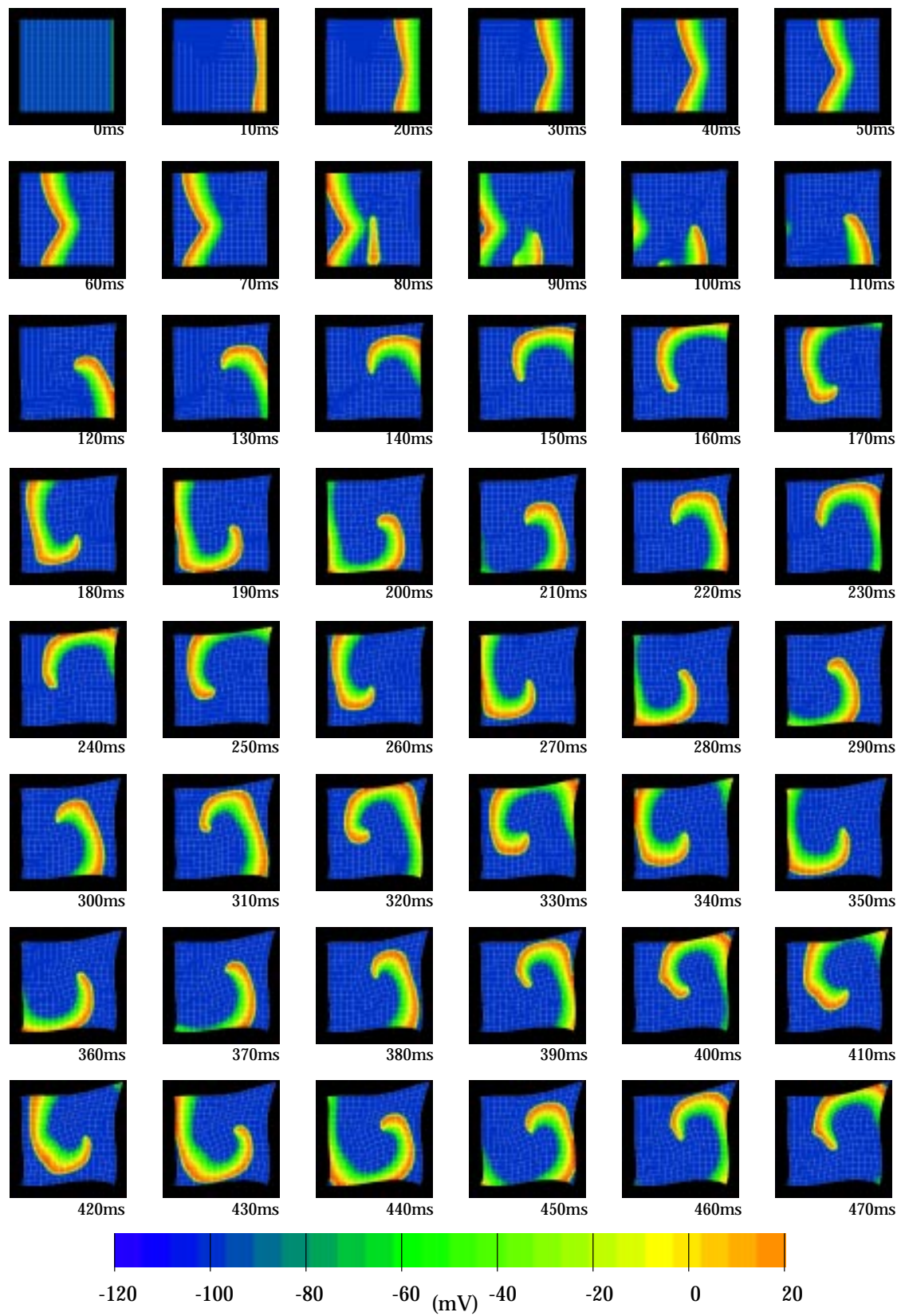


FIGURE 8.3: Spiral wave on a deforming mesh with an S-shaped fibre field.

8.2 Strongly-Coupled Electromechanics

A *strongly-coupled* electromechanical model has a much tighter coupling between the electrical processes and the mechanical processes, as the name implies. In most cases, the coupling between electrical activation and mechanical deformation is assumed to be through the concentration of intracellular calcium ($[Ca]_i$). It requires two additional groups of equations: one which computes the change in $[Ca]_i$, and one which describes how these changes in $[Ca]_i$ produce deformation of the tissue.

Many of the biophysical ionic current models incorporate a measure of changes in $[Ca]_i$, with the Beeler-Reuter model having a simple description (Equation (4.56)), and later models such as the LR-II having a much more complex description of intracellular calcium transport (Section 4.1.9). The simplified models, such as the FHN and VCD models used in earlier examples, do not include such a parameter, and if one of these models needs to be used, then a simple model of calcium change must be developed. In some of the examples presented in this chapter, we choose to use the modified van Capelle-Durrer model (Section 4.2.3), and construct an equation which effectively describes the level of activation by the transmembrane potential, and defines the change in $[Ca]_i$ to be

$$\frac{d[Ca]_i}{dt} = \frac{V_{norm} - [Ca]_i}{\tau_{Ca}} \quad (8.1)$$

where V_{norm} is a normalised transmembrane potential relative to the resting potential and τ_{Ca} is a time constant for the calcium release process. A similar equation may also be included in the FHN model.

There are several possible models which could be used to describe excitation-contraction coupling. These are models which describe the relationship between the level of $[Ca]_i$ and the developed tension. The simplest model is a quasi-static model describing only the steady-state behaviour of the muscle, and defines a direct relationship between $[Ca]_i$ and tension by assuming that the cell is allowed to reach a steady-state solution for a given value of $[Ca]_i$. However, cardiac muscle contracts dynamically, and a more sophisticated model of the dynamic properties of myocardium in which there is a nonlinear function of tension must be defined if this needs to be taken into account. One such model is the *fading memory* model (Bergel and Hunter 1979), however this model will not be used in this thesis due to its complexity.

8.2.1 Steady-state $[\text{Ca}]_i$ -tension relationship

We use a steady-state $[\text{Ca}]_i$ -tension relation such as given in Hunter, Smaill, Nielsen and Grice (1996) which describes isometric tension as a linear function of $[\text{Ca}]_i$.

By subtracting the passive component of tension from the measured total tension (for $[\text{Ca}]_o = 2.5 \text{ mM}$), Hunter, Smaill, Nielsen and Grice (1996) found that the maximally activated *isometric* tension $T_0(\lambda)$ is a linear function of the muscle fibre extension ratio λ with slope $\frac{dT_0}{d\lambda} = 145 \text{ kPa}$ or a non-dimensional slope of $\beta = \left[\frac{1}{T_0} \frac{dT_0}{d\lambda} \right]_{\lambda=1} = 1.45$. At resting sarcomere length ($1.9 \text{ }\mu\text{m}$ or $\lambda = 1$ corresponding to no passive tension), the measured tension was $T_0 = 100 \text{ kPa}$. This leads to the $T_0(\lambda)$ relation in Equation (8.2) for given level of activation.

$$T_0(\lambda) = T_{\text{ref}}[1 + \beta(\lambda - 1)] \quad (8.2)$$

where $T_{\text{ref}} = 100 \text{ kPa}$ is the isometric, actively developed tension at $\lambda = 1$ and saturating $[\text{Ca}]_i$.

The variation of isometric tension with $[\text{Ca}]_i$ under steady state conditions and constant λ , is described by the sigmoidal Hill relation for dose-response behaviour in Equation (8.3).

$$T_0([\text{Ca}]_i) = \frac{[\text{Ca}]_i^h}{[\text{Ca}]_i^h + c_{50}^h} \quad (8.3)$$

where c_{50} is the $[\text{Ca}]_i$ at which the isometric tension is 50% of its maximum, and h is the Hill coefficient, determining the shape of the saturation curve.

The combination of Equations (8.2) and (8.3) results in an expression for the isometric tension in terms of the extension ratio and intracellular calcium, in Equation (8.4).

$$T_0(\lambda, [\text{Ca}]_i) = \frac{[\text{Ca}]_i^h}{[\text{Ca}]_i^h + c_{50}^h} \cdot T_{\text{ref}}[1 + \beta(\lambda - 1)] \quad (8.4)$$

Note that in general $[\text{Ca}]_i$ is also length dependent, since the release of calcium from the sarcoplasmic reticulum is influenced by stretch. A fuller description of this model may be found either in the chapter cited above, or in Nash (1998).

8.2.2 Plane wave propagation

For this example, we use the same problem definition as outlined for the S-shaped fibre field in Section 6.4.3, where the fibre angle at the top and bottom of the mesh is initially 10° , and smoothly curves through 90° in the centre of the mesh. The boundary conditions on these first electromechanical problems restrict the movement of all boundary nodes on the finite element mesh, while allowing the internal nodes to move as necessary according to the contraction of the element. Alternative boundary conditions are specified for later problems as required.

The VCD model is used as above, with a 2:1 conductivity ratio and a Ca^{2+} time constant of $\tau_{\text{Ca}} = 30$. Two waves are initiated at the right-hand edge, the first at 0 ms and the second at 55 ms, which is after the right-hand edge has recovered sufficiently to propagate a second stimulus, but while the first wave is still travelling through the mesh.

It was determined that the equations describing the mechanics would be solved every 2 ms, and the position of the nodes remains constant during that time step. The size of this time step is determined largely by balancing the solution time of the equations against the need to track the deformation. Due to large changes in element size and shape during the simulation, and therefore to large changes in the collocation point spacings, the activation equations need to be solved with a time step of 0.01 ms, or 10% of that used in previous examples, in order to maintain stability using the explicit collocation technique.

The mechanics equations are solved using a Newton-Raphson iterative method which linearises the nonlinear system of equilibrium equations. The method of generalised minimum residuals (GMRES) is used to solve the resulting system of linear equations. Each solution of the mechanics equations requires around 6 or 7 full Newton iterations in order to reduce the two accuracy measures (ratio of unconstrained to constrained residuals, and sum of solution vector increments) to below 10^{-10} mm, with each minor iteration taking approximately 30s (CPU). The activation solution of 200 time steps to give 2 ms of activation took 1m16s (CPU). The total time required for a 2 ms simulation was around 5m10s (CPU), where the additional time is used in computing deformed grid point positions and metric tensors, and in writing out solution files and graphical output. Each 100 ms of

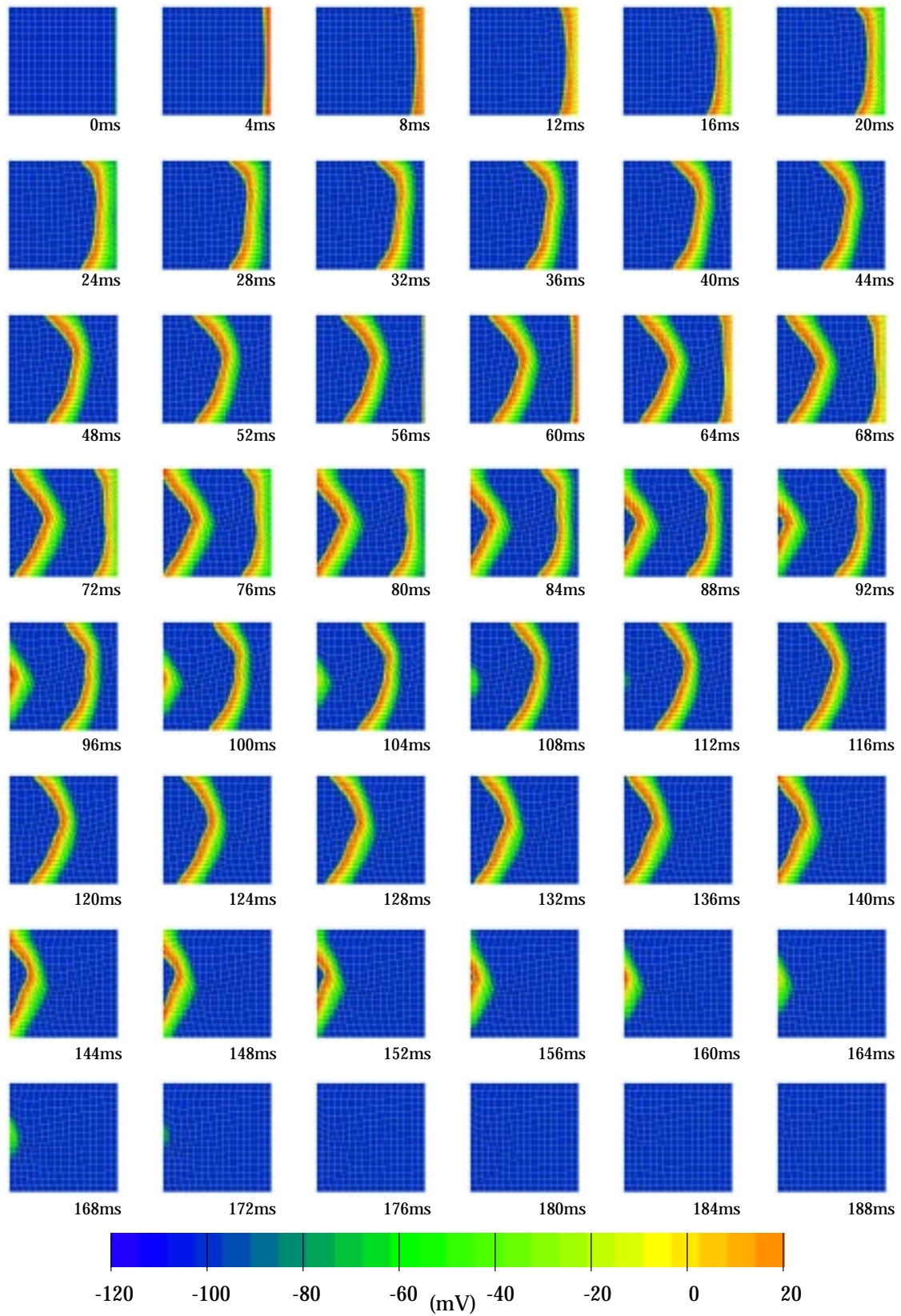


FIGURE 8.4: Plane waves with electromechanical coupling causing deformation. Frames are shown at 4 ms intervals.

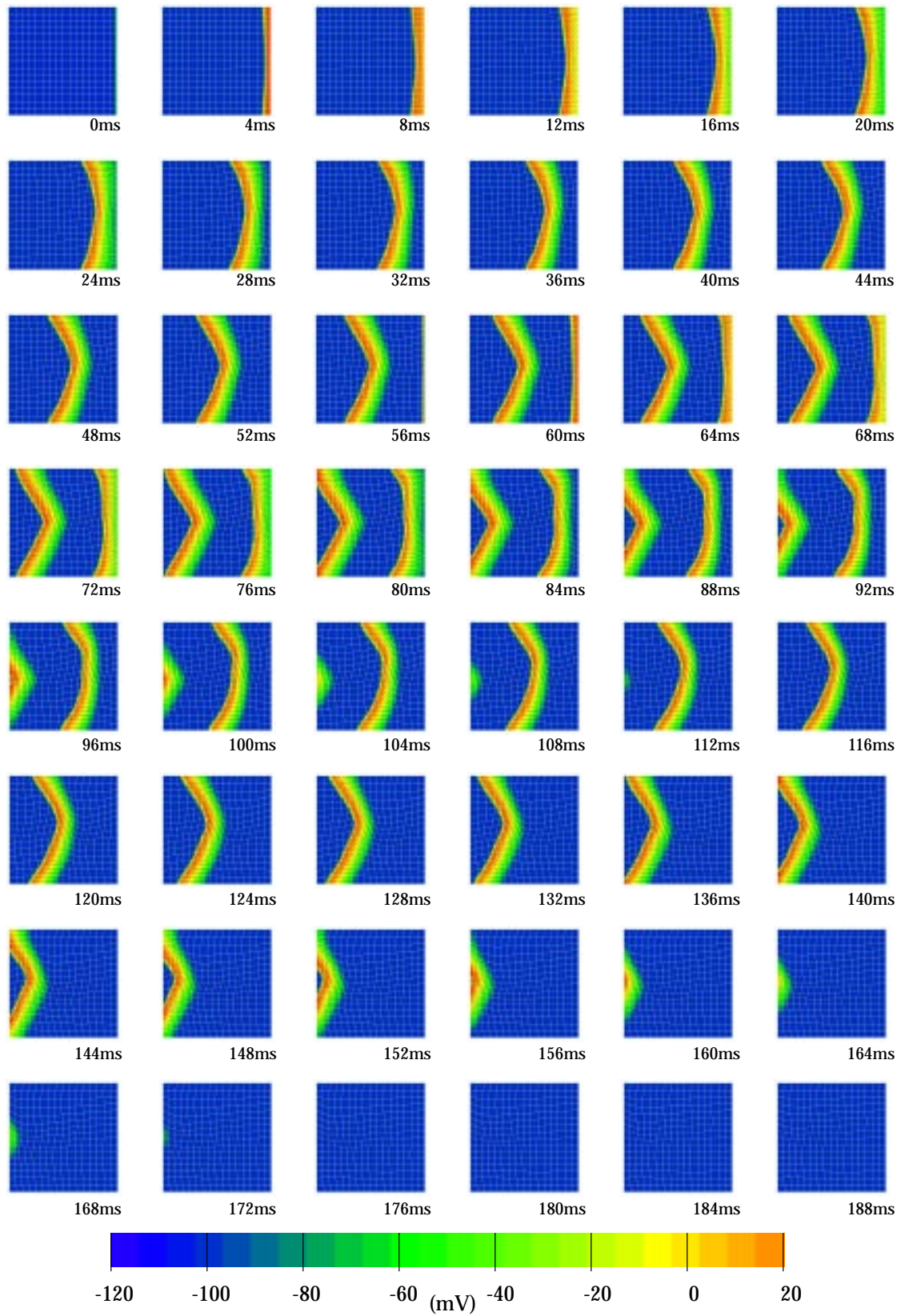


FIGURE 8.5: Plane waves with electromechanical coupling causing deformation.

$$\tau C \alpha = 50.$$

simulation therefore required 258m20s (CPU), or approximately 4.3 hours.


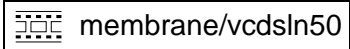
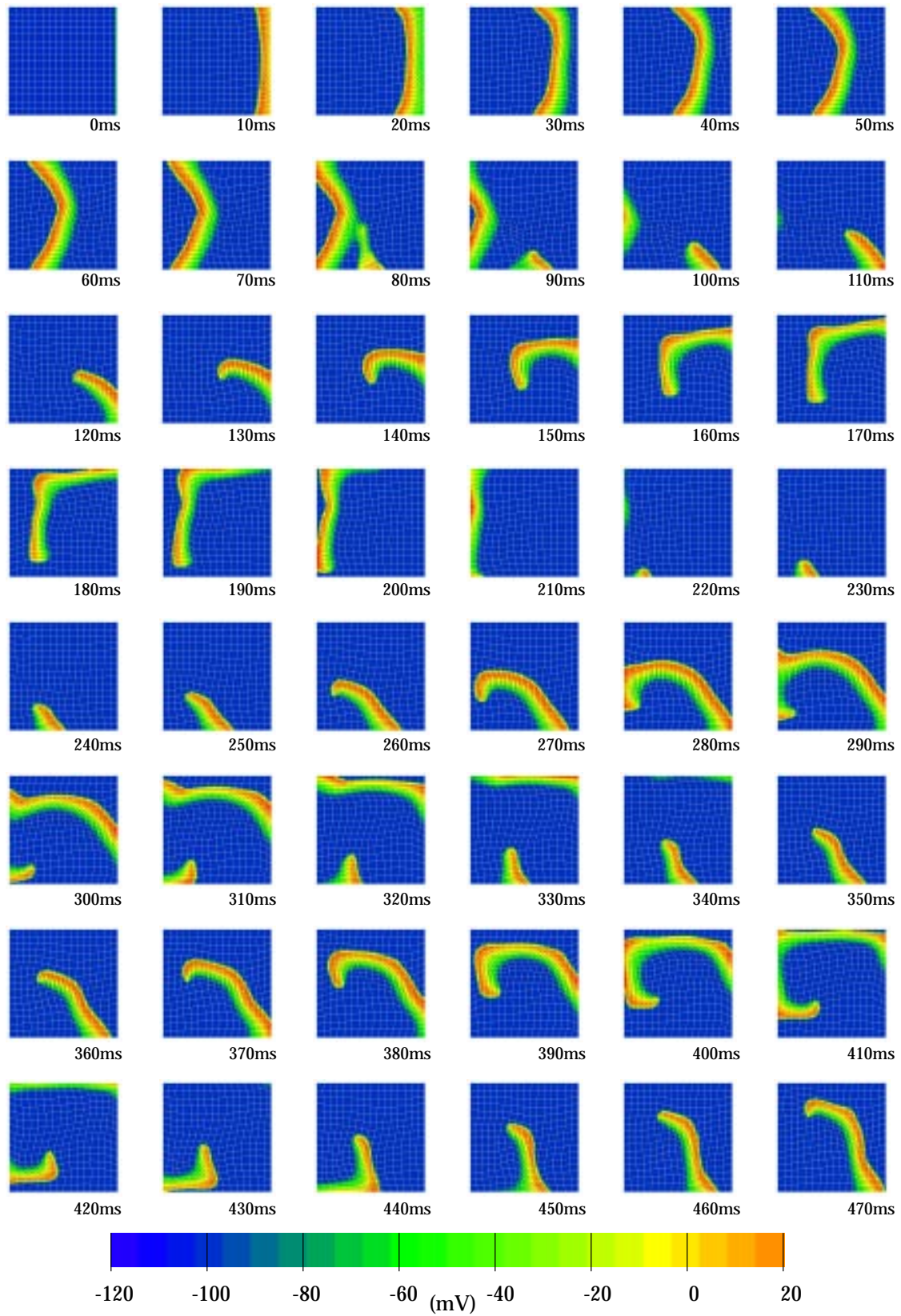
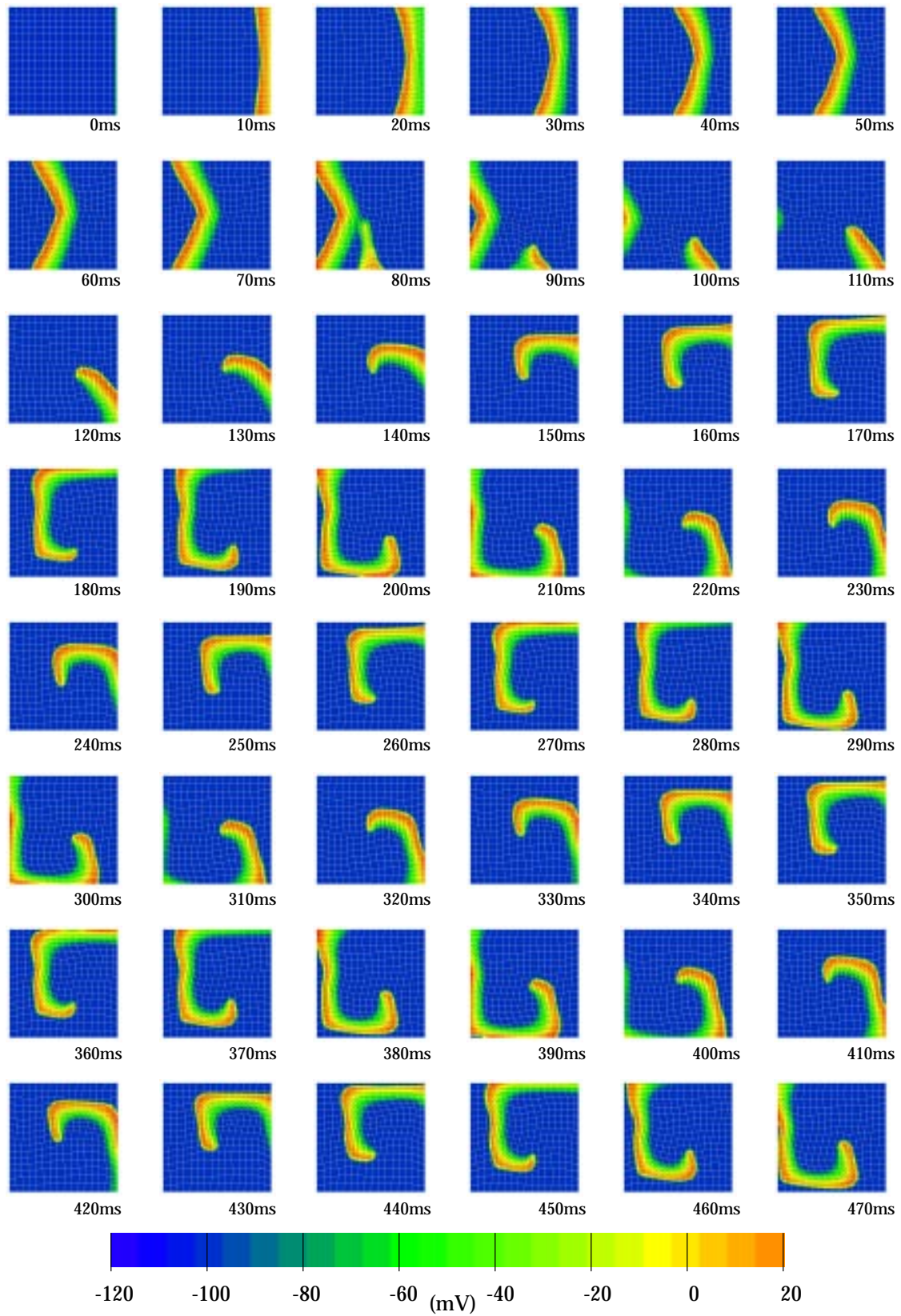
A time series of the resulting activation waves is drawn in Figure 8.4  membrane/vcdsln30, where frames are shown at 4 ms intervals. The second wave is propagating through tissue which is still deformed following the passage of the first wave, and therefore it follows a slightly different path. In particular, the curve in the second wave is less angular than the first, and is several elements higher, as seen by examining the last part of the left-hand wall to be activated for each wave. Note that the elements contract primarily along the fibre direction, so that the central elements are shortening vertically and the top and bottom elements are contracting horizontally in the vicinity of the wavefront.

Figure 8.5  membrane/vcdsln50 shows the same activation pattern when the calcium coupling coefficient is increased to $\tau_{Ca} = 50$ and consequently the deformation is smaller. Each wave is initiated at the same time as in the previous example.

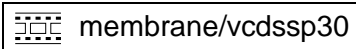
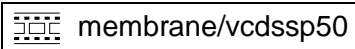
8.2.3 Spiral wave propagation using the VCD model

Applying the second stimulus at a point just behind the initial wavefront will produce one of three possible second waves, as already shown in Section 6.4.3. If the stimulus arrives just before the tissue is recovered sufficiently to support a second wave, the stimulus will die out. A second stimulus arriving during a small window of time immediately after the tissue will generate a second wave produces a unidirectional wave travelling in the opposite direction to the first propagating wavefront. A still later stimulus may cause a pair of wavefronts to propagate, one following the initial wave and one in the opposite direction. If, in addition, the tissue on which the waves are propagating is deforming, then the path of the spiral wave is altered further.

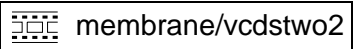

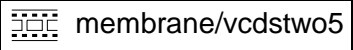
FIGURE 8.6: Propagation of a spiral wave in a coupled system, where $\tau_{Ca} = 30$.

FIGURE 8.7: Propagation of a spiral wave in a coupled system, where $\tau_{Ca} = 50$.

A single rotating wave

Figures 8.6 and 8.7   show the results of a second stimulus at $t = 70$ ms in the same way as previously applied to generate spiral waves in Section 6.4.3. Both time sequences show almost identical propagation of the initial wave and the start of the second wave up until frame 160. Because the $\tau_{Ca} = 50$ system is deforming less than the first system, the subsequent progress of this wavefront is more similar to the non-deforming propagation in Figure 6.20, with the main difference being that the wave on the deforming mesh travels somewhat faster, due to the forces on the mesh from one wavefront pulling the next rotation of the spiral wave around more quickly. The $\tau_{Ca} = 30$ system displays a more irregular behaviour, and the wave almost dies out in frames 210 and 290. The period of rotation is less constant, and the wave travels a different path in each rotation.

Two independent waveltips

If the second stimulus is delayed by 10 ms (that is, the stimulus is applied at $t = 80$ ms) then it is sufficiently late to allow the formation of a pair of secondary waves. Three examples are shown which have varying degrees of coupling. Figure 8.8  shows the effect of defining $\tau_{Ca} = 20$ which causes a large mechanical contraction. Figure 8.9  gives a slightly smaller contraction due to the coupling being $\tau_{Ca} = 30$, and the final example in Figure 8.10  shows the result of setting $\tau_{Ca} = 50$, in which the membrane contracts the least.

In all three examples, frames 90 and 100 show a similar pattern which leads to the creation of the two waves. The initial wave has followed a similar path through the tissue, though the deformation of the elements at the time of the second stimulus varies considerably between each example. In each case, the wave initiated which is propagating to the left is much smaller and travels more slowly than the other initiated wave travelling to the right, due to the fact that it is propagating into tissue which is less recovered from the first wavefront. Due to the variation in contractility of the tissue into which the waves are propagating, the resulting interaction of the

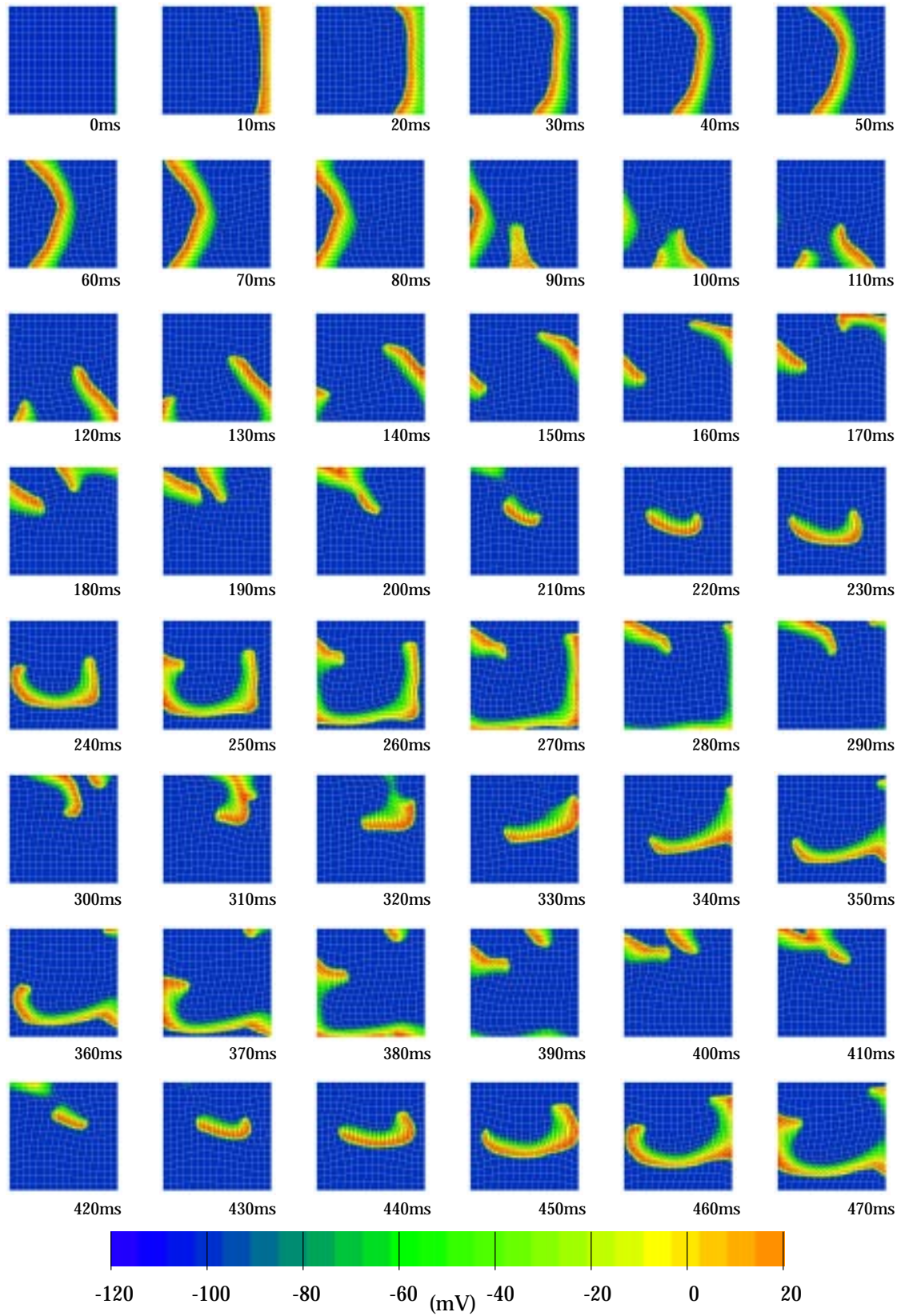


FIGURE 8.8: Two spiral waves are created with a second stimulus 10 ms later.

$$\tau_{Ca} = 20.$$

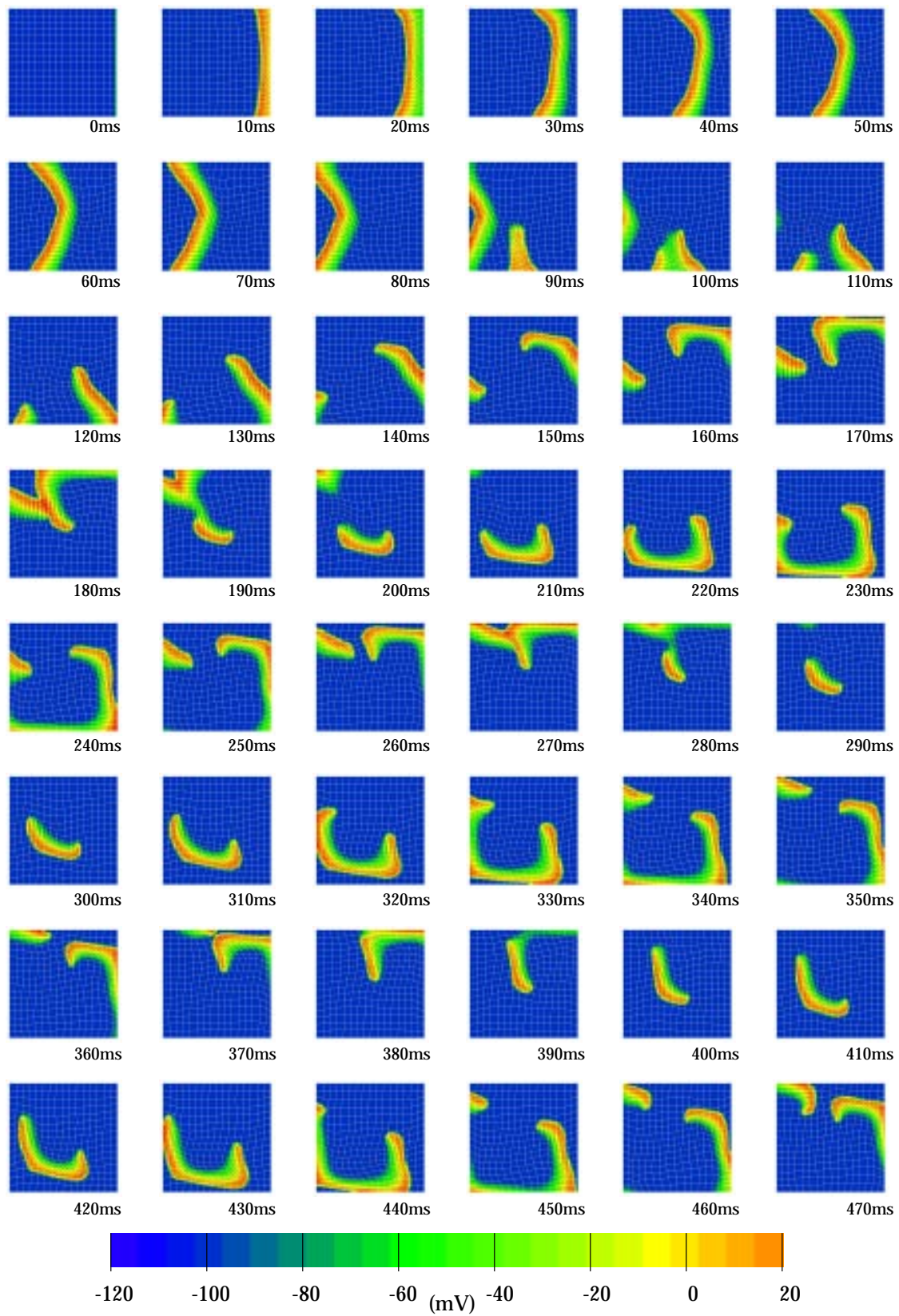


FIGURE 8.9: Two spiral waves are created with a second stimulus 10 ms later.

$$\tau_{Ca} = 30.$$

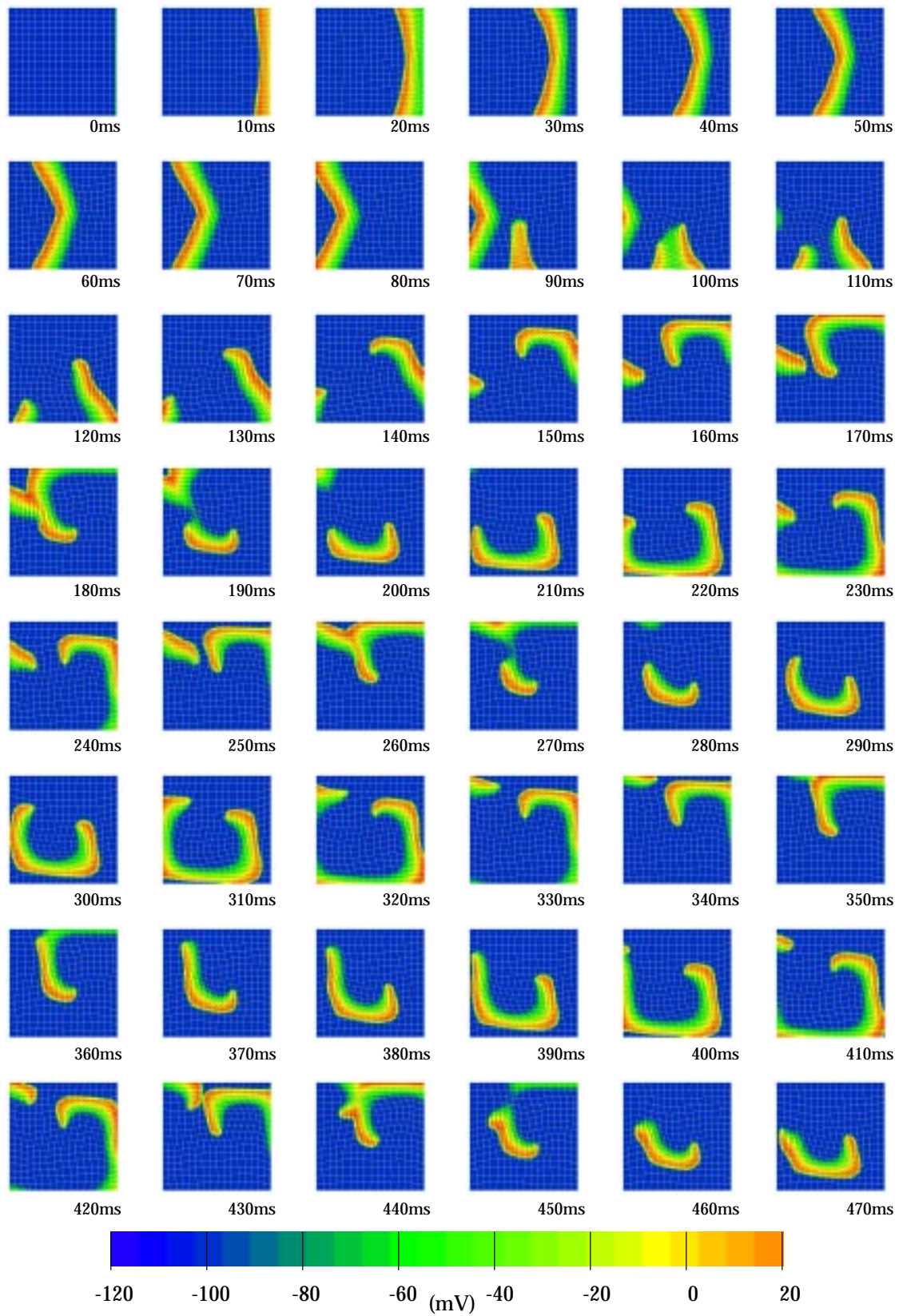


FIGURE 8.10: Two spiral waves are created with a second stimulus 10 ms later.

$$\tau_{Ca} = 50.$$

waves is substantially different.

After a longer time period than drawn in the figures, but as shown in the movie files, the three simulations have a different result. The first example ($\tau_{Ca} = 20$) continues to propagate a pair of rotating waves, with considerable deformation of the mesh. The last ($\tau_{Ca} = 50$) example turns into a single rotating spiral wave, while in the middle example created using $\tau_{Ca} = 30$, the waves die out completely. This clearly shows that there is a large degree of interaction between the evolution and lifespan of a reentrant propagating wave and the deformation of the underlying geometry.

8.2.4 Using a physiological model of $[Ca]_i$

An ionic current model which is based upon physiologically measured parameters contains a description of the change in $[Ca]_i$ during an action potential. In this section, we use the Beeler-Reuter model of membrane kinetics which has a simple model of the calcium change (Equation (4.56)), though it is still much more realistic than the model used with the VCD equation. Later models such as the LR-II and DFN models have an even fuller description of the calcium concentration, and add equations which describe the transport of Ca^{2+} ions between the myoplasm and the different portions of the sarcoplasmic reticulum.

This section presents a number of scenarios which have identical initial conditions and boundary conditions, starting from an activation wave on an isotropic, non-deforming mesh. This mesh is identical to those used above, with the following parameters.


In the isotropic activations, the conductivity is uniformly $0.15 \text{ mS} \cdot \text{mm}^{-1}$, and the anisotropic conductivities have a 2:1 ratio with values of $0.15 \text{ mS} \cdot \text{mm}^{-1}$ in the direction of the fibre and $0.075 \text{ mS} \cdot \text{mm}^{-1}$ in the cross-fibre direction. The stimulus protocol is identical for all simulations. The first stimulus is on the right hand side of the mesh, with an intensity of $0.1 \text{ mA} \cdot \text{mm}^{-3}$ and a duration of 1 ms. The second stimulus has the same intensity, and is applied along the lower half centre-line for a period of 10 ms at a time 1300 ms following the initial pulse. A solution time step of $\Delta t = 0.05 \text{ ms}$ is used in all cases, and the DTAR method is not employed. All other parameters for the BR model are the same as used in Chapter 6.


Even though this is a physiological model of the intracellular calcium concentration, the steady-state mechanics model is derived for concentrations of extracellular calcium which are much easier to obtain. The $[Ca]_i$ is several orders of magnitude smaller than the $[Ca]_e$ and so for these simulations we scaled the value of $[Ca]_i$ by 10^5 in the mechanical model in order to give a realistic contraction. A better solution would be to reformulate the mechanical model so that it generates correct results for an input of $[Ca]_i$, but this is not available in the formulation of the model which we are using.

Three membrane definitions are used. The first is isotropic, the second uses the anisotropic conductivity tensor on a constant θ fibre field and the third uses the same anisotropic conductivities on a fibre field which varies in an “S”-shaped pattern in the same way as described in Section 6.4.3 on page 196. These three options are firstly solved for a non-deforming geometry producing similar results to those shown earlier. The same three cases are then solved in a coupled model under each of two sets of mechanical boundary conditions. The first is as before, in that all boundary points are fixed and all internal points are free to move in order to minimise strains. Secondly, the conditions are relaxed slightly so that only the corner points are fixed, and the boundary points are only constrained to remain in straight lines between the corner points, that is, the external boundaries of the domain remain straight.


Each example is represented in the thesis by a time sequence of 48 images at 100 ms intervals showing the first portion of the activation, and by movies on the CD and the Web which are approximately twice as long.

Non-deforming geometry

These sequences are very similar to those created for the BR model in Chapter 6, except that the conductivities and stimulus times are slightly different. The results of using isotropic conductivities is shown in the first movie sequence in Figure 8.11  membrane/brisnd and shows the evolution of an almost circular spiral, which continues with little variation throughout the observed time.


The sequence shown in Figure 8.12  membrane/br21nd00 shows the effect of

including a 2:1 anisotropy ratio with a constant 0° fibre angle. The wavefront is elongated in the direction of the fibre field, and the wavetip wanders throughout the region.

The third sequence includes the varying fibre angle, and is drawn in Figure 8.13  membrane/br21nd. The initial wavefront propagates less quickly in the cross-fibre direction in the centre of the mesh, as shown in the first frames up to frame 1400, and because of this the second wave only activates at the bottom of the mesh as the central region has not yet recovered sufficiently at this stage to support a second activation. The resulting wavefront takes on a slanted oval shape due to the underlying fibre field.

Deforming geometry with fixed boundaries

The same three above examples are now solved for a deforming mesh, in which the boundary nodes remain fixed, and the elements contract along the fibre direction according to the released $[Ca]_i$. This produces spiral waves which differ markedly from the non-deforming examples above.

The first simulation uses the same isotropic conductivities as above. Although no fibre field is defined for the activation, the elements need to contract along a fibre axis, and therefore the constant 0° fibre field is used only for the mechanical deformation calculations. This results in the time sequence shown in Figure 8.14  membrane/brisd. Because of the fibre field used, the mesh contracts in the direction of the initial wavefront propagation in the centre, though not at the edges due to the fixed boundary nodes, and produces a “V”-shaped activation pattern as the contracting mesh retards the propagation in the centre of the domain. Because the second stimulus is applied on the element boundary, which has moved with the contraction, rather than at the physical centre of the domain, the stimulation is shifted to the left, with a curve back to the boundary. This lower portion of the domain has had more time to recover, and therefore a double spiral is formed. The spiral initially travelling to the left is somewhat slower than the main spiral, after some 8000 ms of interaction (after the diagrams shown in the associated figure, but within the movie file) one wavetip does not continue to propagate, and the spiral reverts to a single wave rotating anti-clockwise.

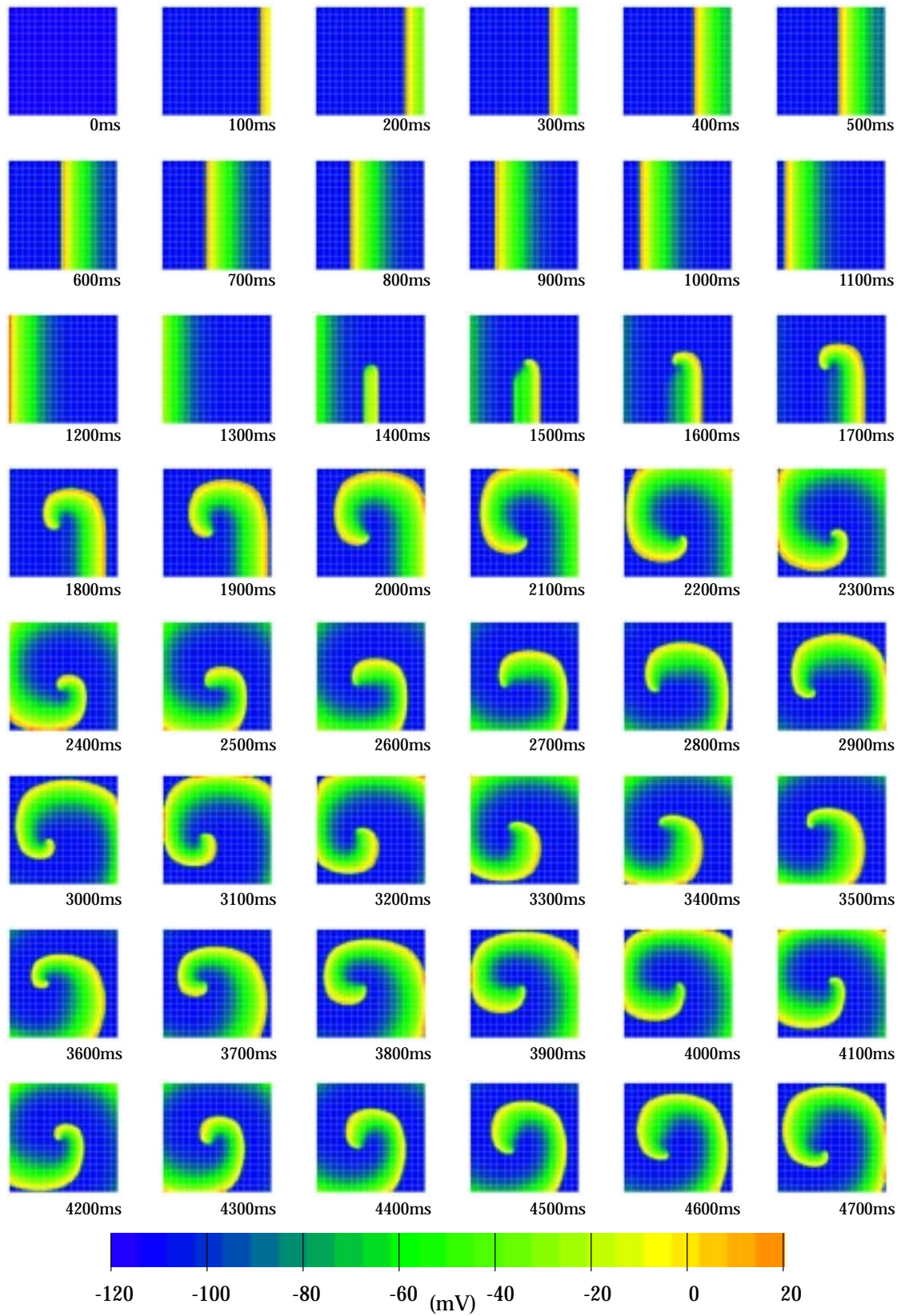


FIGURE 8.11: Isotropic conductivity using the Beeler-Reuter model on a non-deforming mesh.

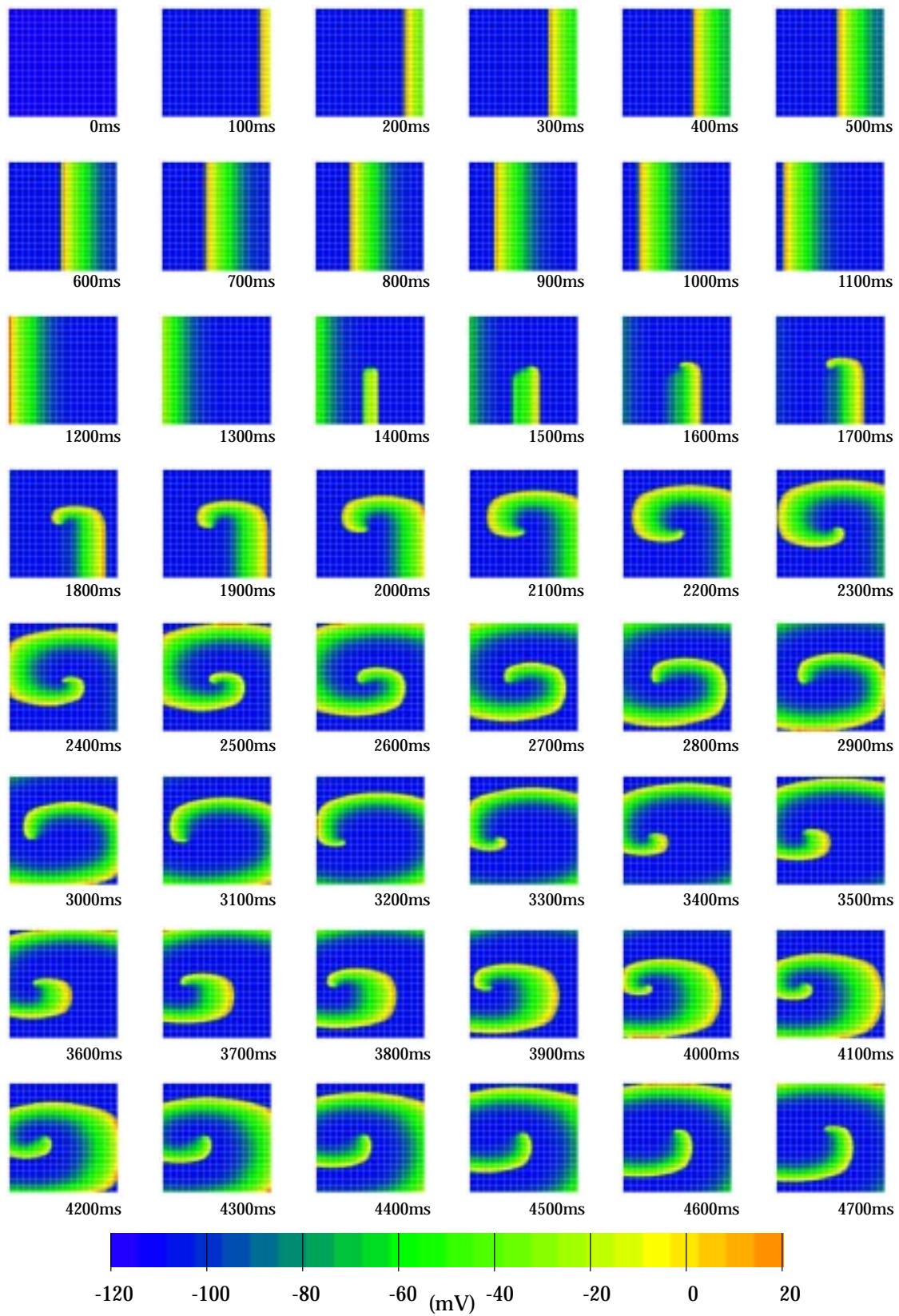


FIGURE 8.12: 2:1 conductivity using the Beeler-Reuter model on a non-deforming mesh which has a constant 0° fibre field.

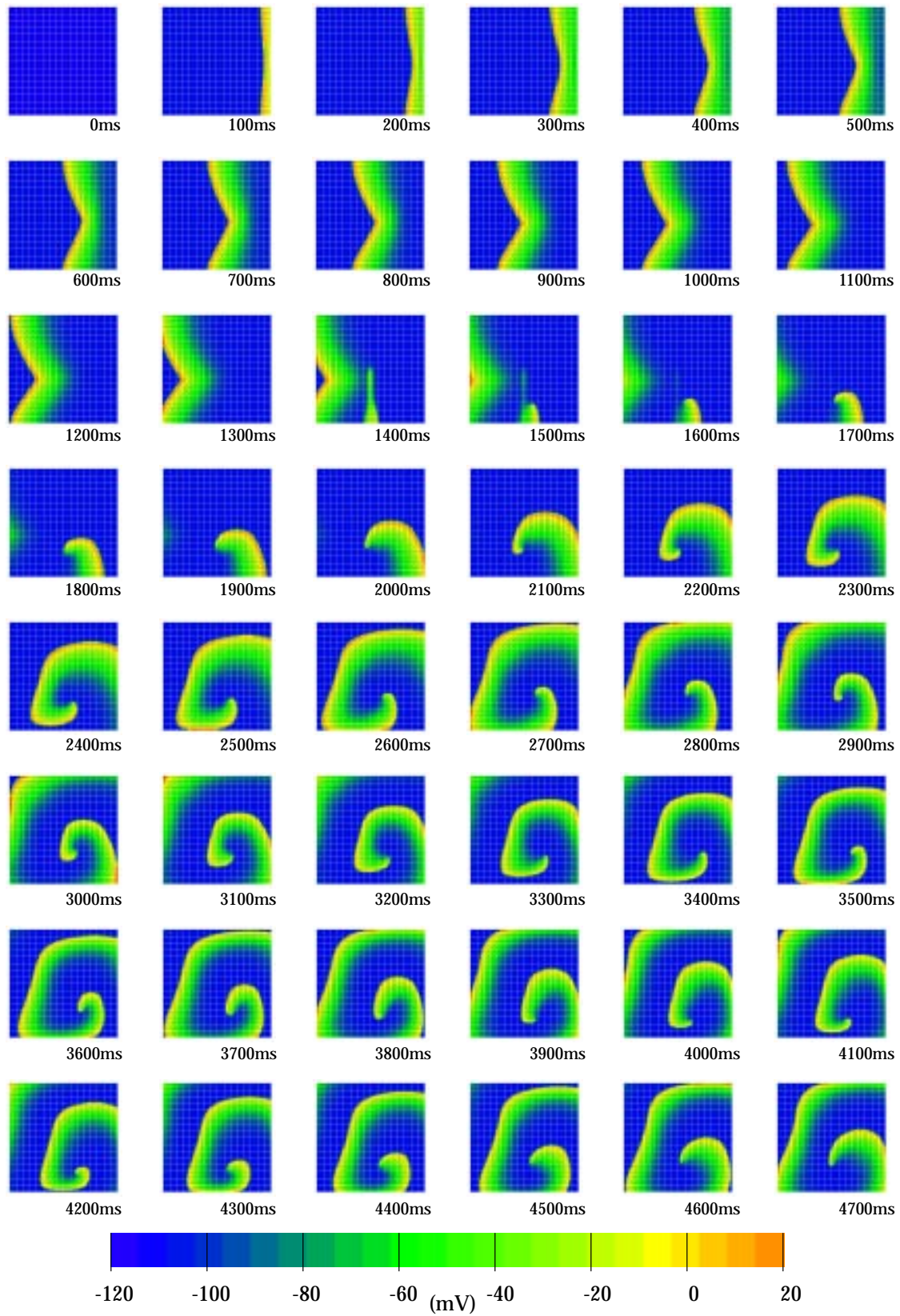





FIGURE 8.13: 2:1 conductivity using the Beeler-Reuter model on a non-deforming mesh which has a varying “S”-shaped fibre field.

An anisotropic conductivity with the same fibre field produces a very similar result, as shown in Figure 8.15  membrane/br21d00, in which a pair of spiral waves is initially created, but the formation of single wave comes earlier in the evolution of the wavefront, and the death of the second spiral can be seen in the final 9 frames of the figure. The anisotropy tends to elongate the spirals as they rotate.

Altering the fibre field changes the wavefront propagation significantly. The sequence in Figure 8.16  membrane/br21d shows this clearly. Because the initial wavefront causes the mesh to contract vertically in the centre of the mesh and horizontally towards the top and bottom edges, the “V”-shape is less pronounced, and the wavefront is more rounded. The wavefront as a whole propagates slightly slower, which encourages the formation of a single spiral. As this spiral rotates, the fibre directions change considerably within an element as it contracts, and the fibre field serves to square the edges of the wavefront. The variation in fibre angle throughout the mesh cause the contraction to be more severe, as each element is contracting in a slightly different direction and affecting each of the other elements, but the rotation of the spiral wave is still very stable.

Deforming geometry with sliding boundaries

The boundary conditions are relaxed in the following three examples, for which only the corner nodes are fixed, and all nodes on the external boundary are restricted to lie in a straight line between the corner nodes. This maintains the geometric shape, but allows a much greater freedom of movement within the finite element mesh.

The result of an isotropic simulation is shown in Figure 8.17  membrane/brisd. The initial wavefront remains planar as the mesh contracts uniformly in a direction perpendicular to the propagation, and the elements elongate away from the wavefront and shorten immediately behind the wavefront. The second stimulus is again shifted to the left of the domain due to the contraction. The resulting single spiral wave is similar to the non-deforming example, except that the horizontal contraction from the 0° fibre field causes the almost-circular wave to shorten in the horizontal direction.

Incorporating anisotropic conductivities gives a very similar result, as seen in

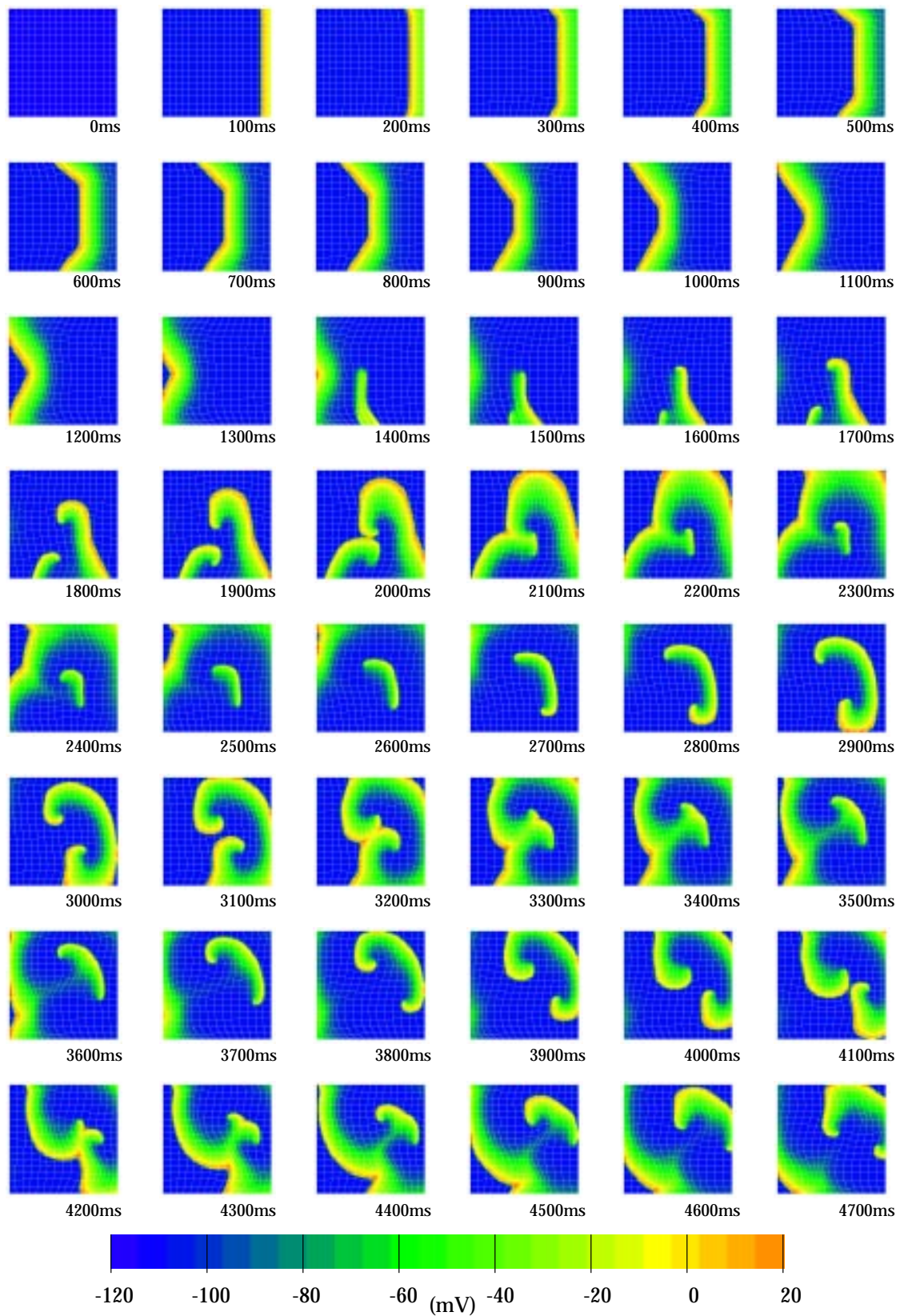


FIGURE 8.14: Isotropic conductivity using the Beeler-Reuter model on a deforming mesh with fixed edges. A constant 0° fibre field is used for aligning the element contraction.

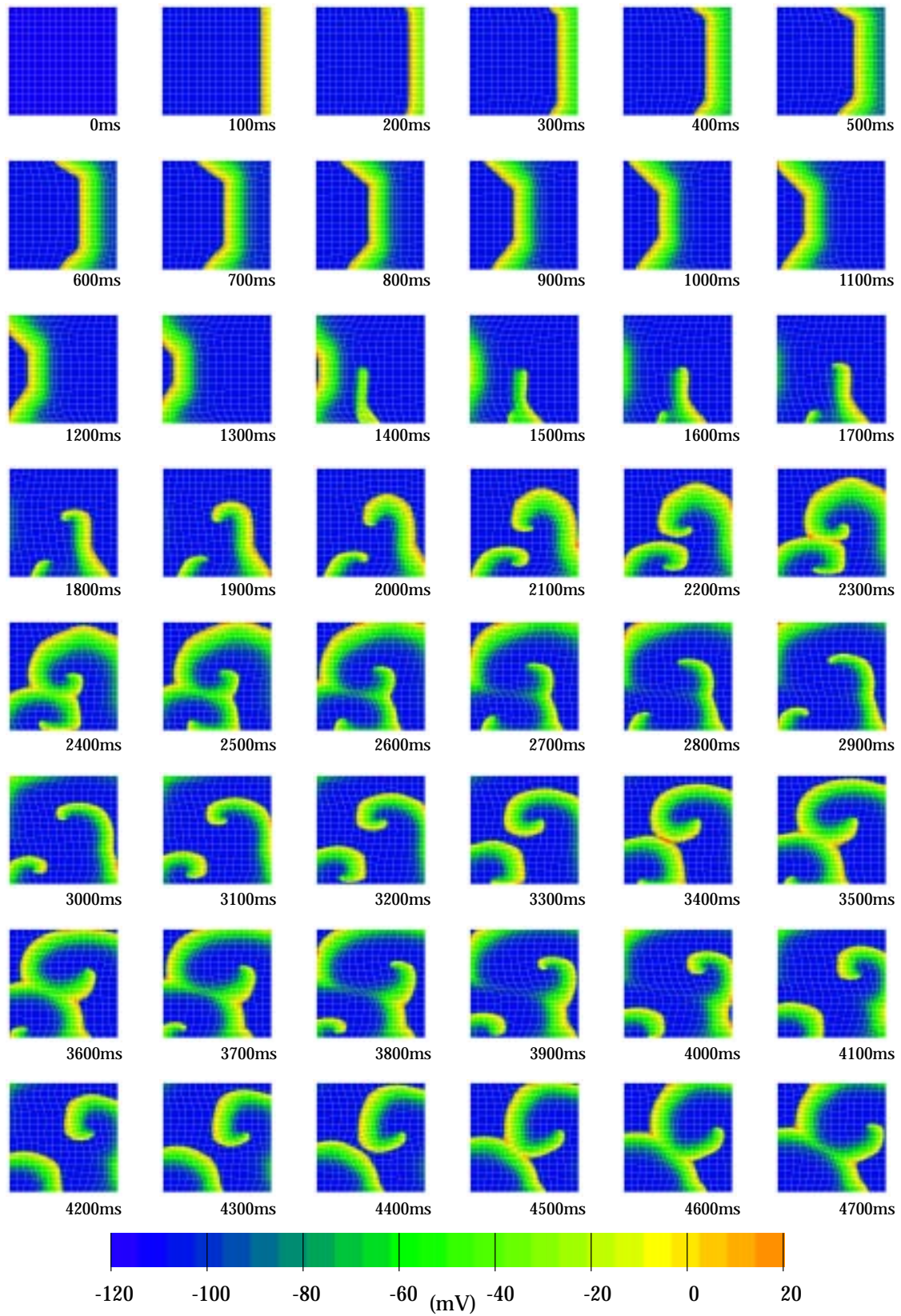


FIGURE 8.15: 2:1 conductivity using the Beeler-Reuter model on a deforming mesh which has a constant 0° fibre field and whose edges are fixed.

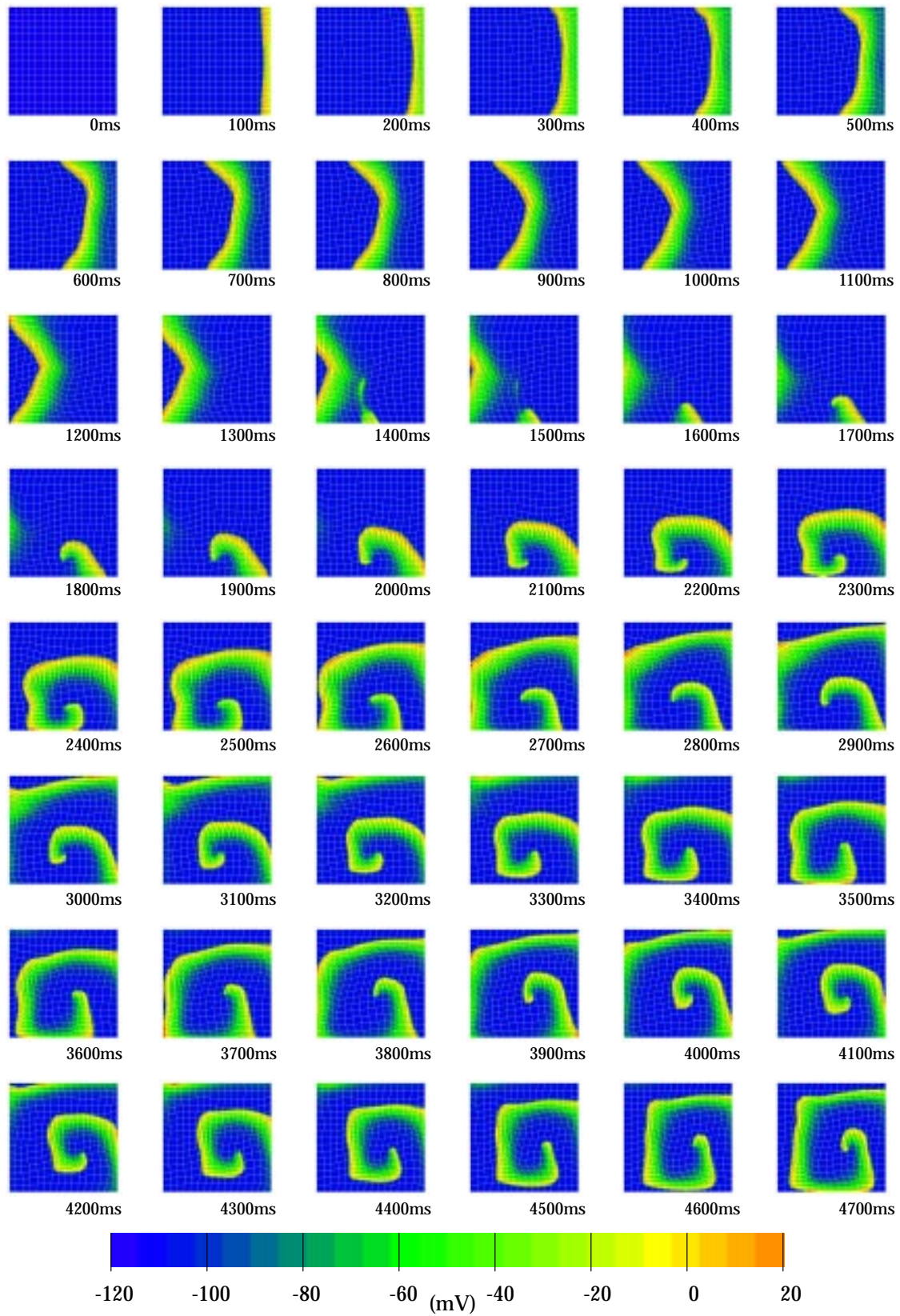
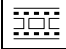
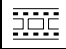


FIGURE 8.16: 2:1 conductivity using the Beeler-Reuter model on a deforming mesh with fixed boundaries, which has a varying “S”-shaped fibre field.

Figure 8.18  membrane/br21d00s. A single spiral again results, though in this case the anisotropy compensates for the horizontal contraction of the finite element mesh, and the wavefront varies between a circular shape in the 5th and 7th rows, and a horizontally elongated shape in the 6th and 8th rows. An example command file for this problem is given in Appendix B as the first example.

The final example uses a varying fibre field and is shown in Figure 8.19  membrane/br21ds. Because of the vertical variation in fibre angle the initial wave does not remain planar, but curves slightly. The second stimulus is only just late enough to produce a second wave, and the resulting spiral is similar in appearance to the earlier example which used the fixed boundary conditions. The movie shows a couple of occasions where the wave almost dies out as the wavetip travels very close to the boundary.

8.2.5 Coupled electromechanics on a 2D cross-section

This simulation is performed on a geometry taken from an MRI image taken across the torso at approximately two-thirds of the distance from the apex to the base. From this, the position of the epicardium is sufficiently resolved to be defined, and the position of the left and right endocardial surfaces is approximated by eye. From the lines defining these boundaries a finite element mesh is created containing 80 elements, with 20 element circumferentially and 4 elements through the LV wall, as shown in Figure 8.20. There are 2 elements through each of the septal and RV walls. No exact information was available for this slice concerning the fibre field, and so the fibre field was defined to be circumferential at all points by aligning it with the elemental ξ_1 -coordinate.

A two dimensional simulation does not contract in a manner similar to a three dimensional heart, and the boundary conditions on the mechanical deformation cannot be specified in a similar way. A model of a full heart would specify cavity pressures against which the mesh would contract, but this cannot easily be translated to a two dimensional model. In this simulation, we resort to a number of force boundary conditions at the points highlighted in Figure 8.20. Point 5 is fixed in space to prevent arbitrary movement of the mesh, and point 2 is restricted to move only parallel to the x -axis which prevents rotation of the mesh. One simulation was

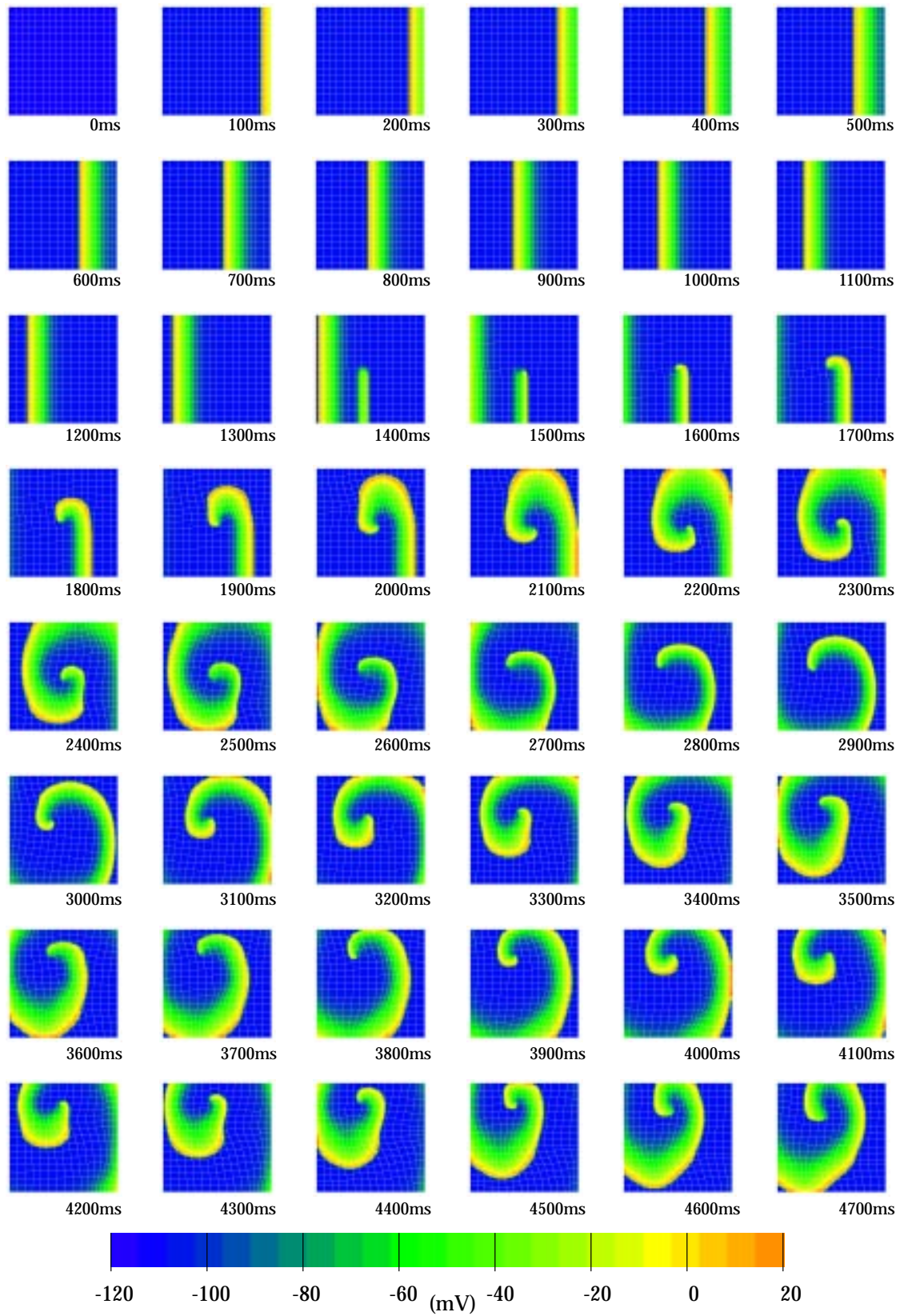


FIGURE 8.17: Isotropic conductivity using the Beeler-Reuter model on a deforming mesh with sliding edges.

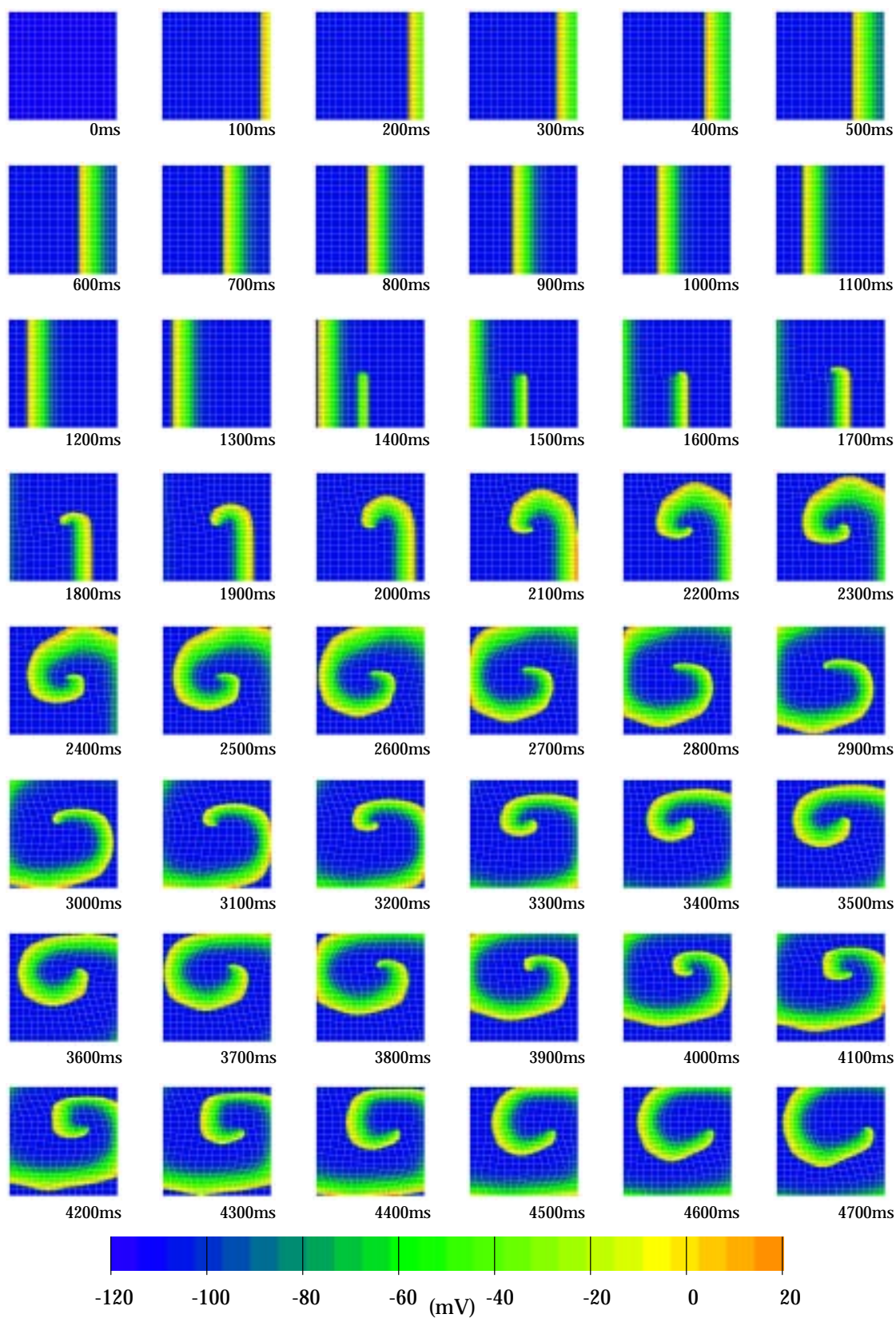


FIGURE 8.18: 2:1 conductivity using the Beeler-Reuter model on a deforming mesh which has a constant 0° fibre field and whose edges are sliding.

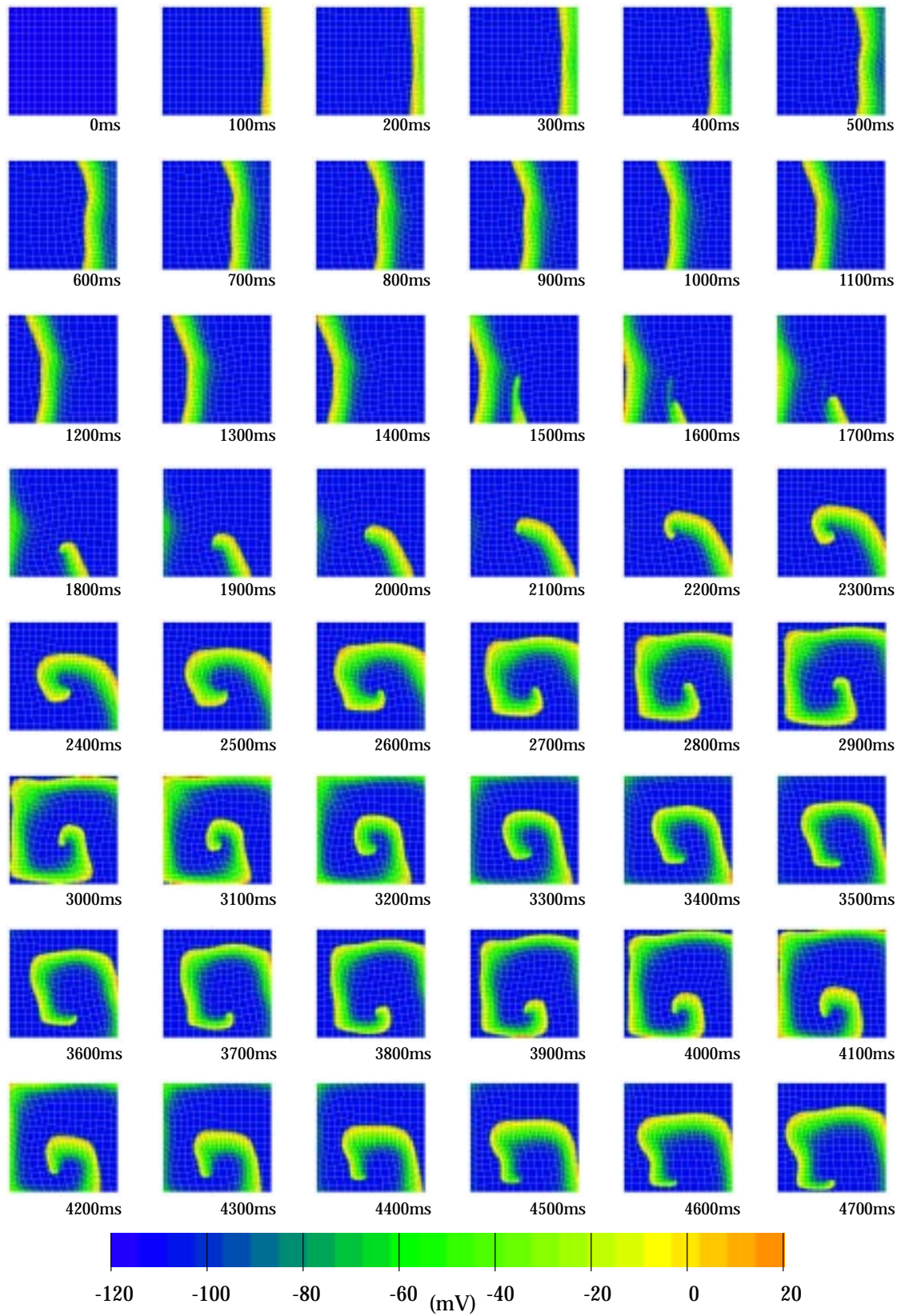


FIGURE 8.19: 2:1 conductivity using the Beeler-Reuter model on a deforming mesh with sliding boundaries, which has a varying “S”-shaped fibre field.

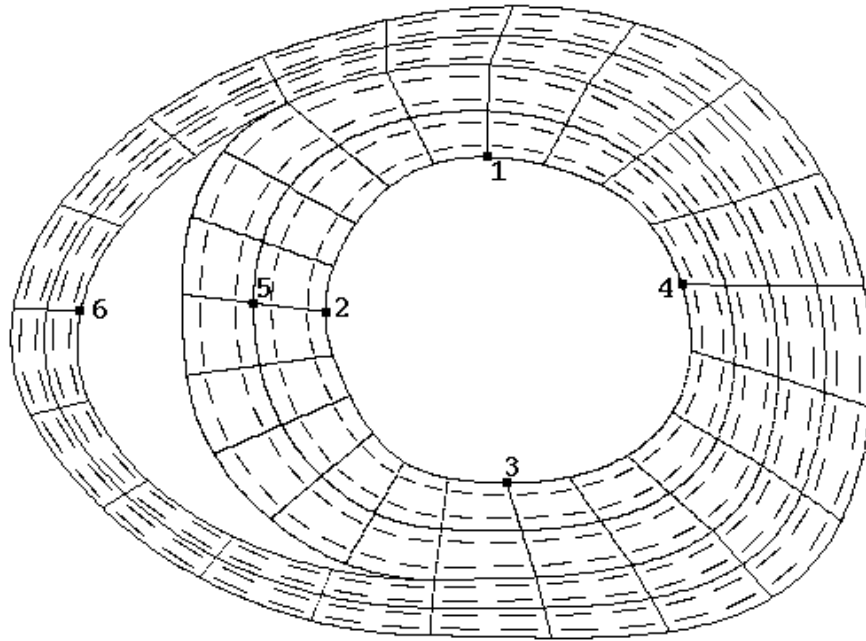
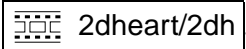


FIGURE 8.20: Undeformed finite element mesh for heart cross-section.

run without any additional forces specified, but the finite element mesh contracted much further than physically possible, with the RV wall contracting until it lay over the top of the septum. Two modifications were made, each of which reduced the contraction. Firstly, the calcium coupling coefficient was reduced by a factor of two to 5×10^4 . This reduced the level of contraction in the finite element mesh. Secondly, several small forces were applied to points on the endocardium to constrain the contraction slightly. Outward forces of 1×10^{-6} kN were applied at points 1 through 4 and 0.5×10^{-6} kN at point 6.

Parameters on the activation model were similar to those used above, with a 2:1 ratio in the conductivities given as $0.2 \text{ mS} \cdot \text{mm}^{-1}$ in the fibre direction and $0.1 \text{ mS} \cdot \text{mm}^{-1}$ in the cross-fibre direction. In order to demonstrate the wave of contraction following the activation wave, we use a non-physiological stimulation. The stimulus is applied along the element boundary line which goes through points 2, 5 and 6. The resulting activation and deformation is shown in a movie sequence in Figure 8.21 .

Because none of the boundary conditions restrict the movement of the epicardium, the mesh displays a much greater degree of contraction than the earlier examples

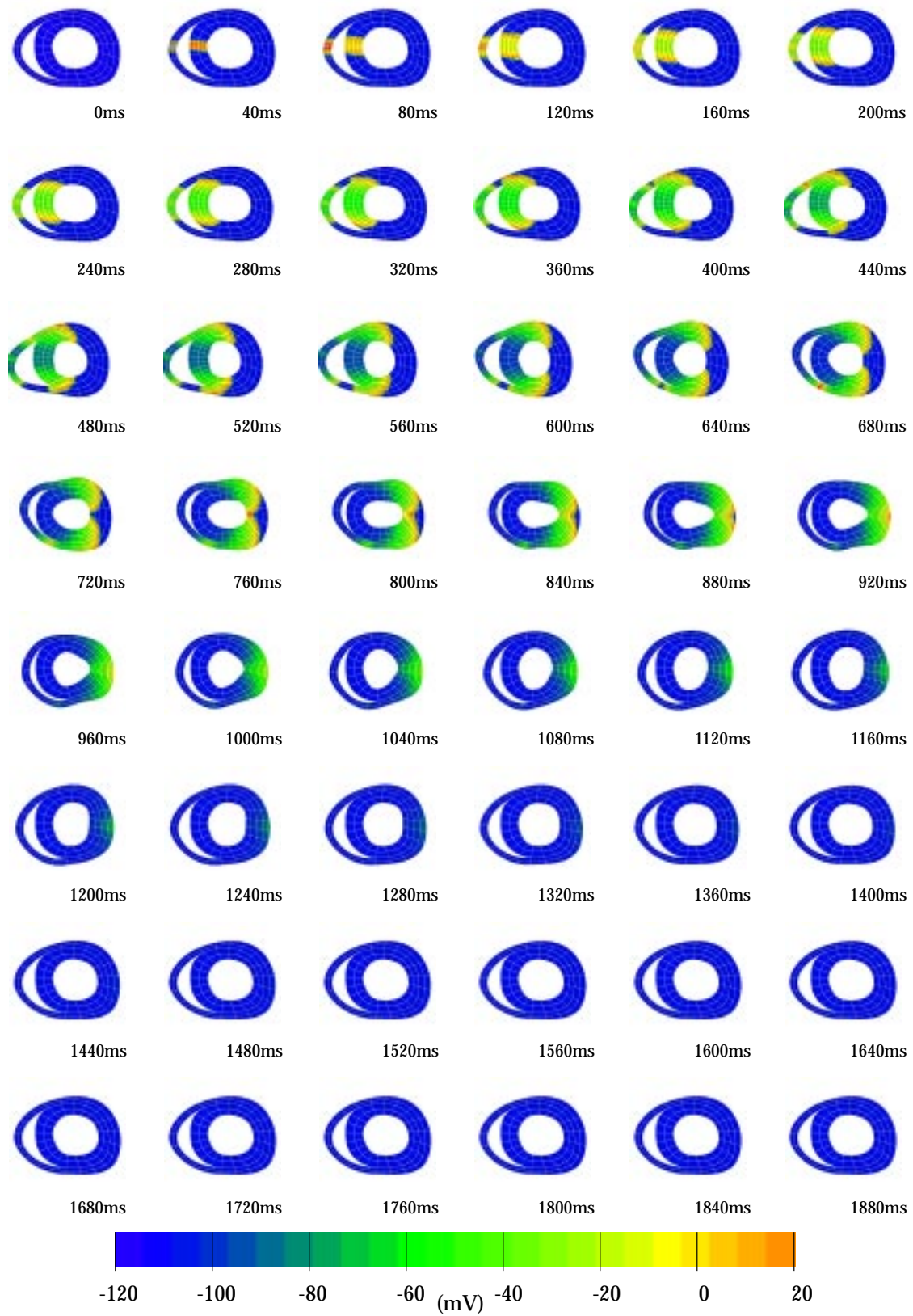


FIGURE 8.21: Activation on a 2D heart cross-section with mechanical deformation.

using squares with fixed boundaries.

8.3 Coupled Electromechanics on a Ventricular Domain

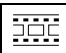
Solving a three-dimensional coupled electromechanics problem is considerably more difficult than the above two-dimensional examples. Whereas the previous examples use membrane theory to describe the mechanical properties of the tissue sheet, the ventricular myocardium requires a different set of material laws and parameters in order to construct a realistic model. The method of constructing this model, and its details can be found in Nash (1998).

Mechanical models are constructed of both the passive and active mechanics present in myocardium. The nonlinear elastic properties of passive myocardium are modelled using a fully three-dimensional orthotropic relationship between the components of the second Piola-Kirchoff stress tensor and Green's strain tensor according to the pole-zero relationship, as in the two-dimensional example. The axial and shear parameters in this model are correlated by a fibre distribution model, which describes the strain energy which is stored in collagenous fibres and other connective tissue. In addition, a fluid shift model is constructed which describes the biphasic properties of ventricular muscle, and allows movement of fluid (mainly blood) through the ventricular walls. This model describes both the movement of fluid within the muscle and the intramural hydrostatic pressure variation, which is assumed to vary in the transmural direction only. Unloaded myocardium is not stress-free, and these residual stresses, and the corresponding strains, are also included in the passive model. As in the two-dimensional examples, the active mechanics are described by a steady-state tension-length- Ca^{2+} relationship.

The methods of applying boundary conditions to the myocardium are also more complex, and include the maintenance of incompressibility, as well as methods of restricting the movements of the ventricular surfaces. The model used for the example below held the apex fixed in μ , and fixed the base in λ . Many other possibilities exist for constraining some, or all of the nodes, such as a pericardial constraint which fixes the λ coordinate of all epicardial nodes. Additionally, cavity pressures must be modelled, as they additionally determine the level of contraction

of the myocardium.

The ventricular finite element model used for this coupled problem is less refined than that used in the previous chapter to describe cardiac activation, and contains 60 elements and 99 nodes. A $9 \times 9 \times 9$ collocation scheme on this mesh produces a total of 33136 collocation points. The CMISS command file which produces this example is given as the second file in Appendix B. The stimulus position is on the upper RV wall, although this is somewhat arbitrary, and makes little difference to the results that are obtained. Even with this refined mesh, each 5ms iteration of both the activation and mechanics models required around 3 hours of CPU time on the SGI supercomputer. This made it difficult to study more than a few simulations.

In order for a visible contraction to be obtained, the calcium coupling coefficient was required to be set to 5×10^5 . Even with this high level of calcium, the contraction is difficult to see in a series of static images, and therefore the results are displayed only in a movie sequence.  emech3d/h60em The movie consists of 17 frames taken at 5ms intervals, with the initial activation seen on the RV wall. Contraction becomes apparent after several frames, however at the 75ms solution, the mechanical deformation solution fails to converge. This is not remedied if the number of iterations allowed to determine convergence is increased. For this reason, the final two frames portray a non-converged geometry, hence the more abrupt movement. At between 90ms and 100ms, the activation solution also fails, possibly due to the deformation. The solution of the activation equation will solve independently, as demonstrated in Section 7.3, and the deformation equations also converge using a simulated level of calcium, however the combination of the two causes some difficulties at this stage.

Chapter 9

Conclusions and Future Work

There are different stages in the process of understanding cardiac structure and function. At the basic level, anatomists and physiologists examine the morphology of cardiac muscle, quantify the energetic function, and measure the mechanical, electrical and ionic changes. Because of the intricacy and complexity of the heart, the knowledge of structures and understanding of function are continually under development. At a slightly higher level, other researchers seek to develop mathematical models of the processes and implement them, usually with the aid of modern computing resources.

These models of different structures and functions are usually developed independently, and are usually also implemented and solved independently. This allows only one function to be examined, even though this function may influence, and be influenced by, a number of other functions. Although in many cases this interdependency may be significant, it is usually ignored. One such interdependency, which is known to be important but is almost always overlooked, is the interaction between the electrical and mechanical processes within cardiac muscle.

The research presented in this thesis develops a framework for solving the cardiac activation equations in the context of a coupled electromechanical system, and recognises the need for integration of the two separate models into a unified structure. In order to solve the activation equations as part of a coupled system of integrated models, a new solution method has been developed. This collocation

method is designed around the particular aspects which are characteristic of cardiac activation, and is suitable for the solution of the model on geometries defined in one, two or three dimensions as required. When modelling ventricular activation, the geometrical model is built upon one of the best, currently available, descriptions of ventricular geometry and microstructure, and both the geometry and the local microstructure are described using high-order basis functions on a finite element mesh. The activation equations themselves are solved at material points defined at fixed ξ positions within the finite element mesh, and because of this method of definition, the collocation points track any deformation specified by the finite element mesh. The activation model uses a bidomain formulation of cellular activation which describes the processes at a macroscopic level using a continuum approach. The ionic currents are computed using any of a number of available cellular ionic current models, and can flexibly incorporate new descriptions of cellular behaviour as the processes are more accurately determined. The particular ionic current model can be chosen so that it provides the required level of information that is desired in the solution, and so that it is solvable in the available computational time.

The collocation method has been designed to integrate easily with models of other aspects of cardiac function, and in this thesis, the main focus has been the coupling of the activation model with a model of mechanical deformation. There is a two-way coupling between these two processes. The activation model includes a description of the intracellular calcium concentration which the mechanical model uses to determine the magnitude of contraction. This contraction causes deformation of the finite element mesh, and consequently moves the grid of collocation points. By using metric information at the collocation points to specify local slope and curvature, the equations can be solved on an irregularly-spaced, deforming grid.

Because the bidomain model of cellular activation is used, the collocation-based activation model on the cardiac geometry can be integrated with a model of torso geometry enabling the computation of the electric field potential within the torso and on the body surface, as has been shown in a proof of concept in this thesis. Presently, this can only be used to compare body surface potentials calculated using the models with ECG and body surface electrode recordings, but the long-term aim is to construct an inverse model by which the activation parameters can be determined from the measured body surface potentials.

The model has also been shown to be useful in determining material parameters using a nonlinear optimising technique, although the convergence to the solution is quite slow. Improvements in the solution time and the accuracy would provide a useful laboratory, or even surgical, tool.

There are a number of areas in which the model could be enhanced further in the future. One of the main deficiencies at this stage is that there is very little knowledge of the values of the components of the three-dimensional conductivity tensor, and whether or not an orthotropic description is required. Experimental measurement of activation in small, three-dimensional blocks of ventricular myocardium will be required to determine these parameters. Standard techniques using an array of plunge electrodes will provide a coarse level of detail, and will need, in the future, to be supplemented by optical mapping methods. These are currently used for two-dimensional studies, but will need to be extended to three-dimensional recordings as well.

There is also a need for more detailed measurement of cardiac microstructure, especially the nature of the branching between adjacent sheets which may give clues as to whether a transversely isotropic or an orthotropic description of the conductivity tensor is required. The structural orientation, as well as the properties of the cardiac cells, has a substantial influence on the propagation of the activation wave.

Modifications to the newer ionic current models are continually being developed, such as recent investigation into the nature of cells in the mid-wall, called *m-cells*, whose properties may play a role in the development of reentrant arrhythmia by varying the ionic channel density of the i_{to} and i_K currents. These, and other ionic currents whose channel densities vary spatially, produce a change in the magnitude and effect of the current depending on location, such as the apparent decrease in the transient outward current i_{to} as you move from the epicardium to the endocardium. This spatial variation of ionic current information can be easily added to the activation model in its current form. Various other molecules may influence the ionic currents, such as an ATP-dependent K^+ current, which activates at low levels of ATP. There are also reports of an ACh-dependent (Acetyl-Choline) K^+ current which is activated by vagal stimulation, leading to hyperpolarisation. Many of these extensions can be made to the more advanced existing ionic current

models, but require the computation of a larger number of parameters, and therefore an increase in computational time.

The use of an explicit finite difference solution technique to solve the activation equations, as used in this thesis, provides sufficient accuracy in many cases, but the timestep is often required to be very small in order for the solution to remain stable and accurate. A useful extension would be to investigate the use of other solution techniques, especially implicit methods which allow a wider range of timesteps. The multigrid technique is one which seems very promising in its ability to reduce solution errors of differing frequencies at a range of collocation grid spacings. The solution method for the extracellular equation present in the bidomain model is also insufficiently accurate at this stage, and a new method is required which maintains the necessary spatial resolution while enabling coupling of the bidomain model to a model of extramyocardial (or torso) potential. In this situation as well, the multigrid technique is a strong contender, although there may be other finite element or wavelet based techniques which are suitable.

The ventricles are activated through the Purkinje fibre network which spreads into the subendocardial region, and a more sophisticated model of initial ventricular activation is required. This will involve determining the location of Purkinje fibre branches and describing activation through the network, which stimulates the ventricular model. At a higher level, the pacemaker activity in the heart is most strongly provided by the SA node in the atrial region, and the construction of an atrial mesh would be a useful continuation in modelling the complete propagation of the wavefront. This would be necessary if the model sought to compare its results with an ECG recording, as the atrial contraction defines the location and magnitude of the "P" wave. This would allow the model to be more useful in a clinical context. Also important in a clinical setting would be the ability to use the activation model to confirm a supposed condition based on body surface recordings.

Tissue metabolism is another important aspect of cardiac function, and may influence the nature of activation and the propagation of the action potential. This would involve modelling the concentration fields of additional chemicals (such as H^+ (pH), ATP, ADP, adenosine and so on) throughout the heart, as well as a description of energy expenditure and oxygen consumption. Once such mathematical models have been generated, they could equally be solved on a

collocation grid, as the behaviour may be very localised.

Each of these additions will also need to be designed to be integrated into a larger model, but given this structure the implementation is conceptually straight-forward. This modular approach also allows the problem complexity to scale with advancing computing technology.

Appendix A

Hammer Projection

The Hammer projection (Raisz 1962) is formed by making an imaginary cut from base to apex through the centre of both the right ventricle and the septum. The epicardial surface is then laid flat and viewed from the outside. The LV is shown in the central half of the map, and the RV is split across the remaining two quarters. This projection preserves both relative surface area and retains the apex as a single point. The Hammer projection is given by

$$x = -k \cos \left(\mu - \frac{\pi}{2} \right) \sin \left(\frac{\theta - \pi}{2} \right) \quad (\text{A.1})$$

$$y = k \sin \left(\mu - \frac{\pi}{2} \right) \quad (\text{A.2})$$

where

$$k = \left[1 + \cos \left(\mu - \frac{\pi}{2} \right) \cos \left(\frac{\theta - \pi}{2} \right) \right]^{-\frac{1}{2}} \quad (\text{A.3})$$

In the projections shown in the thesis, a small portion of the septum shows above the ventricles, and can easily be seen where there is a discontinuity in the field map.

Appendix B

CMISS Command Files

B.1 Two-dimensional coupled electromechanics

The following file is a list of CMISS commands which are used to solve the problem outlined in Section 8.2.4, and for which a constant 0° fibre angle is defined and the boundary nodes are sliding. The resulting output is shown in Figure 8.18.

```
assign MECH=1  
assign ACTVN=2
```

Two problem classes are defined – one which solves the mechanics equations and one which solves the activation equations

```
fem define parameter;r;membrane  
fem reallocate
```

Define the parameter sizes for this problem and allocate memory for the arrays

```
fem define node;r;square16x16
```

Define the 289 nodes for the finite element mesh

```
fem define base;r;membrane
```

Bilinear basis functions are defined for both the mechanics and the activation problem

```
fem define element;r;square16x16
```

Define the 256 finite elements used as the geometry

```
fem define fibre;r;sq16x16-00
```

Define a constant 0° fibre field

```
fem define window
```

Create a graphical output window

Set up mechanical deformation problem

```
fem define equation;r;stress class MECH lock
```

The equation is a finite elasticity model using membrane theory, and the domain is incompressible

```
fem define material;r;membrane class MECH
```

A pole-zero material law is used

fem group node external as bdy_nodes

All nodes on the boundary – this is used if the boundary conditions specify fixed boundary nodes

fem group element 1..16 as bot_elems
 fem group element 241..256 as top_elems
 fem group element 1..241:16 as lhs_elems
 fem group element 16..256:16 as rhs_elems

Element groups along each of the four edges of the mesh

fem group node xi1=0 element lhs_elems as lhs_nodes
 fem group node xi1=1 element rhs_elems as rhs_nodes
 fem group node xi2=0 element bot_elems as bot_nodes
 fem group node xi2=1 element top_elems as top_nodes

Determine which nodes are on the external boundaries of the mesh along each of the four edges

fem define initial;r;slide class MECH

Initial conditions have fixed edges with sliding nodes

fem define solve;r;membrane class MECH

The equations are solved using GMRES with diagonal preconditioning

fem define active;r;stress class MECH

A steady-state tension-length- Ca^{2+} model describes the active parameters

Set up the electrical activation problem

fem define equation;r;br class ACTVN

The Beeler-Reuter ionic current model is used

fem define grid;c class ACTVN deformed

Define the collocation points on the finite element mesh

fem define material;r;br class ACTVN

Read in the Beeler-Reuter material parameters

fem update grid material class ACTVN

Precompute conductivity tensor values

fem group grid xi1=1 oneoff as rhs-line

Group all collocation points on the right-hand boundary of the mesh

fem group grid line 7873 xidirn 2 negative as cline

Group all collocation points which lie in a line below the central point

fem define initial;r;sq16x16-rhs-cline class ACTVN

Initial conditions specify the timing of the stimulations

fem define solve;r;sq16x16 class ACTVN

Define the solution parameters, including the timestep used

fem solve class ACTVN to 0

Write out initial information to the output files

Solve the coupled electromechanics problem

DO HUND=0..9

DO TEN=0..9

DO UNIT=0,2,4,6,8

Loop from 0ms to 998ms in steps of 2ms

fem solve class ACTVN restart to
 HUND//TEN//UNIT

Solve the activation equations up till the current timestep

fem update gauss calcium from_class ACTVN

Update the mechanics equations with the current $[Ca]_i$ from the activation model

fem solve class MECH incr 0. iter 99

Solve the mechanical deformation equations until the solution has converged

fem update grid strain class ACTVN

Update the values of strain at collocation points – this is used only if there are stretch-dependent channels

fem update gauss deformed_fibres collocation

Recompute the deformed fibre field based on the new mesh position

fem define grid;c class ACTVN deformed
 from_class MECH

Redefine the collocation grid given the deformed mesh

fem update grid material class ACTVN	<i>Recompute conductivity tensors in local material coordinates</i>
fem update gauss potential class ACTVN	<i>Transfer transmembrane potential to a gauss-point array for display</i>
fem draw field deformed gauss 1 class MECH basis 2 zmin=-120 zmax=20 noscale	<i>Draw the transmembrane potential field on the deformed mesh</i>
fem draw lines deformed rgb=white	<i>Draw the deformed element boundaries</i>
fem draw fibre deformed dxi 0.5,0.5,0.5 rgb=black	<i>Draw the deformed fibre field</i>
refresh graphics	<i>Update the graphics window</i>
print;vcd-1//HUND//TEN//UNIT portable h=500 w=500	<i>Save the window to a PPM file</i>
ENDDO deassign UNIT	<i>Every hundred milliseconds...</i>
ENDDO deassign TEN	
fem define grid;w;vcd-sp-30-//HUND//99 class ACTVN	<i>Save the current quantities associated with the collocation points</i>
fem define init;w;vcd-sp-30-//HUND//99 class MECH	<i>Save the current deformation of the finite element mesh</i>
ENDDO deassign HUND	<i>End of loop</i>

B.2 Three-dimensional coupled electromechanics

The file below is a command file for the program CMISS which constructs and solves the coupled electromechanics problem on the anatomically accurate ventricular finite element mesh.

assign MECH=1 assign ACTVN=2	<i>Two problem classes are defined – one which solves the mechanics equations and one which solves the activation equations</i>
assign MYOCARD=1 assign LVCAV=2 assign RVCAV=3	<i>Three separate solution regions exist – the myocardial region, and a region for each ventricular cavity</i>
fem define parameters;r;full fem reallocate	<i>Allocate memory for arrays required for this problem</i>
Define the geometry	
fem define coordinates;r;prolate region MYOCARD	<i>Define prolate spheroidal coordinate system</i>
fem define node;r;fullheart region MYOCARD	<i>Read the finite element nodes of the ventricular region</i>
fem define base;r;fullheart	<i>Define the required basis functions – there are 12 of these in all</i>
fem define fibre;r;fullheart region MYOCARD	<i>Read the measured fibre field throughout the myocardium</i>
fem define sheet;r;fullheart region MYOCARD	<i>Read the sheet field throughout the myocardium</i>
fem define element;r;fullheart region MYOCARD	<i>Read the finite element mesh for the myocardium</i>
Define element groups – These groups are used for defining initial conditions and boundary conditions	
<i>Basal Elements:</i>	
fem group elem 3..8 as base_lvfree_epi region MYOCARD	<i>LV freewall epicardium</i>
fem group elem 33..38 as base_lvfree_endo region MYOCARD	<i>LV freewall endocardium</i>
fem group elem 31,32,39,40 as base_septal region MYOCARD	<i>Septum</i>
fem group elem 1,2,9,10 as base_rv region MYOCARD	<i>RV wall</i>
fem group elem base_lvfree_epi,base_lvfree_endo, base_septal,base_rv as base region MYOCARD	<i>All elements adjacent to the basal ring</i>
<i>Equatorial Elements:</i>	
fem group elem 13..18 as equator_lvfree_epi region MYOCARD	<i>LV freewall epicardium</i>

fem group elem 43..48 as equator_lvfree_endo region MYOCARD	<i>LV freewall endocardium</i>
fem group elem 41,42,49,50 as equator_septal region MYOCARD	<i>Septum</i>
fem group elem 11,12,19,20 as equator_rv region MYOCARD	<i>RV wall</i>
fem group elem equator_lvfree_epi,equator_lvfree_endo as equator_lvfree region MYOCARD	<i>LV freewall elements</i>
fem group elem equator_lvfree,equator_septal,equator_rv as equator region MYOCARD	<i>All elements located in the equatorial region</i>
<i>Apical elements:</i>	
fem group elem 21..30 as apex_epi_elems region MYOCARD	<i>Epicardium</i>
fem group elem 51..60 as apex_endo_elems region MYOCARD	<i>Endocardium</i>
fem group elem apex_epi_elems,apex_endo_elems as apex_elems region MYOCARD	<i>All elements adjacent to the apex</i>
<i>Other groupings:</i>	
fem group elem base_lvfree_endo,equator_lvfree_endo, apex_endo_elems as lvfree_endo_elems region MYOCARD	<i>All LV freewall endocardial elements</i>
fem group elem base_lvfree_epi,equator_lvfree_epi, apex_epi_elems as lvfree_epi_elems region MYOCARD	<i>All LV freewall epicardial elements</i>
fem group elem base_rv,equator_rv as rv_elems region MYOCARD	<i>All RV elements</i>
fem group elem base_septal,equator_septal as septal_elems region MYOCARD	<i>All septal elements</i>
fem group elem base,equator,apex_elems as all_elems region MYOCARD	<i>All elements</i>
<i>Define node groups</i>	
fem group node 13,28,41 as apex_nodes region MYOCARD	<i>Apical nodes</i>
fem group node 1,44,2,56,47,3,50,59,4,53 as base_epi_nodes region MYOCARD	<i>Basal epicardial nodes</i>
fem group node 29,62,30,74,65,31,68,77,32,71 as base_lv_endo_nodes region MYOCARD	<i>Basal LV endocardial nodes</i>
fem group node 15,85,18,87,17,83,14,80 as base_rv_endo_nodes region MYOCARD	<i>Basal RV endocardial nodes</i>

fem group node
base_lv_endo_nodes,base_rv_endo_nodes
as base_endo_nodes region MYOCARD *All basal endocardial nodes*

fem group node xi2=1 external elem base as
base_nodes region MYOCARD *All basal nodes*

fem group node xi3=1 external elem
equator_lvfree_epi,equator_rv as
equator_epi_nodes region MYOCARD *Equatorial epicardial nodes*

fem group node xi3=0 external elem
equator_lvfree_endo,equator_septal as
equator_lv_endo_nodes region MYOCARD *Equatorial LV endocardial nodes*

fem group node xi3=0 external elem equator_rv as
equator_rvfree_endo_nodes region
MYOCARD *Equatorial RV freewall endocardial nodes*

fem group node xi3=1 external elem equator_septal
as equator_rvsept_endo_nodes region
MYOCARD *Septal nodes*

fem group node equator_rvfree_endo_nodes,
equator_rvsept_endo_nodes as
equator_rv_endo_nodes region MYOCARD *Equatorial RV endocardial nodes*

fem group node xi3=1 elem
equator_lvfree_endo,apex_endo_elems as
equator_lv_mid_nodes region MYOCARD *Equatorial LV midwall nodes*

fem group node xi3=1 external elem
lvfree_epi_elems,rv_elems as epi_nodes
region MYOCARD *All epicardial nodes*

fem group node equa-
tor_lv_mid_nodes,equator_rv_endo_nodes
as equator_mid_nodes region MYOCARD *All endocardial nodes*

Define dependent variable/material information

fem define equation;r;finelas_tch_incomp region
MYOCARD lock class MECH *The equation which describes the mechanical deformation is 3D incompressible finite elasticity*

fem define material;r;orth_incomp_active_residstrain
region MYOCARD class MECH *The mechanics material parameters is orthotropic and incompressible, with active stress modelling and residual strains specified by a pole-zero law. This material law has 16 parameters*

fem define active;r;active0_00 region MYOCARD
class MECH *The active mechanics use a steady-state tension-length- Ca^{2+} relationship*

fem define initial;r;fullheart_inflate_baseepifixlambda
region MYOCARD class MECH *Initial conditions specify that internal cavity pressures are 1kPa in the LV and 0.2kPa in the RV. The apex is held fixed in μ , and the epicardial base is fixed in λ*

fem define solve;r;newton region MYOCARD class
MECH *The mechanics equations are solved for using the Newton-Raphson method*

Save scale factors for the ventricular wall elements

fem define base;r;fullheart_readse *redefine bases to read in scale factors*

fem def line;w;fullheart region MYOCARD *write out scale factors for wall elements*

fem define base;r;fullheart	<i>redefine bases to calculate scale factors</i>
<i>Define geometry and dependent variable information for LV and RV cavities</i>	
fem define region;r;coupled	<i>Define regions for LV and RV cavities</i>
fem define coordinate;r;lvcavity region LVCAV fem define coordinate;r;rvcavity region RVCAV	<i>Define prolate spheroidal coordinate system for LV and RV cavity</i>
fem define node;r;lvcavity region LVCAV fem define node;r;rvcavity region RVCAV	<i>Read LV and RV cavity nodes</i>
fem define element;r;lvcavity region LVCAV fem define element;r;rvcavity region RVCAV	<i>Read LV and RV cavity elements</i>
fem group element 61..90 as lv_cavity_elems region LVCAV	<i>Group of all LV cavity elements</i>
fem group nodes xi2=1 elem 61..70 as lv_cavity_base_nodes region LVCAV	<i>Group of LV cavity basal nodes</i>
fem group nodes 29,71,32,77,68,31,65,74,30,62 as lv_endo_base_nodes region LVCAV	<i>Group of LV endocardial basal nodes</i>
fem group elem 91..100 as rv_cavity_elems region RVCAV	<i>Group of all RV cavity elements</i>
fem define equation;r;coupled region MYOCARD,LVCAV,RVCAV class MECH lock	<i>Equation is incompressible finite elasticity for the wall, and maintaining constant volume using a fluid mechanics model in the cavities</i>
fem define material;r;cavity region LVCAV class MECH fem define material;r;cavity region RVCAV class MECH	<i>Constant volume constraint for fluid mechanics</i>
fem define initial;r;lvcavity region LVCAV class MECH fem define initial;r;rvcavity region RVCAV class MECH	<i>Basal and apical nodes are held fixed in μ</i>
<i>Define cavity/wall coupling and solution information</i>	
fem define coup;r;coupled class MECH	<i>Coupling is through surface pressures</i>
fem define solve;r;coupled coupled region MYOCARD,LVCAV,RVCAV class MECH	<i>Wall mechanics are solved using Newton-Raphson, and the cavity fluid mechanics are solved using a nonlinear GMRES algorithm with diagonal preconditioning</i>
fem update solution coupled source_region MYOCARD class MECH	<i>Update internal solution variables for coupled problem</i>
fem update solution cavity_reference average 100 in 2 node lv_endo_base_nodes region LVCAV class MECH	<i>Updates reference state of cavity problem</i>
fem update solution cavity_reference average 104 in 2 node 14,18 region RVCAV class MECH	
<i>Read back in scale factors for the ventricular wall elements</i>	
fem define base;r;fullheart_readse	<i>redefine bases to read in scale factors</i>
fem def line;r;fullheart region MYOCARD	<i>read in scale factors for wall elements</i>

fem define base;r;fullheart

redefine bases to calculate scale factors

Define activation problem

fem define equation;r;br class ACTVN

Equation used is a Beeler-Reuter ionic current model

fem define grid;c class ACTVN

Calculate position of collocation points and associated metric tensors and connectivity

fem define material;r;br-ortho class ACTVN

Use an orthotropic conductivity tensor

fem update grid material class ACTVN

Precompute derivatives of the conductivities and metric tensors

fem group grid cube 600 as stimulus

Use a cube of collocation points as the stimulus

fem define initial;r;heart-activation class ACTVN

Initial activation occurs at this group of points

fem define solve;r;heart-activation class ACTVN

Define the solution parameters for the activation model

fem solve class ACTVN to 0.0

Write out initial information to output files

Solve the coupled electromechanical problem

DO HUND=0..3

DO TEN=0..9

DO UNIT=0,5

Set up a loop from 0 to 395 milliseconds in steps of 5 ms

fem define solve;r;heart-activation class
ACTVN

Update activation solution parameters

fem solve class ACTVN restart to
HUND//TEN//UNIT

Solve the activation problem to the appropriate time

fem export point;heart-ref-coupled-brorth-
1//HUND//TEN//UNIT grid class
ACTVN

Save collocation point information at this timestep

fem update gauss calcium from_class ACTVN
to_class MECH factor 10000.0

Update the mechanics equation with new values of $[Ca]_i$ at the gauss points

fem define solve;r;coupled coupled region
MYOCARD,LVCAV,RVCAV class MECH

Update mechanics solution parameters

fem solve increment 0.0 iter 15 error 1.e-4
coupled class MECH

Solve the mechanics equations until the error measure is below 10^{-4} or the iterations exceed 15

fem define initial;w;heartmech-
brorth_def1//HUND//TEN//UNIT region
MYOCARD,LVCAV,RVCAV class MECH

Write out the displacement field at this timestep

fem export node;heartmech-
brorth_def1//HUND//TEN//UNIT field offset
7500 region MYOCARD class MECH

Write out nodal positions at this timestep

fem define grid;c class ACTVN deformed
from_class MECH

Recompute collocation point positions based on new finite element mesh

fem update grid material class ACTVN

Update the conductivity tensors and metric tensors

```
ENDDO
deassign UNIT
ENDDO
deassign TEN
ENDDO
deassign HUND
```

End of solution loop

Bibliography

- Adam, D. (1985), 3-dimensional anisotropic model of myocardial electrical propagation, *in* K. L. Ripley, ed., 'Computers in Cardiology 1985', IEEE Computer Society Press, Washington, D. C., p. 405.
- Agladze, K., Keener, J. P., Müller, S. C. and Panfilov, A. (1994), 'Rotating spiral waves created by geometry', *Science* **264**, 1746–1748.
- Aliev, R. R. and Panfilov, A. V. (1996), 'A simple two-variable model of cardiac excitation', *Chaos, Solitons & Fractals* **7**(3), 293–301.
- Bailie, A. H., Mitchell, R. H. and Anderson, J. M. (1990), 'A computer model of re-entry in cardiac tissue', *Comput. Biol. Med.* **20**, 47–54.
- Bard, Y. (1974), *Nonlinear Parameter Estimation*, Academic Press, New York.
- Barr, R. C. and Plonsey, R. (1984), 'Propagation of excitation in idealized anisotropic two-dimensional tissue', *Biophys. J.* **45**, 1191–1202.
- Bean, B. (1990), 'Calcium channels. gating for the physiologist.', *Nature* **348**, 192–193.
- Beeler, G. W. and Reuter, H. (1977), 'Reconstruction of the action potential of ventricular myocardial fibres', *J. Physiol.* **268**, 177–210.
- Bergel, D. A. and Hunter, P. J. (1979), The mechanics of the heart, *in* N. H. C. Hwang, D. R. Gross and D. J. Patel, eds, 'Quantitative Cardiovascular Studies, Clinical and Research Applications of Engineering Principles', University Park Press, Baltimore, chapter 4, pp. 151–213.
- Berne, R. M. and Levy, M. N., eds (1988), *Physiology*, second edn, The C V Mosby Company.

- Bradley, C. P., Pullan, A. J. and Hunter, P. J. (1997), 'Geometric modelling of the human torso using cubic Hermite elements', *Ann. Biomed. Eng.* **25**, 96–111.
- Briggs, W. L. (1987), *A Multigrid Tutorial*, Society for Industrial and Applied Mathematics, Philadelphia, Pennsylvania.
- Bullivant, D. (1994), EMAP: Electrocardiac Mapping System. An EMAP user manual.
*<http://www.esc.auckland.ac.nz/Groups/Bioengineering/Emap/emap-netscape.html>
- Bullivant, D. (1996), UnEmap system. Summary of basic UnEmap System specifications.
*<http://www.esc.auckland.ac.nz/Groups/Bioengineering/Emap/emap-specs.html>
- Bustamante, J. O., Ruknudin, A. and Sachs, F. (1991), 'Stretch-activated channels in heart cells: Relevance to cardiac hypertrophy', *Journal of Cardiovascular Pharmacology* **17(Suppl. 2)**, S110–S113.
- Caulfield, J. B. and Borg, T. K. (1979), 'The collagen network of the heart', *Lab. Invest.* **40**(3), 364–372.
- Clark, J. W., Shumaker, J. M., Murphey, C. R. and Giles, W. R. (1991), Mathematical models of pacemaker tissue in the heart, *in* Glass, Hunter and McCulloch (1991), chapter 11, pp. 255–288.
- Clerc, L. (1976), 'Directional differences of impulse spread in trabecular muscle from mammalian heart', *J. Physiol.* **255**, 335–346.
- Colatsky, T. J. (1980), 'Voltage clamp measurement of sodium channel properties in rabbit cardiac Purkinje fibre', *J. Physiol. Lond.* **305**, 215–234.
- Colli Franzone, P., Guerri, L. and Rovida, S. (1990), 'Wavefront propagation in an activation model of the anisotropic cardiac tissue: Asymptotic analysis and numerical simulations', *J. Math. Biol.* **28**, 121.
- Colli Franzone, P., Guerri, L. and Taccardi, B. (1993a), 'Potential distributions generated by point stimulation in a myocardial volume: Simulation studies in a model of anisotropic ventricular muscle', *J. Cardiovasc. Electrophysiol.* **4**(4), 438–458.

- Colli Franzone, P., Guerri, L. and Taccardi, B. (1993*b*), 'Spread of excitation in a myocardial volume: Simulation studies in a model of anisotropic ventricular muscle activated by point stimulation', *J. Cardiovasc. Electrophysiol.* **4**(2), 144.
- Colli Franzone, P., Guerri, L. and Tentoni, S. (1990), 'Mathematical modelling of the excitation process in the myocardial tissue: Influence of the fibre rotation on the wavefront propagation and the potential field', *Math. Biosci.* **101**, 155–235.
- Courtemanche, M. and Winfree, A. T. (1991), 'Re-entrant rotating waves in a Beeler-Reuter based model of two-dimensional cardiac electrical activity', *International Journal of Bifurcation and Chaos* **1**(2), 431–444.
- Di Francesco, D. and Noble, D. (1985), 'A model of cardiac electrical activity incorporating ionic pumps and concentration changes', *Phil. Trans. R. Soc. Lond.* **B307**, 353–398.
- Drouhard, J. P. and Roberge, F. A. (1987), 'Revised formulation of the Hodgkin-Huxley representation of the sodium current in cardiac cells', *Comput. Biomed. Res.* **20**, 333–350.
- Dudel, J. and Rüdell, R. (1970), 'Voltage and time dependence of excitatory sodium current in cooled sheep Purkinje fibres', *Pfluegers Archiv. Gesamte Physiol. Menschen Tiere* **315**, 136–158.
- Durrer, D., van Dam, R. T., Freud, G. E., Janse, M. J., Meijler, F. L. and Arzbaecher, R. C. (1970), 'Total excitation of the isolated human heart', *Circulation* **21**, 899–912.
- Ebihara, L. and Johnson, E. A. (1980), 'Fast sodium current in cardiac muscle: A quantitative description', *Biophys. J.* **32**, 779–790.
- Ebihara, L., Shigeto, N., Lieberman, M. and Johnson, E. A. (1980), 'The initial inward current in spherical clusters of chick embryonic heart cells', *J. Gen. Physiol.* **75**, 437–456.
- FitzHugh, R. A. (1961), 'Impulses and physiological states in theoretical models of nerve membrane', *Biophys. J.* **1**, 445–466.
- Flügge, W. (1972), *Tensor Analysis and Continuum Mechanics*, Springer-Verlag, New York.
- Garfinkel, A. (1994), The VCDL model. Personal Fax correspondence.

- Gerhardt, M., Schuster, H. and Tyson, J. J. (1990), 'A cellular automaton model of excitable media including curvature and dispersion', *Science* **247**, 1563–1566.
- Glass, L., Hunter, P. J. and McCulloch, A. D., eds (1991), *Theory of Heart*, Springer-Verlag, New York.
- Grice, I. J. L., Smaill, B. H. and Hunter, P. J. (1993), 'Consistency of canine ventricular architecture: Is there a platonic heart?', *Circ. Res.* . submitted.
- Guevera, M. R. (1991), Mathematical modelling of the electrical activity of cardiac cells, *in* Glass et al. (1991), chapter 10, pp. 239–253.
- Gulrajani, R. M. (1988), 'Models of the electrical activity of the heart and computer simulation of the electrocardiogram', *CRC Crit. Rev. Biomed. Eng.* **16**, 1–66.
- Hagiwara, N., Masuda, H., Shoda, M. and Irisawa, H. (1992), 'Stretch-activated anion currents of rabbit cardiac myocytes', *J. Physiol.* **456**, 285–302.
- Henriquez, C. S. (1993), 'Simulating the electrical behaviour of cardiac tissue using the bidomain model', *CRC Crit. Rev. Biomed. Eng.* **21**(1), 1–77.
- Henze, C., Lugosi, E. and Winfree, A. T. (1990), 'Helical organizing centers in excitable media', *Can. J. Phys.* **68**, 683–710.
- Hilgemann, D. W. and Noble, D. (1987), 'Excitation-contraction coupling and extracellular calcium transients in rabbit atrium: Reconstruction of basic cellular mechanisms', *Proc. R. Soc. Lond. B* **230**, 163–205.
- Hille, B. (1984), *Ionic Channels of Excitable Membranes*, Sinauer, Sunderland.
- Hodgkin, A. L. and Huxley, A. F. (1952), 'A quantitative description of membrane current and its application to conductance and excitation in nerve', *J. Physiol.* **117**, 500–544.
- Hookings, A. G. (1988), A Computer Model of the Electrical Activation of the Heart, Master of engineering thesis, University of Auckland, Auckland, New Zealand.
- Hort, W. (1957), 'Mikrometrische untersuchungen an verschieden weiten meerschweinchenherzen', *Verhandl. Deut. Ges. Kreislaufforsch* **23**, 343–346.
- Hunter, P. J., McNaughton, P. A. and Noble, D. (1975), 'Analytical models of propagation in excitable cells', *Prog. Biophys. molec. Biol.* **30**(2/3), 99–144.

- Hunter, P. J., Nash, M. P. and Sands, G. B. (1996), Computational biology of the heart, *in* Panfilov and Holden (1996), chapter 12.
- Hunter, P. J., Nielsen, P. M. F., Smaill, B. H., Le Grice, I. J. and Hunter, I. W. (1993), An anatomical heart model with applications to myocardial activation and ventricular mechanics, *in* Pilkington et al. (1993), chapter 1, pp. 3–26.
- Hunter, P. J., Smaill, B. H., Nielsen, P. M. F. and Grice, I. J. L. (1996), A mathematical model of cardiac anatomy, *in* Panfilov and Holden (1996), chapter 11.
- Jack, J. J. B., Noble, D. and Tsien, R. W. (1983), *Electric Current Flow in Excitable Media*, Oxford University Press, Oxford, UK.
- Johnson, E. A. (1983), 'The generation of the cardiac action potential: After the first millisecond', *Ann. Biomed. Eng.* **11**, 159–176.
- Karma, A. (1993), 'Spiral breakup in model equations of action potential propagation in cardiac tissue', *Physical Review Letters* **71**, 1103–1106.
- Karpoukhin, M. G., Kogan, B. Y. and Karplus, W. J. (1994), The application of a massively parallel computer to the simulation of electrical wave propagation phenomena in the heart muscle using simplified models. Computer Science Department, UCLA.
- Katz, A. M. (1992), *Physiology of the Heart*, second edn, Raven Press, New York.
- Keener, J. P. (1987), 'Propagation and its failure in coupled systems of discrete excitable cells', *SIAM J. Appl. Math.* **47**, 556–572.
- Keener, J. P. (1988), 'On the formation of circulating patterns of excitation in anisotropic excitable media', *J. Math. Biol.* **26**, 41–56.
- Kikuchi, N. (1986), *Finite Element Methods in Mechanics*, Cambridge University Press.
- Kogan, B. Y., Karplus, W. J., Billett, B. S., Pang, A. T., Karagueuzian, H. S. and Khan, S. S. (1991), 'The simplified FitzHugh-Nagumo model with action potential duration restitution: Effects on 2D wave propagation', *Physica D* **50**, 327–340.
- Kogan, B. Y., Karplus, W. J., Billett, B. S. and Stevenson, W. G. (1992), 'Excitation wave propagation within narrow pathways: Geometric configurations facilitating unidirectional block and reentry', *Physica D* **59**, 275–296.

- Kohl, P., Kamkin, A. G., Kiseleva, I. S. and Noble, D. (1994), 'Mechanosensitive fibroblasts in the sino-atrial node region of rat heart: Interaction with cardiomyocytes and possible role', *Experimental Physiology* **79**, 943–956.
- Krassowska, W. and Neu, J. C. (1994), 'Effective boundary conditions for syncytial tissues', *IEEE Trans. Biomed. Eng.* **41**(2), 143–150.
- Lab, M. J. (1982), 'Contraction-excitation feedback in myocardium: Physiological basis and clinical relevance', *Circ. Res.* **50**(6), 757–766.
- Lab, M. J. (1991), 'Monophasic action potentials and the detection and significance of mechanoelectric feedback in vivo', *Prog. Cardiovasc. Dis.* **34**(1), 29–35.
- Lab, M. J. and Holden, A. V. (1991), Mechanically induced changes in electrophysiology: Implications for arrhythmia and theory, in L. Glass, P. J. Hunter and A. D. McCulloch, eds, 'Theory of Heart', Springer-Verlag, New York, chapter 21, pp. 561–581.
- Le Grice, I. J. (1992), A Finite Element Model of Myocardial Structure: Implications for Electrical Activation in the Heart, PhD thesis, University of Auckland.
- Le Grice, I. J., Hunter, P. J. and Smaill, B. H. (1994), Laminar structure of the heart II: Mathematical model. Submitted.
- LeGrice, I. J. (1992), A Finite Element Model of Myocardial Structure: Implications for Electrical Activation in the Heart, PhD thesis, University of Auckland, New Zealand.
- Leon, L. J. and Horacek, B. M. (1991), 'Computer model of excitation and recovery in the anisotropic myocardium. I: Rectangular and cubic arrays of excitable elements', *J. Electrocardiol.* **24**, 1–14.
- Lerman, B. B., Burkhoff, D., Yue, D. T. and Sagawa, K. (1985), 'Mechanoelectrical feedback: Independent role of preload and contractility in modulation of canine ventricular excitability', *J. Clin. Invest.* **76**, 1843–1850.
- Lorange, M. and Gulrajani, R. M. (1986), 'Computer simulation of the Wolff-Parkinson-White preexcitation syndrome with a modified Miller-Geselowitz heart model', *IEEE Trans. Biomed. Eng.* **33**(9), 862–873.
- Luo, C. H. and Rudy, Y. (1991), 'A model of the ventricular cardiac action potential: Depolarization, repolarization and their interaction', *Circ. Res.* **68**, 1501–1526.

- Luo, C. and Rudy, Y. (1994a), 'A dynamic model of the cardiac ventricular action potential: I. simulations of ionic currents and concentration changes', *Circ. Res.* **74**(6), 1071–1096.
- Luo, C. and Rudy, Y. (1994b), 'A dynamic model of the cardiac ventricular action potential: II. afterdepolarizations, triggered activity, and potentiation', *Circ. Res.* **74**(6), 1097–1113.
- MacCallum, J. B. (1900), 'On the muscular architecture and growth of the ventricles of the heart', *Johns Hopkins Hosp. Rep.* **9**, 307–335.
- MacKenna, D. A. (1994), Contribution of the Extracellular Collagen Matrix to the Mechanics of Ventricular Myocardium, PhD thesis, U.C.S.D.
- Mall, F. P. (1911), 'On the muscular architecture of the ventricles of the human heart', *Am. J. Anat.* **11**, 211–266.
- Mazzanti, M. and DeFelice, L. J. (1990), 'Ca channel gating during cardiac action potentials', *Biophys. J.* **58**, 1059–1065.
- McAllister, R. E., Noble, D. and Tsien, R. W. (1975), 'Reconstruction of the electrical activity of cardiac purkinje fibres', *J. Physiol.* **251**, 1–59.
- McLean, M. R. and Prothero, J. (1987), 'Coordinated three-dimensional reconstruction from serial sections at macroscopic and microscopic levels of resolution; the human heart', *Anat. Rec.* **219**, 434–439.
- McLean, M. R., Ross, M. A. and Prothero, J. (1989), 'Three-dimensional reconstruction of the myofiber pattern in the fetal and neonatal mouse heart', *Anat. Rec.* **224**, 392–406.
- Miller, C. E. and Henriquez, C. S. (1990), 'Finite element analysis of bioelectric phenomena', *CRC Crit. Rev. Biomed. Eng.* **18**(3), 207–233.
- Miller, III, W. T. and Geselowitz, D. B. (1978a), 'Simulation studies of the electrocardiogram I. the normal heart', *Circ. Res.* **43**(2), 301–314.
- Miller, III, W. T. and Geselowitz, D. B. (1978b), 'Simulation studies of the electrocardiogram II. ischemia and infarction', *Circ. Res.* **43**(2), 315–323.
- Moe, G. K., Reinbolt, W. C. and Abildskov, J. A. (1964), 'A computer model of atrial fibrillation', *Am. Heart J.* **67**, 200–220.

- Muler, A. L. and Markin, V. S. (1977a), 'Electrical properties of anisotropic nerve-muscle syncytia. I. distribution of the electronic potential', *Biophysics* **22**, 315.
- Muler, A. L. and Markin, V. S. (1977b), 'Electrical properties of anisotropic nerve-muscle syncytia. II. spread of flat front of excitation', *Biophysics* **22**, 518.
- Muler, A. L. and Markin, V. S. (1978), 'Electrical properties of anisotropic nerve-muscle syncytia. III. steady form of the excitation front', *Biophysics* **22**, 699–704.
- NAG (1993), *NAG Fortran Library – Mark 16*, The Numerical Algorithms Group Ltd, Wilkinson House, Jordan Hill Rd, Oxford, United Kingdom, OX28DR.
- Nash, M. P. (1998), *Mechanics and Material Properties of an Anatomically Accurate Mathematical Model of the Heart*, PhD thesis, University of Auckland, Auckland, New Zealand.
- Nielsen, P. M. F. (1987), *The Anatomy of the Heart: A Finite Element Model*, PhD thesis, University of Auckland, Auckland, New Zealand.
- Nielsen, P. M. F., Le Grice, I. J., Smaill, B. H. and Hunter, P. J. (1991), 'Mathematical model of geometry and fibrous structure of the heart', *Am. J. Physiol.* **260**(Heart Circ. Physiol. 29), H1365–H1378.
- Noble, D. (1962), 'A modification of the Hodgkin-Huxley equation applicable to purkinje fibre action and pacemaker potentials', *J. Physiol.* **160**, 317–352.
- Noble, D. and Noble, S. J. (1984), 'A model of the sino-atrial node electrical activity based on a modification of the DiFrancesco-Noble (1984) equations', *Proc. R. Soc. Lond. B* **222**, 295–304.
- Noble, D. and Tsien, R. W. (1968), 'The kinetics and rectifier properties of the slow potassium current in cardiac Purkinje fibres', *J. Physiol.* **195**, 185–214.
- Noble, D. and Tsien, R. W. (1969), 'Outward membrane currents activated in the plateau range of potentials in cardiac Purkinje fibres', *J. Physiol.* **200**, 205–232.
- Oden, J. T. (1972), *Finite Elements of Nonlinear Continua*, McGraw-Hill Book Company Inc., New York.

- Okajima, M., Fujino, T., Kobayashi, T. and Yamada, K. (1968), 'Computer simulation of the propagation process in excitation of the ventricles', *Circ. Res.* **23**, 203–211.
- Panfilov, A. V. and Holden, A. V. (1993), 'Computer simulation of re-entry sources in myocardium in two and three dimensions', *J. Theor. Biol.* **161**(3), 271–285.
- Panfilov, S. and Holden, A. V., eds (1996), *Computational Biology of the Heart*, Wiley.
- Penefsky, Z. J. and Hoffman, B. F. (1963), 'Effects of stretch on mechanical and electrical properties of cardiac muscle', *Am. J. Physiol.* **204**(3), 433–438.
- Pilkington, T. C. et al., eds (1993), *High-Performance Computing in Biomedical Research*, CRC Press Inc.
- Plonsey, R. and Barr, R. C. (1984), 'Current flow patterns in two-dimensional anisotropic bisyncytia with normal and extreme conductivities', *Biophys. J.* **45**, 557–571.
- Plonsey, R. and Barr, R. C. (1987), 'Mathematical modelling of electrical activity of the heart', *J. Electrocardiol.* **20**(3), 219–226.
- Pollard, A. E., Hooke, N. and Henriquez, C. S. (1993), Cardiac propagation simulation, in Pilkington et al. (1993), chapter 12, pp. 319–358.
- Pullan, A. J., Bradley, C. P. and Hunter, P. J. (1993a), The development of a high order coupled finite element/boundary element torso model, in 'Proceedings IEEE Engineering in Medicine and Biology Society 15th Annual International Conference', IEEE Press, pp. 760–761.
- Pullan, A. J., Bradley, C. P. and Hunter, P. J. (1993b), A high order coupled finite element/boundary element torso model, in 'Proceedings Computers in Cardiology', IEEE Computer Society Press, pp. 309–312.
- Raisz, E. (1962), *Principles of Cartography*, McGraw-Hill Book Company Inc., New York.
- Reinboldt, W., Ledly, R. S., Abildskov, J. A. and Oestreich, A. E. (1963), 'Simulation of the ventricles of the heart', *Proc. 16th Ann. Conf. Eng. Biol. Med* **5**, 32.
- Restivo, M., Craelius, W., Gough, W. P. and El-Sharif, N. A. (1990), 'A logical state model of reentrant ventricular activation', *IEEE Trans. Biomed. Eng.* **37**, 344–353.

- Roberts, D. and Scher, A. M. (1982), 'Effect of tissue anisotropy on extracellular potential fields in canine myocardium in situ', *Circ. Res.* **50**, 342–351.
- Rogers, J. M. and McCulloch, A. D. (1994a), 'A collocation-Galerkin finite element model of cardiac action potential propagation', *IEEE Trans. Biomed. Eng.* **41**(8), 743–757.
- Rogers, J. M. and McCulloch, A. D. (1994b), 'Nonuniform muscle fiber orientation causes spiral wave drift in a finite element model of cardiac action potential propagation', *J. Cardiovasc. Electrophysiol.* **5**, 496–509.
- Ruknudin, A., Sachs, F. and Bustamante, J. O. (1993), 'Stretch-activated ion channels in tissue-cultured chick heart', *Am. J. Physiol.* **264**, H960–H972.
- Savard, P., Roberge, F. A., Perry, J. B. and Nadeau, R. A. (1980), 'Representation of cardiac electrical activity by a moving dipole for normal and ectopic beats in the intact dog.', *Circ. Res.* **46**, 415–??
- Saxberg, B. E. H., Grumbach, M. P. and Cohen, R. J. (1985), A time dependent anatomically detailed model of cardiac conduction, in K. L. Ripley, ed., 'Computers in Cardiology 1985', IEEE Computer Society Press, Washington, D. C., p. 401.
- Scher, A. M. and Young, A. C. (1956), 'The pathway of ventricular depolarization in the dog', *Circ. Res.* **4**, 461–469.
- Schmitt, O. H. (1969), Biological information processing using the concept of interpenetrating domains, in K. N. Leibovic, ed., 'Information Processing in the Nervous System', Springer-Verlag, New York.
- Selvester, R., Collier, C. C. and Pearson, R. B. (1965), 'Analog computer model of the vectorcardiogram', *Circulation* **31**, 1965.
- Selvester, R. H., Kalaba, R., Collier, C. R., Bellman, R. and Kagiwada, H. (1967), 'A digital computer model of the vectorcardiogram with distance and boundary effects: Simulated myocardial infarction', *Am. Heart J.* **74**(6), 792–808.
- Selvester, R. H., Solomon, J. C. and Gillespie, T. L. (1968), 'Digital computer model of a total body electrocardiographic surface map. an adult male-torso simulation with lungs', *Circulation* **38**, 684–690.

- Sepulveda, N. G., Roth, B. J. and Wikswo, J. P. (1989), 'Current injection into a two-dimensional bidomain', *Biophys. J.* **55**, 987–999.
- Sepulveda, N. G. and Wikswo, Jr., J. P. (1987), 'Electric and magnetic fields from two-dimensional anisotropic bisyncytia', *Biophys. J.* **51**, 557–568.
- Sigurdson, W., Ruknudin, A. and Sachs, F. (1992), 'Calcium imaging of mechanically induced fluxes in tissue-cultured chick heart: Role of stretch-activated ion channels', *Am. J. Physiol.* **262**, H1110–H1115.
- Smaill, B. H. and Hunter, P. J. (1991), Structure and function of the diastolic heart: Material properties of passive myocardium, *in* Glass et al. (1991), chapter 1, pp. 1–29.
- Smith, J. M. and Cohen, R. J. (1984), 'Simple finite element model accounts for wide range of cardiac dysrhythmias', *Proc. Natl. Acad. Sci. USA* **81**, 233–237.
- Solomon, J. C. and Selvester, R. H. (1973), 'Simulation of measured activation sequence in the human heart', *Am. Heart J.* **85**(4), 518–524.
- Spach, M. S. and Heidlage, J. F. (1993), A multidimensional model of cellular effects on the spread of electrotonic currents and on propagating action potentials, *in* Pilkington et al. (1993), chapter 11, pp. 289–317.
- Staton, D. J., Friedman, R. N. and Wikswo, Jr., J. P. (1991), 'High-resolution SQUID magnetocardiographic mapping of action currents in canine cardiac slices', *Circulation Suppl.* **84**(II), 667.
- Streeter, Jr., D. D. (1979), Gross morphology and fiber structure of the heart, *in* S. R. Geiger, ed., 'Handbook of Physiology: The Cardiovascular System', Vol. I, American Physiology Society, Bethesda, MD, section 2.
- Streeter, Jr., D. D. and Bassett, D. L. (1966), 'An engineering analysis of myocardial fiber orientation in pig's left ventricle in systole', *Anat. Rec.* **155**, 503–511.
- Streeter, Jr., D. D., Spotnitz, H. M., Patel, D. P., Ross, Jr., J. and Sonnenblick, E. H. (1969), 'Fiber orientation in the canine left ventricle during diastole and systole', *Circ. Res.* **24**, 339–347.
- Taggart, P., Sutton, P. and Lab, M. (1992), 'Interaction between ventricular loading and repolarisation: Relevance to arrhythmogenesis', *Br. Heart J.* **67**, 213–215.

- Trayanova, N. and Pilkington, T. C. (1993), 'A bidomain model with periodic intracellular junctions: A one-dimensional analysis', *IEEE Trans. Biomed. Eng.* **40**(5), 424–433.
- Tung, L. (1978), A Bidomain Model for Describing Ischemic Myocardial D-C Potentials, PhD thesis, M.I.T.
- van Capelle, F. J. L. and Durrer, D. (1980), 'Computer simulation of arrhythmias in a network of coupled excitable elements', *Circ. Res.* **47**, 454–466.
- Wach, P., Killmann, R., Dienstl, F. and Eichinger, C. (1989), 'A computer model of human ventricular myocardium for simulation of ECG, MCG and activation sequence including reentry rhythms', *Basic Res. Cardiol.* **84**, 404–413.
- Wang, C. Y., Bassingthwaighe, J. B. and Weissman, L. J. (1992), 'Bifurcating distributive system using Monte Carlo method', *Mathl. Comput. Modelling* **16**(3), 91–98.
- Weidmann, S. (1952), 'The electrical constants of purkinje fibres', *J. Physiol.* **118**, 348–360.
- Weidmann, S. (1955), 'The effect of the cardiac membrane potential on the rapid availability of the sodium carrying system', *J. Physiol.* **127**, 213–224.
- Weidmann, S. (1970), 'Electrical constants of trabecular muscle from mammalian heart', *J. Physiol.* **210**, 1041–1054.
- Wilson, F. N., MacLoed, A. G. and Barker, P. S. (1933), *The Distribution of the Currents of Action and of Injury Displayed by Heart Muscle and Other Excitable Tissues*, University of Michigan Press, Ann Arbor.
- Winfree, A. T. (1990a), 'Stable particle-like solutions to the nonlinear wave equations of three-dimensional excitable media', *SIAM Review* **32**(1), 1–53.
- Winfree, A. T. (1990b), Ventricular reentry in three dimensions, in D. P. Zipes and J. Jalife, eds, 'Cardiac Electrophysiology From Cell to Bedside', W. B. Saunders Company, chapter 26, pp. 224–234.
- Winfree, A. T. (1990c), 'Vortex action potentials in normal ventricular muscle', *Ann. N. Y. Acad. Sci.* **591**, 190–207.
- Winfree, A. T. (1991), 'Varieties of spiral wave behaviour: An experimentalist's approach to the theory of excitable media', *CHAOS* **1**(3), 303–334.

- Zeng, J., Laurita, K. R., Rosenbaum, D. S. and Rudy, Y. (1995), 'Two components of the delayed rectifier k^+ current in ventricular myocytes of the guinea pig type: Theoretical formulation and their role in repolarization', *Circ. Res.* **77**(1), 140–152.
- Zienkiewicz, O. C. and Taylor, R. L. (1994), *The Finite Element Method*, fourth edn, McGraw-Hill Book Company Europe, Berkshire.

Index

Important references and definitions of the item are indicated by a page number typeset in a **bold** face.

A

actin, **10**, 23, 245
action potential, 11, **16**, **21**, 23, 26, 34, 35, 38, 54, 66, 69, 72, 83, 90, 92, 94, 108, 112, 115, 116, 118, 122, 130, 187, 196, 230, 283
action potential duration (APD), **23**, 78, 112, 114, 116, 118, 119, 121, 122, 189
actomyosin, **11**
anisotropic, 41, 42, 44, 50, 52, 54, 55, 126, 128, 130, 163, 180, 193, 212, 263, 264, 268
apex, **8**, 12, 13, 147, 231, 232, 237, 272, 285
arrhythmia, 1, 2, **27**, 29, 282
ATP, **10**, 107, 282
atrium, 1, 3, **8**, 9, 13, 16–18, 27, 28, 36, 44, 46, 57, 58, 103, 222, 230, 283
AV node, **16**, 17, 21, 26–28

B

base, **8**, 12, 13
base vector, **144**
basis function, **128**, **134–143**, 231
 cubic Hermite, **140**
 linear Lagrange, **134**

 mixed, 142
 multidimensional, **135**, 139, 141
 quadratic Lagrange, **138**

Beeler-Reuter model, *see* ionic current model, Beeler-Reuter

Belousov-Zhabotinsky reagent, 124

bidomain equations, 52, 127, **157**, 162, 201

bidomain model, **45–55**, **200**, 281

boundary conditions, 53, **160**, 202, 205

boundary element method (BEM), 124, **130**

bundle branch block, **28**

bundle of His, **16**, 17

C

cable theory, **47**

calcium concentration

 intracellular $[Ca]_i$, **101**, 110, 250, **262**

 tension relationship, **251**

calcium-induced calcium release, 23, **102**, 110

cardiac anatomy, **8**

cellular automata, **36–42**, 128

Christoffel symbol, **146**

CMISS, **169**, 286

collagen, **13**, 14

collocation method, 132, **154–162**, 281

conductivity tensor, **50**, 52, 150, 158, 212

continuum, 13, 48, 50, 123
 contravariant derivative, 147
 convergence, 173
 spatial resolution, 176
 temporal resolution, 174
 coordinate system
 cylindrical polar, **148**
 material, **50**, 51, 133, 150, **152**, 156,
 157, 222, 231, 248
 prolate spheroidal, **149**, 231
 rectangular cartesian, **147**
 wall, 152
 covariant derivative, 147
 crossbridge, **10**
 cubic model, *see* ionic current model,
 cubic
 current
 potassium, **63**, 68, 76
 sodium, **61**, 67, 73, 83, 88, **91**, 99,
 104, 108
 current density, 51
 curvature, 39

D

depolarisation, 4, **20**, 21–23, 26, 29, 64,
 67, 68, 71, 82, 88, 89, 91, 92,
 112, 114, 121, 245
 Di Francesco-Noble model, *see* ionic
 current model, Di
 Francesco-Noble
 diastole, **8**, 22
 dipole model, 32, **33**
 Drouhard-Roberge model, *see* ionic
 current model,
 Drouhard-Roberge
 DTAR, 128, **164**, 173

E

Ebihara-Johnson model, *see* ionic
 current model,
 Ebihara-Johnson
 eikonal model, **55**, 112, 221
 Einstein summation convention, 133
 electrocardiogram (ECG), 32, **34**
 electromechanical coupling, 11, **23**,
 245, 272, 278, 281
 strong, **250**
 weak, **246**
 electrotonic current, **25**, 221
 Euler method, 125, 160
 excitation-contraction coupling, *see*
 electromechanical coupling
 extracellular
 connective tissue, 14
 domain, **47**, 50, 52–54
 equation, **52**, 132, 162, 163,
 201–209
 ion concentration, **18**, 56, 66, 86,
 94, 102
 extramyocardial
 domain, **48**, 52, 53, 163, 200, 209

F

fading-memory model, 250
 fibre
 angle, 11, 13, 151, **153**, 156, **180**,
 196, 216, 219, 227, **232**, 234,
 264, 268
 axis, **152**, 222, 225, 239, 264
 finite difference method, 55, **124–128**,
 217
 explicit, **125**, 132
 implicit, **126**
 semi-implicit, **127**

- finite elasticity, 246
- finite element, 4
- mesh, 128, 132, 147, **154**, 158, 169, 219, 236, 272, 276
 - method (FEM), 54, 124, **128–130**, 132, 154, 162, 163, 201, 230, 246, 281
 - collocation, **129**
 - Galerkin, 128
 - nodes, **134**, 140, 159, 164, 252
- FitzHugh-Nagumo model, *see* ionic current model, FitzHugh-Nagumo
- fluid shift model, 278
- G**
- GMRES, 252
- H**
- Hammer projection, 239, **285**
- Hill relation, 251
- Hodgkin-Huxley model, *see* ionic current model, Hodgkin-Huxley
- Huygen's wavefront, 5, 35, **42**
- I**
- imbrication angle, **13**, **153**, 223
- index notation, 133
- interpolation function, *see* basis function
- interstitial domain, **49**
- intracellular
- calcium concentration, *see* calcium concentration, intracellular $[Ca]_i$
 - domain, 20, 27, **47**, 50, 54, 202
 - ion concentration, **18**, 56, 66, 94
- ion channel, **17**, **19**, 59
- stretch-activated, 246
- ionic current model, **52**, 54, 131, 281
- Beeler-Reuter (BR), **82**, 93, 100, 105, 114, 127, 187, 196, 250, 262
 - biophysical, 56, 57
 - cubic, **112**, 171
 - Di Francesco-Noble (DFN), **93**, 109, 262
 - Drouhard-Roberge (DR), **91**, 187
 - Ebihara-Johnson (EJ), 54, **87**, 91, 103, 127
 - FitzHugh-Nagumo (FHN), 55, **114**, 126, 183
 - Rogers extensions, **115**, 129, 185, 237
 - Hodgkin-Huxley (HH), 20, 52, **58**, 67, 71, 112
 - Karma, **121**
 - Luo-Rudy I (LRI), **103**, 114
 - Luo-Rudy II (LRII), **106**, 250, 262
 - modifications, **110**
 - McAllister-Noble-Tsien (MNT), **71**, 82, 83, 86, 93–97, 100, 105
 - Noble (1962), **66**, 71, 74, 76, 80, 82
 - simplified, 56, 111
 - van Capelle-Durrer (VCD), **117**, 126, 186, 189
 - modifications, **118**, 250
- ischemia, 1, **29**, 118, 121, 186, 189
- isotropic, 42, 53, 127, **171**, 176, 187, 191, 201, 209, 223, 239, 263, 264, 268
- K**
- Karma model, *see* ionic current model, Karma

L

Laplace's equation, 53, 163
Luo-Rudy model, *see* ionic current
model, Luo-Rudy I

M

mapping system, 30, 212
material coordinate system, *see*
coordinate system, material
McAllister-Noble-Tsien model, *see*
ionic current model,
McAllister-Noble-Tsien (MNT)
mechanics
 active, 250, 278
 passive, 246, 278
metabolism, 283
metric tensor, 144, 158, 179, 248
microstructure, 4, 5, 11, 12–14, 44, 46,
 50, 131, 132, 150, 152, 155, 212,
 230, 232, 237, 240, 245
monodomain equation, 52, 53–55, 127,
 132, 157, 163, 171, 208
movies, 167
multigrid, 163, 201, 283
myosin, 10, 11, 23, 245

N

Neumann, 160
Noble (1962) model, *see* ionic current
model, Noble (1962)
nonlinear optimisation, 6, 216, 282

O

orthotropic, 4, 42, 45, 50, 150, 222, 227,
 240, 247, 282

P

papillary muscle, 9

pole-zero, 246, 278

Purkinje fibre network, 3, 16, 17, 18,
 22, 28, 44–46, 57, 58, 66, 71, 93,
 209, 217, 222, 283

R

refractory
 period, 23, 30, 36, 39, 40, 44, 112,
 189
 state, 19, 26, 36, 37, 39, 41
repolarisation, 22, 23, 61, 76, 78–80, 89,
 112, 114, 121, 127, 128, 131, 196
residual stress, 278
rotors, *see* spiral wave

S

SA node, 15, 21, 26, 27, 103, 283
sarcolemma, 10, 11, 107, 108
sarcomere, 10, 11, 251
sarcoplasmic reticulum, 11, 23, 94, 101,
 103, 106, 245, 251, 262
scale factor, 141, 142
shape function, *see* basis function
sheet, 13, 14, 36, 45, 46, 50, 54, 152,
 230, 282
 angle, 153, 223
 axis, 152
sheet-normal axis, 152, 223
spatial adaption, *see* DTAR
spiral wave, 30, 55, 120, 189, 191, 193,
 196, 227, 248, 255, 262, 264, 268
syncytium, 47
systole, 8

T

temporal adaption, 126
threshold, 22, 23, 26, 39, 76, 104, 112,
 113, 115, 160, 230

torso, 4, 6, 34, 44, 48, 53, 54, 162, 163,
166, 200, 201, **208**, 272, 281, 283

transmembrane potential, 17, 21, 35,
49, 52, 59, 61, 66, 98, 111, 114,
116, 117, 121, 127, 158, 162, 163,
167, 172, 173, 183, 200, 230,
242, 250

transversely isotropic, 11, 44, 50, **222**,
225, 237, 239, 282

troponin, 23, 110

V

van Capelle-Durrer model, *see* ionic
current model, van
Capelle-Durrer (VCD)

vectorcardiogram (VCG), **34**

ventricle, 1, 3, **8**, 9, 11–13, 16, 18, 21, 22,
27, 28, 30, 34, 36, 42, 44, 46, 57,
58, 82, 91, 92, **103**, 108, 111, 131,
147, 149, 150, 152, 153, 166,
167, 187, 217, 222, 230–232,
234, 236, 239, 245, 281, 283, 285

W

weighting function, *see* basis function

Wolff-Parkinson-White (WPW)
syndrome, **28**, 44